A UNITED STATES DEPARTMENT OF COMMERCE PUBLICATION

SECTION A

JOURNAL OF RESEARCH

of the NATIONAL BUREAU OF STANDARDS

JNBAAR 77A (6) 691–786, Nov.-Dec. 1973

Physics and Chemistry

U.S. DEPARTMENT OF COMMERCE
National Bureau of Standards

Journal of Research

of the

National Bureau of Standards

A. Physics and Chemistry

Nov.–Dec. • 1973

VOLUME • 77A

NUMBER • 6

Editor: C. W. Beckett

Associate Editor: D. D. Wagman

Publication dates:
Feb. 1, Apr. 1, June 1, Aug. 1, Oct. 1, Dec. 1, 1973

J. Res. Nat. Bur. Stand. (U.S.), A

JOURNAL OF RESEARCH

The National Bureau of Standards Journal of Research reports research and development in the fields of activity shown at right. Also included from time to time are survey articles on topics closely related to the Bureau's scientific and technical program.

The Journal is published in two separate sections as follows:

A. Physics and Chemistry

Contains papers of interest primarily to scientists working in these fields. Issued six times a year. Annual subscription: domestic, $17.00; foreign, $21.25. Single copy, varies.

B. Mathematical Sciences

Presents studies and compilations designed mainly for the mathematician and the theoretical physicist. Issued quarterly. Annual subscription: domestic, $9.00; foreign, $11.25. Single copy, $2.25.

The National Bureau of Standards[1] was established by an act of Congress March 3, 1901. The Bureau's overall goal is to strengthen and advance the Nation's science and technology and facilitate their effective application for public benefit. To this end, the Bureau conducts research and provides: (1) a basis for the Nation's physical measurement system, (2) scientific and technological services for industry and government, (3) a technical basis for equity in trade, and (4) technical services to promote public safety. The Bureau consists of the Institute for Basic Standards, the Institute for Materials Research, the Institute for Applied Technology, the Institute for Computer Sciences and Technology, and the Office for Information Programs.

THE INSTITUTE FOR BASIC STANDARDS provides the central basis within the United States of a complete and consistent system of physical measurement; coordinates that system with measurement systems of other nations; and furnishes essential services leading to accurate and uniform physical measurements throughout the Nation's scientific community, industry, and commerce. The Institute consists of a Center for Radiation Research, an Office of Measurement Services and the following divisions:

Applied Mathematics — Electricity — Mechanics — Heat — Optical Physics — Nuclear Sciences[2] — Applied Radiation[2] — Quantum Electronics[3] — Electromagnetics[3] — Time and Frequency[3] — Laboratory Astrophysics[3] — Cryogenics[3].

THE INSTITUTE FOR MATERIALS RESEARCH conducts materials research leading to improved methods of measurement, standards, and data on the properties of well-characterized materials needed by industry, commerce, educational institutions, and Government; provides advisory and research services to other Government agencies; and develops, produces, and distributes standard reference materials. The Institute consists of the Office of Standard Reference Materials and the following divisions:

Analytical Chemistry — Polymers — Metallurgy — Inorganic Materials — Reactor Radiation — Physical Chemistry.

THE INSTITUTE FOR APPLIED TECHNOLOGY provides technical services to promote the use of available technology and to facilitate technological innovation in industry and Government; cooperates with public and private organizations leading to the development of technological standards (including mandatory safety standards), codes and methods of test; and provides technical advice and services to Government agencies upon request. The Institute consists of a Center for Building Technology and the following divisions and offices:

Engineering and Product Standards — Weights and Measures — Invention and Innovation — Product Evaluation Technology — Electronic Technology — Technical Analysis — Measurement Engineering — Structures, Materials, and Life Safety[4] — Building Environment[4] — Technical Evaluation and Application[4] — Fire Technology.

THE INSTITUTE FOR COMPUTER SCIENCES AND TECHNOLOGY conducts research and provides technical services designed to aid Government agencies in improving cost effectiveness in the conduct of their programs through the selection, acquisition, and effective utilization of automatic data processing equipment; and serves as the principal focus within the executive branch for the development of Federal standards for automatic data processing equipment, techniques, and computer languages. The Center consists of the following offices and divisions:

Information Processing Standards — Computer Information — Computer Services — Systems Development — Information Processing Technology.

THE OFFICE FOR INFORMATION PROGRAMS promotes optimum dissemination and accessibility of scientific information generated within NBS and other agencies of the Federal Government; promotes the development of the National Standard Reference Data System and a system of information analysis centers dealing with the broader aspects of the National Measurement System; provides appropriate services to ensure that the NBS staff has optimum accessibility to the scientific information of the world. The Office consists of the following organizational units:

Office of Standard Reference Data — Office of Technical Information and Publications — Library — Office of International Relations.

---

[1] Headquarters and Laboratories at Gaithersburg, Maryland, unless otherwise noted; mailing address Washington, D.C. 20234.
[2] Part of the Center for Radiation Research.
[3] Located at Boulder, Colorado 80302.
[4] Part of the Center for Building Technology.

U.S. DEPARTMENT OF COMMERCE
Frederick B. Dent, Secretary
NATIONAL BUREAU OF STANDARDS
Richard W. Roberts, Director

Order all publications from the Superintendent of Documents
U.S. Government Printing Office, Washington, D.C. 20402

The Secretary of Commerce has determined that the publication of this periodical is necessary in the transaction of the public business required by law of this Department. Use of funds for printing this periodical has been approved by the Director of the Office of Management and Budget through June 30, 1976.

JOURNAL OF RESEARCH of the National Bureau of Standards—A. Physics and Chemistry
Vol. 77A, No. 6, November–December 1973

Absolute Isotopic Abundance Ratio and Atomic Weight of a Reference Sample of Rhenium

John W. Gramlich,* Thomas J. Murphy, Ernest L. Garner, and William R. Shields

Institute for Materials Research, National Bureau of Standards, Washington, D.C. 20234

(August 10, 1973)

An absolute value has been obtained for the isotopic abundance ratio of a reference sample of rhenium, using surface emission mass spectrometry. Samples of known isotopic composition, prepared from nearly isotopically pure separated rhenium isotopes, were used to calibrate the mass spectrometers. The resulting absolute $^{185}Re/^{187}Re$ ratio is 0.59738 ± 0.00039, which yields atom percents of $^{185}Re = 37.398 \pm 0.016$ and $^{187}Re = 62.602 \pm 0.016$. The atomic weight calculated from this isotopic composition is 186.20679 ± 0.00031. The indicated uncertainties are overall limits of error based on 95 percent confidence limits for the mean and allowances for the effects of known sources of possible systematic error.

Key words: Absolute ratio; atomic weight; isotopic abundance; rhenium.

1. Introduction

The Isotopic Analysis Section of the National Bureau of Standards is conducting a long term program of absolute isotopic abundance ratio and atomic weight determinations, using solid-sample thermal or surface ionization mass spectrometry. Previous elements studied include silver [1],[1] chlorine [2], copper [3], bromine [4], chromium [5], magnesium [6], lead [7], boron [8], and rubidium [9]. The present work extends the study to rhenium.

To obtain absolute isotopic ratios from the observed or relative measurements made on a mass spectrometer, it is necessary to calibrate the instrument, using samples of accurately known isotopic ratios of the element under study. These synthetic isotopic standards, prepared from chemically pure and nearly isotopically pure separated isotopes, provide a bias correction (calculated isotope ratio/observed isotope ratio) which when applied to the observed isotope ratio of the reference sample being calibrated allow an absolute ratio to be calculated for this sample. The atomic weight can then be calculated from the absolute isotopic abundances and the atomic masses reported by Wapstra and Gove [10].

Natural rhenium consists of two isotopes, ^{185}Re and ^{187}Re, the latter of which is radioactive with reported half-life values ranging from 4×10^{12} to 3×10^{10} years [11, 12]. The more recent determinations trend toward the lower half-life value. Based on the lower half-life value, it would take about 18 million years to produce a 1 ppm change in the atomic weight of rhenium.

Prior to 1955, the accepted atomic weight of rhenium was 186.31 (O = 16) based on the work of Hönigschmid and Sachtleben [13], who determined the ratio of $AgReO_4/AgBr$ to be 1.90735. This calculates to an atomic weight of 186.28 on the presently accepted scale of $^{12}C = 12$. The currently accepted value for the atomic weight is 186.2, based on the relative mass spectrometric measurements of White and Cameron [14] who reported an isotopic composition of 37.07 percent ^{185}Re and 62.93 percent ^{187}Re.

A number of other mass spectrometric determinations of the isotopic composition of rhenium have been reported in the literature [15, 16, 17], none of which may be considered absolute.

For this work seven synthetic isotope standards for rhenium were prepared with $^{185}Re/^{187}Re$ ratios ranging from approximately 10 to 0.1. The wide range in isotopic composition for the synthetic standards was used to further support the supposition that the bias of each instrument was independent of isotopic composition.

2. Experimental Procedure

2.1. Mass Spectrometry

Isotope ratio measurements were made on two solid-sample mass spectrometers. The first instrument was a two stage mass spectrometer constructed from two 90°, 12-in radius flight tubes connected to produce

*NRC–NBS Postdoctoral Research Associate, 1970–72.

[1]Figures in brackets indicate the literature references at the end of this paper.

an "S" configuration. The instrument was equipped with an air operated beam valve [18] and a thin lens "Z" focussing source [19]. Ion detection at the end of the second stage was accomplished with a 17-stage ion multiplier coupled to an amplifier, discriminator, and scaler [18]. The magnetic field of each stage was independently controlled by a controller-gaussmeter. Each mass was brought into focus at the collector by computer switching of the magnetic fields. Timing and data collection were also under computer control.

The second instrument was a single stage 60°, 6-in radius of curvature mass spectrometer equipped with a "Z"-lens source identical to that used in the two stage instrument. The collector was a deep bucket Faraday cage type equipped with a 50 percent transmission grid shadowing a series of suppression grids [19]. The measuring circuit consisted of two vibrating reed electrometers operated as a master-slave combination, a voltage to frequency converter, and a scaler-timer. As with the first instrument, data collection was by computer control.

Prior to this study, it was established that the bias of the two stage instrument was independent of the isotopic ratio through the measurement of a series of seventeen uranium isotopic standards covering a range of isotopic compositions from approximately $^{235}U/^{238}U = 0.005$ to 187. That a single bias correction is valid for the single stage instrument over the range of isotopic compositions measured has been established previously through the measurement of synthetic isotopic mixtures of boron [8], chromium [5], magnesium [6], and rubidium [9].

Samples were mounted on a single tungsten filament which had been previously degassed in a vacuum at a temperature of approximately 2000 °C and under a potential field. No rhenium background was observed from degassed filaments. About 10 μl of sample solution containing 5 mg/ml of rhenium as perrhenic acid in 5 percent sulfuric acid was placed on a tungsten filament. A high purity platinum wire anode, which was cleaned with dilute nitric acid between each plating, was placed on the top of the solution drop and rhenium was electrolytically deposited onto the tungsten at a potential of 2.25 V and a current density of 10 ma/cm^2. Approximately 1 h was required for deposition. The filament was immersed in triple-distilled water, dried under a heat lamp and placed in a bell jar purged with extra-dry hydrogen. The samples were reduced in a hydrogen atmosphere by passing a current through the filament. For samples analyzed on the two stage instrument, the current was increased slowly until white vapors were seen to emanate from the filament. After 5 s at this temperature the current was increased until the filament temperature was just below red heat. The current was turned off after 10 s at this temperature. The above plating and hydrogen reduction procedure was repeated with a second 10 μl drop of solution after which the filament was immediately placed into the mass spectrometer. Samples were analyzed on the two stage instrument at a filament temperature of 1900 °C.

Samples analyzed on the single stage machine were treated in a slightly different manner during the hydrogen reduction step. The filament was heated until fuming was observed. After fuming ceased, the current was slowly increased until the sample deposit started to bubble and change from black to gray in color. The current was maintained at this setting for 1 min and then increased until a faint red glow was observed in the filament. The current was then reduced to a point where the red glow was no longer visible and allowed to remain at this temperature for 30 s. This plating and hydrogen reduction was repeated for a total of three times after which the filament was placed into the mass spectrometer and analyzed at a temperature of 2100 °C.

Although the analysis procedure used by each operator was somewhat different, each operator performed all of his analyses in an identical manner. Filament temperature, heating pattern, signal intensity, and time of data taking were controlled within strict limits. No filament fractionation was observed during the analyses on the two stage instrument, however, at the higher filament temperature used on the single stage mass spectrometer a small amount of fractionation (less than 0.1%) was observed during the analyses.

2.2. Purification of the Separated Isotopes

Electromagnetically separated ^{185}Re and ^{187}Re isotopes, in the form of rhenium metal powder, were obtained from the Isotopes Division, Oak Ridge National Laboratory of the Union Carbide Nuclear Company. The ^{185}Re was designated Series PF Sample 184501 and the ^{187}Re was designated Series DD Sample 135001. The Certificates of Analysis which accompanied each sample included a semiquantitative spectrographic analysis which showed that the principal impurities were sodium, potassium and calcium at greater than 0.1 percent. While these elements would not interfere with the assay method for rhenium, several others which were reported at the 0.02 to 0.05 percent concentration range could interfere. Among these elements were molybdenum, vanadium, tungsten, bismuth, mercury, tin, silver, lead, and platinum all of which interfere with the assay of rhenium by tetraphenylarsonium chloride [20, 21] by forming insoluble compounds.

To reduce these impurities to a level low enough so that they could not cause a significant error in the determination of the rhenium ion in solutions of these isotopes, the separated isotope samples were further purified by a combination of chloride precipitation to remove insoluble chlorides, cation exchange to remove cationic inpurities, anion exchange to remove anionic impurities and electro-deposition to separate the purified rhenium from the organic material dissolved from the ion exchangers.

Each separated isotope was treated as follows: The rhenium metal powder (about 0.5 g) was dissolved in 50 ml of 4*N* nitric acid. The resulting solution was evaporated to constant volume at about 50 °C. (The

temperature was kept low so as to minimize the loss of rhenium through volatilization.) The residue was taken up in a little water and 1 ml of 6*N* hydrochloric acid was added to precipitate insoluble chlorides. The solution was again evaporated to constant volume at about 50 °C, and the residue taken up in about 75 ml H_2O. The solution was filtered through fine textured filter paper and passed through a cation exchange column containing about 20 ml of AG 50×8, 100–200 mesh, strongly acidic cation exchange resin to remove cationic impurities. The column was washed with 100 ml of water and the eluent was evaporated to about 35 ml.

The perrhenic acid solution was then passed through an anion exchange column containing 35 ml of AG 1×8 resin, 100–200 mesh, strongly basic anion exchange resin. The anionic impurities were eluted by successive elution with 50 ml H_2O, 100 ml of a solution 1*N* in NH_4OH and 1*N* in NH_4Cl, 75 ml H_2O, 100 ml 1*N* HNO_3, and 50 ml H_2O. Rhenium was then eluted with 350 ml of 10*N* HNO_3. This solution was then evaporated to constant volume of perrhenic acid with the last few ml being evaporated at about 50 °C to minimize the loss of rhenium. The residue was taken up in 200 ml of 5 percent (w/v) H_2SO_4, transferred to a 400 ml quartz beaker and diluted to 300 ml with 5 percent (w/v) H_2SO_4.

Rhenium metal was electrodeposited onto a platinum gauze cylindrical cathode (cylinder 5 cm × 1.2 cm) at an applied potential of 2.6V. The solution was stirred magnetically using a Teflon[2] covered stirring bar. After overnight electrolysis, the cathode was washed with water and the rhenium dissolved with 50 ml of 8*N* HNO_3. The electrodeposition was repeated until no rhenium deposited on overnight plating (five electrodepositions). After each plating, the rhenium was dissolved with the 50 ml of 8*N* HNO_3. A small amount of 30 percent H_2O_2 was added to the electrolyte between electrolysis to dissolve the rhenium which deposted on the stirrer or beaker.

The nitric acid solution containing the purified rhenium was evaporated to constant volume of perrhenic acid at low heat (50 °C). The residue was then taken up in a few ml of 6*N* HCl and again evaporated to perrhenic acid at low heat. This addition and evaporation of HCl was repeated six times to insure the removal of nitrate ion which interferes with the assay method for rhenium.

2.3. Preparation and Analysis of the Separated Isotope Solutions

The purified $H^{185}ReO_4$ and $H^{187}ReO_4$ were taken up in about 50 ml of H_2O, filtered, and transferred to special 200 ml borosilicate glass flasks. These flasks were constructed from volumetric flasks by cutting the neck of each flask about 1 cm from the body and tooling the neck for a No. 0 polyethylene stopper. The solutions were diluted to about 140 ml and 0.5 ml of 30 percent H_2O_2 was added to each. After loosly closing the flask with polyethylene stoppers, the solutions were heated overnight at low heat to insure the complete oxidation of any reduced rhenium to the perrhenate state. The excess hydrogen peroxide was then removed by adding a small piece of platinum foil to each solution and heating the loosly stoppered flask overnight.

A preliminary assay of the rhenium content of each separated isotope solution was effected by adding 2 ml of 2*N* NaCl and 2 ml of 2 percent tetraphenylarsonium chloride solution to a 15 ml, fine porosity, borosilicate glass filtering crucible. A weighed 1 ml portion of the rhenium solution was added and mixed by swirling to precipitate tetraphenylarsonium perrhenate. After standing two hours, the solution was removed from the crucible by vacuum suction and the precipitate was washed three times with small amounts of water. The approximate rhenium content of the solution was calculated from the weight of the precipitate and the weight of the solution. The volume of the solution was then adjusted so the concentration would be close to 18 μmol Re/g.

Previous tests with known rhenium solutions showed that this method is accurate to about 1 percent of the rhenium present.

The solution of $H^{185}ReO_4$ was designated "Re 185" and the solution of $H^{187}ReO_4$ was designated "Re 187".

(a) Nitrate Analysis—Since nitrate ion forms an insoluble compound with the tetraphenylarsonium ion, $(C_6H_5)_4As^+$, used to assay the rhenium, both solutions were analyzed for nitrate. The "Re 185" solution was analyzed for nitrate ion before the addition of hydrogen peroxide by the brucine sulfate test [22] and was found to contain less than 0.0001 percent NO_3^-. The "Re 187" solution was analyzed for nitrate after the addition of hydrogen peroxide. It was necessary to make the sample alkaline and evaporate to dryness to destroy the last trace of H_2O_2 before determining nitrate by brucine test. This solution was also found to contain less than 0.0001 percent NO_3^-.

(b) Impurity Analysis—Samples of the "Re 185" and "Re 187" solutions were analyzed for impurity elements by isotope-dilution spark source mass spectrometry [23] Samples equivalent to about 5 mg of Re were spiked with 10^{-7}g of ^{109}Ag, ^{137}Ba, ^{44}Ca, ^{111}Cd, ^{53}Cr, ^{65}Cu, ^{54}Fe, ^{113}In, ^{41}K, ^{26}Mg, ^{97}Mo, ^{62}Ni, ^{206}Pb, ^{195}Pt, ^{82}Se, ^{117}Sn, ^{86}Sr, ^{125}Te, ^{203}Tl, ^{183}W, and ^{67}Zn. The solutions were evaporated to small drops, evaporated onto gold wires and analyzed by spark source mass spectrometry. In addition to these elements Bi and Mn which are mononuclidic elements were estimated by comparing to other nuclides. Table 1 shows the results of these analyses as well as the results of the analysis of a doped natural rhenium sample which was purified in the same manner as the separated isotope. This sample had been doped with 0.1 percent of Ag, Bi, Cr, Mn, Mo, Pb, Sn, and V to determine the efficiency of the purification in removing elements which could interfere with the assay of the rhenium solutions.

[2] A commercial material is identified in this paper in order to adequately specify experimental procedure. Such identification does not imply recommendation or endorsement by the National Bureau of Standards.

TABLE 1. *Analysis of purified rhenium*

Element	Natural Re (ppm)	"Re 185" (ppm)	"Re 187" (ppm)
Ag	[a] 0.3	1	1
Ba	0.5	2	0.5
Bi [b]	[a] 0.2	0.2	0.2
Ca	3	5.8	5
Cd	2	5	4
Cr	[a] 1	1.5	0.4
Cu	25	5.7	12
Fe	11	10	5.1
K	6	18	16
Mg	2	1.6	1.2
Mn [c]	[a] 0.5	0.5	0.5
Mo	[a] 0.7	≤ 9	2
Ni	4	4	1
Pb	[a] 1.7	4.3	2.3
Pt		160	14
Se	< 3	< 5	< 3
Sn	[a] 0.8	2.7	1
Sr	0.2	0.5	0.2
Te	0.3	1	1
V [c]	[a] ≤ 0.5	≤ 0.5	≤ 0.5
W	≤ 5	≤ 3	2
Zn	3	17	3

[a] Concentration before purification – 1000 ppm.
[b] Compared to ^{206}Pb.
[c] Compared to ^{53}Cr and ^{54}Fe.

The only element that was detected at a concentration level high enough to interfere with the assay of rhenium was platinum at 160 ppm in the "Re 185" solution. This apparently came from the platinum cathode used for the rhenium purification. To determine how much of this platinum precipitated with the tetraphenylarsonium perrhenate in the assay of the "Re 185" solution, the material was analyzed for platinum by isotope dilution–spark source mass spectrometry. After the assay, one of the precipitated samples was dissolved in acetone and an amount equivalent to 5 mg of Re was spiked with 10^{-7} g ^{195}Pt. Enough water was added to make the solution about 50 percent in H_2O and the solution was passed through a cation exchange column (6.5 cm × 1.2 cm filled to 3.5 cm with AG 50 × 8, 100–200 mesh cation exchange resin) and washed with about 20 ml of water to free the solution of tetraphenylarsonium ion. The eluate was evaporated and analyzed by spark source mass spectrometry as the previous samples. The platinum was found to be 20 ppm in the precipitate and a small correction (35 ppm) based on the Pt being present as $[(C_6H_5)_4As]_2PtCl_6$ has been applied to the weights of precipitate in the assay of the "Re 185" solution.

2.4. Assay of Separated Isotope Solutions

Four weighed portions of about 15 g were withdrawn from each separated isotope solution in the following manner. A 4-in platinum needle was inserted through a No. 0 polyethylene stopper and used to replace the stopper in the flask. A 20 ml polyethylene hypodermic syringe was attached to the Kel-F hub of the needle and the desired amount of solution was withdrawn. The syringe was then disconnected from the hub and the tip was capped with a Kel-F cap. Any static charge that might be present on the plastic syringe was dissipated by wiping it with a damp lintless towel. The syringe and contents were weighed on a semimicrobalance to ± 0.02 mg. The solution was then delivered from the syringe into a 100 ml Teflon-FEP beaker and the syringe was again capped, wiped and weighed. The weight of the sample was determined from the weights of the syringe before and after delivery of the sample. Two samples were withdrawn from each solution before the calibration samples were withdrawn and two samples were withdrawn after the calibration samples to insure that no change in concentration occurred during this time interval (about 6 h).

Each weighed portion was then assayed as follows: A tetraphenylarsonium chloride reagent solution was prepared by diluting 150 ml of a 2 percent (w/v) solution of tetraphenylarsonium chloride hydrochloride $[(C_6H_5)_4AsCl \cdot HCl \cdot H_2O]$ to 650 ml with subboiling distilled acetone (the 2% tetraphenylarsonium chloride solution was filtered twice through close textured filter paper before use). Sixty-five ml of this reagent solution was added to the weighed portion of the separated isotope solution. The solution was mixed with a Teflon rod and the rod was removed and washed with acetone. The acetone was allowed to evaporate from the uncovered beaker in a Class-100 clean air hood and the evaporation continued until all of the acetone evaporated and about 20–25 ml of solution remained in the beaker (about 20 h). (Tetraphenylarsonium perrhenate is soluble in the initial acetone-water mixture and slowly cyrstallizes from the solution as the acetone evaporates producing relatively large crystals when compared to the usual method of precipitation.)

The crystalized tetraphenylarsonium perrhenate, $(C_6H_5)_4AsReO_4$, was transferred with 0.1 percent tetraphenylarsonium chloride solution to a tared 15 ml fine porosity borosilicate glass filtering crucible. Since it was not possible to completely transfer the salt, the material remaining in the beaker was dissolved with acetone and the acetone evaporated at 50 °C. As much of the salt as possible was washed into the filtering crucible using the dilute reagent solution. This dissolution in acetone, evaporation, and transfer procedure was repeated twice more so that the amount of material remaining in the beaker was small. The material in the crucible was washed three times with water and the crucible and contents were dried at 125 °C for 3 h. (The filtrate and original beaker were reserved for the determination of dissolved and untransferred rhenium.)

The filtering crucible and contents were cooled in a desiccator, transferred to the case of a microbalance and allowed to stand for several hours. The crucible and contents were then weighed to ±0.002 mg. A buoyancy correction for the glass crucible was made by averaging three empty tare crucibles. The air weight of the $(C_6H_5)_4AsReO_4$ was then determined and converted to vacuum weight using a measured value of 1.93 as the density of the salt at 23 °C. The micromoles

(μmol) of rhenium present in the salt was determined using a calculated atomic weight for rhenium and 1971 atomic weight values for the other elements. The formula weights used were 632.3032 for $(C_6H_5)_4As^{185}ReO_4$ and 634.2834 for $(C_6H_4)_4As^{187}ReO_4$.

The filtrate from the precipitation of the tetraphenylarsonium perrhenate was transferred to the original beaker and about 50 ml of acetone was added to insure that any untransferred salt dissolved. The "Re 185" solutions were spiked with about 1.1 μmol of ^{187}Re and the "Re 187" solutions were spiked with 1.1 μmol of ^{185}Re for determining soluble and untransferred rhenium by isotope dilution mass spectrometry.

The spiked solution was mixed, evaporated to dryness, and the residue was taken up with 10 ml of a solution that was 50 percent 2*N* HCl and 50 percent acetone by volume. This solution was passed through an anion exchange column (6.5 × 1.2 cm filled to 3.5 cm with AG 1 × 8, 100–200 mesh anion exchange resin) washed with a few ml of the acetone–2*N* HCl mixture followed by 25 ml of 1*N* HCl. The rhenium was eluted from the column with 30 ml of 8*N* HNO_3 and the eluate was evaporated to dryness on a hot plate at low heat. The residue was taken up with 15 ml of 5 percent H_2SO_4 and the rhenium was electrodeposited as rhenium metal onto a platinum wire cathode by electrolysis at 2.4V applied potential for 16 h from a stirred solution. The rhenium metal was then stripped from the platinum wire cathode with 2–3 ml of 8*N* HNO_3 and the resulting solution evaporated to dryness at low heat. This residue was taken up with about 0.05 ml of 5 percent sulfuric acid and the 185/187 ratio was determined by surface emission mass spectrometry. The rhenium found as μmol Re was added to the rhenium from the gravimetric determination to yield the total rhenium in the sample. Table 2 shows the results of these analyses.

This method of determining the concentration of rhenium solutions was previously tested on solutions containing known amounts of rhenium. Six solutions were prepared from high-purity zone-refined rhenium in the approximate concentration of the separated isotope solutions, 16.8 to 20.2 μmol Re/g. This high purity rhenium was found to contain about 15 ppm of Fe and Al by spark source–isotope dilution analysis. Several other elements were detected at less than 5 ppm so that the detected impurities totaled about 60 ppm. Four samples containing from 250 to 290 μmol of rhenium were withdrawn from each solution and the rhenium concentrations were determined as described above. Comparison of the calculated and measured concentrations detected a positive bias of about 0.03 percent but this would have a negligible effect on ratios.

Pooling the results of the separated isotope solutions as shown in table 2 with the results of the six sets described above yields a value of 0.0018 μmol/g for the standard deviation of an individual measurement (24 degrees of freedom). The standard error for the average of four determinations is therefore 0.0009 μmol/g and the uncertainty of the concentration is 0.0018 μmol/g at the 95 percent confidence level. This corresponds to an uncertainty of 0.010 percent for solutions containing 18 μmol Re/g.

2.5. Isotopic Analyses of the Separated Isotope Solutions

Each of the separated isotope solutions were analyzed four times on each of the instruments. Sources were cleaned between the analyses of the two solutions as a precaution against the possibility of cross-contamination from the source parts, however tests showed that the two separated isotopes could be analyzed back-to-back on the same source with no detectable cross-contamination. Because of the poor precision obtained from measuring large ratios on very small signals on the single stage instrument, those analyses have not been included in the average isotopic compositions reported in table 3, even though the isotopic compositions obtained on the single stage machine fall within the stated error limits. In addition, seven analyses on each separated isotope obtained on the two stage instrument prior to this study are indistinguishable from the values reported in table 3. The isotopic compositions of the separated isotopes given in table 3 have been corrected for mass

TABLE 2. *Concentration of rhenium isotope solutions*

Solution	Sample No.	Weight solution g	Rhenium		Total rhenium μmol	Conc. solution μmol Re/g
			From ppt μmol	From I.D. μmol		
"Re 185"	1	15.04219	269.844	0.596	270.440	17.9788
	2	15.19842	272.648	.597	273.245	17.9785
	3	15.54660	278.914	.608	279.522	17.9796
	4	15.44233	277.033	.604	277.637	17.9790
				Average		17.9790
"Re 187"	1	15.47475	277.143	0.713	277.856	17.9554
	2	15.57072	279.006	.546	279.552	17.9537
	3	15.31739	274.299	.732	275.031	17.9555
	4	15.30674	274.201	.617	274.818	17.9541
				Average		17.9547

spectrometric bias, with changes becoming negligible after three rounds of iteration.

TABLE 3. *Isotopic composition of separated rhenium isotopes used in calibration samples*

Separated isotope		Isotopic composition (atom percent)
"Re 185"	^{185}Re	[a] 99.5516 ± 0.0022
	^{187}Re	0.4484 ± 0.0022
"Re 187"	^{185}Re	0.6769 ± 0.0034
	^{187}Re	99.3231 ± 0.0034

[a]The uncertainties are based on a minimum error of 0.5 percent for the ratio determinations. The calculated 95 percent confidence limits are well below this value.

2.6. Preparation of Calibration Samples

Seven calibration samples were prepared by mixing weighed portions of the "Re 185" and "Re 187" solutions to produce $^{185}Re/^{187}Re$ ratios ranging to 10 : 1 to 1 : 10 with two of them bracketing the observed natural ratio of 0.60 within a few percent. The portions were withdrawn from the flasks and weighed in the manner previously described for the assay of the solutions. To eliminate any possibility of change in concentration of a isotope solution with time, the portions for the calibration samples were withdrawn from the flasks between the samples taken for assay over a period of about 6 h.

Table 4 shows the composition of these calibration samples. The isotopic ratio of each calibration sample was calculated from the isotopic analysis of the separated isotopes and the μmol of rhenium from each separated isotope solution as determined from the assay and weight of solution taken.

Each calibration sample was thoroughly mixed and evaporated to dryness at low heat (≈ 50 °C) on a hot plate. Each sample was evaporated separately to avoid any possibility of cross-contamination due to the volatility of perrhenic acid. The calibration samples were then taken up in 5 percent sulfuric acid (w/v) so that 1 ml of solution contained 5 mg of rhenium.

2.7. Isotopic Analyses of the Calibration Mixes and the Standard Sample

Two complete sets of analyses of the calibration mixes and the standard sample were made, one by Operator #1 using the two stage instrument and one by Operator #2 using the single stage instrument. Each set consisted of 22 analyses of the standard sample made in a simple alternating pattern with three analyses each of the seven calibration mixes.

3. Results and Discussion

The results for the seven calibration mixes are summarized in table 5. For each operator, there are no statistically significant differences between any of the values of the correction factor. Table 6 includes the observed and corrected experimental $^{185}Re/^{187}Re$ values for the standard sample as well as the final absolute value for the isotopic ratio, with its associated uncertainty components.

The calculation of the atomic weight of the reference sample of rhenium is summarized in table 7.

A limiting factor in the accuracy of an atomic weight for naturally occurring rhenium is the variability in the natural isotopic composition. Although a complete survey of the consistency of this element's isotopic composition in nature has not been undertaken, more than 10 years of measurements in this laboratory on rhenium filaments have shown no major variation in the $^{185}Re/^{187}Re$ ratio among various lots of rhenium from different manufacturers.

TABLE 4. *Composition of rhenium calibration samples*

Sample No.	Isotope solution	Weight solution g	^{185}Re μmol	^{187}Re μmol	Isotope ratio $^{185}Re/^{187}Re$
1	"Re 185"	10.22737	183.05331	0.82458	9.362302
	"Re 187"	1.05092	0.12772	18.74123	
2	"Re 185"	1.97036	35.26624	0.15886	1.990891
	"Re 187"	0.98778	0.12005	17.61524	
3	"Re 185"	1.08449	19.41061	0.08744	0.511999
	"Re 187"	2.14960	0.26124	38.33418	
4	"Re 185"	1.14364	20.46929	0.09221	0.594056
	"Re 187"	1.94937	0.23691	34.76344	
5	"Re 185"	1.08309	19.38556	0.08732	0.628257
	"Re 187"	1.74429	0.21199	31.10621	
6	"Re 185"	1.03372	18.50191	0.08334	0.107832
	"Re 187"	10.26552	1.24759	183.06674	
7	"Re 185"	1.14517	20.49668	0.09233	1.029355
	"Re 187"	1.11881	0.13597	19.95193	

TABLE 5. *Determination of mass spectrometer bias*

Calibration sample No.	Isotopic ratio $^{185}Re/^{187}Re$			Correction factor	
	Calculated	Operator I	Operator II	Operator I	Operator II
1	9.362302	9.42064	9.40931	0.993807	0.995004
2	1.990891	2.00258	2.00046	.994163	.995217
3	0.511999	0.515458	0.514415	.993289	.995303
4	.594056	.597981	.596917	.993436	.995207
5	.628257	.632928	.631193	.992620	.995348
6	.107832	.108639	.108361	.992572	.995118
7	1.029355	1.03585	1.03403	.993730	.995480
Mean values of correction factors				0.993374	0.995240

TABLE 6. *Observed and corrected $^{185}Re/^{187}Re$ values for the standard sample*

	Observed ratios	Correction factor	Corrected ratios
Operator I	0.601415	0.993374	0.597430
Operator II	0.600191	0.995240	0.597334
Mean			0.59738 ± 0.00039

Uncertainty Components:

95 percent confidence limits on ratio determinations	±0.00016
Bounds due to possible systematic error in composition of separated isotopes	±0.00011
Bounds due to possible systematic error in chemical analysis	±0.00012

TABLE 7. *Summary calculations of the atomic weight of rhenium*

Value	Uncertainty components			
	Overall limit of error[a]	Mass spectrometric analytical error	Possible systematic error in composition of separated isotopes	Possible systematic error in chemical analysis
Atomic weight = 186.20679	±0.00031	+0.00012	±0.00009	±0.00010
Nuclidic masses [10] ($^{12}C = 12$)				
$^{185}Re = 184.953007$	±0.000014			
$^{187}Re = 186.955791$	±0.000014			
Atomic percent				
$^{185}Re = 37.398$	±0.016	±0.006	±0.005	±0.005
$^{187}Re = 62.602$	±0.016	±0.006	±0.005	±0.005
Isotopic ratio				
$^{185}Re/^{187}Re = 0.59738$	±0.00039	±0.00016	±0.00011	±0.00012

[a] The overall limit of error is the sum of the 95 percent confidence limits for the ratio determinations and terms covering effects of known sources of possible systematic error.

The authors are indebted to Hsien H. Ku for the statistical analysis of the experimental data, and to Paul J. Paulsen for the spark source mass spectrographic analyses of the rhenium separated isotopes and the reference sample.

4. References

[1] Shields, W. R., Garner, E. L., and Dibeler, V. H., J. Res. Nat. Bur. Stand. (U.S.), **66A** (Phys. and Chem.), No. 1, 1–3 (Jan.–Feb. 1962).

[2] Shields, W. R., Murphy, T. J., Garner, E. L., and Dibeler, V. H., J. Am. Chem. Soc. **84**, 1519–1522 (1962).

[3] Shields, W. R., Murphy, T. J., and Garner, E. L., J. Res. Nat. Bur. Stand. (U.S.), **68A** (Phys. and Chem.), No. 6, 589–592 (Nov.–Dec. 1964).

[4] Catanzaro, E. J., Murphy, T. J., Garner, E. L., and Shields, W. R., J. Res. Nat. Bur. Stand. (U.S.), **68A** (Phys. and Chem.), No. 6, 593–599 (Nov.–Dec. 1964).

[5] Shields, W. R., Murphy, T. J., Catanzaro, E. J., and Garner, E. L., J. Res. Nat. Bur. Stand. (U.S.), **70A** (Phys. and Chem.), No. 2, 193–197 (March–April 1966).

[6] Catanzaro, E. J., Murphy, T. J., Garner, E. L., and Shields, W. R., J. Res. Nat. Bur. Stand. (U.S.), **70A** (Phys. and Chem.), No. 6, 453–458 (Nov.–Dec. 1966).

[7] Catanzaro, E. J., Murphy, T. J., Shields, W. R., and Garner, E. L., J. Res. Nat. Bur. Stand. (U.S.), **72A** (Phys. and Chem.), No. 3, 261–267 (May–June 1968).

[8] Catanzaro, E. J., Champion, C. E., Garner, E. L., Marinenko, G., Sappenfield, K. M. and Shields, W. R., Nat. Bur. Stand. (U.S.), Spec. Publ. 260–17, 70 pages (Feb. 1969).

[9] Catanzaro, E. J., Murphy, T. J., Garner, E. L., and Shields, W. R., J. Res. Nat. Bur. Stand. (U.S.), **73A** (Phys. and Chem.), No. 5, 511–516 (Sept.–Oct. 1969).

[10] Wapstra, A. H. and Gove, N. B., Nuclear Data Tables **9**, 265–301 (1971).

[11] Hirt, B., Tilton, G. R., Herr, W., and Hoffmeister, W., Earth Science and Meteorites, J. Geiss, E. D. Goldberg, Eds. North-Holland Publishing Co., Amsterdam, 1963), pp. 273–280.

[12] Watt, D. E., and Glover, R. N., Phil. Mag. **7**, 105–114 (1962).

[13] Hönigschmid, O., and Sachtleben, R., Z. Anorg. Allgem. Chem. **191**, 309–317 (1930).

[14] White, J. R., and Cameron, A. E., Phys. Rev. **74**, 991–1000 (1948).

[15] Barton, G. W., Gibson, L. E., and Tolman, L. F., Anal. Chem. **32**, 1599–1601 (1960).

[16] McKinney, C. R., and Maymes, D., Proc. Am. Soc. Test. Mater., Committee E–14, 403–407 (1963).

[17] Riley, G. J., J. Sci. Instrum. **44**, 769–774 (1967).

[18] Shields, W. R., (Ed.), Nat. Bur. Stand. (U.S.) Tech. Note 456, 47 pages (Nov. 1968).

[19] Shields, W. R. (Ed.), Nat. Bur. Stand. (U.S.) Tech. Note 426, 53 pages (Sept. 1967).

[20] Willard, H. H. and Smith, G. M., Ind. Eng. Chem., Anal. Ed., **11**, 305–306 (1939).

[21] Tribalat, S., A Survey of the Different Methods for The Determination of Rhenium, in "Rhenium", Gosner, B. W., Ed. (Esleiver, New York, N.Y., 1962), p. 198.

[22] Taras, M. J., Nitrogen, in "Colorimetric Determination of Nonmetals," Boltz, D. F., Ed. (Interscience, New York, N.Y., 1958), Chap. IV, pp. 141–144.

[23] Kuehner, E. C., Alvarez, R., Paulsen, P. J., and Murphy, T. J., Anal. Chem. **44**, 2050–2056 (1972).

(Paper 77A6–791)

JOURNAL OF RESEARCH of the National Bureau of Standards—A. Physics and Chemistry
Vol. 77A, No. 6, November–December 1973

Reflection Correction for High-Accuracy Transmittance Measurements on Filter Glasses

K. D. Mielenz and R. Mavrodineanu

Institute for Materials Research, National Bureau of Standards, Washington, D.C. 20234

(July 27, 1973)

Multiple reflections in the sample compartment of a spectrophotometer constitute a source of systematic bias in transmittance measurements on filter glasses. This bias may be removed by applying a numerical correction obtained from measurements on tilted samples in polarized light. For a high-accuracy spectrophotometer, this correction was found to be of the order of several 10^{-4} transmittance units, independent of polarization, but slightly wavelength dependent.

Key words: Correction for reflections; reflections, multiple; spectrophotometry, high accuracy; systematic bias in spectrophotometry; transmittance, correction.

1. Introduction

The sample compartment of most spectrophotometers is designed such that the monochromator exit slit is focused into the sample by a lens, and is refocused into the detector by another lens (fig. 1). This beam geometry is preferred by instrument designers for intensity reasons and other convenience gains, but may constitute a source of significant systematic errors of the measured data. One of these errors is caused by multiple reflections between the two lenses and the sample surfaces [1, 2, 3].[1]

For high-accuracy applications this error can be eliminated by means of a numerical correction, ΔT, which converts the measured transmittance, T_M, into the correct value

$$\tau = T_M + \Delta T. \tag{1}$$

[1] Figures in brackets indicate the literature references at the end of this paper.

A simple but accurate method to determine this correction is described in this paper.

The specific spectrophotometric application discussed is the measurement of the transmittance of glass filters to an accuracy of $\pm 10^{-4}$ transmittance units. For the particular high-accuracy spectrophotometer used [4], the correction ΔT was found to be of the order of several 10^{-4} transmittance units, independent of polarization throughout the visible spectrum, and applicable for filters with widely different indices of refraction. The correction was found to be slightly wavelength dependent.

2. Theoretical Background

A detailed discussion of the reflection errors affecting the measurement of filter transmittances may be found in reference [3]. A summary is given here in order to provide the theoretical foundation for the experimental work described in section 3.

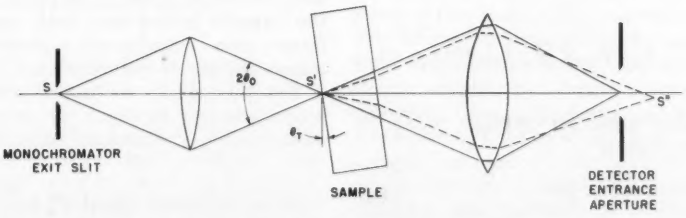

FIGURE 1. *Sample-compartment optics of a focused-beam spectrophotometer.*

The purpose of the measurement is assumed to be the determination of the normal-incidence transmittance,

$$\tau=\frac{\tau_i(1-r)^2}{1-r^2\tau_i^2}, \tag{2a}$$

of a glass filter surrounded by air. The filter is characterized by its thickness t and complex refractive index $n(1+i\kappa)$, so that for each wavelength λ the normal-incidence internal transmittance τ_i and Fresnel reflectance r appearing in eq (2a) are given by

$$\tau_i=e^{-4\pi n\kappa t/\lambda}, \tag{2b}$$

$$r=\left(\frac{n-1}{n+1}\right)^2. \tag{2c}$$

This quantity τ can be measured accurately with specially designed instrumentation in which the sample is placed normal to a collimated beam of light, the collimation being effected by off-axis mirror optics in a manner which reduces reflection errors to a negligible level [3, 5]. A conventional spectrophotometer does not permit such a direct measurement of τ because of the above-mentioned reflection error, even if its lenses were arranged to produce a collimated rather than the usual focused beam.

The cause of this error is illustrated in figures 2a and 2b. According to the first of these, the radiant flux received by the detector during the clear-space measurement is

$$\phi_0=T_1T_2(1+R_1R_2+\ldots), \tag{3a}$$

where the initial flux is taken as unity, and where T_1, R_1, T_2, and R_2 are the fractional fluxes transmitted or reflected into the detector by all components (lenses, slit jaws, detector housing, etc.) in front of and behind the sample area, respectively. When a sample with transmittance T and reflectance R is inserted, the flux into the detector is

$$\phi=T_1TT_2(1+R_1R_2T^2+RR_2+R_1R+\ldots), \tag{3b}$$

as indicated in figure 2b. Within the approximation that all contributions due to four or more reflections are considered negligibly small, the measured transmittance is

$$\begin{aligned}T_M&=\phi/\phi_0\\&=T[1+(R_1+R_2)R-R_1R_2(1-T^2)].\end{aligned} \tag{3c}$$

The correction which must be applied to T_M to eliminate the reflection bias is

$$T-T_M=\Delta T+\Delta T', \tag{4a}$$

where

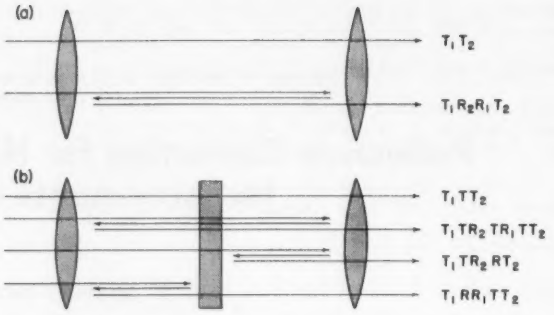

FIGURE 2. *Reflected beams in a spectrophotometer with lenses.*

$$\Delta T=-(R_1+R_2)RT, \tag{4b}$$

$$\Delta T'=R_1R_2T(1-T^2). \tag{4c}$$

The first of these two error terms, ΔT, is due to the fact that the insertion of the sample has created the two additional beams shown at the bottom of figure 2b. This error is greatest when the sample is normal to the optic axis, and may be eliminated by sufficiently tilting the sample so that these two beams no longer reach the detector. The other error component, $\Delta T'$, arises from the fact that the second beam from the top in figure 2b passes the sample three times, whereas the direct beam passes it only once. Since this residual error cannot be avoided by tilting the sample, it is clear that tilting is an effective means to eliminate reflection errors only if $\Delta T'$ is substantially smaller than ΔT. Equations (4b, c) suggest that this should be the case for any well-designed spectrophotometer for which these reflection errors are not unduly large. To show this, we assume that R_1 and R_2 are both of the order of a few percent, and that glass filters with an average transmittance $T\sim 0.5$ and reflectance $R\sim 0.08$ are used as samples. This leads to $\Delta T/\Delta T'\sim 10$, showing $\Delta T'$ to be a significantly smaller error in such circumstances. Whether or not this estimate holds must be ascertained individually for any given spectrophotometer.

Tilting the sample introduces obliquity errors, and therefore does not yield an accurate measurement of the normal-incidence transmittance τ unless further corrections are applied. These errors arise from a decrease of internal transmittance due to increased pathlengths in the sample for oblique light incidence and, secondly, from a variation of reflection losses at the sample boundaries with angle of incidence. The latter also introduces a dependence of measured transmittance on polarization.

For glass filters measured with a conventional spectrophotometer in which the monochromator exit slit is imaged onto the sample, these errors are given by

$$\begin{aligned}T=\tau[1+(1/2n^2)\,(\ln\tau_i)\,(\theta_T^2+\frac{2}{3}\,\theta_0^2)\\ \pm(4r/n)\,\theta_T^2+\ldots],\end{aligned} \tag{5}$$

where T is the measured transmittance (corrected for reflection errors); τ, τ_i, and r are the normal-incidence values of transmittance, internal transmittance, and Fresnel reflectance as given by eqs (2a, b, c); θ_T and θ_0 are the tilt angle and the cone angle of the incident light; and where the upper and lower signs of the last term pertain to the two cases in which the light is S or P polarized in the tilt plane. Equation (5) was derived in reference [3] under the assumption that the monochromator exit slit is sufficiently short to approximate a point source, and that the focusing lens is underfilled so that the grating or prism constitutes the limiting aperture. This aperture is assumed to be square, subtending the same angle $2\theta_0$ in the horizontal and vertical planes. The sample is assumed to be tilted only in one of these planes. The small-angle approximation given in eq (5) is estimated to be accurate to 10^{-4} transmittance units for angles θ_T and θ_0 up to about 10°.

For average transmittances and tilt angles of a few degrees, these obliquity effects are of the order of 10^{-3} transmittance units. Since this is the same magnitude as estimated above for the reflection error, it is clear that for a spectrophotometer with lenses an accurate measurement of the normal-incidence transmittance τ cannot be achieved without numerical correction for either source of error. If the sample is tilted in order to reduce the reflection error, an obliquity correction must be applied. Vice versa, a reflection correction is necessary if the sample is normal to the optic axis so that obliquity effects are minimized. Although these two alternatives are equivalent, the latter was chosen in this work since it constitutes the simpler approach for routine measurements of transmittance.

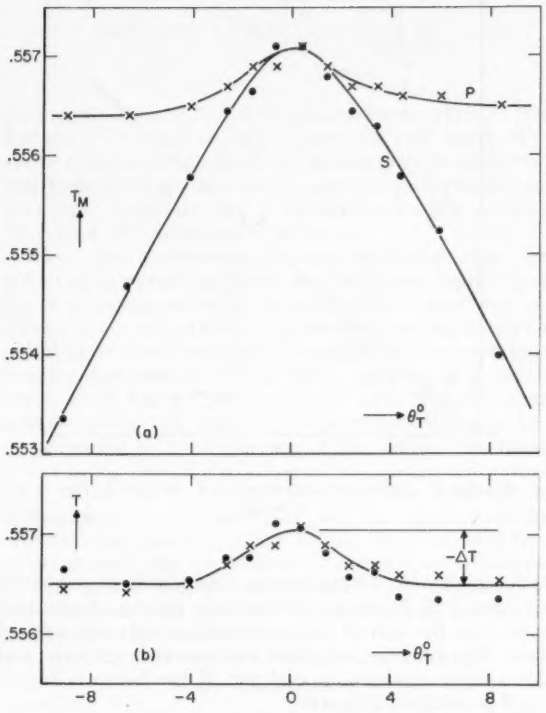

FIGURE 3. *(a) Measured transmittance* T_M *versus tilt angle* θ_T *for 55 percent filter in* S *and* P *polarized light at* $\lambda = 574$ *nm.*
(b) The same data after application of tilt correction.

3. Experimental Procedure

The preceding theoretical discussion does not permit a precise calculation of the required reflection correction. Representing fractional fluxes which actually reach the detector, the quantities R_1 and R_2 appearing in equations (4b, c) are complicated and generally unknown functions of the relative positions of sample compartment elements, lens curvatures, location of aperture stops, and other beam-geometry factors. This makes it necessary to measure the correction. Such a measurement may be performed as follows.

Each of a series of filters with different transmittances is measured for different known tilt angles θ_T, and for S and P polarization of the incident light. This yields a set of raw data T_M, such as plotted in figure 3a. These are transformed into corrected data T by adding the tilt-correction given by eq (5),

$$(\Delta T)_{\text{tilt}} = -T_M\left[(1/2n^2)\ \ln\left(\frac{T_M}{1-2r}\right) \pm (4r/n)\right]\theta_T^2, \quad (6)$$

where the approximate values T_M and $T_M/(1-2r)$ were substituted for τ and τ_i on the right-hand side, and where estimates of n and r may be used. As indicated by figure 3b, these corrected transmittances T are constant for sufficiently large positive or negative tilt angles, but near normal incidence exhibit the 'reflection hump' whose height represents the desired reflection correction ΔT to be applied for this particular value of transmittance. From the measurements performed on all of the filters one may then determine the dependence of ΔT on T, as illustrated by figure 4. According to eq (4b), this dependence should be linear. In the work described here, these measurements were made as follows.

A series of four Schott NG–4 glass filters with nominal transmittances 0.1, 0.2, 0.3, and 0.5, an evaporated metal-on-glass filter with a nominal transmittance 0.4, and a clear glass plate were used. All of these samples were 50 mm × 50 mm × 2 mm in size, and flat and plane-parallel to within a few fringes of mercury-green light. The spectrophotometer used to perform the measurements was fully described in a previous issue of this journal [4], and will not be discussed here. The filters were placed in the sample compartment of this spectrophotometer on a vertical rectangular holder adapted to a rotary horizontal table with 10 cm diameter. This table had a scale divided in 360° with a vernier reading to 5 min, and was held on the single-sample carriage of the spectrophotometer (see ref. [4], fig. 2) with a vertical mounting rod. This sample carriage unit consists of a platform provided with vertical holders which can be moved laterally by a

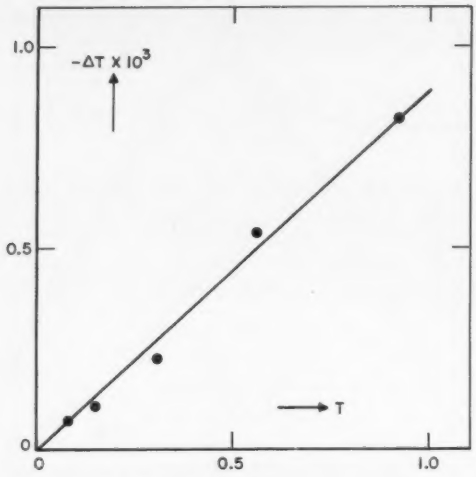

FIGURE 4. *Reflection correction* ΔT *versus* T *for* λ *=574 nm.*

rack and pinion arrangement. The platform, mounted on four ball bushings which ride on two horizontal rods, can be moved pneumatically across the optical axis. This remote-controlled movement is smooth, and the sample position in and out of the beam is reproducible within 0.025 mm.

A sheet polarizer of 9.5 cm diam was used to produce the S and P polarized radiation. This polarizer was held in a ball bearing rotating mount with a circular scale divided from 0 to 360°. It was placed on the optical bench in front of the entrance slit of the predisperser-monochromator aggregate of the spectrophotometer between the circular neutral wedge and the flat front-surface mirror (see ref. [4], fig. 3). This placement of the polarizer on the source side of the spectrophotometer avoids the additional reflection errors which would occur if the polarizer were put in the sample compartment of the spectrophotometer, but requires that the monochromator does not significantly depolarize the incident radiation or rotate its plane of polarization. This was ascertained by testing the monochromator between crossed polarizers at the wavelengths at which the measurements were performed.

Each transmittance measurement was performed in S and P polarized radiation and for tilt angles varying by $\pm 10°$ about the normal position. Each measurement resulted from the ratio I/I_0 of the attenuated to the unattenuated radiation value, each I and I_0 being the average of 50 individual measurements. The measurements were repeated four times.

4. Results

Using the procedures outlined in section 3, the numerical values of the reflection correction ΔT were determined for the four neutral-density glass filters and the clear glass plate, at the wavelength $\lambda = 574$ nm. This yielded the result represented by the straight line in figure 4; namely,

$$\Delta T/T = -8.9 \times 10^{-4}, \qquad \text{for } \lambda = 574 \text{ nm}. \tag{7a}$$

Each of the individual values of ΔT could be measured to a precision better than 10^{-4} transmittance units. There was no evidence suggesting a dependence of ΔT on polarization.

Secondly, the measurements on the clear glass plate were repeated for $\lambda = 400$ nm and 650 nm. Together with the previously obtained result for 574 nm, this showed the wavelength dependence indicated in figure 5. This dependence is also linear, and may be expressed as

$$\Delta T/T = -1.26 \times 10^{-6}(\lambda - 574 \text{ nm}), \qquad \text{for } T = 0.92. \tag{7b}$$

These results were then combined into the final empirical expression.

$$\Delta T/T = -8.9 \times 10^{-4}[1 + 1.4 \times 10^{-3}(\lambda - 574 \text{ nm})], \tag{8}$$

for the correction ΔT to be applied for different transmittances T and wavelengths λ. This formula agrees with all individual measurements of ΔT to within $\pm 5 \times 10^{-5}$ transmittance units.

The correction ΔT so obtained represents only the first of the two error terms appearing in eq (4a), above. The exact value of the second term $\Delta T''$ cannot be determined within the context of this paper, but a quantitative estimate may now be obtained as follows. From eqs (4b) and (7a) it may be seen that, for this spectrophotometer and for the appropriate value $R \sim 0.08$ for the filters used,

$$\frac{1}{2}(R_1 + R_2) \sim 6 \times 10^{-3}. \tag{9a}$$

Provided that this arithmetic average of R_1 and R_2 is not substantially different from their geometric average $(R_1 R_2)^{1/2}$, it follows from eq (4b) that

$$\Delta T'' \sim 3.6 \times 10^{-5}\, T(1 - T^2), \tag{9b}$$

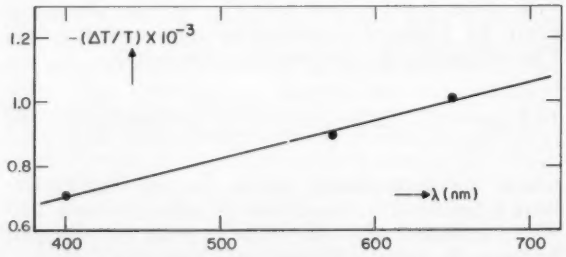

FIGURE 5. *Reflection correction* ΔT *versus* λ *for* T *= 0.92*

or $\Delta T' \sim 1.4 \times 10^{-5}$ for $T = 0.577$, for which this error is a maximum. Although this argument is not mathematically exact, it suggests that the residual reflection error $\Delta T'$ is entirely negligible for the spectrophotometer used here.

According to eq (4b), the correction ΔT depends on the reflectance R and, therefore, on the refractive index n of the sample. Using eqs (4b) and (2c) it is easily seen that

$$d(\Delta T) = -\frac{8r(R_1 + R_2)T}{(n+1)^2}\, dn. \tag{10}$$

For $n = 1.5$, $r = 0.04$, $T = 0.5$, and the above value (9a) for $(R_1 + R_2)$, this is reduced to $d(\Delta T) \sim 3 \times 10^{-4}\, dn$, showing that ΔT will not be affected by more than 10^{-4} transmittance units as long as $dn < 0.3$, or $1.2 < n < 1.8$. Hence it may be concluded that the above values of ΔT are applicable to virtually all filter glasses. Other types of samples, such as coated glasses, will of course require a different correction. For example, measurements on the evaporated metal-on-glass filter with transmittance 0.4 at 474 nm yielded a value, $\Delta T = -1.4 \times 10^{-3}$, which is about four times larger than indicated by figure 3 for uncoated samples.

5. Conclusion

Based upon this work, all transmittance measurements on glass filters with this high-accuracy spectrophotometer are performed with the sample accurately aligned normal to the optic axis. In addition to the reflection correction given by eq (8) and the detector nonlinearity correction discussed in reference [4], an f-number correction is applied to remove the residual bias due to the nonparallel radiation in the sample compartment. This latter correction is given by eq (5) as

$$(\Delta T)_f = -(T/3n^2)\left(\ln \frac{T}{1-2r}\right)\theta_0^2;$$

its magnitude is 1.3×10^{-4} transmittance units, or less, for the $f/10$ cone of light ($\theta_0 = 0.05$ rad) used. With these corrections applied, all measurements made with this high-accuracy spectrophotometer yield the normal-incidence transmittance τ defined by eq (2a) within a 10^{-4} limit of instrumental accuracy.

This spectrophotometer was designed and constructed to permit calibration of solid and liquid filters for transmittance with a well-defined accuracy (4). These filters are used as Standard Reference Materials (SRM's) to check the photometric scale of conventional spectrophotometers. SRM 930a consists of a set of three glass filters (Schott NG–4) with nominal transmittances 0.1, 0.2, and 0.3. Their transmittance values are certified to ± 0.5 percent of the value, this uncertainty being the sum of random and systematic errors. The latter are principally due to the inherent inhomogeneity and instability of the glass, surface effects, and positioning the filters. They exceed by a large margin the instrumental corrections discussed in this paper. Hence, the certified transmittances of previously issued standard filters remain unaffected by these corrections.

6. References

[1] Gibson, K. S., and Balcom, M. M., J. Res. Nat. Bur. Stand. (U.S.), **38**, 601 (1947).

[2] Goldring, L. S., Hawes, R. C., Hare, G. H., Beckman, A. O., and Stickney, M. E., Anal. Chem. **25**, 869 (1953).

[3] Mielenz, K. D., J. Res. Nat. Bur. Stand. (U.S.), **76A** (Phys. and Chem.), No. 5, 455–467 (Sept.–Oct. 1972).

[4] Mavrodineanu, R., J. Res. Nat. Bur. Stand. (U.S.), **76A** (Phys. and Chem.), No. 5, 405–425 (Sept.–Oct. 1972).

[5] Mielenz, K. D., Eckerle, K. L., Madden, R. P., and Reader, J., Appl. Optics **12**, 1630 (1973).

(Paper 77A6–792)

JOURNAL OF RESEARCH of the National Bureau of Standards—A. Physics and Chemistry
Vol. 77A, No. 6, November–December 1973

Temperature-Pressure Phase Relationships in Niobium Pentoxide

J. L. Waring, R. S. Roth, and H. S. Parker

Institute for Materials Research, National Bureau of Standards, Washington, D.C. 20234

(July 23, 1973)

A pressure-temperature (P–T) section of the phase equilibrium diagram for Nb_2O_5 has been determined. Four single phase regions, H-Nb_2O_5, B-Nb_2O_5, and two L-Nb_2O_5 areas, were characterized by x-ray powder diffraction data. The superstructure of L-Nb_2O_5 was indexed on the basis of similarities to the known superstructures of L-Ta_2O_5 and confirmed with single crystal electron diffraction data. The correct unit cell is orthorhombic with $a=6.168$, $b=29.312$, $c=3.938$ Å, with the b axis 8 times the subcell (8×3.664 Å).

Key words: Niobium pentoxide; phase relationships; pressure; temperature.

1. Introduction

Niobium pentoxide has been reported to occur in at least eight different polymorphic forms under varying experimental conditions. The polymorphs of Nb_2O_5 and their structural relationships to each other have been discussed by A. D. Wadsley and S. Andersson [1].[1] These authors postulated that some of the various modifications should have stability fields in the relevant ranges of the pressure-temperature (P–T) phase diagram. They put forward a "not impossible" phase diagram (fig. 1) based on no experimental evidence. S. Tamura [2] reported a temperature-pressure diagram (fig. 2) for Nb_2O_5 postulating the boundaries between H-Nb_2O_5 and L-Nb_2O_5 and B-Nb_2O_5 and L-Nb_2O_5 based on experiments utilizing an opposed piston apparatus. H-Nb_2O_5 is the stable polymorph which occurs at high temperatures and atmospheric pressure, L-Nb_2O_5 is the metastable polymorph formed during precipitation and B-Nb_2O_5 is the high pressure form [1]. In the present study only these three previously reported phases were found to occur in the system at the temperatures and pressures studied.

In this study, it was necessary to determine which of the multitude of possible polymorphs represent equilibrium phases and which represent metastable phases. The Nb_2O_5 specimens were equilibrated in an apparatus which is capable of heating materials in a uniform temperature zone up to about 1400 °C and 150,000 psi[2] isostatic pressure in an environment free of contaminants.

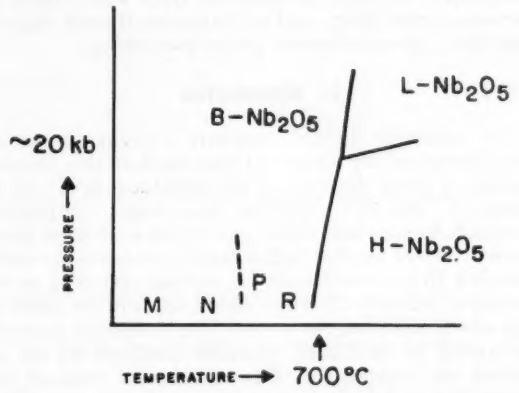

FIGURE 1. *Tentative temperature-pressure phase diagram for various* Nb_2O_5 *modifications (taken from Wadsley and Andersson [1] and modified according to present notation).*

2. Sample Preparation

The Nb_2O_5 used in this investigation was found by spectrographic analysis to contain less than about 0.01 percent Si, 0.001 percent Ca and Mg. The presence of As, Cu, and Ta was questionable. The starting materials were prepared as follows: The Nb_2O_5 (low temperature form) was dried at 130 °C for 19 h. Portions of the dried material were sealed in 5 mm O.D. × 25 mm long Pt tubes and heated to 1450 °C for 60 h to form H-Nb_2O_5, the high temperature polymorph. This material was reannealed in air at 1000 °C for 1 h to minimize any slight reduction which may have occurred. The B-polymorph of Nb_2O_5 was formed by heating the high temperature modification (H-Nb_2O_5)

[1] Figures in brackets indicate the literature references at the end of this paper.

[2] The use of psi, bar, and kbar follows the current common practice of workers in the field. Note that 1 bar = 10^5 N/m² (or pascal) = 10^6 dyn/cm² = 0.9869 atm = 14.504 psi. The accepted international standard (SI) unit of pressure is the pascal or newton per meter squared.

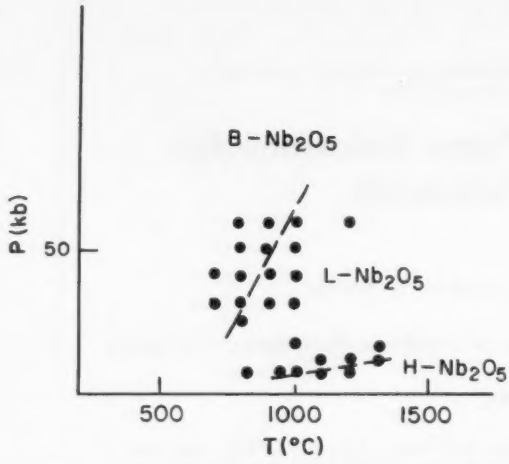

FIGURE 2. *Pressure/temperature/structure relationships for* Nb_2O_5 *(after Tamura [2]).*

at 900 °C for 19 h at about 70,500 psi. For some experiments, $LiNbO_3$ or distilled H_2O was added to increase crystallinity and to determine if such impurities affect the equilibrium phase assemblage.

3. Apparatus

An internally heated pressure system similar to that described by Yoder [3] was used in this investigation. A block diagram of the apparatus is shown in figure 3. An air operated, two stage compressor (labeled A) supplies argon gas to the system at pressure to 30,000 psi. For higher initial pressures the valve (labeled B) is closed and the moving piston of an intensifier (labeled C) is advanced against the head of gas which has filled the vessel. The intensifier piston is advanced by hydraulic pressure supplied by an air driven oil compressor. The differential ratio of the intensifier is 5:1 thus providing a maximum pressure of 150,000 psi. The valve (labeled D) isolates the pressure vessel during a run. Pressures of up to 150,000 psi can be obtained in a few minutes *provided the system is tight.* Since a minimum of 16 h was needed to achieve equilibrium in most of the samples studied, at least in the lower P–T range, particular attention had to be paid to obtaining a relatively leak free system. Experimental results were discarded if a pressure drop greater than 500 psi occurred during a run.

3.1. Pressure Measurement

The pressure was determined as a function of the change in resistance of a "seasoned" manganin wire coil when measured with a dc Carey-Foster Bridge [4]. The resistance of the manganin coils was approximately equal to 120 Ω and the coils were calibrated by the supplier against a dead weight gage. Two coils were used for a comparison measurement. One coil acted as a pressure sensor and the other served as a

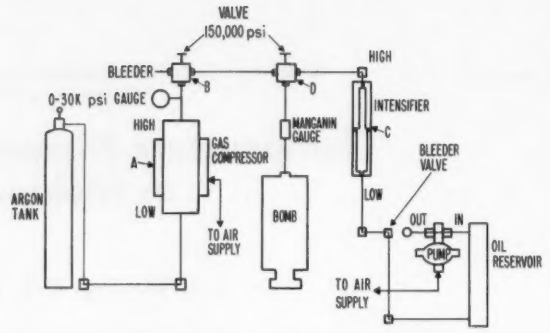

FIGURE 3. *Schematic block diagram of pressure-temperature apparatus having a working range up to 1400 °C and 150,000 p.s.i.*

dummy gage for temperature compensation. A least squares fit by computer analysis of the correction data for the manganin coils used in this study has shown that the resistance-pressure curve in the range 0–150,000 psi can be described best by a parabolic equation of the type $R = B_0 + B_1P + B_2P^2$ where $B_0 = 1.20357$, $B_1 = 1.9926470 \times 10^{-5}$ and $B_2 = 8.0085893 \times 10^{-13}$. Errors in absolute pressure may be as much as 20 bar at 150,000 psi due to uncertainties in the pressure scale [3].

3.2 Temperature Measurement

The temperature was measured with a Pt-Pt10 percent Rh thermocouple. Bell [5] has shown that the effect of pressure on Pt-10 percent Rh thermocouples at the pressures attained in this work are within the limits of error in the temperature measurement. For this reason no correction for pressure has been applied to the temperature measurements. The temperatures reported can be considered accurate to at least ± 20 °C. Yoder [3] reported the results of probing the thermal gradient of his system with a thermocouple. A zone of even heating ± 5 °C was found to exist over a distance of about 5 cm. As our system is nearly identical, this time consuming process was not repeated.

4. Phase Equilibria

A P–T phase equilibrium diagram for Nb_2O_5 (fig. 4) has been constructed from the x-ray data given in table 1. These data were obtained from specimens quenched (thermocouple indicates cooling to ambient temperature in less than a minute) by turning off the electrical power to the furnace and then reducing the pressure. Equilibrium was considered to have been approached when the x-ray powder diffraction patterns of specimens successively heated for longer times and/or at higher temperatures and/or pressures (quenched to ambient temperature and pressure) showed no significant change. X-ray diffraction powder patterns were made using a high angle record-

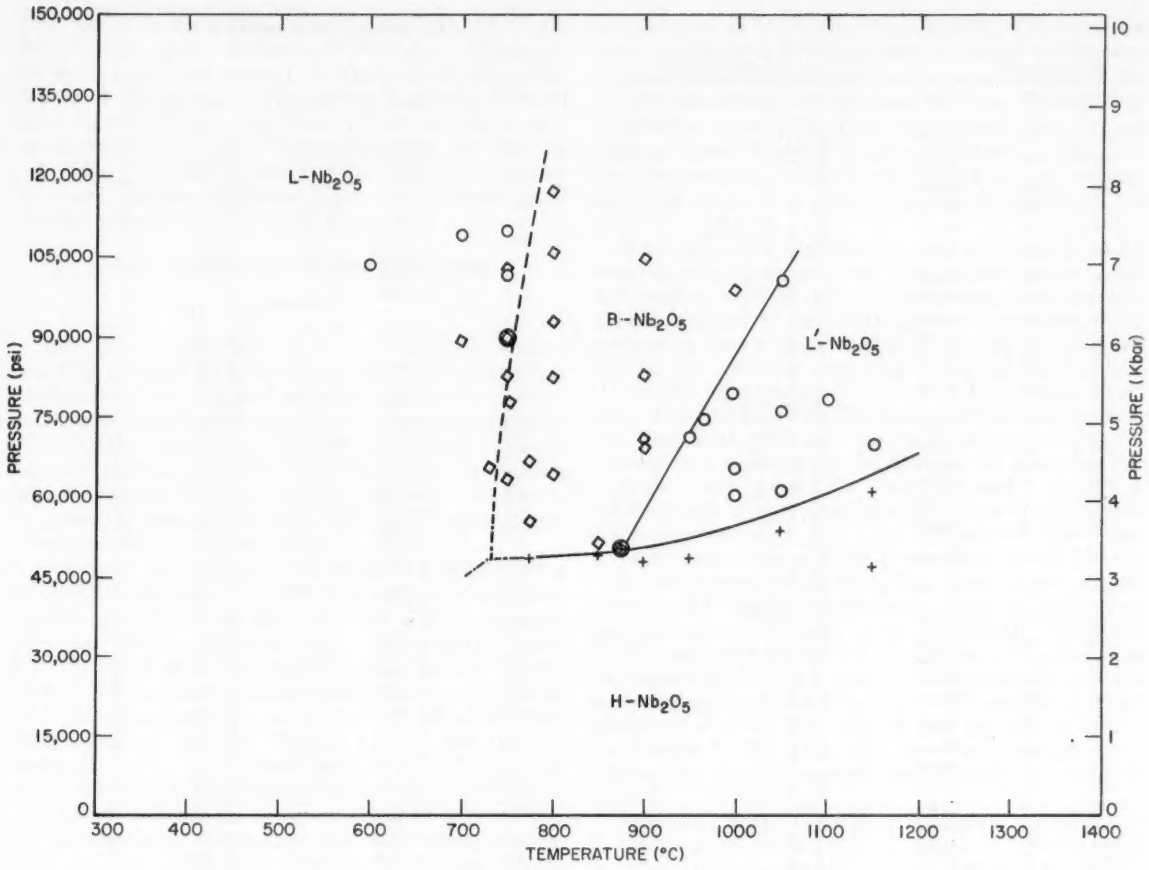

FIGURE 4. *Pressure-temperature* (P–T) *phase equilibrium diagram for* Nb_2O_5.

Dot dash curves—delineate phase boundaries which could not be determined. Dashed curve—delineates phase boundaries where reversibility was not established.

○—L-Nb_2O_5
+—H-Nb_2O_5
◇—B-Nb_2O_5

Symbols refer to phases interpreted as equilibrium (see table 1 for experimental data).

ing Geiger counter diffractometer and nickel-filtered copper radiation with the Geiger counter scanning the 2θ angular range at 1/4° 2θ/min and the radiation being recorded on the chart at 1° 2θ/in. The unit cell dimensions reported are estimated to be accurate within about two standard deviations.

The phase diagram can be described as consisting of four single phase regions in the temperature-pressure range investigated. They are designated H-Nb_2O_5, L-Nb_2O_5, B-Nb_2O_5 and L′-Nb_2O_5. In a previous study the N-form of Nb_2O_5 was synthesized at atmospheric pressure with the addition of $LiNbO_3$ [6]. However, in the present study this phase was found to transform to B-Nb_2O_5 at 800 °C and 64,000 psi and may be considered to become unstable with increasing pressure. No other polymorphs of Nb_2O_5 have been found to occur in this study.

4.1. H-Nb_2O_5 (High Temperature Form)

The crystal structure of the high temperature form of Nb_2O_5 (H-Nb_2O_5) was reported by Gatehouse and Wadsley [7]. The structure consists of infinite chains of 3×5 blocks of octahedra at one level and isolated blocks of 3×4 octahedra at the next level with tetrahedral positions at the block junctions. This phase, with a reported x-ray density of 4.55 [8], was found to occur at the highest temperature and lowest pressure (fig. 4). All experiments conducted in the P–T range lower than that given in table 1 and figure 4 showed no change in the starting material. Therefore, the low temperature boundary of the H-Nb_2O_5 field could not be determined because equilibrium could not be achieved in this portion of the system in laboratory time.

520-812 O-LF - 73 - 2

Table 1. Temperature-Pressure Experimental Data for Nb_2O_5.

Heat Treatment[a/b/]			X-ray Diffraction Analyses[c/]
Temp °C	Time hr	Pressure psi	
600	144	103,000	H → H + L L → L + tr H
700	1	89,000	H → H + L L → L
700	168	108,500	H → L + tr H L → L
730	72	66, 200	B → B
746	22	101,100	H → L + H + tr B L → L + tr H and B
750	48	63,100	H → B L → B
750	96	77,200	H → L + H L → L + tr B
750	64	82,400	B → B
750	16	89,400	H → L + tr H L → L
750	127	107,200	B → B
751	168	108,000	H → L L → L
775	115	47,500	H → H L → L + tr H B → B + tr H
775	24	54,760	H → B + tr H L → B + L
775	43	66,540	H → B + tr L L → B + L
800	19	64,000	L → L + tr B
800	21	82,000	L → L + tr B
800	68	92,000	H → B + tr L L → B + L
800	24	105,000	H → B + L L → B + L
800	19	118,000	H → B + L L → L + H B → B
850	120	48,700	H → H L → L + H
850	144	51,400	H → B + tr H L → B + L
875	24	50,000	H → H L → B + L
900	112	47,500	L → L + tr H
900	19	68,000	H → B
900	16	70,400	H → B + H L → B + L
900	16	82,500	H → B + tr L L → B + L
900	36	104,000	H → B + tr L L → B + L
950	17	48,300	L → L + H
951	64	70,600	H → B + L L → L + tr B
965	64	75,000	H → L
995	65	79,160	H → L L → L
1000	19	60,000	L → L
1000	16	65,200	B → L
1000	48	98,000	H → L + B L → B + tr H
1050	16	53,000	H → B + L + tr H L → B + L
1050	192	60,750	H → L
1050	16	75,500	H → L
1050	16	100,000	H → L H → L
1100	16	77,700	H → L
1150	289	46,600	H → H L → L + tr H
1150	144	60,600	H → H L → H
1150	113	69,500	H → L L → L

a/ The starting materials were prepared as follows: L-Nb_2O_5 - dried at 130°C for 19 hours, H-Nb_2O_5 - calcined at 1450°C for 60 hours in large sealed Pt tube and reannealed in air at 1000°C for one hour. B-Nb_2O_5 - H-Nb_2O_5 was heated at 900°C for 19 hours in a series of small Pt tubes at a pressure of 70,500 psi.

b/ All specimens were quenched in sealed Pt tubes. Some specimens were heated at appropriate temperatures in Au tubes and it was found that for Nb_2O_5 the experimental results were the same for both the Pt and Au tubes.

c/ The phases identified are given in the order of the amount present at room temperature. The phases are not necessarily those present at the temperature and pressure to which the specimen was heated.

H = high temperature-low pressure polymorph of Nb_2O_5

L-Nb_2O_5 = represents both L-Nb_2O_5 and L'Nb_2O_5 which occur experimentally in two different portions of the system separated by the field of B-Nb_2O_5. The x-ray patterns of the specimens prepared in these two fields are identical except for degree of crystallinity.

B = intermediate temperature and high pressure polymorph of Nb_2O_5.

The phase(s) underlined have been interpreted as non-equilibrium under the specified temperature-pressure conditions.

Table 2. Indexed X-ray Diffraction Powder Pattern for B-Nb_2O_5 (CuKα radiation)[a/]

hkℓ[b/]	d_{obs}	$2\theta_{obs}$	$2\theta_{calc}$	I[c/]
$20\bar{2}$	6.16	14.37	14.38	14
$11\bar{1}$	3.644	24.42	24.41	79
111	3.315	26.87	26.87	64
$40\bar{2}$	3.077	28.99	28.99	100
311	2.982	29.94	29.94	81
002	2.6868	33.32	33.33	43
311	2.5034	35.84	35.83	31
$02\bar{2}$	2.4422	36.77	36.77	11
$40\bar{2}$	2.3480	38.30	38.31	7
$02\bar{1}$ $51\bar{1}$ $11\bar{2}$	2.2218	40.57	40.54 40.55 40.59	14
$51\bar{0}$	2.1980	41.02	41.03	12
$22\bar{1}$	2.1667	41.65	41.65	7
600	2.0518	44.10	44.11	17
420	1.9133	47.48	47.49	29
$51\bar{1}$	1.8879	48.16	48.18	7
$60\bar{2}$	1.8827	48.30	48.30	7
022	1.8068	50.47	50.46	43
$40\bar{2}$	1.8057	50.50	50.52	36
$11\bar{3}$	1.7233	53.10	53.10	10
$31\bar{3}$	1.7081	53.61	53.59	21
$71\bar{1}$	1.7028	53.79	53.81	57
$42\bar{2}$	1.6920	54.16	54.14	29
$13\bar{0}$ $11\bar{3}$	1.6143	57.00	57.00 57.01	7
620	1.5710	58.72	58.73	6
$13\bar{1}$	1.5604	59.16	59.15	6
800	1.5382	60.10	60.09	13
$80\bar{2}$	1.5150	61.12	61.11	6
$33\bar{1}$	1.4947	62.04	62.05	9
$62\bar{2}$	1.4915	62.19	62.20	14
711	1.4831	62.58	62.60	26
602	1.4577	63.80	63.78	4
422	1.4512	64.10	64.10	7
313	1.4378	64.79	64.79	6
331	1.4217	65.62	65.62	14
$71\bar{3}$	1.3965	66.95	66.93	7
004	1.3433	69.98	69.99	4
820	1.3013	72.59	72.56	7
$82\bar{2}$ $60\bar{4}$	1.2784	73.50	73.49 73.52	7

a/ Specimen heated to 900°C for 19 hrs at 70,500 psi in a sealed Pt tube and quenched.

b/ Indexed on the basis of a monoclinic unit cell a=12.744±0.001Å, b=4.8845±0.0006Å, c=5.5629±0.0006Å and β=105°1.9'±0.5'.

c/ Observed intensity, peak height.

4.2. B-Nb_2O_5

The existence of B-Nb_2O_5 was first reported by Laves, Petter and Wulf [9] who described it as zeta-Nb_2O_5. Schäfer, Schulte, and Gruehn [10] formed several new phases from the reaction $Nb_2O_5(s) + 3NbX_5(g) \rightleftarrows 5NbOX_3(g)$ X = Cl, Br, or I. One of the new phases formed in this reaction was called B and is the same phase which Laves named zeta. In this paper, the B-nomenclature is used. The stability field of B is shown in figure 4. B-Nb_2O_5 is thus the medium temperature, high pressure polymorph of Nb_2O_5. B-Nb_2O_5 has not been previously synthesized by pressure equilibrium conditions below about 30 kbar [2], but was found to form under equilibrium conditions in the present work at pressures as low as 3.5 kbar.

This phase can be transformed reversibly, B-Nb_2O_5 ⇆ L-Nb_2O_5 and B-Nb_2O_5 ⇄ H-Nb_2O_5. However, B-Nb_2O_5 would not revert to L-Nb_2O_5 at the low temperature boundary (L′). This phase has been indexed after Laves, Petter, and Wulf [9] on the basis of a monoclinic unit cell. The parameters, $a=12.744$, $b=4.884$, $c=5.563$ Å, and $\beta=105°1.9'$, were refined by least squares analyses from the indexed x-ray powder pattern given in table 2.

4.3. L-Nb_2O_5 (Low Temperature Form)

a. Stability

The low temperature form of Nb_2O_5 (L-Nb_2O_5) was first reported by Brauer [11]. This is the apparently metastable form obtained when the material is precipitated from solution and crystallized at low temperatures. When heated this phase will gradually change to poorly formed H-Nb_2O_5, which becomes more crystalline with increasing time and temperature. Once H-Nb_2O_5 is formed it does not revert to L-Nb_2O_5 at atmospheric pressure at any temperature.

The only oxide known to stabilize L-Nb_2O_5 at a temperature in excess of 1000 °C at ambient pressure is Sb_2O_4 [12]. However, both F^- and $(OH)^-$ probably also can be incorporated into this structure type [13, 14] which may also result in stabilization. Apparently L-Nb_2O_5 has a stability field at higher pressures and temperatures, as postulated by Wadsley and Andersson [1] and by Tamura [2]. In the present work, H-Nb_2O_5 was transformed to L-Nb_2O_5 and in turn L-Nb_2O_5 was transformed to H-Nb_2O_5 (see table 1). In figure 4, L-Nb_2O_5 is shown to occur as both the low temperature-high pressure and high temperature-high pressure (L′-Nb_2O_5) forms of Nb_2O_5 (see discussion sec. 5).

b. Structure

Numerous attempts to index the x-ray powder diffraction pattern of L-Nb_2O_5 have been reported in the literature. All such previous attempts were based on very limited powder data. Frevel and Rinn [15] first indexed L-Nb_2O_5 with a monoclinic unit cell and the orthorhombic subcell was indicated by Holser [16] to be similar to that of Ta_2O_5 and U_3O_8. An orthorhombic unit cell for L-Nb_2O_5 was proposed by Zvinchuck [17] with a b axis approximately 12 times the subcell. Terao [18] also showed an orthorhombic subcell and postulated a monoclinic supercell for L-Nb_2O_5 very similar to that of Frevel and Rinn [15]. From selected area electron diffraction of oxidized thin films, Spyridelis, Delavignette, and Amelinckx [19] reported that "in niobium pentoxide the spacing between the superlattice spots in the linear group is somewhat larger than in tantalum pentoxide corresponding to a smaller long spacing in direct space (which varies from 20 to 30 Å)". The authors stated that although the specimen temperature is difficult to estimate on beam heating they felt that sufficient specimen heating had occurred so that they were observing diffraction data taken from a specimen of H-Nb_2O_5. Subsequently, precharacterized specimens of H-Nb_2O_5 were examined by Allpress, Sanders and Wadsley [20] by electron diffraction and found to be much different from the films described by Spyridelis et al. [19]. They concluded that, "in our opinion these films are much more likely to consist of low-temperature T-Nb_2O_5 (L-Nb_2O_5) or an oxygen-deficient phase, or a mixture of phases closely related to it."

With increased temperature and pressure L-Nb_2O_5 was found in the present work to become more crystalline and a number of superstructure lines become clearly evident in the x-ray diffraction pattern. This pattern is very similar to that of the phase $15Ta_2O_5 \cdot 2WO_3$, the smallest unit cell found for the L-Ta_2O_5 (L-Nb_2O_5) type phases [21, 22, 23]. The crystal structure of $15Ta_2O_5 \cdot 2WO_3$ has been reported by Stephenson and Roth [24] and the x-ray diffraction powder pattern was indexed on the basis of an orthorhombic unit cell with $a=6.175$, $b=29.29$, and $c=3.874$ Å with the aid of intensities obtained from single crystal diffractometer data. For this composition, the b-axis is eight times the subcell ($b=3.661\times 8=29.29$ Å).

In the present work all of the lines of the powder pattern of L-Nb_2O_5 can be indexed on the basis of an orthorhombic cell with $a=6.168\pm.001$, $b=29.312\pm.001$ and $c=3.936\pm.001$ A, with a and c similar to the values previously reported for the subcell. As is the case with $15Ta_2O_5 \cdot 2WO_3$, the b axis exhibits a multiplicity of 8 times the subcell and the true b axis is $b=3.664\times 8=29.312\pm.001$ Å. The indexed x-ray diffraction powder pattern for L-Nb_2O_5 is given in table 3.[3]

Selected area electron diffraction patterns of L-Nb_2O_5 were made by J. G. Allpress, CSIRO, Melbourne, Australia, from a specimen heated to 1000 °C at 70,000 psi for 19 h. These patterns confirm that the correct unit cell is dimensionally orthorhombic with the parameters derived from the powder data. A typical example of diffraction from the *hkO* plane is shown in figure 5. It can be seen in this diffraction pattern that there is a multiplicity of 8 along the b axis.

For a phase with $m=8$ the ideal composition is $M_{16}O_{42}$ [21, 23, 24]. The compound $15Ta_2O_5 \cdot 2WO_3$ has the formula $Ta_{15}WO_{40.5}$ for eight subcells whereas the low temperature form of Nb_2O_5 would correspond to $Nb_{16}O_{40}$ with two oxygen ions missing and would have a slightly different ordering scheme. Since the crystal structure of $15Ta_2O_5 \cdot 2WO_3$ has been reported from single crystal data [24] it is possible to calculate the intensities of the x-ray diffraction powder pattern of this material. The Fortran program used for the computation was developed by Smith [25] and modified by Evans [26]. The calculated integrated intensities of the powder pattern agree quite well with those published for the observed powder data [22]. The integrated intensities for the L-Nb_2O_5 powder pattern were calculated utilizing the same coordinates. The

[3] R. Nolander and R. Norin (Acta Chem. Scand. 26 3814 (1972)) have also indexed a powder pattern of "T-Nb_2O_5" with the unit cell: $a=6.170$, $b=29.25$, $c=3.928$ Å.

Table 3. Indexed X-Ray Diffraction Powder Pattern for L-Nb_2O_5 (CuKα radiation)[a/]

hkl[b/]	d_{obs}	$2\theta_{obs}$	$2\theta_{calc}$	I_{obs}[c/]	I_{calc}[d/]
130	5.217	16.98	16.98	5	6
060	4.886	18.14	18.14	1	2
001	3.934	22.58	22.57	88	100
170	---	---	25.70	--	3
180	3.151	28.30	28.31	100	82
200	3.085	28.92	28.93	44	33
210	3.0680	29.08	29.09	15	22
190	---	---	31.03	--	<1
250	2.7298	32.78	32.78	5	1
260	2.6078	34.36	34.36	3	1
171	2.6080	34.46	34.46	1	2
181	2.4597	36.50	36.50	48	36
201	2.4278	37.00	37.00	21	14
211	2.4200	37.12	37.13	10	9
2,10,0	2.1250	42.51	42.51	3	1
1,13,0	2.1177	42.66	42.66	4	2
320	---	---	44.46	--	1
2,11,0	2.1534	44.91	44.92	6	1
330	2.0128	45.00	45.02	6	3
1,14,0	1.9828	45.72	45.72	1	2
002	1.9689	46.06	46.08	24	19
1,13,1	1.8646	48.80	48.79	6	2
370	---	---	49.34	--	2
0,16,0	1.8322	49.72	49.73	16	8
321	1.8084	50.42	50.41	1	1
380 331	1.7931	50.88	50.88 50.90	23	12
390	---	---	52.60	--	1
371 182	1.6693	54.96	54.96 54.96	24	20
0,16,1	1.6603	55.27	55.26	23	12
202	1.6592	55.32	55.32	23	12
2,15,0	1.6507	55.63	55.63	3	2
381	1.6316	56.34	56.34	15	9
391	---	---	57.94	--	1
2,16,0	1.5750	58.56	58.56	10	6
400	1.5420	59.94	59.93	4	1
410	1.5396	60.04	60.03	4	1
3,13,0	1.5195	60.92	60.93	3	<1
450	1.4912	62.20	62.19	1	<1
460	---	---	63.18	--	1
3,14,0	---	---	63.34	--	1
2,16,1	1.4622	63.58	63.57	9	5
401	1.4351	64.92	64.89	4	1
332	1.4070	66.38	66.39	3	1
372	---	---	69.80	--	1
0,16,2	1.3409	70.12	70.12	5	4
382	1.3255	71.06	71.06	8	6
003	---	71.90	---	--	2

[a/] Specimen heated to 700°C at 108,500 psi for 168 hours in a sealed Pt tube and quenched.

[b/] Indexed on the basis of an orthorhombic unit cell a=6.199Å, b=29.124Å, and c=3.938Å.

[c/] Observed intensity peak heights

[d/] Calculated peak intensity using Fortran program described by D. Smith [25] and modified by E. Evans [26] (based on assumptions given in text).

following assumptions were made for the calculation: space group Pm was chosen, and the z coordinates were fixed either at 0 or 1/2. Oxygen number 21 (notation of [24]) was found to be absent 3 out of 4 times in two unit cells of $15Ta_2O_5 \cdot 2WO_3$ and assumed to be completely absent in Nb_2O_5. The calculated peak intensities of L-Nb_2O_5 [25] (given in table 3) were found to be in good agreement with those observed in the x-ray powder diffraction pattern and to agree within experimental error with those calculated for $15Ta_2O_5 \cdot 2WO_3$. The L-Nb_2O_5 specimen from which these computations were made was heated at 700 °C for

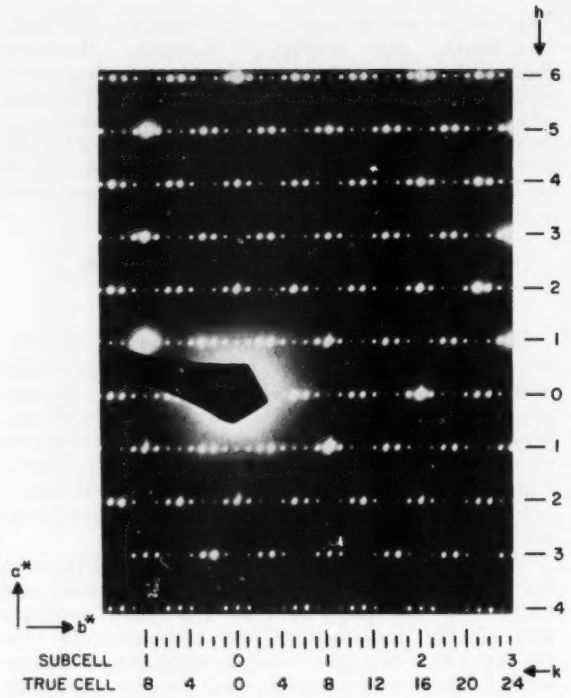

FIGURE 5. *Selected area electron diffraction photograph of the* hk0 *plane of a crystal of* L-Nb_2O_5 *taken from a specimen heated to 1000 °C at 70,000 psi for 19 hours.*

The superstructure of 8 times the subcell is clearly evident, as marked on the lower margin.

168 h at 108,500 psi. Since crystals in this specimen were too small for single crystal x-ray diffraction studies, an attempt was made to grow single crystals of low Nb_2O_5 under pressure by the addition of H_2O. The resulting material was still very fine grained and unsuitable for single crystal x-ray diffraction studies. The x-ray powder pattern was indexed on the basis of a similar orthorhombic cell with the b axis multiplicity of 8 and slightly different unit cell dimensions, $a = 6.199$ Å, $b = 3.640 \times 8 = 29.124$ Å, and $c = 3.938$ Å.

5. Discussion

In figure 4 L-Nb_2O_5 and L′-Nb_2O_5 are shown to occur in two different portions of the system, separated by the field of B-Nb_2O_5. The x-ray diffraction patterns of specimens prepared in these two fields are identical except for degree of crystallinity. There are at least two possible interpretations of the data.

The first possibility is that an unknown high temperature phase may be postulated to cool metastably through the B-field and then transform to a stable phase of the L-Nb_2O_5 type. The low temperature form of Nb_2O_5 may possibly go through an infinite series of structurally subtle transitions of the sort reported for L-Ta_2O_5 [21, 24] involving a change in the multiplicity of the b axis. This type of transition would involve a

change in vacancy ordering and therefore in density. The structure of this original high temperature phase is, or course unknown, but may be postulated as being similar to H-Ta_2O_5 (previously found for Nb_2O_5 only from melted specimens containing some ZrO_2 [27]).

The second possibility is that a high temperature-high pressure polymorph may be assumed to be a phase of the L-Nb_2O_5 type which, on cooling through the B-field metastably, goes through a series of transitions to the $m=8$ phase at atmospheric temperature and pressure. In the first case L-Nb_2O_5 is the stable phase only in the low temperature-high pressure region. In the second case L-Nb_2O_5 is stable only in the high temperature-high pressure region and the B-polymorph is stable to ambient temperature at high pressures. Either case is equally possible even if the $m=8$ phase is maintained at all temperatures and pressures. The correct situation could only be solved by a high resolution high pressure-high temperature (above 900 °C) x-ray study. Unfortunately such an apparatus was not available.

The authors wish to express their thanks to J. G. Allpress, CSIRO, Melbourne, Australia, for the electron diffraction examination, to H. Yoder and G. Speicher of the Geophysical Laboratory, Carnegie Institute of Washington for their many helpful comments during the course of this work, and to J. Filliben of the National Bureau of Standards for his help in the mathematical computation involved in the pressure measurement. The writers are especially indebted to instrument maker L. Schneider of NBS for his assistance in repairing and modifying the equipment.

6. References

[1] Wadsley, A. D., and Andersson, S., Perspectives in Structural Chemistry Vol. **III**, p. 1, edited by J. D. Dunitz and J. A. Ibers (John Wiley and Sons, New York, 1970).
[2] Tamura, S., J. Mater. Sci. **7** 298 (1972).
[3] Yoder, H. S., Jr., Trans. Amer. Geophy. Union **31** 827 (1950).
[4] Laus, F. A., Electrical Measurements, (McGraw-Hill, New York, 1938).
[5] Bell, P. M., Boyd, F. R., Jr., and England, J. L., Accurate Characterization of the High-Pressure Environment, Nat. Bur. Stand. (U.S.), Spec. Publ. 326, p. 63, edited by E. C. Lloyd (1971).
[6] Roth, R. S., Parker, H. S., Brower, W. S., and Waring, J. L., Fast Ion Transport in Solids, Solid State Batteries and Devices, sponsored by Advanced Study Institute, Belgirate, Italy (1972). Edited by W. vanGool (North Holland Publishing Co., Amsterdam, Holland, 1973), p. 217.
[7] Gatehouse, B. M., and Wadsley, A. D., Acta Cryst. **17** 1545 (1964).
[8] Holzberg, F., Reisman, A., Berry, M., and Berkenbilt, M., J. Am. Chem. Soc. **81** 3182 (1959).
[9] Laves, F., Petter, W., and Wulf, H., Naturwissenschaften **51** 633 (1964).
[10] Schäfer, H., Schulte, F., and Gruehn, R., Angew. Chem. **76** 536 (1964).
[11] Brauer, G., Z. anorg. allgem Chem. **248** 1 (1941).
[12] Roth, R. S., and Waring, J. L., Amer. Min. **48** 1348 (1963).
[13] Andersson, S., and Aström, Acta Chemica Scan. **18** 2233 (1964).
[14] Jahnberg, L., and Andersson, S., Acta Chemica Scan. **21** 615 (1967).
[15] Frevel, L. K., and Rinn, H. N., Anal. Chem. **27** 1329 (1955).
[16] Holser, W. T., Acta Cryst. **9** 196 (1956).
[17] Zvinchuck, R. A., Crystallography C.C.C.R. **3** 744 (1958).
[18] Terao, N., Japanese Journal of Applied Physics **2** 156 (1963).
[19] Spyridelis, J. S., Delavignette, P., and Amelinckx, S., Phys. stat. sol. **19** 683 (1967).
[20] Allpress, J. G., Sanders, J. V., and Wadsley, A. D., Phys. stat. sol. **25** 544 (1968).
[21] Roth, R. S., and Waring, J. L., J. Res. Nat. Bur. Stand. (U.S.), **74A** (Phys. and Chem.), No. 4, 485–493 (July–Aug. 1970).
[22] Roth, R. S., Waring, J. L., and Parker, H. S., J. Solid State Chem. **2** 445 (1970).
[23] Roth, R. S., and Stephenson, N. C., The Chemistry of Extended Defects in Non-Metallic Solids, p. 167, Edited by L. Eyring and M. O'Keeffe, (North Holland Publishing Co., Amsterdam, 1970).
[24] Stephenson, N. C., and Roth, R. S., Acta Cryst. **B27** 1110 (1971).
[25] Smith, D. K., A. Revised Program for Calculating Powder Diffraction Patterns, Lawrence Radiation Laboratory, Livermore, Calif.
[26] Personal communication, E. Evans, National Bureau of Standards (1973).
[27] Roth, R. S., Waring, J. L., Brower, W. S., and Parker, H. S., NBS Special Publ. 364, p. 183, Proceedings of 5th Materials Research Symposium, Edited by R. S. Roth and S. J. Schneider (1972).

(Paper 77A6–793)

JOURNAL OF RESEARCH of the National Bureau of Standards—A. Physics and Chemistry
Vol. 77A, No. 6, November–December 1973

Nuclear Magnetic Resonance of ^{113}Cd and ^{199}Hg in Cd-Mg and Cd-Hg Solid Solutions

V. V. Zhukov,* I. D. Weisman, and L. H. Bennett

Institute for Materials Research, National Bureau of Standards, Washington, D.C. 20234

(August 10, 1973)

The current theoretical and experimental situation with respect to Knight shifts and bulk susceptibility of Cd in pure Cd and in Cd-Mg and Cd-Hg alloys is reviewed. New experimental isotropic and anisotropic Knight shift data on ^{113}Cd in Cd-Mg and Cd-Hg alloys and on ^{199}Hg in Cd-Hg alloys are presented. The behavior of the ^{199}Hg sites is found to be remarkably similar to that of the ^{113}Cd site in the Cd-Hg alloys. However the ratio of isotropic Knight Shift of ^{199}Hg to ^{113}Cd is somewhat greater than the ratio of ^{199}Hg to ^{113}Cd atomic hyperfine fields suggesting that there is more local electronic "*s*" character at the Fermi surface in the alloy than in the pure metals. This is consistent with the theoretical picture of Cd in which phonon scattering induced by increasing temperature or alloying smears and weakens the lattice potential which in turn leads to a more "*s*" like Fermi surface.

Further, the ^{113}Cd Knight shift is found to be a useful tool for monitoring the phase segregation that occurs in Cd-Mg due to internal oxidation and for determining the concentrations of solutes such as Hg and Mg in Cd-Hg and Cd-Mg alloys.

Key words: Anisotropic Knight shift; Cd; Cd-Hg; internal Mg oxidation; isotropic Knight shift; Knight shift.

1. Introduction

The purpose of this paper is threefold: (1) To review the current theoretical and experimental situation with respect to Knight shifts and electronic structure in metallic Cd. The mechanisms which are thought to be responsible for the peculiar temperature dependences of the pure Cd Knight shift and bulk susceptibility are noted. The implications with respect to the Cd band structure of recent measurements of the Cd Knight shifts in Cd-Mg and Cd-Hg alloys are discussed. (2) To contribute some new experimental Knight shift data on solid solutions of isovalent Cd-Mg and Cd-Hg alloys. These include isotropic and anisotropic Knight shifts at ^{113}Cd and ^{199}Hg sites in Cd-Mg and Cd-Hg alloys. (3) To discuss the use of nuclear magnetic resonance as a sensitive probe of the kinetics of Mg oxidation which takes place in Cd-Mg alloys, and the use of the Knight shift to measure the alloy concentration.

2. General Observations

The isotropic and anisotropic Knight shift and the susceptibility of Cd are very temperature dependent. Earlier it was suggested that there might be a correlation between the temperature dependences of the Knight shift and the susceptibility [1].[1] Although a correlation between the isotropic and anisotropic Knight shift on the one hand and the susceptibility on the other exists, it is not linear as we will show below.

The isotropic part of the Knight shift of *hcp* Cd changes from 0.35 percent to 0.58 percent (an increase of 70%), in going from liquid helium temperatures to 594 K [1–5]. It further increases by 33 percent (to 0.79%) upon melting of the metal [2]. Over the same temperature range, the anisotropic part of the Knight shift varies by a factor of 6 in magnitude, and changes sign, progressing from −0.01 percent at liquid helium temperature [4–7] to 0.05 percent at [3, 8, 9] 300 K.

The magnetic susceptibility of pure Cd is diamagnetic and anisotropic [10]. There is a temperature dependence which is a function of the angle between the applied magnetic field (used in measuring the susceptibility) and the hexagonal symmetry axis (*c* axis). This is illustrated in figure 1. The susceptibility measured along the *c* axis, $\chi_{\parallel}$, increases in magnitude by a factor of 3 in going from high to low temperature. The susceptibility measured perpendicular to the *c* axis $\chi_{\perp}$ is essentially temperature independent.

* Guest-worker at the NBS. Permanent address: Physical Technical Institute of Low Temperature (Academy of Sciences of the Ukr. SSR) Kharkov, 310086 USSR.

[1] Figures in brackets indicate the literature references at the end of this paper.

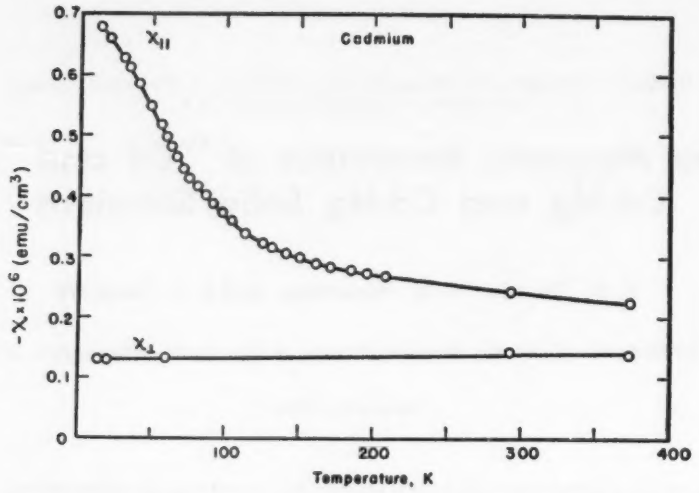

FIGURE 1. *The experimentally measured magnetic susceptibility of* Cd *metal single crystal as a function of temperature.*

$\chi_{\parallel}$ is the susceptibility measured parallel to the c axis and $\chi_{\perp}$ is the susceptibility measured perpendicular to the c axis. Both $\chi_{\parallel}$ and $\chi_{\perp}$ are diamagnetic. (From ref. [10]).

It is of interest to see whether or not the Knight shift and the susceptibility have the same functional dependence upon temperature, and thus a linear relationship to each other. Figure 2a shows the anisotropic Knight shift parameter $\mathcal{K}_{ax}$ as a function of the magnetic anisotropy, $\chi_{\parallel}-\chi_{\perp}$ and of the average susceptibility [11], $(\chi_{\parallel}+2\chi_{\perp})=3$ with temperature as the implicit variable. Figure 2b shows the isotropic Knight shift plotted against the average susceptibility. The data were obtained from the works previously mentioned [3, 4, 10]. The reason for plotting $\mathcal{K}_{ax}$ against $\chi_{\parallel}-\chi_{\perp}$ is to test for the possibility of a common orbital contribution [11]. The obvious departure from linearity in each case suggests that the Knight shift and susceptibility arise predominantly from different mechanisms. Temperature dependent terms other than spin paramagnetism must be operative in either the Knight shift or the susceptibility or both. This will be mentioned further in the following discussion.

The Brillouin zone and some parts of the Cd Fermi surface are shown [12] in figure 3. For our purposes the most important parts of the Fermi surface are the neck (waist) of the second zone hole monster (which appears in fig. 3a near point M), the third zone lens of electrons centered at point Γ, and the third zone needles of electrons at point K. Figure 3b shows a section in the plane MΓK using the repeating zone representation of the Fermi surface. The sections of the monster which are thought to contribute to the Knight shift are clearly visible in the figure.

The peculiar dependence of both isotropic and anisotropic shifts has been attributed to the effects of lattice vibrations on the Cd band structure [13, 14]. In the pseudopotential approximation, the increasing phonon modulation of the band structure weakens the pseudopotential [15] of pure Cd, leading to a more free electron like behavior at the Fermi surface. The important parts of the Fermi surface insofar as the Knight shift is concerned are the sections of 2d-zone-hole monster in the ΓM direction and lens of the third band, which are a mixture of "*s*" and "*p*" like electronic states [14]. At $T=0$ K, "*p*" contributions to the anisotropic Knight shift from the monster almost completely cancel the corresponding contribution from the lens. As the temperature is raised the decrease and symmetrizing of the pseudopotential increases the relative amount of "*s*" character on the monster at the expense of "*p*" character. However the electronic character at the lens is unaffected. It then follows that the isotropic and anisotropic Knight shifts will increase. The isotropic shift increases because of the corresponding increase in "*s*" character, the anisotropic shift because of the decrease in "*p*" character that opposes the positive lens contribution. The jump in isotropic shift at the melting point can be explained as an abrupt change in the density of states in the liquid state of the metal brought about by the disappearance of long-range order in the solid state [14, 16]. Calculations by Jena et al. [17] show that core polarization contributions do not exceed 10 percent of the low temperature isotropic Knight shift.

Kasowski [14] and Jena and Halder [16] have calculated the value of the Knight shift at selected temperatures between 0 K and the melting point and upon melting. On the basis of these theoretical works it is possible to partition the contributions to the changes in the isotropic Knight shift over three temperature ranges as shown in table 1. The table shows an oscillation in the importance of the roles played by the density

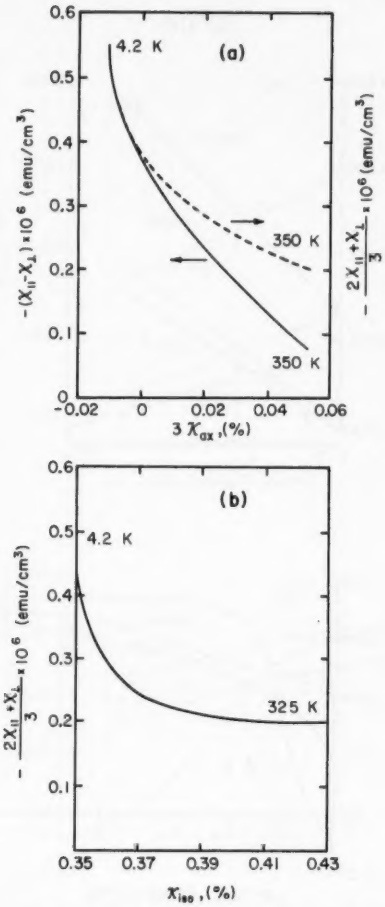

FIGURE 2. *Knight shifts of* ^{113}Cd *versus susceptibility with temperature as the implicit variable in the approximate range of 4.2 to 325–350 K.*

See text for definition of $\chi_{\parallel}$ and $\chi_{\perp}$.

(a) The anisotropic Knight shift is plotted against the experimentally measured magnetic anisotropy, $\chi_{\parallel}-\chi_{\perp}$, which is shown in solid curve. The anisotropic shift is also plotted against the averaged experimental susceptibility $(\chi_{\parallel}+2\chi_{\perp})/3$ which is shown as a dashed curve. Note that $\chi_{\parallel}-\chi_{\perp}$ is plotted on the left hand ordinate axis whereas $(\chi_{\parallel}+2\chi_{\perp})/3$ is plotted on the right hand ordinate axis.

(b) Isotropic Knight shift plotted against the averaged experimentally measured susceptibility. The data have been taken from refs. [3, 4, and 10].

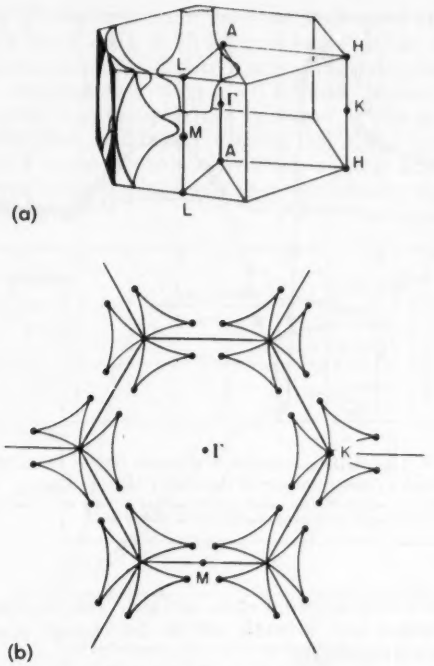

FIGURE 3. *Parts of the Fermi surface of* hcp Cd (*from ref.* [12]).

[a] Symmetry points of the Brillouin zone and second zone hole sheets in single-zone segments.

[b] Section in the MΓK plane (see text).

TABLE 1. *Partitioning of isotropic Knight shift changes between the density of states and the electronic density*

	Solid Cd			Liquid Cd
	0 K	462	594 [a]	
$\mathcal{K}_{iso}$,%)	0.35	0.47	0.59	0.79
$\Delta\mathcal{K}_{iso}$(%)	0.12	0.11	0.21	
% increase in $\mathcal{K}_{iso}$	34	24	36	
Fraction of $\Delta\mathcal{K}_{iso}$ due to density of states changes	1/2	1/8	4/5	
Fraction of $\Delta\mathcal{K}_{iso}$ due to explicit changes in $\langle\|\psi(0)\|^2\rangle_F$	1/2	7/8	1/5	

[a] Melting point.

of states and the wavefunction through the electronic density, $<|\psi(0)|^2>_F$, in producing the increases in isotropic shift observed in the solid at 462 and 594 K (the melting point) and in the liquid. Below 462 K the density of states accounts for half the change in Knight shift. Between 462 and 594 K the wavefunction structure presumably determined by the symmetrizing of the pseudopotential produces 7/8 of the increment observed in the measurement of $\mathcal{K}_{iso}$, the isotropic shift. It should be noted that in the region 0–462 K the density of states is found to increase by only 17 percent and thus the spin susceptibility increases from [14] 0.54 to 0.63×10^{-6} emu/cm^3. This would seem to rule out the possibility that the decrease in diamagnetic susceptibility might arise from an increase in spin paramagnetism.

In summarizing the situation for pure Cd,

(1) Neither the isotropic nor the anisotropic Knight shift is linearly proportional to the susceptibility.

(2) According to the recent work by Kasowski [14], most of the Knight shift (anisotropic and isotropic) temperature dependence can be explained by the changes in electronic character at the monster and

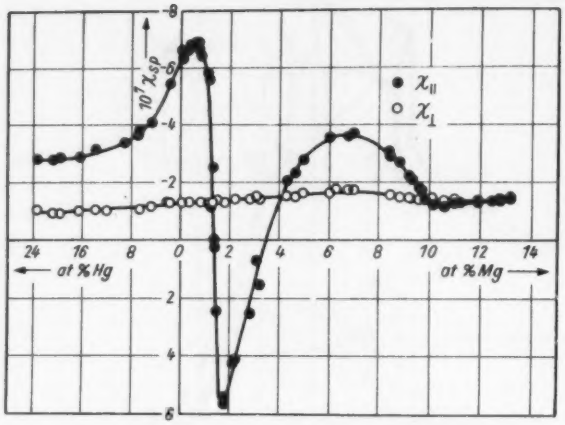

FIGURE 4 *Magnetic susceptibility of single crystal* Cd *alloys as a function of concentration of* Hg *and of* Mg *at 4.2 K.*

χ is plotted in emu/(cm)³. The vertical scale is inverted so that χ values above the horizontal axis in the figure are diamagnetic. (From refs. [18 and 19]).

lens portions of the Fermi surface. This mechanism contributes only a small part of the change observed in the susceptibility.

In order to understand the electronic behavior in pure Cd a series of low temperature susceptibility measurements on Cd-Mg and Cd-Hg alloys were carried out by Svechkarev et al. [18, 19]. Their data, taken at 4.2 K, is shown in figure 4. The striking features in the variation of the susceptibility measured parallel to the *c* axis are the diamagnetic peaks at 0.5 and 6.5 at. % Mg and the sharp paramagnetic peak at 1.8 at. % Mg. Later Zhukov and Svechkarev [7, 20, 21] followed up with Knight shift measurements on the ^{113}Cd site in these alloys. They found that although the isotropic and anisotropic shifts increased with the addition of Mg or Hg neither one followed the drastic variations in the susceptibility reported by Svechkarev et al. [18, 19]. The data of Zhukov and Svechkarev along with that of others is shown in figures 5 and 6. In the interest of clarity their data points are shown only on the isotropic shift of Cd in Cd-Mg alloys at 20.4 K. McClure and Martyniuk [22] have calculated the orbital susceptibility of Cd as a function of Hg or Mg concentration under the assumption [18, 19] that the susceptibility behavior is dominated by contributions from electrons in closely spaced energy bands near Brillouin zone boundaries. Such a region occurs in the vicinity of symmetry point K in Cd. Their particular model calculation reproduces the experimental susceptibility behavior rather well.

It would then appear that the bulk susceptibility and iso- and anisotropic Knight shifts do not track one another with concentration because they are determined by distinctly different regions of the Fermi surface. In pure Cd, the Knight shift is primarily associated with the spin paramagnetism and wavefunctions on the parts of the Fermi surface in the

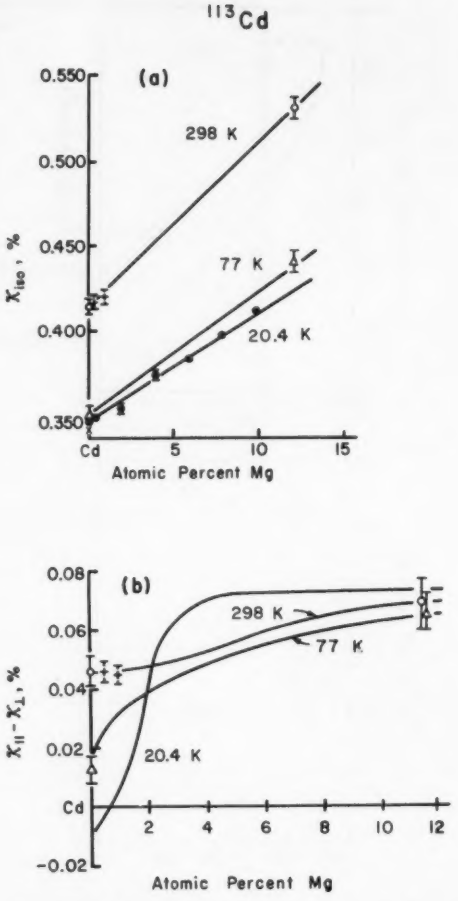

FIGURE 5. *Knight shifts at the* ^{113}Cd *site in* Cd-Mg *alloys as a function of* Mg *concentration at three different temperatures.*

(a) Isotropic shifts. The solid curves represent the data of Zhukov and Svechkarev (refs. [7, 20, 21]) at the indicated temperature. Some representative data points from their work are shown by the closed circles. The crosses are room temperature data points from Borsa and Barnes (ref. [3]), the x is from Williams and Sharma (ref. [4]), and the open circles and triangles show data we have obtained in this investigation at respectively room and liquid nitrogen temperatures (assuming a nominal concentration of 12 at. % Mg). All data points have been scaled so that the pure ^{113}Cd Knight shift is 0.415 percent at 293 K. (ref. [30]). (b) Anisotropic shifts: The identification of the data is the same as in (a).

vicinity of symmetry points M (monster) and Γ (lens) [14]. The principal contributions to the susceptibility come from the needles of the Fermi surface (point K). The variation in susceptibility as a function of Mg and Hg alloying arises from a turning off and on of an orbital (diamagnetic term) rather than a large increase in spin paramagnetism. The potential changes introduced by alloying with isoelectronic Mg and Hg produce an approximately monotonic variation in the isotropic and anisotropic Knight shifts which are quite different than the drastic changes in the diamagnetic susceptibility introduced by interband electronic contributions at point K [18, 19]. This would explain why no corresponding drastic changes in the Knight shift are observed. Such a finding is also consistent

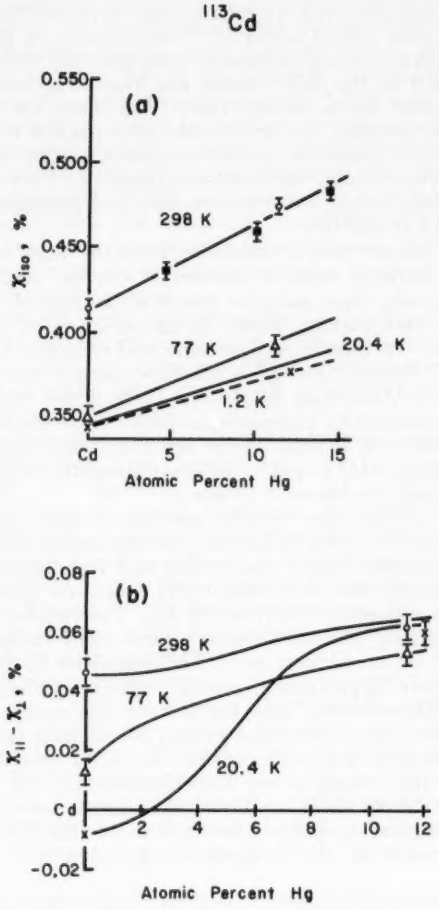

FIGURE 6. *Knight shifts at the* ^{113}Cd *site in* Cd-Hg *alloys as a function of* Hg *concentration between liquid helium and room temperatures.*

(a) Isotropic shift: The solid curves represent the data of Zhukov and Svechkarev at 20.4, 77 and 298 K (refs. [7, 20, 21, and 25]). The open circles and triangles reflect new data from this study at respectively room and liquid nitrogen temperatures. The x's are superimposed from the 1.2 K data of Williams and Sharma (ref. [4]) and the closed squares are from the work of Grant and Henry at room temperature (ref. [34]). All data points have been scaled so that the pure ^{113}Cd Knight shift is 0.415 percent at 298 K and 0.350 percent at 4.2 K. (ref. [30]).

(b) Anisotropic shifts: The identification of data is the same as in (a). The datum from Williams and Sharma (ref. [4]) for Cd+12 at. % Hg was plotted under the assumption that these authors give $\frac{1}{3}(\mathcal{K}_{\parallel} - \mathcal{K}_{\perp})$. (From ref. [35]).

with recent Knight shift measurements [23] on Ga, Al, and In in pseudobinary alloys of $AuGa_2$, $AuAl_2$, and $AuIn_2$ and with Knight shift and susceptibility measurements on ^{71}Ga in $AuGa_2$ at temperatures above 500 K [24]. In the case of $AuGa_2$ at high temperatures it is found that the susceptibility is increasing, with increasing temperature while the Knight shift is relatively constant.

In addition Zhukov and Svechkarev [17, 21, 25] have experimentally extracted the concentration dependence of the structure of the wavefunctions insofar as they contribute to the ratio $3\mathcal{K}_{ax}/\mathcal{K}_{iso}$. Figure 7 is a plot of this ratio as a function of concentration for Cd-Mg and Cd-Hg at 20.4 K and as a function of temperature for pure Cd. The three curves are similar in form and suggest a correlation between impurity concentration and temperature in terms of affecting the wavefunction (band structure) via the lattice potential. Figure 8 expresses this correlation directly where the temperature calibration has been provided by the pure Cd in figure 7.

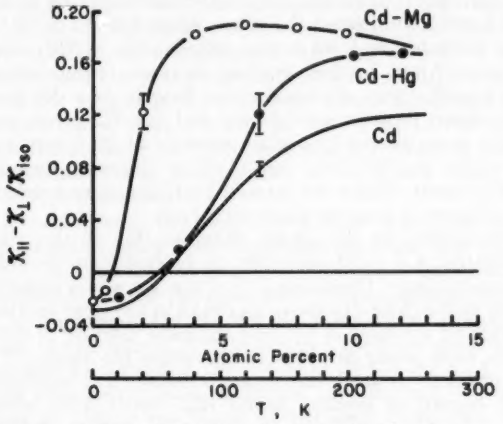

FIGURE 7. *Ratio of* ^{113}Cd $(\mathcal{K}_{\parallel} - \mathcal{K}_{\perp})/\mathcal{K}_{iso}$ *plotted against concentration (in at. %) of* Mg *and* Hg *in* Cd-Mg *and* Cd-Hg *alloys respectively at 20.4 K and against temperature in pure* Cd.

A typical error bar is indicated on each curve. (From refs. [20 and 21]).

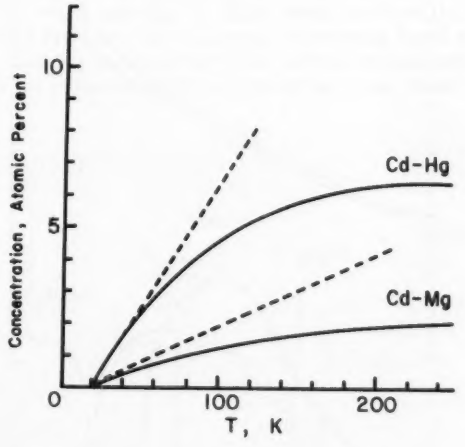

FIGURE 8. *Concentration-temperature correspondence based on the* ^{113}Cd *ratio* $\mathcal{K}_{ax}/\mathcal{K}_{iso}$ *extracted from figure 7 for* Cd-Mg *and* Cd-Hg *alloys.*

See text. The dotted lines are the slopes of the curves at C = 0. Note that in the case of Cd-Mg it takes 3–4 times less solute than in Cd-Hg to produce an effect on the lattice potential equivalent to the same change in temperature. (From refs. [20 and 21]).

3. New Experimental Data

3.1. Sample Preparation, Characterization and Experimental Procedure

The Cd-Mg alloy was prepared by melting weighed amounts of the constituents under flux in a resistance furnace. The molten alloy was mixed by stirring with a graphite rod and then chill cast in a steel mold. The powder was obtained by remelting the ingot in a 350 °C paraffin oil bath contained in a stainless steel beaker. A high speed homogenizer (7000 rpm) operating under the bath comminuted the alloy. After cooling to 70 °C the particles and oil were sieved with a 200 mesh screen. After further cooling to room temperature the paraffin was removed using hexane in a dry box. The dried powder was sieved and the 325 mesh particles were sealed in a glass capsule at 10^{-5} torr and annealed at 300 °C for 100 h. After resieving through a 325 mesh screen the passed particles were found to be spheres of average diameter 10 μm.

According to the phase diagram (fig. 9) the alloy prepared, Cd + 12 at.% Mg, is probably in the solid solution range. Oxidation [27] of the Mg was a problem here and will be discussed in detail in the next section. Weighed amounts of Cd and Hg were allowed to react with each other at room temperature for about 12 h in order to reduce the vapor pressure and minimize the hazard of heating liquid Hg. The Cd-Hg alloys were then prepared by melting the constituents in a quartz tube sealed under 10^{-5} torr vacuum. A resistance furnace which maintained a temperature of 400 °C was used for the melt. Mixing was assured by shaking the molten metal several times. The alloy was then cast by inverting the quartz tube allowing the molten material to freeze in a cool extension of the quartz tube. After cooling the ingot was transferred to a glass tube sealed under 10^{-5} torr vacuum and homogenized for 100 h at 250 °C.

The powder was prepared by filing the ingot under liquid nitrogen using a number 4 cut file, and collecting only those particles which would pass through a 325 mesh screen. These filings were sealed under 10^{-5} torr vacuum in a glass tube and annealed 6 h at 250 °C. Sieving through a 325 mesh screen was then repeated. According to recent Cd-Hg phase diagram measurements by Claeson et al. [28], our Cd-Hg alloys lie within the α-phase solid solution range (fig. 10). The filings were found to be small irregular foils with an average thickness of 10 μm.

The Cd-Mg alloy powder prepared under oil was examined by x-ray diffraction. Interpolation between the measured lattice parameters and the diagram of Svechkarev and Solnyshkin [27] indicated that the sample contained 9.4(1) at. % Mg. Two weeks after preparation, additional x-ray lines attributable to "pure" Cd metal were seen. The intensities of the Cd lines were approximately equal to those of the alloy lines. Three weeks later the powder was reexamined with the x-ray diffractometer and broadening as well as substantial weakening of the alloy lines were noted along with strong sharp lines for metallic Cd. The growth of the Cd x-ray lines with time is associated with internal oxidation discussed in section 3.4. The discrepancy in the composition between the x-ray

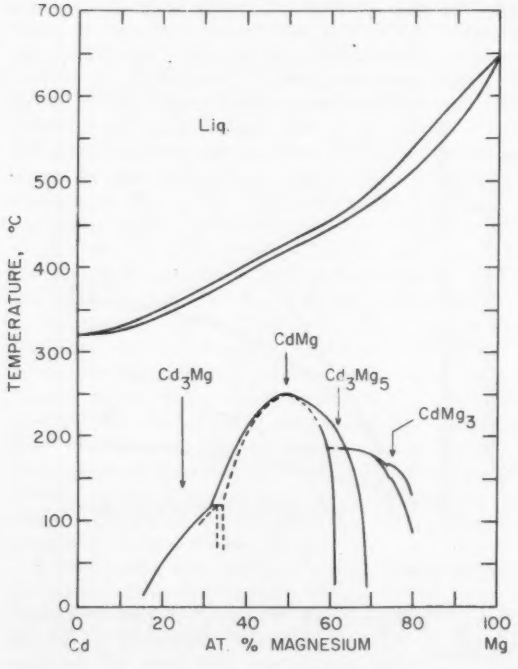

FIGURE 9. Cd-Mg *phase diagram.*

The Cd + 12 at. % Mg alloy is probably within the α-phase solid solution region (From ref. [26]).

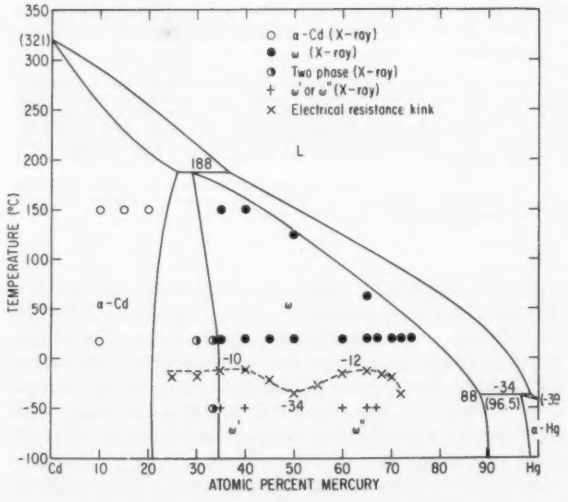

FIGURE 10. Cd-Mg *phase diagram.*

An alloy of Cd + 12 at. % Hg is well within the α-phase solid solution region. (From ref. [28]).

measurement and the weighed (12 at. % Mg) constitutents is not understood at the present time but we will consider that the alloy concentration is about 12 at. % because this is the nominal composition and because this value agrees with the NMR data shown in figure 5a. It would be useful to use other analytical techniques, including perhaps electron microprobe, to resolve this matter. Simultaneous with the x-ray determinations, NMR measurements were made on this alloy with the interesting result that the Knight shift may be more precise than the x-ray diffraction pattern for obtaining the concentration in the presence of phase segregation.

X-ray diffraction patterns on the Cd-Hg alloys yielded the Hg concentrations shown in table 2. The interpolation between concentration of Hg and lattice parameter is also taken from the work of Svechkarev and Solnyshkin [27].

Measurements of the Knight shift were made on a Varian[2] wide line crossed coil spectrometer (V-4200B) at magnetic fields of 16kG(^{113}Cd) and 10kG(^{199}Hg). A signal averaging computer (Varian C-1024) was employed with repetitive field sweeps to improve signal to noise. To obtain temperatures of 4.2 and 77 K, a cold finger Dewar was inserted into the probe. For studies at these temperatures the sample was sealed in a glass vial under a fraction of an atmosphere of helium gas.

The resonance parameters were measured using the ^{113}Cd and ^{199}Hg isotopes both of which have spin $I = 1/2$ and thus the spectra are not complicated by quadrupole effects. The skin depth at these frequencies exceeds the average particle dimensions in the pure Cd at 77 K and in the Cd alloys at all temperatures. The isotropic and anisotropic Knight shift parameters were extracted using the method of Lebedev [7, 29].

TABLE 2. *Concentration of* Hg *(at. %) in* Cd-Hg *alloys determined by x-ray diffraction and NMR*

Nominal concentration [a]	X-ray diffraction determination	Isotropic Knight shift determination
1.5		1.6(5)
3		2.4(5)
6	5.6(5)	6.0(5)
8	8.1(3)	8.2(5)
10	9.3(3)	9.6(5)
12	11.3(3)	12.0(5)

[a] As determined by initial weighing of constituents prior to alloy preparation.

3.2. Knight Shift Results

Some NMR line profiles on pure Cd were made at 16kG at room and at nitrogen temperatures in this study in order to improve the accuracy of the lower field anisotropy measurements of the previous study [7, 21, 25]. An illustration of the resolution of the ^{113}Cd powder pattern available at the higher fields at $T = 298$ K is shown in figure 11.

The Cd NMR in a Cd+12 at. % Hg alloy was investigated. The numbers obtained for the isotropic and anisotropic Knight shifts on the ^{113}Cd site at two temperatures (77 K and 298 K) agree reasonably well with data from the previous work (see figure 6).

The ^{199}Hg resonance was observed in all of the Cd-Hg alloys—described in section 3.1. The isotropic and anisotropic Knight shifts which were measured at 4.2, 77 and 298 K are plotted against concentration in figure 12. The concentrations were determined from the ^{113}Cd Knight shifts as will be described in the section on metallurgical applications. The linewidths with the anisotropy subtracted out [7, 29] varied between 15 and 20 G. The more dilute alloys had the narrow lines. Knight shifts of the ^{199}Hg in the alloy were referenced to ^{199}Hg in liquid Hg metal at room temperature. The Knight shift of ^{199}Hg was taken as 2.72(1) percent [30].

By combining the isotropic Knight shift data from the previous work with the numbers from this study (fig. 5 and fig. 6) it is possible to obtain a linear least squares fit to the isotropic shift versus concentration, C, in the case of **Cd**-Mg, **Cd**-Hg and Cd-**Hg**. The equations of the line of $\mathcal{K}$ (C) versus C at 4 temperatures are listed in table 3. In the case of **Cd**-Hg at 4.2 K only two points from Williams and Sharma [4] were used to obtain the slope of the line. Note that the slope of $\mathcal{K}$ (C) provides a practical method of measuring C to within $\pm 1/2$ at. %.

3.3. Discussion of Knight Shift Results

It should be noted that the behavior of both isotropic and anisotropic ^{199}Hg shifts as a function of alloying was qualitatively similar to the corresponding curves at the ^{113}Cd site (fig. 6). This would confirm that the Cd and Hg atom are observing a common band structure. Similar behavior in which solvent and solute atom "see" a common band structure has been found pre-

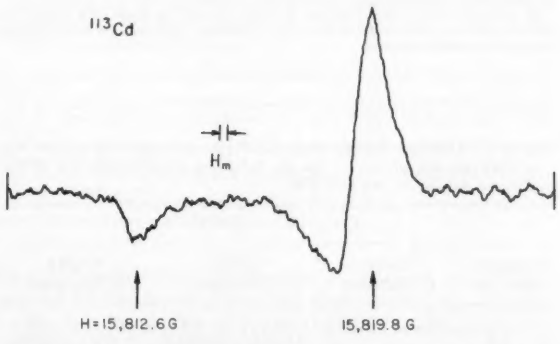

FIGURE 11. *Typical trace of the* ^{113}Cd *absorption derivative spectrum versus magnetic field in pure metallic* Cd *powder at 298 K and at 16kG.*

A modulation of 0.25G and an integrator time constant of 0.3 s were employed. The trace represents 250 digitally stored sweeps each of 25 s duration through the line.

[2] This instrument is identified in order to adequately specify the experimental procedure. In no case does such identification imply recommendation or endorsement by the National Bureau of Standards, nor does it imply that the instrument identified is necessarily the best available for the purpose.

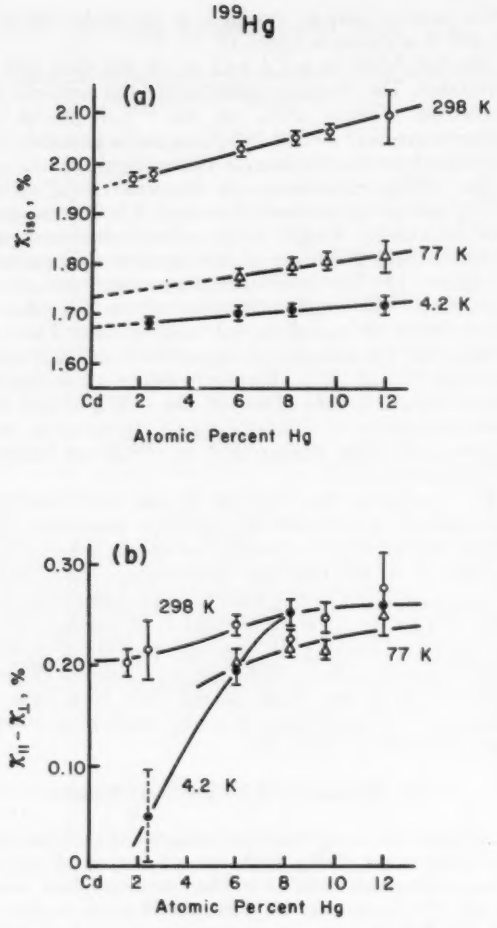

FIGURE 12. *Knight shifts of* ^{199}Hg *in* Cd-Hg *alloys versus* Hg *concentration.*

The open circles are 298 K data, the triangles are 77 K data and the closed circles are 4.2 K data.

(a) Isotropic Knight shifts. The solid lines represent least squares fits to the data and the dashed lines are extrapolations of the fitted lines to C=0.

(b) Anisotropic Knight shift. The large uncertainty (dashed bar in the 4.2 K datum) was introduced by the combined effects of low Hg concentration and noise from random sample motion in the liquid helium bath.

TABLE 3. *Isotropic Knight shifts (in %) as a function of solute* (Mg *or* Hg) *concentration,* C, *(in at. %) from least-squares fits to the data in figures 5a, 6a and 10a*

$$\mathcal{K}(C) = \mathcal{K}_0 + \Delta\mathcal{K} \cdot C$$

Temperature K	Cd-Mg (^{113}Cd site)		Cd-Hg (^{113}Cd site)		Cd-Hg (^{199}Hg site)	
	$\mathcal{K}_0$	$\Delta\mathcal{K}$	$\mathcal{K}_0$	$\Delta\mathcal{K}$	$\mathcal{K}_0$	$\Delta\mathcal{K}$
4.2			[a] 0.350 + 0.0025C		1.674 + 0.004C	
20.4	0.350 + 0.006C		0.350 + 0.003C			
77	0.353 + 0.007C		0.353 + 0.004C		1.737 + 0.007C	
298	0.415 + 0.009C		0.415 + 0.005C		1.952 + 0.012C	

[a] This value of $\mathcal{K}_{iso}$ was obtained only from two points (see text).

viously in pseudobinary alloys [23] of $AuGa_2$ and $AuIn_2$.

We have evaluated the ratio $[\mathcal{K}_{Hg}(C)/\mathcal{K}_{Cd}(C)]$ in the Cd-Hg alloys at C=0, 5, 10 at. % Hg and at 4.2, 77 and 298 K. The values for the three concentrations were averaged together at each temperature and the results are shown in table 4. The average over all 3 temperatures is listed at the bottom of the table. In the simplest possible common band picture, this ratio should be equal to the ratio of hyperfine fields in the free atoms [9], $H_{Hg}^{atom}/H_{Cd}^{atom} = 3.69$. This follows because

$$\mathcal{K} \propto \xi H^{atom} \chi_p$$

in which ξ is the fractional amount of electronic "*s*" character at the site and χ_p is the spin susceptibility.

The deviation of the experimental ratio $[\mathcal{K}_{Hg}/\mathcal{K}_{Cd}]$ from the theoretical estimate of $H_{Hg}^{atom}/H_{Cd}^{atom}$ may imply unequal ξ factors at the two sites. For example if it is assumed that $\xi_{Cd} = 0.33$ in Cd metal [9] the ξ_{Hg} has a value of 0.42 in the Cd alloy. This is to be compared [9] with $\xi_{Hg} = 0.21$ in solid metallic Hg. Interestingly enough, $\xi_{Hg} = 0.49$ in the liquid [30].

To ascertain the effects of volume changes on the ratio $\mathcal{K}_{Hg}/\mathcal{K}_{Cd}$, we list in table 5 the atomic sizes of Mg, Cd, and Hg evaluated using four different criteria [31]. It is clear from table 5 that in all cases the atomic size increases in going from Cd to Hg. The Cd lattice compresses the Hg solute relative to a metallic Hg lattice and if other factors are ignored, the product ξH_{Hg} would be larger than in solid Hg metal. However the decrease in size using any of the criteria in table 5 lead to volume changes that are too small to explain the observed factor of two increase in ξ.

TABLE 4. *Average ratio of* ^{199}Hg *and* ^{113}Cd *Knight shifts*

Temperature, K	$[\mathcal{K}_{Hg}/\mathcal{K}_{Cd}]$
4.2	4.68(9)
77	4.77(14)
298	4.58(10)
Total average:	4.67(11)

TABLE 5. *Atomic sizes of* Mg, Cd *and* Hg *(from Pearson ref.* [31])

	Pearson's atomic volume (Å)^3	Pauling's single bond radii valence 2 (Å)	Pauling's ionic radii valence 2 (Å)	Teatum, Gschneider and Waber CN 12 radii (Å)
Mg	23.240	1.364	0.65	1.602
Cd	21.581	1.485	0.97	1.568
Hg	23.4	1.490	1.10	1.573

Figure 13 shows the increased ξ factor of Hg as a probe in Cd superposed on the ξ factors computed for a large number of pure metals. The new point, i.e., ^{199}Hg in Cd (closed circle) appears more appropriate to the Ag-Cd-In row than the ^{113}Cd in Cd. A possible explanation is that the Cd lattice already has an anomalously low ξ_{Cd} factor [9] because of anisotropy effects. Adding Hg destroys the anisotropy by producing a dis-

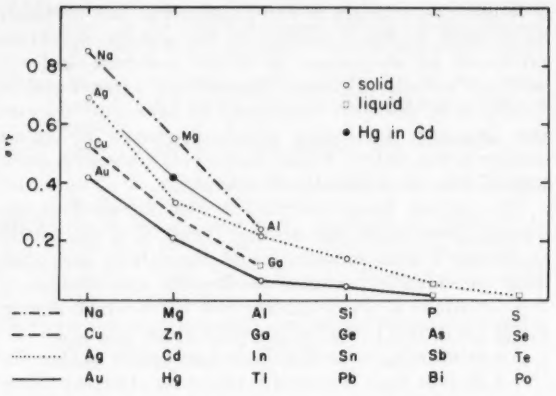

FIGURE 13. *Behavior of ξ factors for metallic elements as a function of their position in the periodic table.*

(From ref. [9]). The ^{199}Hg site ξ factor (0.42) obtained in Cd-Hg alloys is shown as a closed circle. This point is related to Ag on one side and to In on the other by the partially extended solid line. The ξ value is to be contrasted with the ξ factor of ^{113}Cd (0.33) in Cd. See text.

ordered lattice with weaker and a more symmetric lattice potential [14, 20, 21]. This in turn leads to an increase in electronic "*s*" character at the Fermi surface which is sensed by both the ^{113}Cd and ^{199}Hg Knight shifts.

3.4. Metallurgical Applications of the Knight Shift

Using the x-ray measurement of concentration, the isotropic and anisotropic Knight shifts for one alloy, Cd + 12 at. % Hg, are shown at 77 and 298 K in figure 6. The room temperature point fits reasonably well on the straight line constructed from previous data where the concentrations were deduced from more extensive x-ray diffractometry. Alternatively, it was possible to assign Hg concentrations in Cd-Hg alloys by measuring the room temperature isotropic ^{113}Cd Knight shift and superimposing this value on the curve corresponding to 298 K in figure 6a. Both the x-ray and Knight shift determinations of the Hg concentration in these alloys are shown in table 2. It should be noted that the concentrations determined from the Knight shifts are in good agreement with the x-ray determinations in four alloys. The ^{113}Cd lineshapes indicated that the alloys were all single phase.

Another application was the use of the ^{113}Cd isotropic Knight shift to study the kinetics of Mg oxidation in the Cd-Mg alloy. We found that the isotropic Knight shift provides a more precise method for monitoring the kinetics of Mg oxidation mentioned earlier in connection with sample preparation than conventional x-ray diffractometry. This is illustrated in figure 14 where four traces of the Cd spectrum from the Cd + 12 at. % Mg alloy taken during a 2 month period at room temperature are shown in chronological order. Approximately 2 weeks after sample preparation, oxidation of the Mg and its effective removal from the solid solution matrix is evident by the appearance of the pure Cd line on the right-hand side of the figure. On the

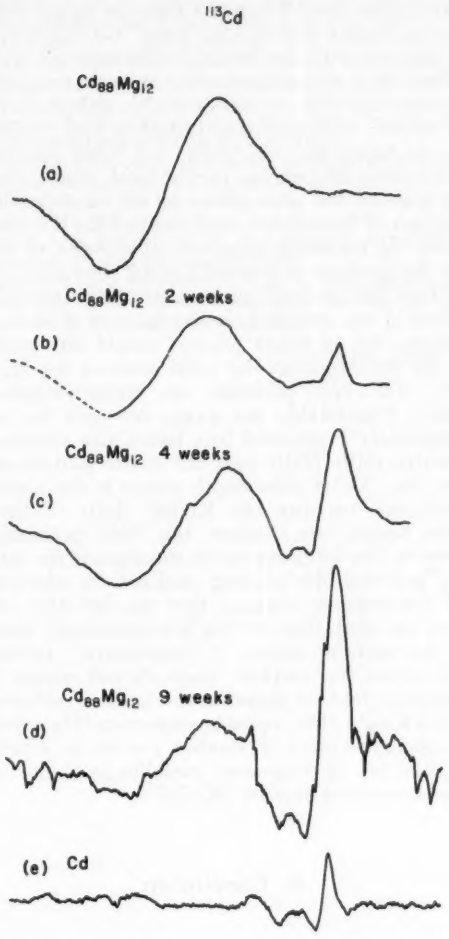

FIGURE 14. *Traces of the* ^{113}Cd *absorption derivative spectrum in an alloy (initially prepared to be a* Cd + 12 *at. % Mg alloy) versus magnetic field (increasing to the right) at room temperature in the neighborhood of 16kG. In each case the narrow line on the right corresponds to "pure" metallic* Cd *and the broader line on the left corresponds to the alloy.*

(a) Spectrum observed immediately after sample was prepared. There is no trace of "pure" Cd.
(b) Spectrum observed two weeks after sample was prepared, with the sample stored at room temperature in a screw-cap vial. The relative NMR intensity of "pure" Cd is 5 percent.
(c) Spectrum observed 5 weeks after sample was prepared. The relative NMR intensity of "pure" Cd is 16 percent.
(d) Spectrum observed 9 weeks after sample was prepared. The relative NMR intensity of "pure" Cd is 54 percent.
(e) Spectrum of ^{113}Cd in a sample consisting only of pure metallic Cd under the same experimental conditions as (a) through (d).

basis of figure 5a it is possible to assign a concentration of 12.5(5) at. % Mg to the shifted alloy line visible on the left-hand side of figure 11b. The relative amount of "pure" metallic Cd in the alloy phase is about 5 percent as determined from the resonance intensity of the spectrum [32]. At this point the x-ray diffraction indicated the existence of a pure Cd line but the intensity was insufficient to permit its resolution from

the main alloy line. When the trace in figure 11c was taken the relative intensity of "pure" Cd had increased to 16 percent with no change in the isotropic shift of the alloy. An x-ray measurement at approximately the same time that this trace was made, indicated a two-phase region with well resolved alloy and "pure" Cd peaks. In figure 11d the "pure" Cd NMR intensity is approximately 54 percent of the total. Again the isotropic shift of the alloy phase is unchanged. The investigation of Svechkarev and Solnyshkin [27] showed that the Mg oxidation proceeds to a depth of 20 μm below the surface of a solid Cd-Mg alloy after which no further Mg precipitation occurs. Since the bulk of the alloy in our sample is in the form of spheres of 10 μm diam, the oxidation process would ultimately remove all the Mg from the solid solution leaving only "pure" Cd and probably an oxygen-magnesium complex. Presumably the x-rays see only the atoms approximately 1 μm and less below the surface. On the contrary the NMR sees the entire particle to the extent that the rf skin depth exceeds the diameter. Furthermore because the Knight shifts of the two metallic phases are distinct, the NMR is capable of monitoring the intensity ratios throughout the interval over which the Mg is being oxidized. In addition the NMR observations suggest that the kinetics of this process are such that the Mg is continuously removed from the metallic phase at progressively increasing depths below the surface. There do not appear to be any intermediate Cd phases in this process, otherwise a third Cd Knight shift would be expected. It is important to mention that here is another system in which the NMR can be an important metallurgical monitoring probe in studying kinetics [32–33].

4. Conclusion

The ^{113}Cd and ^{199}Hg isotropic and anisotropic Knight shifts have been measured in Cd-Mg and Cd-Hg alloys. The ^{113}Cd shifts are in agreement with previous work. The ^{199}Hg shifts in Cd-Hg qualitatively reproduce the behavior of the ^{113}Cd shifts in the same alloys as a function of Hg concentration. However the ratio of ^{199}Hg to ^{113}Cd isotropic shift exceeds the corresponding hyperfine field ratio suggesting that the relative fraction of electronic "*s*" character at the Fermi surface is greater in the alloy than in either of the pure metals. Volume changes are too small to account directly for the observed increase in the ^{199}Hg ξ factor. The increase in "*s*" character at the Hg site is consistent with the theoretical model of the anisotropic Cd band structure in which phonon scattering induced by increases in temperature or alloying leads to a weaker more symmetric lattice potential.

Recent nonlocal pseudopotential band calculations [36] on Cd-Mg and Cd-Hg alloys tend to support this approach. These calculations are for the most part in agreement with the results of the earlier simpler local potential approach [20, 21]. For example, in Cd-Mg it is found that changes in the Knight shift can probably be related to the variation in the energy spectrum produced by decreases in lattice constant and c/a induced by alloying with Mg. On the other hand in Cd-Hg it is probably necessary to take into account the impurity scattering which produces an effect similar to the Debye-Waller factor [14] (phonon scattering) in order to explain the Knight shifts.

The recent band calculation also shows that the energy spectrum at the needles (point K) is insensitive to Debye-Waller modulation of the lattice potential. This provides a justification for the explanation of the variations in susceptibility [18, 19] in which smearing of the lattice potential has been neglected [22].

An interesting metallurgical observation is that the ^{113}Cd Knight shift is a useful probe for studying phase segregation and for measuring solute concentrations in Cd-Hg alloys.

We are indebted to D. B. Fickle for sample preparation, to R. L. Parke for technical assistance and to C. J. Bechtoldt for the x-ray diffractometry measurements. We thank R. E. Watson, H. Schone, J. Gardner, P. Soven, J. R. Anderson, and R. V. Kasowski for helpful discussions. We also acknowledge the assistance of G. C. Carter and D. J. Kahan of the Alloy Data Center, NBS.

5. References

[1] Schone, H. E., Phys. Rev. Letters **13,** 12 (1964).
[2] Seymour, E. F. W., and Styles, G. A., Phys. Letters **10,** 269 (1964).
[3] Borsa, F., and Barnes, R. G., J. Phys. Chem. Solids **27,** 567 (1966).
[4] Williams, D., and Sharma, S. N., Can. J. Phys. **48,** 1416 (1970).
[5] Goodrich, R. G., Khan, S. A., and Reynolds, J. M., Phys. Rev. **3B,** 2379 (1971).
[6] Sharma, S. N., and Williams, D. L., Phys. Letters **25A,** 738 (1967).
[7] Zhukov, V. V., Zhuk, G. M., Svechkarev, I. V., Phys. Nizk. Temp. N17, 3, FTINT AN Ukr. SSR, Kharkov (1972) (In Russian).
[8] Drain, L. E., Metal. Rev. **119,** 195 (1967).
[9] Bennett, L. H., Watson, R. E., and Carter, G. C., J. Res. Nat. Bur. Stand. (U.S.), **74A** (Phys. and Chem.), No. 4, 569–610 (July–Aug. 1970).
[10] Marcus, J., Phys. Rev. **76,** 621 (1949).
[11] Ross, J. W., Fradin, F. Y., Isaacs, L. I., and Lam, D. J., Phys. Rev. **183,** 645 (1969).
[12] Hurd, C. M., The Hall Effect in Metals and Alloys (Plenum Press, New York, 1972).
[13] Kasowski, R. V., and Falicov, L. M., Phys. Rev. Letters **22,** 1001 (1969).
[14] Kasowski, R. V., Phys. Rev. **187,** 891 (1969).
[15] Stark, R. W., and Falicov, L. M., Phys. Rev. Letters **19,** 795 (1967).
[16] Jena, P., and Halder, N. C., Phys. Rev. Letters **26,** 1024 (1971).
[17] Jena, P., Das, T. P., Gaspari, G. D., and Mahanti, S. D., Phys. Rev. **1B,** 1160 (1970).
[18] Svechkarev, I. V., and Kusmicheva, L. B., Phys. Status Solidi, Sol. **37,** K113 (1970).
[19] Svechkarev, I. V., Kusmicheva, L. B., and Poltoratsky, V. I., Magnetic Properties of Zinc and α-phase of Binary Solid Solutions of Mercury and Magnesium in Cadmium, FTINT AN Ukr. SSR, Kharkov (1972) (In Russina).

[20] Zhukov, V. V., Zhuk, G. M., and Svechkarev, I. V., Abstracts of Reports at the XVIIth Congress Ampere, Turku, Finland (Aug. 1972). Full text in English available from authors upon request.
[21] Svechkarev, I. V., Zhukov, V. V., and Zhuk, G. M., Phys. Nizk. Temp. N20, 77, FTINT AN Ukr. SSR, Kharkov (1972) (In Russian).
[22] McClure, J. W., and Martyniuk, J., Phys. Rev. Letters **29**, 1095 (1972).
[23] Carter, G. C., Weisman, I. D., Bennett, L. H., and Watson, R. E., Phys. Rev. **B5**, 3621 (1972).
[24] Warren, W. W., Jr., Shaw, R. W., Jr., Menth, A., DiSalvo, F. J., Storm, A. R. and Wernick, J. H., Phys. Rev. **B7**, 1247 (1973).
[25] Zhukov, V. V., Fenster, M. Ia., Svechkarev, I. V., and Zhuk, G. M., Phys. Nizk. Temp. N18, 58, FTINT AN Ukr. SSR. Kharkov (1972) (In Russian).
[26] Phase diagram prepared by the National Bureau of Standards Alloy Data Center from Hansen, M., Constitution of Binary Alloys (McGraw-Hill Book Co., Inc., New York 1958) and Elliott, R. P., Constitution of Binary Alloys, First Supplement (McGraw-Hill Book Co., Inc., New York, 1965).
[27] Svechkarev, I. V., and Solnyshkin, D. D., Phys. Nizk. Temp. N18, 119, FTINT AN Ukr. SSR, Kharkov (1972) (In Russian).
[28] Claeson, T., Luo, H. L. Anantharaman, T. R. and Marriam, M. F., Acta Met. **14**, 285 (1966).
[29] Lebedev, Ya. S., J. Struct. Chem. 4, 19 (1963) (Translated from: Zhurnal Structurn. Khimii **4**, 22 (1963)).
[30] This value is the result of a critical evaluation of Knight shifts by the National Bureau of Standards Alloy Data Center.
[31] Pearson, W. B., The Crystal Chemistry and Physics of Metals and Alloys (Wiley Interscience, New York, 1972).
[32] Bennett, L. H. and Carter, G. C., Met. Trans. **2**, 3079 (1971).
[33] Bennett, L. H., Acta Met. **14**, 997 (1966).
[34] Grant, R. F., and Henry, W. G., Can. J. Phys. **39**, 841 (1961).
[35] Daughterty, M., and Hewitt, R. R., Phys. Rev. **5B**, 3450 (1972).
[36] Kasowski, R. V., private communication.

(Paper 77A6–794)

520-812 O-LF - 73 - 3

JOURNAL OF RESEARCH of the National Bureau of Standards—A. Physics and Chemistry
Vol. 77A, No. 6, November-December 1973

The Pair Correlation Function in Liquid ^{4}He

Raymond D. Mountain and Harold J. Raveché

Institute for Basic Standards, National Bureau of Standards, Washington, D.C. 20234

(June 28, 1973)

The pair correlation function obtained from the neutron diffraction data of Mozer, De Graaf, and Le Neindre, is given for liquid ^{4}He at several thermodynamic states above and below the superfluid transition. A method for smoothly and accurately extrapolating the pair function into the limit of zero internuclear separation is considered. The pair function is computed from an approximation integral equation for the ground state wave function and compared to the experimental results.

Key words: Ground state wave function; liquid ^{4}He; neutron diffraction data; pair correlation function; short range behavior; structure factor; superfluid transition.

1. Introduction

The intensity of elastically scattered neutrons in an isotopic fluid defines [1][1] the structure factor, $S(\kappa;\rho,T)$, which is a function of $\kappa=|\boldsymbol{\kappa}-\boldsymbol{\kappa}_0|$, where $\boldsymbol{\kappa}_0$ is the wave vector of the neutron before scattering, and $\boldsymbol{\kappa}$ the wave vector after scattering. The quantities ρ and T are respectively the density and temperature of the fluid sample. The structure factor is of particular interest as its Fourier transform, $g_2(r_{12};\rho,T)$, with respect to the internuclear distance r_{12}, defines the local structure of the fluid.

$$g_2(r_{12};\rho,T)=1 + (2\pi^2\rho r_{12})^{-1}\int_0^\infty d\kappa\kappa \sin \kappa r_{12}\,[S(\kappa;\rho,T)-1]. \quad (1)$$

The function $g_2(r_{12};\rho,T)$ is necessarily positive and is usually referred to as the pair correlation function; we will adopt this nomenclature. Both neutron and x-ray [2] measurements of $S(\kappa;\rho,T)$ in ^{4}He have been made, but data of high statistical accuracy, for several thermodynamic states in 1–3 K range, have only recently been reported [3]. The motivation for experiments at low temperatures is to explore the changes in the behavior of the local structure of liquid ^{4}He that might accompany the transition at $T=T_\lambda$ from normal to superfluid [4]. In addition, it is also known [5] that measurements of the isothermal density derivative of $g_2(r_{12};\rho,T)$ are a measure of the magnitude and range of the correlation between three atoms. Quite recently, Mozer, De Graaf, and Le Neindre [6, 7] have done neutron diffraction measurements of high statistical accuracy for several thermodynamic states in liquid ^{4}He. The thermodynamic states at which the scattering experiments were performed are listed in table 1. The table also includes the value of the superfluid transition temperature, T_λ, for each density considered. All temperatures in table 1 are known to within ± 0.005 K, and all densities to within ± 0.25 percent.

TABLE 1. *Thermodynamic states for* g_2 (r; ρ, T) *in liquid* ^{4}He
The bracketed number in the pressure column is the observed pressure in the Pascal unit; 1 atm = 0.101325 MPa.

ρ(atoms/Å^3)	T(K)	T_λ(K)	P(atm),	(MPa)
0.0230	1.860	2.135	4.31	(0.44)
.0230	2.050	2.135	3.96	(0.40)
.0230	2.130	2.135	3.60	(0.37)
.0230	2.140	2.135	3.60	(0.37)
.0230	2.300	2.135	3.79	(0.38)
.0230	2.840	2.135	5.25	(0.54)
.0236	2.020	2.107	6.50	(0.66)
.0236	2.860	2.107	7.81	(0.79)
.0245	1.940	2.050	11.60	(1.18)
.0245	2.860	2.050	12.51	(1.27)

This manuscript reports the values of $g_2(r_{12};\rho,T)$ obtained from applying eq (1) to the data of Mozer, De Graaf, and Le Neindre; we also present the results of two other computations involving the pair function. The first is an investigation of an algorithm for the short range ($r_{12}\to 0$) behavior of $g_2(r_{12};\rho,T)$. The other computation gives a comparison of the experimental results for the pair function and the results obtained from an approximate integral equation for the ground state value, $T=0$, of the pair function.

[1] Figures in brackets indicate the literature references at the end of this paper.

Table 2. The pair correlation function, $g_2(r_{12};\rho,T)$, for liquid ^{4}He as a function of internuclear distance, r_{12}, temperature, T, and density, ρ.

$\rho(\text{Å}^{-3})$	.0230	.0230	.0230	.0230	.0230	.0230	.0236	.0236	.0245	.0245
T(K)	1.860	2.050	2.130	2.140	2.300	2.840	2.020	2.860	1.940	2.860
r_{12}(Å)										
.123	.400	.784	1.714	1.454	1.762	1.498	1.242	.915	.850	.518
.245	.437	.743	1.559	1.365	1.612	1.403	1.184	.928	.826	.574
.368	.481	.681	1.329	1.228	1.389	1.254	1.088	.929	.780	.638
.491	.514	.600	1.060	1.056	1.126	1.067	.961	.899	.706	.674
.614	.518	.509	.789	.865	.857	.857	.810	.823	.606	.658
.736	.485	.415	.549	.670	.612	.645	.643	.700	.484	.579
.859	.417	.324	.361	.485	.407	.448	.475	.543	.355	.449
.982	.325	.242	.228	.320	.248	.280	.318	.372	.233	.294
1.104	.223	.170	.143	.181	.133	.150	.182	.212	.129	.145
1.227	.127	.111	.089	.071	.051	.059	.075	.080	.049	.025
1.350	.045	.062	.046	-.011	-.007	.000	-.001	-.013	-.007	-.053
1.473	-.019	.023	.003	-.068	-.050	-.035	-.049	-.069	-.044	-.090
1.595	-.064	-.007	-.045	-.102	-.083	-.059	-.075	-.094	-.066	-.096
1.718	-.093	-.027	-.093	-.118	-.105	-.079	-.084	-.099	-.076	-.082
1.841	-.108	-.032	-.128	-.119	-.115	-.096	-.079	-.088	-.072	-.058
1.963	-.104	-.020	-.136	-.105	-.107	-.101	-.057	-.060	-.047	-.026
2.086	-.073	.015	-.107	-.071	-.075	-.083	-.013	-.012	.004	.021
2.209	-.008	.076	-.033	-.010	-.011	-.027	.060	.062	.086	.091
2.332	.100	.167	.084	.087	.090	.076	.166	.168	.200	.191
2.454	.252	.289	.241	.226	.233	.228	.307	.307	.344	.327
2.577	.442	.440	.428	.404	.412	.420	.476	.473	.513	.494
2.700	.654	.615	.632	.614	.619	.636	.663	.659	.698	.684
2.823	.867	.803	.838	.834	.835	.853	.853	.851	.887	.882
2.945	1.060	.990	1.031	1.043	1.039	1.053	1.032	1.035	1.066	1.071
3.068	1.216	1.161	1.197	1.219	1.213	1.218	1.187	1.195	1.223	1.233
3.191	1.326	1.299	1.325	1.345	1.341	1.339	1.308	1.320	1.343	1.355
3.313	1.390	1.392	1.408	1.418	1.418	1.413	1.390	1.403	1.420	1.431
3.436	1.415	1.435	1.448	1.444	1.448	1.444	1.430	1.440	1.451	1.460
3.559	1.411	1.430	1.450	1.435	1.440	1.438	1.431	1.436	1.439	1.447
3.682	1.387	1.388	1.421	1.404	1.407	1.405	1.398	1.399	1.394	1.403
3.804	1.347	1.324	1.371	1.360	1.358	1.354	1.340	1.340	1.327	1.338
3.927	1.295	1.251	1.307	1.307	1.301	1.293	1.267	1.269	1.251	1.263
4.050	1.230	1.182	1.237	1.245	1.236	1.228	1.190	1.197	1.175	1.186
4.172	1.156	1.122	1.164	1.174	1.167	1.161	1.118	1.129	1.104	1.112
4.295	1.078	1.071	1.092	1.098	1.095	1.094	1.056	1.068	1.041	1.046
4.418	1.003	1.028	1.024	1.021	1.024	1.029	1.006	1.014	.988	.987
4.541	.941	.988	.963	.953	.960	.966	.966	.967	.942	.938
4.663	.898	.949	.911	.900	.908	.9.0	.932	.925	.904	.897
4.786	.872	.911	.871	.865	.870	.866	.901	.889	.875	.865
4.909	.861	.879	.843	.846	.846	.837	.874	.862	.853	.842
5.031	.859	.856	.827	.838	.836	.827	.852	.844	.840	.829
5.154	.860	.845	.823	.836	.834	.831	.840	.836	.836	.827
5.277	.861	.846	.830	.837	.839	.847	.839	.840	.842	.834
5.400	.866	.858	.847	.845	.850	.867	.851	.852	.857	.852
5.522	.876	.879	.871	.860	.867	.886	.874	.873	.880	.878
5.645	.895	.905	.898	.885	.890	.904	.904	.899	.911	.910
5.768	.923	.934	.926	.919	.919	.923	.935	.929	.944	.944
5.890	.955	.962	.953	.957	.952	.943	.965	.959	.978	.978
6.013	.987	.987	.979	.992	.984	.969	.991	.988	1.007	1.008
6.136	1.015	1.009	1.005	1.021	1.013	.999	1.013	1.014	1.030	1.032
6.259	1.035	1.027	1.030	1.040	1.038	1.030	1.031	1.035	1.046	1.050
6.381	1.049	1.039	1.056	1.053	1.057	1.058	1.046	1.052	1.057	1.064
6.504	1.059	1.048	1.078	1.061	1.072	1.078	1.058	1.065	1.065	1.074
6.627	1.067	1.054	1.094	1.070	1.082	1.088	1.068	1.073	1.071	1.080
6.750	1.073	1.059	1.099	1.079	1.088	1.089	1.073	1.077	1.075	1.083
6.872	1.076	1.062	1.094	1.086	1.087	1.085	1.074	1.077	1.075	1.081
6.995	1.073	1.064	1.078	1.087	1.080	1.076	1.069	1.073	1.071	1.073

We proceed next, to the results for $g_2(r_{12};\rho,T)$ and then in section 3, we discuss the short range behavior. The computation of the pair function from the Percus-Yevick approximation will be given in section 4; the article concludes, at section 5, with a discussion of results.

2. Pair Function from Scattering Data

The results of applying eq (1) to the neutron diffraction measurements are given in table 2, where we have listed $g_2(r_{12};\rho,T)$ as a function of r_{12} for all the thermodynamic states shown in table 1.

Table 2, continued. The pair correlation function, $g_2(r_{12};\rho,T)$, for liquid ^{4}He as a function of internuclear distance, r_{12}, temperature, T, and density, ρ.

7.118	1.063	1.062	1.058	1.079	1.067	1.066	1.061	1.065	1.062	1.061
7.240	1.047	1.055	1.038	1.062	1.049	1.053	1.049	1.053	1.047	1.045
7.363	1.028	1.042	1.022	1.039	1.030	1.038	1.034	1.037	1.028	1.027
7.486	1.009	1.025	1.011	1.016	1.012	1.021	1.019	1.020	1.009	1.008
7.609	.995	1.007	1.003	.995	.998	1.003	1.003	1.003	.991	.991
7.731	.986	.991	.996	.982	.988	.987	.990	.988	.977	.977
7.854	.981	.979	.986	.974	.980	.975	.978	.976	.968	.966
7.977	.979	.972	.974	.970	.973	.967	.971	.968	.963	.959
8.099	.975	.970	.963	.968	.966	.963	.966	.963	.961	.956
8.222	.971	.971	.955	.965	.960	.962	.964	.962	.961	.956
8.345	.967	.972	.952	.962	.956	.960	.965	.962	.963	.958
8.468	.965	.973	.955	.959	.955	.959	.967	.963	.965	.963
8.590	.965	.973	.962	.958	.959	.959	.969	.965	.969	.968
8.713	.970	.973	.970	.961	.966	.961	.972	.969	.974	.974
8.836	.977	.976	.977	.968	.976	.968	.976	.974	.980	.980
8.958	.985	.981	.983	.977	.985	.978	.980	.981	.987	.987
9.081	.993	.987	.989	.988	.992	.991	.987	.988	.994	.994
9.204	1.000	.995	.997	.999	.999	1.003	.994	.997	1.000	1.002
9.327	1.005	1.002	1.006	1.008	1.005	1.012	1.002	1.005	1.007	1.011
9.449	1.010	1.007	1.015	1.016	1.010	1.018	1.010	1.011	1.013	1.018
9.572	1.014	1.011	1.021	1.022	1.017	1.020	1.017	1.017	1.019	1.024
9.695	1.018	1.014	1.025	1.026	1.023	1.021	1.022	1.022	1.023	1.028
9.817	1.021	1.016	1.024	1.027	1.027	1.022	1.025	1.025	1.026	1.029
9.940	1.022	1.019	1.021	1.026	1.029	1.022	1.025	1.026	1.027	1.027
10.063	1.021	1.020	1.019	1.024	1.027	1.022	1.023	1.026	1.025	1.023
10.186	1.018	1.019	1.018	1.021	1.022	1.021	1.019	1.023	1.021	1.018
10.308	1.014	1.015	1.017	1.017	1.016	1.018	1.014	1.018	1.015	1.012
10.431	1.009	1.011	1.017	1.012	1.010	1.014	1.009	1.011	1.008	1.007
10.554	1.004	1.006	1.014	1.007	1.005	1.008	1.004	1.005	1.002	1.001
10.677	1.000	1.002	1.009	1.002	1.001	1.003	1.000	.999	.997	.997
10.799	.997	1.000	1.001	.998	.999	.998	.998	.996	.994	.994
10.922	.994	.999	.993	.994	.997	.993	.996	.995	.992	.992
11.045	.992	.999	.987	.991	.994	.989	.995	.994	.991	.990
11.167	.991	.998	.985	.990	.991	.986	.993	.993	.991	.989
11.290	.990	.995	.985	.989	.987	.985	.991	.991	.990	.987
11.413	.989	.991	.987	.988	.984	.984	.989	.988	.988	.985
11.536	.989	.988	.988	.986	.982	.985	.988	.985	.987	.984
11.658	.990	.986	.989	.985	.983	.988	.987	.984	.986	.984
11.781	.992	.987	.988	.985	.986	.992	.988	.985	.987	.987
11.904	.995	.990	.988	.986	.991	.995	.991	.988	.989	.992
12.026	.998	.995	.990	.990	.996	.998	.994	.993	.994	.997
12.149	1.000	.999	.993	.994	1.001	1.000	.997	.999	.999	1.002
12.272	1.002	1.001	.997	.999	1.003	1.001	1.001	1.003	1.003	1.006
12.395	1.002	1.002	1.002	1.003	1.004	1.002	1.003	1.005	1.007	1.007
12.517	1.002	1.001	1.005	1.006	1.003	1.003	1.004	1.005	1.008	1.007
12.640	1.001	1.001	1.007	1.007	1.003	1.005	1.005	1.005	1.008	1.006
12.763	1.001	1.002	1.008	1.007	1.003	1.006	1.005	1.006	1.007	1.006
12.885	1.002	1.003	1.009	1.007	1.004	1.006	1.005	1.007	1.006	1.007
13.008	1.004	1.005	1.009	1.008	1.006	1.006	1.005	1.008	1.006	1.008
13.131	1.005	1.006	1.009	1.009	1.008	1.005	1.005	1.009	1.007	1.009
13.254	1.006	1.007	1.008	1.009	1.009	1.004	1.005	1.009	1.007	1.009
13.376	1.005	1.006	1.006	1.009	1.009	1.004	1.005	1.007	1.006	1.007
13.499	1.004	1.004	1.004	1.007	1.006	1.003	1.004	1.005	1.004	1.004
13.622	1.002	1.003	1.002	1.005	1.004	1.002	1.003	1.002	1.002	1.000
13.744	1.001	1.002	1.001	1.002	1.001	1.001	1.003	.999	1.000	.998
13.867	1.000	1.001	1.000	1.000	.999	1.000	1.002	.997	.998	.997
13.990	1.001	1.001	1.000	.998	.998	.998	1.001	.996	.997	.996
14.113	1.001	1.000	.999	.997	.998	.997	.999	.996	.997	.996
14.235	1.000	.999	.997	.995	.997	.996	.998	.996	.997	.996
14.358	.998	.997	.995	.994	.997	.997	.996	.996	.997	.996
14.481	.996	.996	.993	.992	.996	.997	.995	.996	.997	.995

There are two regions of r_{12} which reflect the principal uncertainties in measurements of $S(\kappa;\rho,T)$; these are the small and large r_{12} values. The structure factor is positive and must satisfy,

$$\lim_{\kappa\to 0} S(\kappa;\rho,T) = \rho k_B T \kappa_T \qquad (2)$$

and

$$\lim_{\kappa\to\infty} S(\kappa;\rho,T) = 1, \qquad (3)$$

where k_B is the Boltzmann constant and κ_T the isothermal compressibility. The experimentally accessible regions of κ, the magnitude of the change in the neutron wave vector upon scattering, is limited. Therefore, in practice, one must necessarily extrapolate from a given small value of κ to zero in order to satisfy eq (2) and one must also truncate $S(\kappa;\rho,T)$ at a finite value of κ in satisfying eq (3). In the Fourier transform, the errors introduced in satisfying eq (2)

Table 2, continued. The pair correlation function, $g_2(r_{12};\rho,T)$, for liquid ^{4}He as a function of internuclear distance, r_{12}, temperature, T, and density, ρ.

14.603	.994	.996	.992	.992	.995	.998	.995	.997	.996	.995
14.726	.995	.996	.993	.994	.994	.998	.995	.997	.996	.995
14.849	.996	.996	.996	.996	.995	.998	.996	.997	.995	.996
14.972	.999	.998	.999	.999	.997	.998	.997	.997	.996	.997
15.094	1.001	.998	1.001	1.002	.999	.999	.998	.997	.996	.998
15.217	1.002	.999	1.002	1.003	1.001	.999	.999	.998	.998	.999
15.340	1.001	.999	1.001	1.002	1.002	1.000	.999	.999	1.000	1.000
15.463	.999	1.000	1.000	1.000	1.002	1.000	1.000	1.001	1.001	1.002
15.585	.997	1.000	.999	.999	1.001	1.000	1.000	1.002	1.003	1.003
15.708	.998	1.000	1.000	.999	1.000	1.000	1.001	1.004	1.004	1.005
15.831	1.000	1.000	1.002	1.000	1.000	1.000	1.002	1.004	1.004	1.005
15.953	1.002	1.001	1.003	1.002	1.000	1.002	1.002	1.004	1.003	1.004
16.076	1.004	1.002	1.003	1.003	1.001	1.004	1.003	1.004	1.002	1.003
16.199	1.005	1.002	1.002	1.003	1.001	1.006	1.003	1.003	1.002	1.001
16.322	1.003	1.003	1.000	1.003	1.002	1.006	1.003	1.002	1.001	1.000
16.444	1.001	1.003	.999	1.001	1.002	1.005	1.002	1.000	1.001	1.001
16.567	.999	1.002	1.000	1.001	1.003	1.002	1.002	1.000	1.002	1.001
16.690	.998	1.001	1.001	1.001	1.003	.999	1.001	.999	1.002	1.002
16.812	1.000	1.000	1.003	1.002	1.002	.996	1.000	.999	1.001	1.002
16.935	1.002	1.000	1.004	1.002	1.002	.995	1.000	.999	1.000	1.001
17.058	1.003	.999	1.003	1.002	1.001	.997	.999	1.000	.999	.998
17.181	1.002	.999	1.000	1.001	.999	1.000	.999	.999	.998	.996
17.303	1.000	.999	.998	.999	.998	1.002	.999	.999	.997	.995
17.426	.997	.999	.996	.997	.997	1.003	.999	.998	.997	.995
17.549	.996	.999	.996	.996	.997	1.001	.999	.998	.997	.997
17.671	.996	.999	.997	.996	.998	.998	.999	.997	.998	.999
17.794	.998	.999	.999	.998	.999	.996	.999	.997	.998	1.001
17.917	1.001	.999	1.001	.999	1.001	.995	.999	.998	.999	1.001
18.040	1.003	.999	1.002	1.000	1.001	.996	.999	.999	.999	1.001
18.162	1.003	.999	1.001	1.000	1.000	.998	.999	1.001	1.000	1.000
18.285	1.001	1.000	1.000	.999	.999	1.001	.999	1.002	1.000	.999
18.408	.998	1.000	.999	.999	.998	1.002	.999	1.002	1.001	.999

effect the accuracy of the large r_{12} behavior of $g_2(r_{12};\rho,T)$. The errors introduced in satisfying eq (3) give the unphysical oscillations about the value zero which are shown in table 2. Mozer et al. have given [6, 7] an extended discussion of the extrapolation to $\kappa=0$, and we will, in the following section, discuss an algorithm to smoothly and accurately extend $g_2(r_{12};\rho,T)$ to the value zero which it must necessarily have at $r_{12}=0$. It suffices to mention here that in the numerical evaluation of the Fourier transform, eq (1), $S(\kappa;\rho,T)$ was truncated to unity for $\kappa \geq 7$ Å^{-1}. The statistical accuracy of the resulting pair functions is estimated to be within ± 3 percent.

3. Short Range Behavior

The negative values of $g_2(r_{12};\rho,T)$ in table 2 are unphysical and are introduced into eq (1) by truncating $S(\kappa;\rho,T)$. For physical systems, the pair function must approach zero in value as the internuclear distance approaches zero, and the approach to zero is presumably monotone.

We consider a method for smoothly extrapolating the results in table 2 to the value $g_2=0$; as we will discuss, the method also applies to classical liquids. Consider the pair function for $r_{12} \leq d$ and denote the function on this interval by $\tilde{g}_2(r_{12} \leq d)$. The form [8, 9]

$$\tilde{g}_2(r_{12} \leq d) = g_2(d;\rho,T)\ \exp\left\{\lambda\left[1-\left(\frac{d}{r_{12}}\right)^m\right]\right\} \qquad (4)$$

will be investigated, where we choose d as the smallest value of r_{12} for which the pair function has a statistical accuracy equivalent to that at larger r_{12} values. The number $g_2(d;\rho,T)$ is the value of $g_2(r_{12};\rho,T)$ at $r_{12}=d$. For a given value of m, the quantity λ is determined by the continuity of the derivative of the pair function and $\tilde{g}_2(r_{12} \leq d)$,

$$\lambda = \frac{d}{m}\left(\frac{g_2'(r_{12};\rho,T)}{g_2(r_{12};\rho,T)}\right)_{r_{12}=d}. \qquad (5)$$

The values $m=5$ and $m=10$ were considered and the typical agreement is shown in figures 1 and 2. In figure 1, the solid curve is the experimental result for ^{4}He at $\rho=0.0230$/Å^3 and $T=2.050$ K; the crisscross denotes the value of d. The dashed curve is for $m=5$ and $\lambda=2.423$, and the dashed-dotted curve for $m=10$ and $\lambda=1.211$. Similarly in figure 2, the solid curve is the experimental result for ^{4}He at $\rho=0.0230$/Å^3 and $T=2.840$ K; the dashed curve is eq (2) with $m=5$, $\lambda=2.032$ and the dashed-dotted curve corresponds to $m=10$, $\lambda=1.016$. As we have already mentioned, the results in figures 1 and 2 are typical of the results obtained using all the helium data in table 2, and from this we infer $m=5$ is a good choice for ^{4}He. To determine whether the algorithm also has utility in classical liquids, we investigated the data of Yarnell, Katz, Wenzel, and Koenig [10] taken for liquid argon near its triple point, $\rho=0.0215$/Å^3 and $T=85$ K. The results are shown in figure 3 where the solid curve is the experimental data, the dashed-dotted curve is eq (2) with $m=12$, $\lambda=2.670$ and the dashed curve corresponds

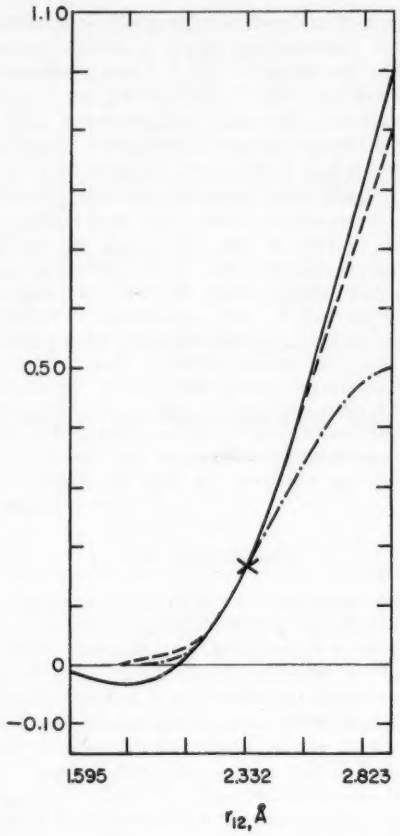

FIGURE 1. *The short range behavior of* $g_2(r_{12})$ *in liquid* ^{4}He.

The solid curve is the experimental result at $\rho = 0.0230/\text{Å}^3$, $T = 2.050$ K; the dashed curve is $\bar{g}(r_{12} \leqslant d)$, eq (4), with $m = 5$, $\lambda = 2.423$; the dashed-dotted curve is the same function with $m = 10$, $\lambda = 1.211$. The crisscross denotes the value of d.

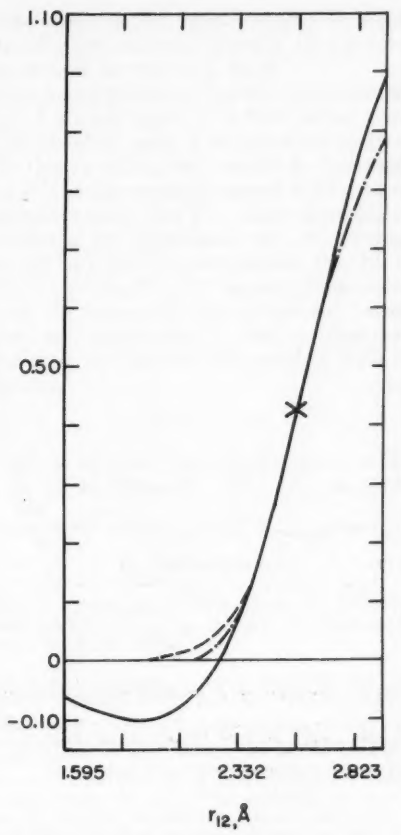

FIGURE 2. *The same as figure 1, except the experimental result is at* $T = 2.840$ *K; the dashed curve is for* $m = 5$, $\lambda = 2.032$; *the dashed-dotted curve for* $m = 10$, $\lambda = 1.016$.

For $2.332\ \text{Å} \leqslant r_{12} \leqslant 2.867$, the dashed curve is identical to the solid curve.

to $m = 5$, $\lambda = 6.407$. Relative to the data for ^{4}He, the argon results suggest that for classical fluids, $m = 12$ is a better choice.

4. Percus-Yevick Approximation

For a fluid system at $T = 0$, where the wave function, $\Psi_N^{(0)}$, for a set of N atoms is given by the Bijl-Dingle-Jastrow form [11],

$$\Psi_N^{(0)} = \prod_{1 \leqslant i < j \leqslant N} \exp\{-\tfrac{1}{2}\phi(r_{ij})\}, \tag{6}$$

the Percus-Yevick (P.Y.) approximation [12], may be used [13] to obtain an approximate integral equation for $g_2(r_{12})$ in terms of $\phi(r_{12})$. The result is,

$$g_2(r_{12}) = \exp\{-\phi(r_{12})\}[1 + \rho \int d\mathbf{r}_3 g_2(r_{13})[g_2(r_{23}) - 1] \\ [1 - \exp\{\phi(r_{13})\}]]. \tag{7}$$

Shiff and Verlet [14] have found from computer simulation studies, that for a Hamiltonian whose interaction energy, $U(r_{12})$, is the Lennard-Jones function,

$$U(r_{12}) \sim \left[\left(\frac{\sigma}{r_{12}}\right)^{12} - \left(\frac{\sigma}{r_{12}}\right)^{6}\right],$$

the function

$$\phi(r_{12}) = \left(\frac{1.16\sigma}{r_{12}}\right)^{5}, \tag{8}$$

minimizes the ground state energy. Using eq (8) and the algorithm given by Mandel, Bearman, and Bearman [15], we have solved eq (7) for $g_2(r_{12})$. All computations were done in units of σ, which for ^{4}He is [14],

$$\sigma = 2.556\ \text{Å}. \tag{9}$$

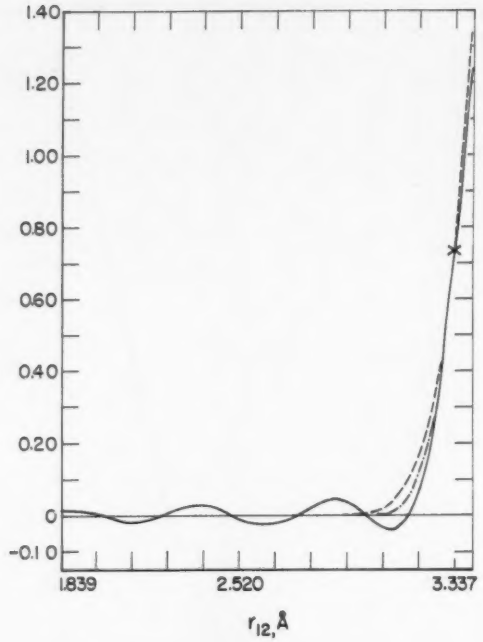

FIGURE 3. *The short range behavior of* $g_2(r_{12})$ *in liquid* Ar.

The solid curve is the experimental result from reference [8]; $\rho = 0.0215/\text{Å}^3$, $T = 85$ K. The dashed curve is eq (4) with $m = 5$, $\lambda = 6.407$; the dashed-dotted curve is the same function with $m = 12$, $\lambda = 2.700$. The crisscross denotes the value of d. For the largest r_{12} values shown, the dashed-dotted curve is identical to the solid curve.

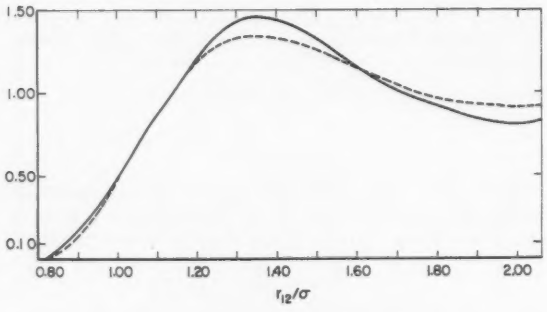

FIGURE 4. *The pair correlation function for liquid* ^{4}He *in units of* $\sigma = 2.556$ Å *at* $\rho\sigma^3 = 0.409$.

The solid curve is the experimental result at $T = 1.940$ K. The dashed curve is the P.Y. approximation, eq (7), with the ground state function defined by eqs (6) and (8).

The results for $\rho\sigma^3 = 0.409$, which with eq (9) corresponds to $\rho = 0.0245/\text{Å}^3$, are shown in figure 4. The dashed curve is the P.Y. solution and the solid curve is the measured value at $\rho = 0.0245/\text{Å}^3$ and $T = 1.940$ K. In considering the relative agreement, which is within ± 15 percent, we wish to emphasize that there are three sources of error: (a) the uncertainty between eqs (6) and (8) and the true ground state of helium, (b) the P.Y. approximation, (c) the contribution of excited

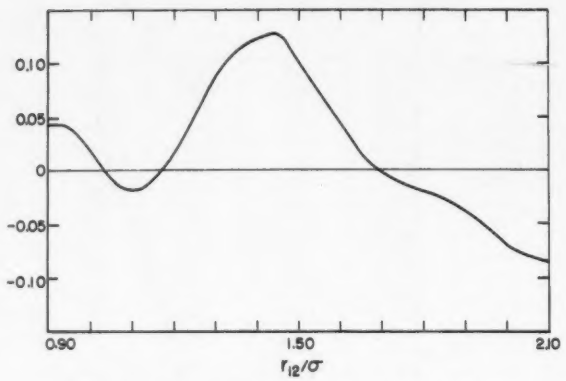

FIGURE 5. *The difference,* $g_2^{expt.} - g_2^{P.Y.}$, *at* $\rho\sigma^3 = 0.394$.

The experimental result is at $T = 2.020$ K.

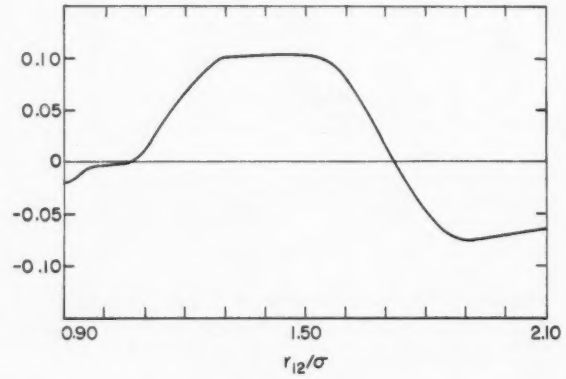

FIGURE 6. *Same as figure 5, except* $\rho\sigma^3 = 0.394$ *and experimental result is at* $T = 1.860$ *K.*

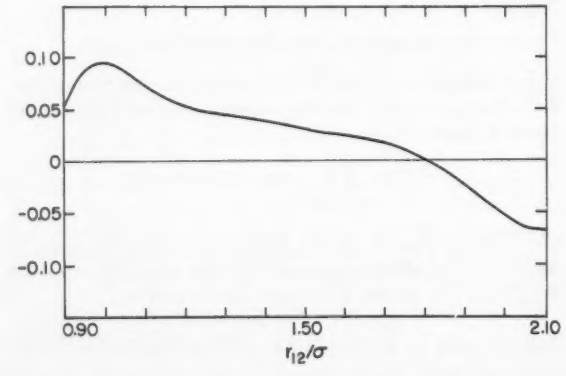

FIGURE 7. *Same as figure 5, except* $\rho\sigma^3 = 0.365$ *and experimental result (ref. [14]) is at* $T = 0.79$ *K.*

quantum states. Keeping this in mind, it is of interest to consider effects of finite temperature. The results are shown in figures 5, 6, and 7, where we have plotted $g_2^{\text{expt.}} - g_2^{\text{P.Y.}}$ for $\rho\sigma^3 = 0.394$, 0.384, and 0.365 respectively. The experimental data used in constructing figures 5 and 6 correspond, respectively, to the measurements at $\rho = 0.0236/\text{Å}^3$, $T = 2.020$ K and $\rho = 0.0230/\text{Å}^3$, $T = 1.860$ K. The experimental data used in figure 7 were obtained from the x-ray measurements of Achter and Meyer [3]; these data are at $\rho = 0.0219/\text{Å}^3$ ($\rho\sigma^3 = 0.365$) and $T = 0.79$ K. The results in figures 5, 6, and 7 indicate that at intermediate values of the internuclear separation, the P.Y. approximation characteristically underestimates the pair correlation in liquid ^{4}He, and at larger values of r_{12}/σ, the P.Y. approximation characteristically overestimates the measured values. Little, if anything, can be inferred from the differences at small internuclear separations, $r_{12}/\sigma < 1$, since the measurements are, as we have already remarked, not as accurate as the data at larger separations.

5. Discussion

In a separate article [16], we have employed the data in table 2 in the study of several properties of the pair and triplet correlation functions. We reiterate one property that is particularly germane to this article. We consider table 2 in the vicinity of the first maximum of $g_2(r_{12};\ \rho,\ T)$, $r_{12} \sim 3.5$ Å, and the second minimum, $r_{12} \sim 5.3$ Å. The magnitude of $g_2(r_{12};\ \rho,\ T) - 1$ is referred to as the structure in the pair function. Table 2 shows that below T_λ, the structure is a decreasing function of temperature as the temperature is lowered at fixed density. The same dependence on temperature is observed as the temperature is lowered, at fixed density, from above T_λ, but below the boiling point, to temperatures below the superfluid transition. For classical fluids the pair correlation function is [16] an increasing function of temperature as the temperature is lowered at fixed density.

The algorithm given in eq (4) is, from figures 1, 2, and 3, a simple and accurate procedure for smoothly extending the values of the pair function inside the first maximum, to the value $g_2 = 0$. The short range behavior is very difficult to measure and perhaps the algorithm will prove useful in presenting experimental results from diffraction experiments. As we have already noted, the method appears to have utility in classical as well as quantum fluids.

It should be emphasized that the computations given in section 4 strictly apply to a fluid whose wave function at the absolute zero of temperature is given by eq (6). With this in mind, the results in figures 4 thru 7 show the P.Y. approximation is with $\pm$ 15 percent of the experimental results. The P.Y. approximation typically underestimates the magnitude and extent of the first peak in $g_2(r_{12})$ but overestimates the function at somewhat larger ($r_{12} \geq 1.8\sigma$) values of the internuclear separation. As expected, the agreement between the calculated and experimental results improves when the calculated results are compared to data at lower temperatures.

The authors express their appreciation to B. Mozer for the use of the diffraction data prior to publication.

6. References

[1] Larsson, K., Dahlborg, U., and Sköld, K., in Simple Dense Fluids, edited by H. L. Frisch and Z. W. Salsburg (Academic Press, New York, 1968).
[2] Ibid.
[3] Achter, E. K., and Meyer, L., Phys. Rev. **188**, 291 (1969).
[4] London, F., Superfluids, Vol. **II**, (John Wiley & Sons, New York, 1954).
[5] Raveché, H. J., and Mountain, R. D., J. Chem. Phys. **53**, 3107 (1970).
[6] Mozer, B., Le Neindre, B., and De Graaf, L. A., Neutron Diffraction Studies in Liquid ^{4}He, submitted to Phys. Rev. A.
[7] Mozer, B., and Le Neindre, B., Neutron diffraction study of liquid ^{4}He at constant density, submitted to Phys. Rev. A.
[8] Wu, F. Y., and Feenberg, E., Phys. Rev. **122**, 739 (1961).
[9] Woo, C. W., and Massey, W. E., Phys. Rev. **164**, 256 (1967).
[10] Yarnell, J. L., Katz, M. J., Wenzel, R. G., and Koenig, S. H., Phys. Rev. A**7**, 2130 (1973).
[11] Bijl, A., Physica **7**, 869 (1940); Dingel, R. B., Phil. Mag. **40**, 573 (1949); Jastrow, R., Phys. Rev. **98**, 1479 (1955).
[12] Percus, J. K., and Yevick, G. Y., Phys. Rev. **110**, 1 (1958).
[13] Feenberg, E., Theory of Quantum Fluids (Academic Press, New York, 1969), Chapter 6.
[14] Schiff, D., and Verlet, L., Phys. Rev. **160**, 208 (1967).
[15] Mandel, F., Bearman, R. J., and Bearman, M. Y., J. Chem. Phys. **52**, 3315 (1970).
[16] Raveché, H. J., and Mountain, R. D., Structure studies in liquid ^{4}He, submitted to Phys. Rev. A.

(Paper 77A6–795)

JOURNAL OF RESEARCH of the National Bureau of Standards—A. Physics and Chemistry
Vol. 77A, No. 6, November–December 1973

Molecular Basis of Flame Inhibition*

J. W. Hastie

Institute for Materials Research, National Bureau of Standards, Washington, D.C. 20234

(July 19, 1973)

The role played by inorganic chemical additives in fire retardancy and flame inhibition is considered. Particular attention is given to the molecular level aspects of commercially important systems containing compounds of antimony, halogens, and phosphorus. The flame inhibiting function of metal containing additives is also discussed.

Key words: Fire retardants flame inhibition; flames.

Contents

	Page
1. Background	733
1.1. Introduction	733
1.2. Chemical aspects of flame inhibition	734
2. Retardancy chemistry relating to pyrolyzing substrates	734
2.1. The antimony oxide-halogen example	735
2.2. The triphenylphosphine oxide example	738
3. Molecular nature of flames and their inhibition	738
3.1. Nature of flames	738
3.2. Rating of flame inhibitors	740
3.3. Flame microstructure	742
3.4. Halogen inhibitors	743
3.5. Non-Halogen system inhibitors	746
a. Solid inhibitors containing alkali metals	747
b. Other metal inhibitors	747
3.6. Synergistic systems—The antimony oxide-halogen example	749
3.7. Phosphorus as a flame inhibitor	750
3.8. Smoke suppression	750
3.9. Pressure effects	752
4. Conclusions	752
5. References	753

1. Background

1.1. Introduction

It has long been recognized that the addition of chemical substances to combustible materials can considerably reduce the degree of flammability. In the specific case of textile fabrics, an extensive technology has developed through which a wide range of chemically distinct incorporants can be utilized to retard flammability while other desirable properties such as permanence of treatment, appearance, wear resistance, and hand texture are retained [1–6][1].

A well-developed empiricism has been elaborated which relates retardant characteristics such as elemental composition, chemical structure, and degree of loading to the reduction of flammability. The literature of this and related fields offers considerable deductive insight into the mechanisms by which fire retardants function. However, it is apparent, as Lyons [2] has stated, that:

> "Although much can be deduced from the results of applied studies in the literature, there have been relatively few experiments conducted specifically to determine the mechanisms of retardance. At this stage, most of what can be said is highly speculative."

While the undoubted successes of applied chemistry in flame retardancy are clearly apparent, it has become increasingly important, as requirements for reducing the flammability of combustible materials become more stringent, to develop a detailed understanding at the molecular level of the mechanisms by which flame retardants operate. Knowledge of these essential chemical processes can, for example, permit more sophisticated design of retardants for particular applications and perhaps define the performance limits to be expected of particular retardant systems under service or test conditions. Candidate retardant materials can be selected more efficiently for screening if their chemistry can be related to the fundamental basis of retardant action. Retardants can be formulated that optimize performance and minimize undesirable

*Presented at Polymer Conference Series: Flammability Characteristics of Materials Utah, June (1973).

[1] Figures in brackets indicate the literature references at the end of this paper.

side effects such as formation of smoke and toxic reaction products.

The combustion of a fabric, or organic polymer, involves a preflame thermal degradation of the material, resulting in the evolution of flammable volatiles, and the gas phase pyrolysis or oxidation of the evolved gases. Chemical fire retardants may operate in the solid phase to modify the thermal degradation process or in the gas phase by yielding volatile products that inhibit the flame reactions. A given retardant formulation may, of course, operate in both modes.

For purposes of discussion the general subject of fire chemistry may be usefully visualized in terms of the contributing phenomena of ignition, propagation, and cessation, as indicated by table 1. Note that a fundamental description of fire propagation and cessation (i.e., inhibition or extinction) and the production of toxic gases and smoke requires an understanding of flame chemistry and at a molecular level.

TABLE 1

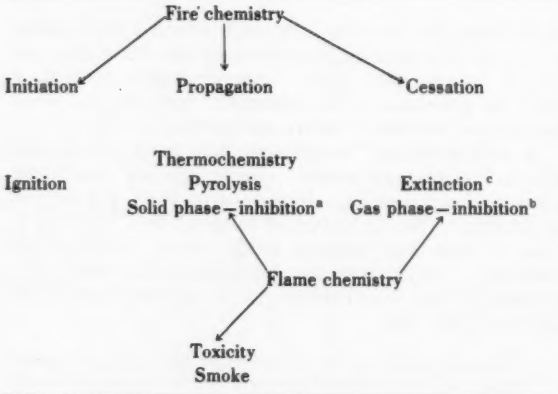

[a] Production of noncombustibles on pyrolysis.
[b] Pyrolysis accompanied by in situ release of flame poisons.
[c] External introduction of flame poisons.

The detailed mechanism of solid-phase retardant action is a complex problem of organic reactions in the solid state. For the degradation of cellulose, for example, both free radical reactions and acid-catalyzed rearrangement pathways have been suggested. Speculations have been offered concerning the role of retardants such as phosphorus compounds in modifying the degradation [7]. This aspect of fire retardancy will not be considered in the present discussion, which focuses attention on the gas-phase mode of flame inhibition.

The purpose of this paper, then, is to consider the molecular level mechanistic aspects of the gas-phase mode of fire retardancy. In dealing with this problem at the molecular level it will become apparent that there are fundamental connections in the details of the mechanisms underlying the phenomena of flame inhibition, fire extinction and smoke production. It is axiomatic that the question of toxic gas production is also related to these phenomena although this will not be pursued here.

1.2. Chemical Aspects of Flame Inhibition

It is now recognized that the inhibition or extinguishment of flames can more effectively be achieved by chemical, rather than physical, means. However in practical fire retardancy situations, both physical and chemical effects operate. For the present discussion we will be concerned only with the chemical aspects of flame inhibition.

A number of reviews and surveys, concerned primarily with the chemical aspects of flame inhibition, have been made [8–13]. Discussions of the relationship of flame inhibition chemistry to fire extinguishment or fire proofing in general may be found in a number of comprehensive literature sources [2–4, 14].

In practical systems the manner in which the additives are released to the flame, or potential flame, system is of importance. One of the theories based on empirical data requires the additive to be "at the right place at the right time." Thus, to some extent the protection of flammable substrates requires that the vapor release properties of the inhibitor be related to the fuel release properties of the flammable substrate. As an example one may cite the antimony oxide—organic halogen formulations used to reduce the flammability of organic polymers where the antimony-halogen component is released at about the same time as the polymer decomposes (e.g., see Pitts [15]).

The considerable variety of chemical systems used to impart fire retardancy to materials has been documented by Lyons [2]. A satisfactory theory of flame inhibition has not yet been derived, although it is generally agreed that the additives presumably interfere with the concentration of the flame propagating radicals H, OH, O, and perhaps CH_3 and HO_2. The influence of additives on flame speed, also known as burning velocity, is particularly revealing in that only small amounts of additives are required to strongly affect flame propagation. It is also apparent that the inhibiting action of additives, such as halogens, cannot be explained merely in terms of a reduction of the equilibrium concentration of radicals due to hydrogen halide formation. Evidently the function of the additive is catalytic and flame inhibition is primarily a kinetic phenomenon [9].

2. Retardancy Chemistry Relating to Pyrolyzing Substrates

A microscopic view of an idealized burning system is expressed by the schematic of table 2. It is considered that the function of substrate additives is to provide a source of "radical traps" to the gas phase where they may function either in the preflame or reaction zone regions of the flame.

TABLE 2. *Microscopic view of a burning system*

Post flame gases	Equilibrium attained. Thermodynamics describe post-combustion products.
Reaction or luminous zone	Excessive dissociation
	Back diffusion of radicals
Preflame region	$H + O_2 \rightarrow HO_2$ $\searrow$ $OH + O$
Substrate	Inorganic chemistry of substrate may be described by thermodynamics, but organics usually in metastable condition.

The usual macroscopic criteria for defining a gas phase, as opposed to a condensed phase, mode of retardancy activity are summarized in table 3.

2.1. The Antimony Oxide–Halogen Example

The well-known antimony oxide–halogen fire retardent system, where the halogen is an organic chloride or bromide, serves as an example of the application of such criteria and the underlying molecular aspects involved.

Table 4 summarizes the main reasons why an intensive consideration of this system appears to be warranted.

Among practicing fire retardancy chemists, synergism is one of the more desirable goals. The achievement of a synergism allows the utilization of flame inhibiting additives at lower concentrations, and the antimony oxide–halogen combination represents one of the more important synergistic fire proofing combinations. The synergistic nature of this system is exemplified by the fact that a fireproofed epoxy system containing 15 percent Br can be replaced by a combination of 5 percent Br + 3 percent Sb_4O_6. Thus the quantity of halogen needed is reduced by the presence of Sb_4O_6 (i.e. 2 Sb_2O_3).

The combination of antimony(III) oxide, Sb_2O_3, with a halogen source, most commonly a halogenated organic material, is a well known example of a synergistic flame retardant system [16]. The ability of antimony to enhance the effectiveness of halogen-based flame retardants was first demonstrated for cellulosic fabrics treated with chlorinated paraffins and antimony trioxide [17]; the synergism has also been shown, inter alia, in polyester resins [18–20], polystyrene resins [21], and polyolefins [22]. Use of antimony compounds in conjunction with halogenated flame retardants is also documented for polyurethanes, polyacrylonitrile, and polyamides [2, 16]. Despite the availability of some alternative materials and uncertainties in supply leading to a continuing search for other substitutes, it is likely that the use of antimony chemicals for this purpose will increase significantly over the next few years, particularly in plastics [23].

TABLE 3. *Macroscopic criteria of chemical mechanism*

Gas phase:
Loss of retardant element from substrate
Insensitivity to structure
Sensitivity to oxidant
No change in composition of volatiles
Solid phase:
Enhanced char formation
Retention of retardant element in substrate
Retardant element ineffective in gas phase
Retardancy activity sensitive to structure of substrate
Retardancy insensitive to oxidant, e.g., O_2 or N_2O
Change in composition of volatile pyrolysis products in presence of retardant

TABLE 4. *Antimony oxide–halogen system as a model study*

A. Widespread use
e.g. in both natural and synthetic fibers, plastics, wood, paper, paint, etc.
B. Is synergistic
e.g. 3% Sb_4O_6 + 5% Br = 15% Br
C. Has gross characteristics of a gas phase process
e.g. antimony and halogen lost on pyrolysis
D. Exists a need for substitute systems due to a marked fluctuation in availability and price of Sb_2O_3

This fire retardant system has been in use for more than 30 years. However as recently as 1967 no satisfactory theory had been suggested to explain the synergism between halogen and antimony compounds in imparting fire retardancy to polymer compositions [4].

The recent literature contains numerous speculations as to the mechanism, including the following:

- –formation in situ of antimony chloride which may react with cellulose to alter the course of thermal decomposition and/or form a "heavy vapor tending to extinguish the flame" [24].
- –formation in the flame of nonvolatile, antimony-containing solid or liquid particles whose surface provides a site for dissipation of energy with resulting modification of the flame chemistry (e.g., formation of HO_2 rather than HO–wall effect) [25].
- –"formation of an antimony oxygen halogen intermediate compound which increases the presence of halogen radicals with resulting

interference in the free radical mechanism of the flame propagation" [21].

—"formation of antimony halides or oxyhalides which may act by blanketing the flame" [26].

—". . . the oxygen inhibiting effect of the heavy vapors of antimony chloride or oxychloride in addition to the physical inhibition of the oxidation chain reaction (wall effect) and chemical inhibition by chlorine" [3].

It is known that much of the antimony is vaporized during burning [27] or char formation [24]. The ignition behavior of polyester resins inhibited by antimony-halogen systems has been considered to indicate the likelihood of gas phase inhibition [19, 20]. Further, the observation [27] that Sb_2O_3 inhibits the burning of chlorinated polyethylene in oxygen, but not in nitrous oxide, suggests inhibition of gas phase reactions specific to the fuel-oxidizer system. On the other hand, some involvement of antimony in decomposition of the solid phase is indicated by the fact that char formation may be enhanced in antimony-containing systems [2, 4].

The synergistic action clearly involves interaction of Sb_2O_3 with a decomposition product of the halogenated material, presumably HCl. Optimum conditions for retardancy depend on the gross ratio of antimony to chlorine and on the ease of decomposition of the chlorinated species [2]. In an extensive series of studies on cotton fabric, optimum weight ratios of chlorinated paraffin to antimony oxide were found to be somewhat in excess of those required for conversion to SbOCl [17]. A study of the flammability of polyethylene by the oxygen index method, however, indicated a maximum effect with six chlorine atoms per atom of antimony (with one Sb present per 100 C_2 units). At this level of antimony loading, a chlorine:antimony ratio of 2 was insufficient to produce the optimum effect [22].

Antimony oxychloride, SbOCl, is itself effective as a flame retardant [15] and has been proposed as the product responsible for flame retardant effects in cellulose systems [17]. The thermal decomposition of this substance has been studied by Belluomini et al. [28], and more recently by Pitts et al. [29], who also investigated its flame retardancy effect in flexible urethane foam. By trapping the gaseous products, the latter workers deduced $SbCl_3$ to be the only volatile species. On the other hand, an early literature report [30] suggests that SbOCl vaporizes an appreciable amount of SbOCl species.

A summary of some typical macroscopic observations relating to antimony-halogen action is given in table 5. From these results it is apparent that the retardancy mechanism is of the gas-phase type. More recent mass spectrometric experiments using the Kundsen effusion method convincingly support this view [32]. Basically, the experimental procedure involves the passing of HCl gas over solid Sb_2O_3, contained in a Knudsen cell, and the composition of the effusing molecular beam is determined by a line-of-sight mass spectrometric analysis. The principal observations from this molecular level study are listed in table 6.

TABLE 5. *Macroscopic observations relating to antimony-halogen action*

Cotton—Sb_2O_3—plasticized PVC
1. Treated material chars at 280 °C; untreated fabric relatively unaffected
2. 80% of Sb vaporized
(Read and Heighway-Bury [24])
Chlorinated polyethylene—Sb_2O_3
1. Loss of Sb in vapor when chlorine present
2. Sb_2O_3 ineffective in absence of Cl
3. L.O.I. shows effect in O_2—N_2 (chain branching), not in N_2O—N_2 (nonchain branching)
4. Composition of volatile gases independent of presence of Sb_2O_3
(Fenimore and Jones [27])
Sb-Halogen system reduces crack growth, facilitates homogeneous char development in unsaturated polyester resins
(Einhorn [3])
Ignition behavior of polyester resins suggests gas-phase inhibition
(Learmonth, et al. [19])

L.O.I. is a common abbreviation for the limiting oxygen index flame retardancy test, e.g., see ref. [27].

TABLE 6. *Molecular level observations in the* Sb_2O_3—HCl *system*

1. HCl reacts rapidly with Sb_2O_3 solid at $T \simeq 240$–460 °C to yield $SbCl_3$ and H_2O as the only vapor species.
2. Solid SbOCl forms at $T \simeq 200$–250 °C.
3. Solid SbOCl decomposes to yield $SbCl_3$ over the range $T \simeq 250$–450 °C.
4. Solid Sb_2O_3, in the absence of halogens, does not vaporize over the typical pyrolysis temperature regime of 300–450 °C.

For conditions where SbOCl solid is present an unusual mode of release of antimony and halogen to the vapor phase occurs, as indicated by the results shown in figure 1. These results were obtained under Knudsen effusion conditions where normally equilibrium is achieved and therefore Clausius-Clapeyron-type plots, as shown in figure 2, should yield lines with slopes proportional to the reaction enthalpy changes. The results may be interpreted to indicate that only part of the decomposition regime achieves equilibrium, i.e.,

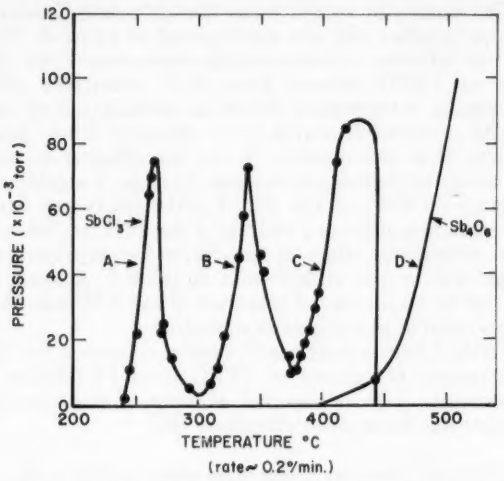

FIGURE 1. *Pressure variation of the vapor species* $SbCl_3$ *(curves A, B, and C) and* Sb_4O_6 *(curve D) as a function of temperature and time using solid* SbOCl *as a source and a heating rate of about* $0.2\,C°\,min^{-1}$.

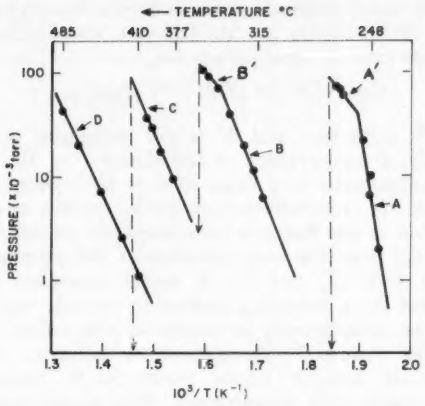

FIGURE 2. *Clausius-Clapeyron log p versus 1/T plots of the vapor species generated by* SbOCl *as given by figure 1.*

segments A' and B' of figure 2. For the most part, e.g., segments A and B, a considerable activation energy, of about 70 kcal mol^{-1}, is required. It is suggested that this activation energy barrier, which most likely is a solid phase diffusion controlled process, is the reason for the observed action [15] of other metal oxides on the decomposition of SbOCl as shown by figure 3. Similarly the improved retardancy effect provided by a partial replacement of Sb_2O_3 with $2ZnO \cdot 3B_2O_3 \cdot 3.5H_2O$, also known as Firebrake ZB, may be due to a lowering of the activation energy barrier [33].

The substrate reactions in the antimony oxide-halogen system are summarized in table 7.

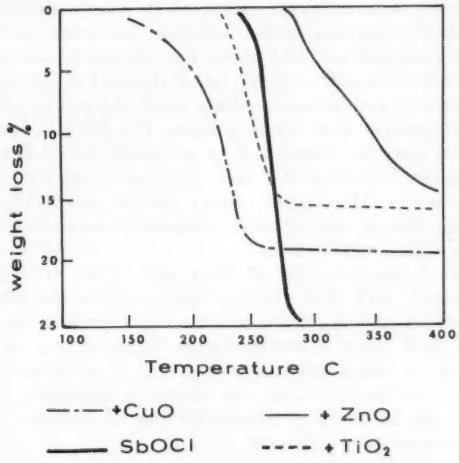

FIGURE 3. *Thermogravimetric analysis curves of antimony oxychloride-metal oxide mixtures, from Pitts [15].*

TABLE 7. *Antimony oxide—halogen substrate reactions*

	Typical substrate of $[R \cdot HCl + Sb_2O_3 + \text{fabric}]$	
	$[R \cdot HCl] \longrightarrow R + HCl$	~ 250 °C
	$2HCl + [Sb_2O_3] \longrightarrow 2[SbOCl] + H_2O$	Temperature Increasing
A	$5[SbOCl] \longrightarrow [2\,SbOCl \cdot Sb_2O_3] + SbCl_3$	
B	$4[2SbOCl \cdot Sb_2O_3] \longrightarrow 5[SbOCl \cdot Sb_2O_3]^* + SbCl_3$	
C	$3[SbOCl \cdot Sb_2O_3] \longrightarrow 4[Sb_2O_3] + SbCl_3$	
D	$2[Sb_2O_3] \longrightarrow Sb_4O_6$	~ 500 °C

Square brackets denote solids.

*Could also be $[2SbOCl \cdot 3Sb_2O_3]$, i.e., see [28].

As the vapor pressure of $SbCl_3$ is now known for the system $HCl + Sb_2O_3$ (or SbOCl), one may derive the Langmuir rate of vaporization i.e.,

$$G = P/[17.14\ (T/M)^{1/2}]\ \text{g/cm}^2\ \text{s}$$

where P is in torr and M is the molecular weight. Typically, a temperature of 550 K and $P \sim 10^{-1}$ torr would correspond to a value of $G \simeq 10^{-2}$ g/cm² s. At this rate the concentration of $SbCl_3$ species entering the region of the flame is approximately calculated to be greater than the concentration of the propagating radicals OH, H, and O. It would therefore seem inefficient for a retarding system to provide vaporization rates substantially in excess of this value. However, the "normal" decomposition behavior of an oxychloride system would result in G increasing exponentially with temperature. This would result in the synergistic system being effective only over a very narrow temperature interval due to the rapid depletion of sample for pressures in considerable excess of 10^{-1} torr. The relevant point to be made regarding the SbOCl decomposition scheme, however, is that the decomposition rate does not increase monotonically with temperature (see fig. 1) due to the formation of relatively stable intermediate solid phases. In effect, for sufficiently slow heating rates, the SbOCl decomposition may be described as a "triple shot" fire extinguisher. For relatively high heating rates one would not resolve this "triple shot" effect; however, the average rate of vaporization would still be far less than that of a "normal" system.

Thus it appears that at least part of the synergism associated with this system derives from the ability of Sb_2O_3 to moderate the release of halogen to the gas phase and over a considerable temperature range. This effect has a parallel in the use of substrate free radical initiators, such as dicumyl peroxide [34], which are believed to delay the loss of halogen from the decomposing polymer.

2.2. The Triphenylphosphine Oxide Example

A second example of a fire retardant system where vapor phase processes form the basis for flame inhibition is the triphenylphosphine oxide-Nylon 6-polyethyleneterephthalate system (i.e., TPPO-Ny6-PET). The effect of small additions of TPPO and Nylon 6 on the flammability of the PET polyester is indicated in table 8. Macroscopic evidence for a vapor phase mode of inhibiting action has been obtained recently by Bostic and Barker [35].

TABLE 8. *Effect of triphenylphosphine oxide* (TPPO) *on flammability of polyester* [a]

Pure polyester	Burns
Polyester + 1 *mol* % TPPO	Self extinguishing in 3–8 s
Polyester + TPPO + Nylon-6 (1% each)	Nonburning or self extinguishing in 0–3 s

[a] From Bostic and Barker [35].

The results of recent mass spectrometric Knudsen reactor studies [36] are summarized in figure 4. The curves indicate a nonmonotonic dependence for the rate of TPPO release from PET substrates with increasing temperature which is reminiscent of the SbOCl system. However it is apparent from these results that this system is not as efficient as the antimony oxide-halogen system. That is, a significant fraction (~ 50%) of the TPPO retardant is lost from the substrate prior to pyrolysis of the PET or Nylon 6. The synergistic effect of the Nylon-6 component, as suggested by the observations in table 8, appears to be due to an increased retention of the TPPO so that it is available at a higher temperature.

Table 9 lists a suggested reaction sequence for the mechanism of release of TPPO from PET-Nylon 6 substrates. A more detailed account of these recent studies has been given elsewhere [36].

TABLE 9. *Reactions leading to the release of TPPO to the vapor phase* [a]

Reaction			Temperature
	[TPPO]	⟶ TPPO (g)	90 °C
Complex A	[TPPO · PET]	⟶ TPPO	160 °C
Complex B	[TPPO · PET]	⟶ TPPO	200–240 °C
Complex P^1	[TPPO · Ny6 · PET]	⟶ TPPO	220–320 °C
Complex C	[TPPO · Ny6]	⟶ TPPO	130–210 °C

[a] Square brackets denote condensed phase.

3. Molecular Nature of Flames and Their Inhibition

3.1. Nature of Flames

The following discussion considers the flame retarding action of inhibitors such as $SbBr_3$, TPPO, and other additives or extinguishants of practical interest. However, in order to discuss mechanisms of flame inhibition it is first necessary to define the mechanisms of flame propagation. This involves consideration of the basic chemical and kinetic character of flames as summarized briefly in tables 10 and 11.

Examples of flame reaction mechanisms are given in table 12. It is generally agreed that the most important step in normal flame propagation is the chain branching reaction:

$$H + O_2 = OH + O.$$

As with the previous discussion of substrate chemistry, the chemistry of flames may be discussed in terms of both macroscopic and microscopic observations. However, in such gas phase systems, as opposed to the condensed phase, it is possible to rigorously interrelate both macroscopic and microscopic phenomena as suggested in table 13. That is, given the molecular level details of the flame chemistry, one can compute from basic thermodynamic and kinetic principles the macroscopic flame properties.

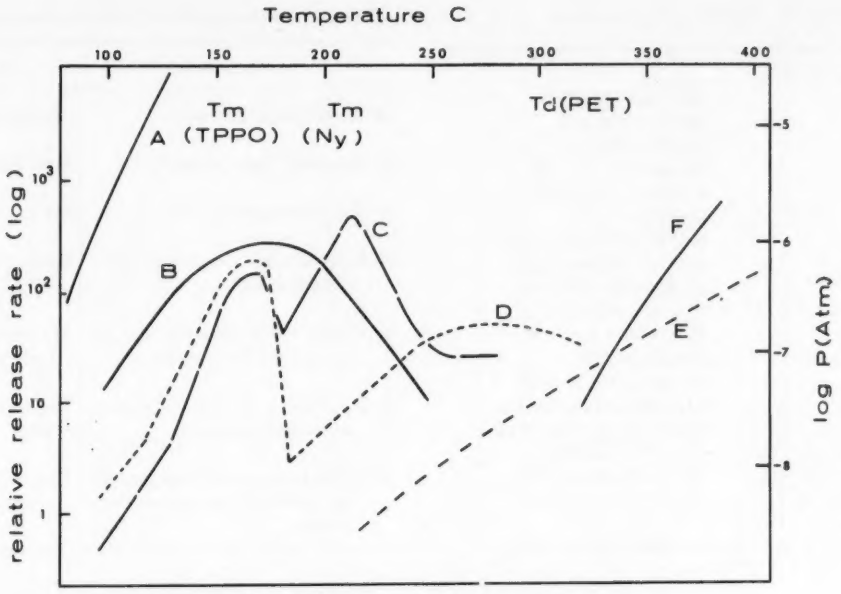

FIGURE 4. *Vaporization rates of TPPO (except for case F) as a function of temperature for various triphenylphosphine oxide (TPPO)-Nylon 6 (Ny-6)-polyethyleneterephthalate (PET) systems: A is for pure TPPO solid, B is for 6.7 mol percent TPPO in Ny-6, C is for 1 percent TPPO in PET, D is for 1 percent TPPO + 1 percent Ny-6 in PET, E is for pure TPPO × 10^{-6} and F is for the caprolactam monomer vapor from Ny-6; Tm and Td indicate melting and decomposition temperatures respectively.*

TABLE 10. *Molecular nature of 1 atm flames*

Species-type	Examples	Typical concentration (mole fraction)
Stable reactants and products	CH_4, O_2 CO_2, H_2O	0.99 total
Intermediates	C_2H_2, CH_3CHO,	10^{-2}
	C_4H_2	10^{-4}
Radicals	H, OH, O, CH_3	10^{-2}
	HO_2, C_2H	10^{-4}
Positive ions	H_3O^+, CHO^+	$\leq 10^{-5}$
Negative ions	OH^-, Cl^-	$\leq 10^{-7}$

TABLE 11. *Time scale in 1 atm flames* (T ~ *2000 K*)

Gas velocity	=	$10^2 - 10^3$ cm s^{-1}
Reaction zone thickness	=	10^{-2} cm
Residence time—at reaction zone	=	$10^{-4} - 10^{-5}$ s
Chemical reaction—bimolecular	$\leq$	10^{-5} s (for 20–30 k cal mol^{-1} activation energy)
Relaxation of excited species		
—Translational	=	10^{-8} s
—Rotational	=	$10^{-6} - 10^{-7}$ s
—Vibrational	=	$10^{-6} - 10^{-3}$ (10^{-4} typical) s
Electronic—chemiluminescence	$\geq$	10^{-3} s
Diffusion velocity		
—H atoms	=	100 cm s^{-1}
—O atoms	=	10 cm s^{-1}

520-812 O-LF - 73 - 4

TABLE 12. *Flame reaction mechanisms*

Rich $H_2-O_2-N_2$[a]:	$OH+H_2 \rightarrow H_2O+H$
	$H+O_2 \rightarrow OH+O$
	$O+H_2 \rightarrow OH+H$
	$H+H+M \rightarrow H_2+M$
	$H+H_2O \rightarrow OH+H_2$
	$O+H_2O \rightarrow 2OH$
	$H+OH+M \rightarrow H_2O+M$
	$H+OH+H_2O \rightarrow 2H_2O$
	$H+O_2+M \rightarrow HO_2+M$
	$H_2+HO_2 \rightarrow H_2O_2+H$
	$H_2O_2+M \rightarrow 2OH+M$
	$H+HO_2 \rightarrow 2OH$
	$H+H_2O_2 \rightarrow H_2O+OH$
	$OH+H_2O_2 \rightarrow H_2O+HO_2$
	$2HO_2 \rightarrow H_2O_2+O_2$
Hot-rich CH_4-O_2:	$CH_4+H=H_2+CH_3$
Hot-lean CH_4-O_2:	$CH_4+OH=H_2O+CH_3$
Cool CH_4-O_2:	$CH_4+O_2=HO_2+CH_3$

[a] e.g., see Wilde, K. A., Combust. Flame **13**, 43 (1972).

TABLE 13. *Flame chemistry—tools and techniques*

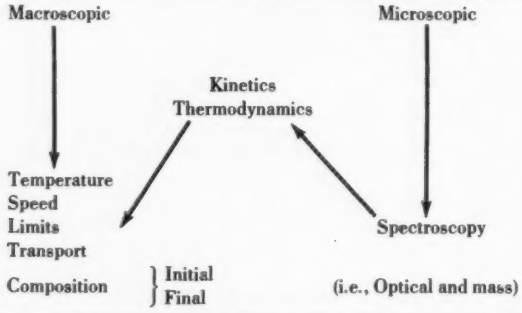

In dealing with the problem of flame inhibition and extinction a systems approach such as that given in table 14 is suggested. The nature of the experimental, theoretical and basic data requirements is also indicated.

3.2. Rating of Flame Inhibitors

The degree of effectiveness of a flame inhibitor can simply be determined from the quantity of the inhibitor needed to extinguish a flame. This quantity will vary with the flame type, i.e., if premixed or diffusion, and the ratio of fuel to oxidant. If the addition of an inhibitor is made to a premixed laminar flow hydrocarbon-oxygen flame, where the reaction zone is luminous, one can determine the effect of the inhibitor, in the absence of extinction, by noting a shift of the reaction zone to a position further downstream from the burner opening. This shift results from a decrease in the burning velocity of the flame due to the presence of the inhibiting agent.

TABLE 14. *Flame inhibition and extinction—systems approach*

Programs	Classification
(a) Identify flame species	Spectroscopy
(b) Determine flame kinetics	Basic data
(c) Test kinetic models	Theory—flame equations
(d) Determine optimum flame species for inhibition	Basic data
(e) Design stable molecular precursors to inhibitor species	Thermodynamics, kinetics basic data
(f) Determine solid sources of such molecular precursors	Thermochemistry, basic data
(g) Define chemistry of incorporation of additives to polymer substrates	Thermochemistry, solid state—structural studies

Burning velocity measurements on premixed laminar flow flames provide the main basis for the screening of flame inhibiting agents. Flame inhibition measurements are less frequently made on diffusion flames, due to the difficulty in defining a fundamental flame strength parameter such as burning velocity and also the strong geometrical influences on diffusion flame propagation. However the recent use of an opposed jet burner has provided a means of measuring inhibitor effectiveness in terms of the flow conditions required to produce a hole in the diffusion flame [37].

As the primary purpose of determining the relative efficiency of flame inhibitors relates to their potential application in the area of fire extinguishment and fire prevention, it is pertinent to examine the usefulness of data obtained primarily on model premixed laminar flow flames. Friedman has considered this point on several occasions [10, 13].

The propagation of real, as opposed to laboratory fires, frequently involves diffusion and turbulent flame conditions. However there is evidence for a correspondence between the speed of turbulent flame propagation and the laminar flow burning velocity. Friedman also notes that a diffusion flame does contain a region of premixing at the base and it has not been generally established whether the inhibitor functions in this region or not. It is also found, with CH_3Br, for example, that a similar amount of inhibitor can extinguish both a diffusion and a premixed flame and this strongly suggests the premixed region to be the relevant area of inhibition [38].

One can also argue from the results of flame structure studies on supposedly diffusion flames that such flames resemble fuel rich premixed systems. For example, the chemical structure of a flame generated by passing methane along a tube into the ambient atmosphere, as shown by figure 5, indicates a significant concentration of O_2 and N_2 even near the center

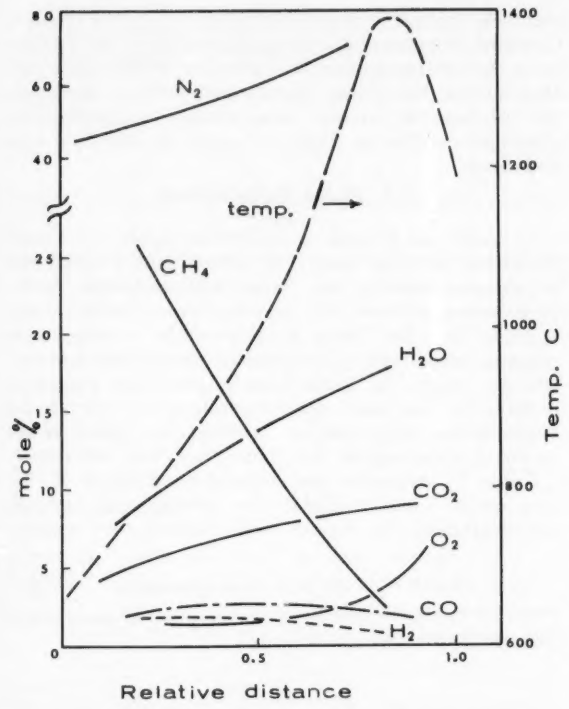

FIGURE 5. *Composition and temperature profiles for a CH_4—air diffusion flame, taken relative to the center of the CH_4 fuel column (i.e. zero relative distance) and the CH_4—air boundary (i.e., 1.0 relative distance).*

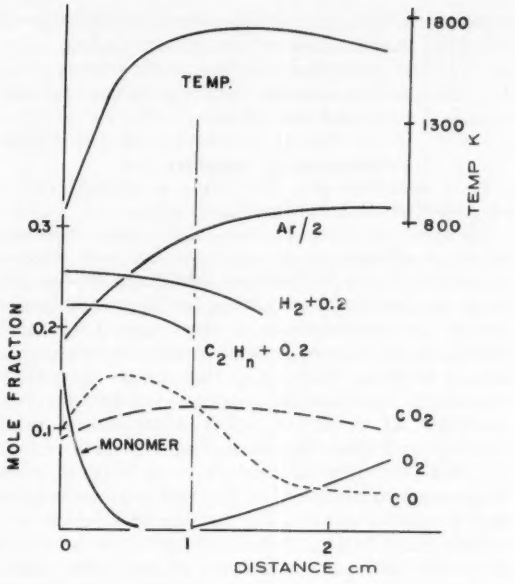

FIGURE 6. *Composition and temperature versus distance above polymer surface profiles for a polymethyl methacrylate candle flame (from Fenimore and Martin, [40]).*

of the fuel column [39]. Similarly, the preflame region of a polymethylmethacrylate candle flame contains appreciable levels of argon from the surrounding argon-oxygen atmosphere, together with incomplete combustion products such as CO and H_2 as shown in figure 6 [40].

One can reasonably conclude, therefore, that the measurements of inhibitor reduction of flame speed for premixed flames is an appropriate means of rating potential fire retardants.

As Dixon-Lewis [41] and co-workers have demonstrated, given the basic kinetic and transport properties for the flame reactions, it is possible to quantitatively calculate burning velocities. However, to date this can only be done for the H_2-O_2 flame system, since the basic data and mechanistic understanding are lacking for hydrocarbon and other flames.

Similarly, if the flame kinetics of an additive were known, then it would be possible to predict from basic principles the magnitude of the reduction in flame speed due to inhibition. Since such correlations of flame speed with basic flame data are not feasible at the present time, it is necessary to develop less sophisticated mathematical models for flame inhibition.

The need for such models has recently been emphasized by Fristrom and Sawyer [9], and these authors have developed a model which allows the definition of new parameters for evaluating flame inhibitors in terms of measurable macroscopic variables such as O_2 concentration, inhibitor concentration and the change in burning velocity. The model has as a basis the notion that the inhibitor sets up a reaction that competes with the chain branching reaction, i.e.:

$$H + O_2 \rightarrow OH + O$$

by abstracting H atoms, e.g.:

$$H + HCl \rightarrow H_2 + Cl.$$

The model follows from the experiments of Wilson, et al., [42] where, in the presence of an inhibitor, the preflame zone is extended and the reaction zone narrows. Inhibition is considered to occur primarily in the preflame region where the chain branching reaction is slow and radical recombination is more important. In this model the inhibitor reduces the level of radicals in the preflame region, but at the reaction zone the concentration may be increased over that for an uninhibited flame. In effect, the radical profiles shift downstream to a higher temperature region, where their competition with the inhibitor is more favorable.

From the mathematical model a figure of merit for an inhibitor, using burning velocity data, may be defined as:

$$\phi_v = \frac{[O_2]}{[I]} \frac{\delta V}{V_0},$$

where ϕ_v is the figure of merit for the inhibitor,

$[O_2]$ is the initial oxygen concentration,

$[I]$ is the initial inhibitor concentration,

V_0 is the burning velocity in the absence of any inhibitor, and

δV is the change in burning velocity due to the presence of the inhibitor.

It is assumed that the flame is slightly fuel rich, i.e., the H atom is the dominant radical.

In practice, ϕ_v correlates with other measures of inhibitor effectiveness, such as blow-off limits and extinction limits for halogen inhibitors. It also follows from the definition of ϕ_v that the degree of inhibition should be proportional to the amount of inhibitor added to the flame. Experimental observations (e.g., see Lask et al. [43]), show that this is approximately valid for a variety of homogeneous inhibitors.

Values of ϕ_v for a selected variety of inhibitor types have been calculated from the data of Lask et al. [43], and unpublished data of Wagner cited by Morrison and Scheller [44] for *n*-hexane fueled flames, and D. Miller et al. [45], for H_2 fueled flames. The values listed in the table 15 are given in approximate order of increasing effectiveness as flame inhibitors and we shall refer to this table later when discussing specific inhibitor types.

At this point it is sufficient to note that only for the case of CO_2 is the degree of inhibition explainable in terms of a physical effect such as cooling. The magnitude of ϕ_v greater than unity for the other inhibitors can only be explained in terms of chemical effects. Common commercial extinguishants such as Freons have ϕ_v values similar to the value of 8.4 given for Br_2. Of the two flame types considered in the table the *n*-hexane/air system more closely resembles the chemical conditions likely to occur in practical fire situations.

TABLE 15. *Relative effectiveness, ϕ_v, of selected flame inhibitors*

Inhibitor [c]	Flame type	
	n-hexane/air [a] ϕ_v	H_2-air [b] ϕ_v
CO_2	0.86	
Cl_2	1.8	[d] −0.26
$Si(CH_3)_4$	3.9	
CCl_4	4.2	
Br_2	8.4	
$SiCl_4$	10.5	3.5
$(CH_3)_3PO_4$	23	
$SbCl_3$	26	
$TiCl_4$	30	10
$SnCl_4$	31	12.9
$POCl_3$	31	7.2
PCl_3	39	4.5
PBr_3	39	
CrO_2Cl_2	≧ 244	
$Fe(CO)_5$	356	19
$Pb(C_2H_5)_4$	390	

[a] From data given by Lask et al. [43], for a stoichiometric mixture.

[b] From data given by D. Miller et al. [45], for a mixture with 1.75 fuel equivalence ratio.

[c] Amounts of inhibitor used varied from 0.015 percent to several volume percent.

[d] Negative sign indicates flame speed increase rather than decrease.

3.3. Flame Microstructure

In order to provide a molecular basis for flame inhibition it is necessary to identify the elementary reactions involving the flame inhibition and flame propagating radicals. For the ideal case of a premixed laminar flow flat flame it is possible to determine reaction rates and in some cases identify elementary reaction steps. The basic flame relationships are given in table 16. The main experimental input is seen to be the species concentration profiles, i.e., plots of X_i versus z, from which the derivatives are calculated.

Table 17 compares the general capabilities of the two major tools available for determining species concentrations in flames with satisfactory spatial

TABLE 16. *Some basic flame relationships* [a]

Diffusion velocity (normal to flame front)

$$Vi = -\frac{dXi}{dz}\left(\frac{Di}{Xi}\right)$$

Fractional mass flow

$$Gi = Xi\,\frac{Mi}{\bar{M}}\left(\frac{v+Vi}{v}\right)$$

Net reaction rate

$$\frac{dXi}{dt} = \frac{dGi}{dz}\left(\frac{\rho v}{Mi}\right)$$

Reaction mechanism e.g., for

$$i + l \rightarrow j + m, \quad -\frac{dXi}{dt} = \frac{dXj}{dt} = k[Xi][X_l]$$

Mass balance

$$\sum_i \frac{n_i G_i}{Mi} = \text{const.}$$

Notation

X_i = mole fraction of species i

Vi = diffusion velocity

v = gas velocity

ρ = density

z = distance

D = diffusion coefficient

M = molecular weight

n_i = number of atoms of an element in species i

k = reaction rate constant

[a] See e.g., Fristrom, R. M., and Westenburg, A. A., Flame Structure, (McGraw-Hill Co., New York, 1965).

resolution. The present discussion focuses attention on the application of mass spectrometry to flame structure determination and a chronology of the more significant developments in this area is given in table 18.

TABLE 17. *Tools for concentration profile measurements—general capabilities*

Optical spectroscopy	Mass spectroscopy
Detection of most atoms and diatomic species	Detection of most species
OH radical	All radicals e.g., H, OH, O, CH_3, HO_2
Detects excited states	—
Combustion products—difficult to resolve	Good capability
Absolute concentration—some difficulty in both cases	
Fair spatial resolution	Good spatial resolution
No perturbation of system	Some perturbation by probes

TABLE 18. *Chronology of flame mass spectrometry for—uncharged species*

Author	Reference	Year	Technique
Eltenton	[47]	1947	Low pressure flame (L. P.), radicals ? flame modulation.
Foner & Hudson	[48]	1953	L. P. radicals molec. beam modul.
Bryce, et al.	[49]	1956	L. P., radicals ? no modulation.
Fristrom, et al.	[50]	1961–1963	L. P., microprobe.
Fenimore, et al.	[51]		
Dixon Lewis	[52]	1963	1 Atm., stables no modul.
Milne & Greene	[53]	1966	1 Atm., radicals, mol. beam modul.

Figure 7 shows a schematic of an apparatus used to measure both stable products and reactive intermediates in 1 atm flames at concentration levels down to about 1 ppm [46]. Typical results obtained with this system for CH_4 fueled flames are given in figures 8 and 9.

3.4. Halogen Inhibitors

Halogen systems are among the most widely used commercial reagents for fire prevention and extinguishment. For example, one can cite (a) the early use of CCl_4 as a portable source of fire extinguishment; (b) the current use of Freons such as CF_3Br as an extinguishant particularly in connection with fuel fires associated with aircraft mishaps, and also for the protection of electronic equipment; and (c) the incorporation of phosphorus-halogen or antimony-halogen (among others) formulations in materials such as natural and synthetic fabrics, furniture materials, paints, wood, paper, etc., e.g., see Lyons [2].

Halogen systems have also received the most attention by workers interested in the basic mechanism of flame inhibition. It should be recognized that in some instances the halogen treatments serve to alter the course of decomposition of substrates such that only relatively nonflammable gases are produced during the pyrolysis or oxidation processes. However, the present discussion is restricted to the retardancy aspects that involve vapor phase chemistry in the inhibition process.

In practical fire systems the halogen species can be introduced into the gas phase by mechanical means, as with Freon protection systems, or by chemical means, as with the release of HCl from decomposing polyvinylchloride, or as phosphorus chlorides or oxychlorides formed during decomposition of a polymer substrate, or as antimony halides from polymer substrates.

As is evident from the high ϕ_v values given in table 15 halogen species rank as chemical inhibitors and must therefore interfere with the chemistry associated with flame propagation. Some clues as to the nature of this interference are provided from macroscopic observations such as: (a) the effectiveness of halogens increases in the order fluorides $\ll$ chlorides $<$ bromides $\leq$ iodides; (b) CF_3Br is about four times more effective than CF_4 in preventing combustion of *n*/hexane air mixtures; (c) CF_3Br is a good inhibitor in hydrocarbon-air flames but is mediocre in H_2-air flames; (d) Br_2 has very little effect on $CO—O_2$ flames but is effective when small amounts of H_2 are introduced; and (e) in Br-substituted hydrocarbons and fluorocarbons the inhibitor effectiveness increases with the number of Br atom substitutions and, in certain instances, can be directly proportional to this number. For example, in a stoichiometric methane-air flame, the following ϕ_v values are found: Br_2 [24], CH_3Br [12], HBr [11], CF_3Br [17]. The high value for CF_3Br seems anomalous and this has been attributed to a possible role of the CF_3 radical in flame inhibition.

From these macroscopic observations it can be concluded that the flame inhibition must involve an

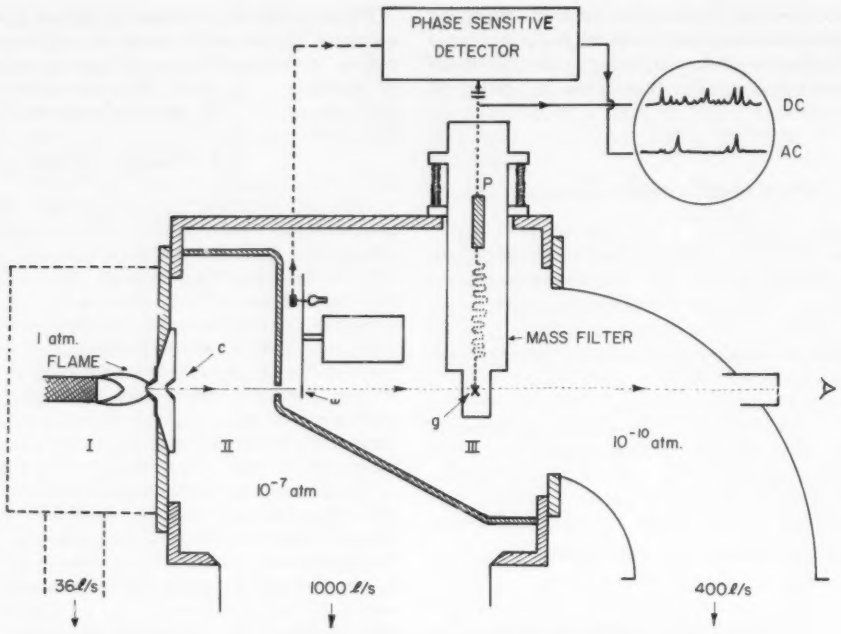

FIGURE 7. *Schematic of mass spectrometric system for sampling 1 atm flames.*

A representative gas sample passes through a cone system (c) into an evacuated chamber (region II); the beam then passes through an adjustable orifice into region III, which contains a wheel (w) for mechanical modulation of the beam, an ion source (g) for partial conversion of the molecular species into positive ions, and a mass filter and ion detection system (p), (from Hastie, [46]).

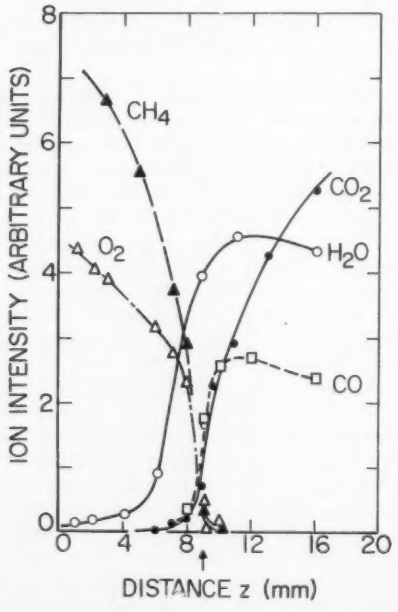

FIGURE 8. *Concentration profiles for major reactants and products in a 1 atm fuel-rich CH_4-O_2 flame, (from Hastie, [46]).*

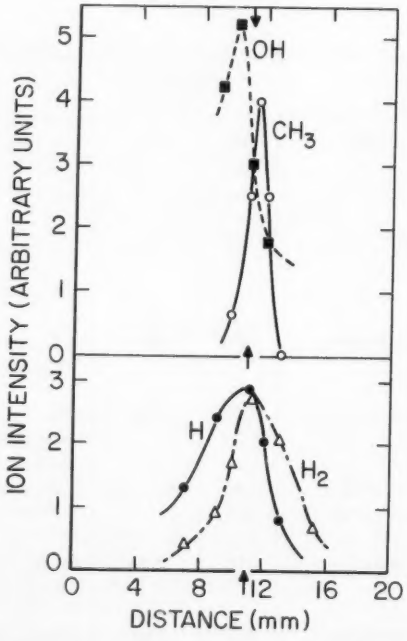

FIGURE 9. *Concentration profiles for the main radical species in a fuel-rich CH_4-O_2 flame, (from Hastie, [46]).*

interaction between species containing a halogen and a radical containing a H-atom, such as H or OH.

A more detailed description of the likely flame inhibiting mechanism has been derived from experiments carried out at the molecular level, such as the mass spectrometric microprobe sampling experiments described by Wilson et al. [42], or by Pownall and Simmons [54].

Before discussing the current status of the mechanistic understanding of halogen flame inhibition, it should be noted that a considerable variety of mechanisms have been proposed in recent years. For example, Mills [55] suggested that the inhibiting function of halogen species may be one of electron attachment followed by dissociation to generate active inhibitor species, e.g.:

$$CF_3Br + e \rightarrow Br^- + CF_3$$

$$CF_3 + H \rightarrow CF_3H^*$$

$$Br^- + H \rightarrow HBr + e.$$

He cites the observation of negative halogen ions in flames as support for this theory. However the concentration of such ions is now known to be at least several orders of magnitude less than for the neutral species and their effect on the flame propagating radicals is negligible.

Creitz [11] suggests that halogenated extinguishing agents act as catalytic agents for the recombination of oxygen atoms. The formation of OX, where X may be Cl or Br, as an intermediate is suggested; i.e.:

$$O + X + M \rightarrow OX + M$$

or

$$O + X_2 \rightarrow OX + X.$$

Other workers have suggested that the halogens reduce the concentration of OH in the flame. Rosser et al. [56] observed a decrease in the emission intensity of OH and an increase in that for CH due to the presence of CH_3Br or HBr in hydrocarbon flames. The observed radiation was not from a very well defined part of the flame, both reaction zone and post flame regions being included. It is well known from flame spectrophotometry studies that emission intensity may not necessarily be correlated directly with radical concentration.

In time resolved studies on the low pressure explosive combustion of styrene-oxygen mixtures, Petrella [57] observed that the production of OH was delayed in the presence of HBr.

The general situation with regard to the action of halogens on OH in flames remains unsettled, and some of the apparent difficulty may be related to the use of different flames for inhibition studies. In particular, Wilson et al. [42] have obtained indirect evidence for an increase in the maximum OH level in low pressure lean CH_4—O_2 flames containing HBr. However, using 1 atm lean propane fueled flames, Pownall and Simmons [54] provide indirect evidence for a reduction in the maximum OH concentration in the presence of HBr.

Levy et al. [58] suggest the inhibiting action of HBr to be:

$$HBr + OH \rightarrow H_2O + Br$$

in lean methane flames. This is analogous to the suggestion of Wilson [59] that methyl bromide reacts as follows:

$$CH_3Br + OH \rightarrow CH_2Br + H_2O.$$

However, more recently, Wilson and co-workers [42] have suggested an alternative mechanism involving H-atom reactions.

From the recent review of Fristrom and Sawyer [9], the current status of halogen inhibition is as follows. The primary reactions responsible for flame propagation are generally agreed to be:

$$H + O_2 = OH + O$$

and

$$O + H_2 = OH + H$$

$$OH + H_2 = H_2O + H.$$

In cool flames one must also consider reactions involving HO_2 such as:

$$H + O + M \rightarrow HO_2 + M^*$$

and

$$H + HO_2 \rightarrow OH + OH.$$

From the low pressure flame mass spectrometric studies reported by Wilson et al. [42], it is evident that the introduction of halogen species into a premixed CH_4/O_2 flame leads to the production of the hydrogen halide, HX, early in the flame. It was observed that the formation of H_2CO is inhibited and the production of H_2 enhanced. This provides indirect evidence for a removal of H atoms from the flame and the predominant reaction is considered to be:

$$H + HBr \rightarrow H_2 + Br.$$

This is known to be a fast reaction under flame conditions and Fristrom and Sawyer [9] have demonstrated that it can effectively compete with the chain branching reaction in the preflame region. They also show that the observed degree of inhibition is greater than that which would be predicted by considering the above reaction to reach equilibrium (i.e., to be balanced). The mechanism by which Br is removed from the system has not been established although under relatively cool flame conditions, the reaction:

$$HO_2 + Br \rightarrow HBr + O_2$$

could serve to replenish the inhibitor source. Similarly, the reaction

$$Br + H + M \rightarrow HBr + M^*$$

is possible (Day et al. [60]). The reaction:

$$X + RH \rightarrow HX + R$$

has also been suggested. Such a reaction relies on the presence of fuel (RH) and hence can only function in the preflame mixture.

The production of HBr from other initial sources such as RBr can readily be achieved by reactions of the type:

$$H + RX \rightarrow HX + R;$$

as R is most likely less reactive than H, this reaction is also flame inhibiting.

Note that this inhibition mechanism readily accounts for the noninhibiting properties of fluorides, since the high stability of HF provides an excessively high activation energy barrier for a reaction with H atoms to result. The much lower effectiveness of chloride as compared with bromide inhibitors is probably due to the HCl reaction being very close to thermoneutral, and hence it is likely that the reaction can proceed in the back direction to generate H atoms. The probable importance of the back reaction is evident from the observation that Cl_2 actually promotes flame propagation in H_2-air flames, as shown by the negative ϕ_v given in table 15.

This seems to be a very satisfactory model for halogen flame inhibition although it does not account for all of the experimental observations (see Pownall and Simmons [54]). More recent species profile studies also support the model in that H atoms are found to be present in relatively high concentration in the preflame region and in fuel-rich mixtures the radicals O and OH are almost negligible in this region (Hastie [46]). The production of HBr in the preflame region under 1 atm flame conditions has also been established (Hastie [61]).

Another test of the model is provided by the ignition temperature studies of Morrison et al. [44]. The model suggests that the flame reactions are shifted to a higher temperature region and hence the ignition temperature would be expected to be higher in the presence of the halogen inhibitor. Morrison et al. [44] find the expected increase in ignition temperature for methyl halides, $SnCl_4$ and BBr_3. However $SiCl_4$, $TiCl_4$, CrO_2Cl_2 and $Fe(CO)_5$ have no effect on the ignition temperature and CCl_4 actually decreases the ignition temperature. Evidently the model is not of wide generality and it should be noted that the supporting flame microstructure evidence was obtained with 0.05 atm lean CH_4-O_2 flames.

In the higher temperature reaction zone region of flames, reactions involving H, OH, and O are known to be balanced and a pseudo-equilibrium exists between these species. Hence under these conditions, arguments as to whether OH, O, or H are the inhibited species are not particularly critical, as a reduction of any of these radicals would serve to inhibit chain branching.

It is known that inhibition is more effective in cooler than in hotter, faster burning flames, and Friedman [13] has suggested that this is due to the higher radical concentrations in the hotter flames. Alternatively, one could argue that in the hotter flames the excess in radical concentration over the equilibrium level is not nearly as great as for cooler flames. Hence from the kinetic, non-equilibrium nature of the inhibition process, one would expect a better degree of inhibition in the cooler flames. The high temperature dissociation of HX for example, could also reduce its effectiveness in the hotter flames.

Flame cooling effects due to thermal dissociation of halogen species, such as Br_2, are negligible compared to the observed chemical effects (Simmons and Wolfhard [62]). The degree of inhibition observed for Cl_2 is low enough to be consistent with thermal dissociation as a cooling and slightly flame inhibiting process.

It should be noted that the apparent low effectiveness of CF_3Br on the fuel side of diffusion flames (Creitz [11]) is explained by Friedman [10] simply as an artificial geometry effect, since the flame itself would be located on the air side of the stagnation point.

3.5. Non-Halogen System Inhibitors

It is apparent from the classification of inhibitor effectiveness given in table 15 that non-halogenated compounds such as $(CH_3)_3PO_4$, $Pb(C_2H_5)_4$ and $Fe(CO)_5$ are one to two orders of magnitude more effective than halogen inhibitors. However systems of this type have not yet been utilized in practice, except that lead tetraethyl has been used to modify the preignition knocking phenomena of internal combustion systems. It is not unreasonable to speculate that the modes of action in flame inhibition and knock prevention may be related. Unfortunately, despite considerable experimental effort, the mechanism of knock inhibition has not been definitively established.

The metal and phosphorus halides indicated in table 15 also show a degree of inhibition which is in considerable excess of what can be accounted for in terms of their halogen content. This is particularly evident in the H_2-air flame where Cl_2 itself does not provide any flame inhibition. It is clear that the metals and phosphorus can themselves lead to flame inhibition and, more importantly, to a much greater degree than the halogen inhibitors. The two order of magnitude difference in ϕ_v between $Si(CH_3)_4$ and $Pb(C_2H_5)_4$ suggests that the inhibition mechanism is particularly sensitive to the properties of the metal itself. In fact, some metals show no inhibition at all. For example, the addition of several percent of Al_2Cl_6 vapor to premixed fuel-rich CH_4/O_2 flames produced a reduction in burning velocity that could be accounted for entirely from the amount of halogen present [63].

Metals such as Fe, Cr, and Ti, and their oxides, have low vapor pressures under normal flame conditions and their introduction to flames can result in the formation of condensed particles. These particles are highly luminous and are readily observed in the region of the reaction zone and the post flame gases. It has been argued, therefore, that these metals perturb the flame

chemistry via heterogeneous rather than homogeneous reactions. A clue to the possible effectiveness of heterogeneous, as opposed to homogeneous inhibition, is provided by the observation of Jost et al. [64], where the flame inhibiting effect of $Fe(CO)_5$ reached a limiting upper concentration level. At the higher concentration levels, condensed particles should form and the decreased rate of effectiveness with composition implies that heterogeneous inhibition is less effective than homogeneous reactions. The question of heterogenous versus homogeneous inhibition has received considerable attention in connection with the function of the commercially used solid extinguishants such as the alkali metal bicarbonates.

a. Solid Inhibitors Containing Alkali Metals

It is found that about 10^{-3} mol fraction of powdered alkali metal salts such as K_2SO_4, Na_2CO_3, $KHCO_3$, and $NaHCO_3$ can reduce the flame speed of CH_4-air flames by 50 percent. Thus ϕ_v factors of about 100 are indicated. Powders of alkali metal salts are also found to be more effective on a weight basis than CF_3Br in a counter flow diffusion flame [37]. Their effectiveness usually follows the order Li < Na < K < Rb. Carbonates are observed to be twice as effective as the alkali metal chlorides.

Flame temperature calculations (Dodding et al. [65]) show that the effect of decomposing $NaHCO_3$ on flame cooling is small and that the mode of inhibition must be chemical in nature. In general the smaller the initial particle size of the powder introduced to the flame, the greater the degree of inhibition found (e.g., Dodding et al. [65]; and Rosser et al. [66]).

From these observations, arguments have been given in favor of both solid and vapor phase inhibition mechanisms. Rosser et al. [66] favored a gas phase mechanism, since they calculated that under flame conditions an appreciable vaporization and dissociation of the solid powders should occur. The more recent study of Birchall [68] using town gas-air flames also supports this view. His observations of a relatively high efficiency for the alkali metal oxalates was accounted for by a model where the reactions:

$$K_2C_2O_4 \cdot H_2O\ (s) \rightarrow K_2C_2O_4\ (s) + H_2O$$

and

$$K_2C_2O_4\ (s) \rightarrow K_2CO_3\ (s) + CO,$$

resulted in the production of sub-micron size carbonate particles within the flame. These particles would then readily vaporize and decompose to yield the active inhibitor species. The following order for the effect of the anion on the alkali metal efficiency was indicated: oxide (i.e., oxalate) > cyanate > carbonate > iodide > bromide > chloride > sulfate > phosphate. This order represents the ease with which the alkali metal can be released to form the active species. It should also be noted that the presence of Cl_2 gas retards the efficiency of the oxalate and cyanate. Also Friedman and Levy [67] have observed that the introduction of elemental Na or K vapor to the fuel side of methane-air counter flow diffusion flames has no effect on the flame strength.

Most workers agree that the active gas phase species would be the hydroxide, KOH. Under equilibrium conditions this is much more stable than the oxides or elemental K. Under very lean flame conditions the oxides may also be important (69). The reaction:

$$K + OH + M \rightarrow KOH + M$$

is considered to be kinetically more favorable than the endothermic process:

$$KOH + OH \rightarrow H_2O + KO.$$

The reaction:

$$KOH + H \rightarrow H_2O + K$$

is considered to be the one responsible for flame inhibition. The poisoning effect of halogens is most likely due to the known stability of the alkali halides in flames resulting in a loss of KOH, for example.

b. Other Metal Inhibitors

The refractory nature of the other inhibiting metals and their oxides increases the likelihood of solid formation and a heterogeneous mode of inhibition. Radical recombinations on solid particles should lead to a temperature rise at the particle. For Cr concentrations greater than 10^{15} cm^{-3} in H_2-O_2-N_2 flames, particles were observed which showed a higher temperature than the flame gases, i.e.:

$$Cr_2O_3(s) + H + H \rightarrow Cr_2O_3\ (s) + H_2.$$

However, at lower concentrations it was found that the recombination of H-atoms occured via a homogeneous reaction (Bulewicz and Padley [70]).

In these studies observations were made downstream of the reaction zone and the question arises as to whether the additives have an opportunity to form solids in the preflame region or not. Very little has been done to answer such a question. However, from the light scattering experiments of Cotton and Jenkins [71], it is evident that for the case of Ba at concentrations of 10^{-5}-10^{-6} mol fraction in a 1600 K H_2-O_2-N_2 flame, solids do form prior to the reaction zone. These flames did not show the streakiness which is commonly observed when solid particles are present. However, in spite of the presence of solids the observed catalytic effect of alkaline earth metals on the recombination of H-atoms could be explained solely in terms of a homogeneous mechanism.

Indirect evidence for the formation of solids in the pre-reaction zone region of a low pressure CH_4 flame containing $Fe(CO)_5$ additions was reported by Vree et al., [72].

The post reaction zone radical recombination studies made in the presence of metal catalysts, represent the

only molecular basis studies that have a bearing on the likely flame inhibiting function of metal containing species. The results of these studies have dispelled the often relied-upon notion that the presence of metallic elements at ppm concentration levels has no effect on flame chemistry.

The survey experiments of Bulewicz and Padley [73, 70] as typified by figures 10 and 11, indicate that the elements Mg, Cr, Mn, Sn, U, and Ba had a pronounced effect on the recombination of H atoms, whereas Na, Co, Ni, Cu, V, Zn, Ga, Th, Ce, and La were found to be ineffective as catalysts for H-atom recombination. Some of the results were interpreted in terms of the models given in table 19. That is, the diatomic metal oxide species catalyses the recombination of H or OH radicals via metal hydroxide intermediates.

Many of these oxides and hydroxides are known to be stable under typical flame conditions. Unfortunately, only Sn and Cr are available for comparison with the flame speed measurements represented by table 15. However, both of these elements show high ϕ_v values and they are also among the most effective catalysts for H-atom recombination. Hence it is reasonable to conclude that the role of the metallic flame inhibitors is somewhat analogous to that of the halogens, in that the overall effect results from catalysis of H-atom recombination.

It appears that the oxide-hydroxide mechanism relies on a rather special set of energetics. In particular, MOH must be stable under flame conditions but must readily react with a H-atom when the opportunity arises. Ideally this last step should be exothermic to reduce the probability of a reverse reaction. A more critical set of energetic conditions is revealed by the case of Sn [74], where the initial step involved is,

$$SnO + H \rightarrow SnOH^*$$

TABLE 19. *Mechanisms for H-atom recombination* [a]

Sn:	
$SnO + H + X$	$\rightarrow SnOH + X$
$SnOH + H$	$\rightarrow SnO + H_2$
M = Ca, Sr, Ba:	
$MOH + H$	$\rightarrow MO + H_2$
$MO + H_2O (+X)$	$\rightarrow M(OH)_2 (+X)$
$M(OH)_2 + H$	$\rightarrow MOH + H_2O$

[a] See refs: [71], [73], [74].

with $SnOH^*$ being produced in an excited electronic state which crosses to another state before undergoing further reaction with another H-atom to produce H_2 and ground state SnO. Such subtleties in energetics readily account for the stricking variance in the ability of metals to inhibit flames or at least catalyze radical recombination.

The poisoning effect of Cl_2 on the alkali metal flame inhibition can also be expected to occur for some of the other metal inhibitors. In particular, flame systems containing metals such as Ba, Cr, and Ca, and a halogen source can be expected to form stable MCl and MCl_2 species. This would reduce the effectiveness of these metals, as they would not be available to participate in the MO—MOH inhibition sequence. On

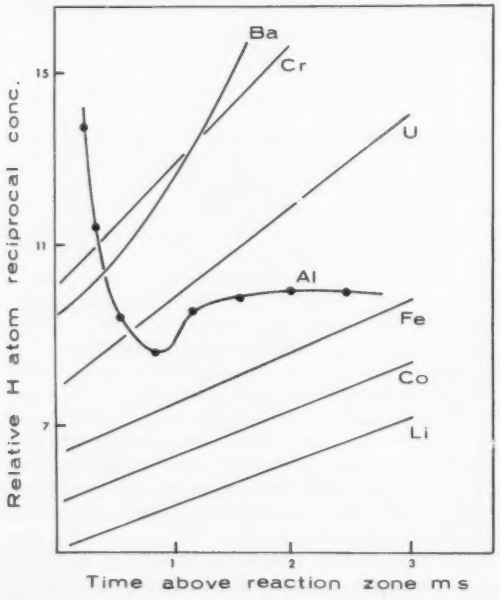

FIGURE 10. *Effect of metal additives on H-atom concentration as a function of time (i.e., distance) relative to the reaction zone in 1 atm H_2-O_2-N_2 fuel-rich flames: curves are vertically displaced for clarity (from Bulewicz and Padley [73]).*

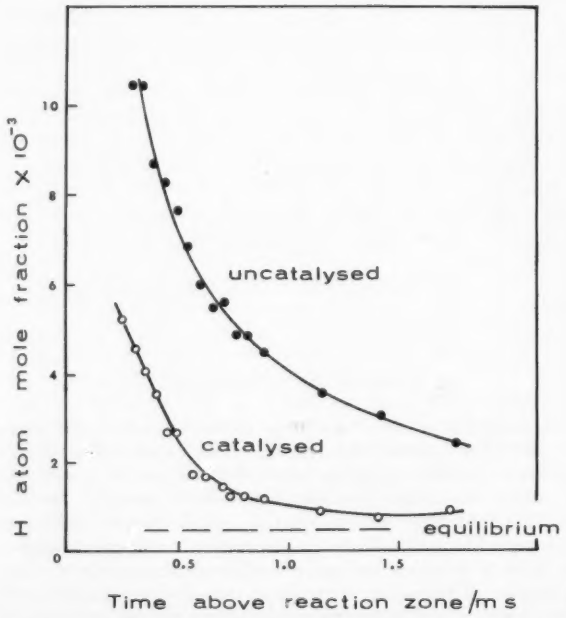

FIGURE 11. *Effect of* Cr *on* H-*atom recombination in a 1 atm H_2-O_2-N_2 fuel-rich flame (from Bulewicz and Padley, [70]).*

the other hand, metals such as Sb and Sn have relatively weak metal-halogen bonds and the halogen poisoning effect would be minimal in these cases.

3.6. Synergistic Systems—The Antimony Oxide-Halogen Example

From the previous discussion of experiments relating to the substrate chemistry involved in the release of halogen and antimony, in the form of $SbCl_3$, to the vapor phase it was suggested that the main role of antimony was to moderate the release of halogen to the flame. However, there is evidence to suggest that, given the opportunity to enter the vapor phase, antimony, in the absence of a halogen, can provide a useful degree of flame inhibition. In particular, triphenylstibine shows all the characteristics of an effective vapor phase flame inhibitor [40]. Furthermore, the high value of ϕ_v for $SbCl_3$ as compared with Cl_2 or CCl_4 (see table 15) also is indicative of antimony, itself, being involved in the flame inhibiting process. In fact, the ϕ_v rating for $SbCl_3$ is not very different from that for $SnCl_4$ and it is reasonable to consider the possibility of an oxide-hydroxide inhibition process analogous to that suggested earlier for Sn.

From the results of a recent mass spectrometric analysis of $SbCl_3$ and $SbBr_3$ in 1 atm fuel rich CH_4-air flames [61] one can suggest a very plausible mechanism for the role of antimony trihalides as flame inhibitors. The results of the analysis are summarized by the species concentration profiles shown in the figure 12.

The appearance of CH_3Br and HBr in the preflame region is in accord with the observations of Wilson et al. [42], for halogen additions in low pressure flames. Their model for halogen inhibition also provides the best explanation for this system. The role of antimony as an inhibitor most likely involves the species SbO and Sb which are shown to be the major antimony species in the region of the reaction zone. It should be noted that under the present conditions, i.e., antimony halide mole fractions of $10^{-4}-10^{-3}$, no condensation to form solids is possible and heterogeneous mechanisms do not require consideration.

A set of likely reactions involving antimony halides in these flames is given in the table 20. The reactions 4(a)–4(e) are analogous to those suggested for Sn flame inhibition. It would appear from the profile data of figure 12 that inhibition involving SbO species would occur primarily in the region of the reaction zone. This contrasts with the suggested role of HBr where preflame processes are important. Thus we are left with the not unreasonable conclusion that different flame inhibitors may operate in quite different flame regions. Furthermore, as the metal-type inhibitors appear to be more effective than the halogens, it is suggested that inhibition at the reaction zone is more desirable than in the preflame region. It should be noted that the main source of H atoms in the preflame region is from diffusion out of the reaction zone, so that inhibition at this zone could be expected to have a similar delay-effect on the flame reaction to that suggested by the halogen inhibition model.

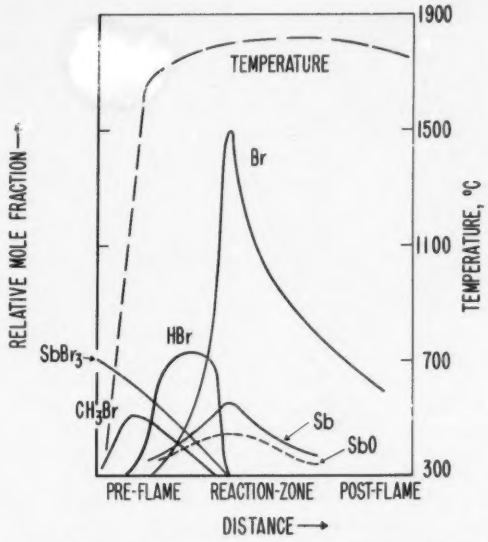

FIGURE 12. *Concentration profiles for species resulting from* $SbBr_3$ *addition to a 1 atm fuel-rich* CH_4-O_2 *flame, (Hastie [61]).*

TABLE 20. *Reactions involving antimony trihalides in* CH_4-O_2 *flames* [a]

1.	(a)	$SbX_3 + H \rightarrow HX + SbX_2$
	(b)	$SbX_3 \rightarrow SbX_3^* \rightarrow X + SbX_2$
	(c)	$SbX_3 + CH_3 \rightarrow CH_3X + SbX_2$
2.	(a)	$SbX_2 + H \rightarrow HX + SbX$
	(b)	$SbX_2 + CH_3 \rightarrow CH_3X + SbX$
3.	(a)	$SbX + H \rightarrow Sb + HX$
	(b)	$SbX + CH_3 \rightarrow Sb + CH_3X$
4.	(a)	$Sb + O + M \rightarrow SbO + M^*$
	(b)	$Sb + OH + M \rightarrow SbOH + M^*$
**	(c)	$SbOH + H \rightleftharpoons SbO + H_2$
**	(d)	$SbO + H \rightarrow SbOH^*$
	(e)	$Sb + H_2O \rightleftharpoons SbO + H_2$
5.	(a)	$X + X + M \rightarrow X_2 + M^*$
	(b)	$X_2 + CH_3 \rightarrow CH_3X + X$
	(c)	$X + CH_3 + M \rightarrow CH_3X + M^*$
**6.	(a)	$HX + H \rightarrow H_2 + X$
	(b)	$HX + CH_3 \rightarrow CH_4 + X$
7.	(a)	$X + HO_2 \rightarrow HX + O_2$
8.	(a)	$CH_3X + H_2 \rightarrow CH_4 + HX$
	(b)	$CH_3X + H \rightarrow CH_4 + X$ or $CH_3 + HBr$
	(c)	$CH_3X \rightarrow CH_3X^* \rightarrow CH_3 + X$

**Reactions leading directly to flame inhibition.

[a]See also ref. [61].

3.7. Phosphorus as a Flame Inhibitor

From the previously discussed studies relating to TPPO-Nylon6-PET substrates, it was concluded that the observed flame inhibition was related to the release of TPPO to the vapor phase, i.e., the flame.

A clue to the possible function of phosphorus additives as flame inhibitors is given by the observations of Fenimore and Jones [75] on low pressure fuel-rich H_2 flames containing phosphorus. The species HPO was spectroscopically identified in the post combustion gases by its characteristic green chemiluminescence. From indirect mass action-type considerations the species P_2 was also believed to be a major P-containing species.

More recent studies of phosphorus chemistry in flames using the molecular beam sampling mass spectrometric technique have established the nature of the phosphorus intermediate species resulting from the decomposition of TPPO in 1 atm CH_4- and H_2-fueled flames [76]. Typical results are given in figure 13. For the fuel rich systems studied, the main species are P_2, PO, and PO_2 with lesser amounts of P, HPO, and PN. A catalytic reaction scheme involving these species and leading to H atom recombination is suggested in table 21.

TABLE 21. *Probable reactions leading to inhibition in flames containing phosphorus*

$(C_6H_5)_3PO$	→	PO, P, and P_2
$H + PO + M$	→	$HPO + M$
$OH + PO$	=	$HPO + O$
$HPO + H$	=	$H_2 + PO$
Other likely reactions		
$P_2 + O$	=	$P + PO$
$P + OH$	=	$PO + H$

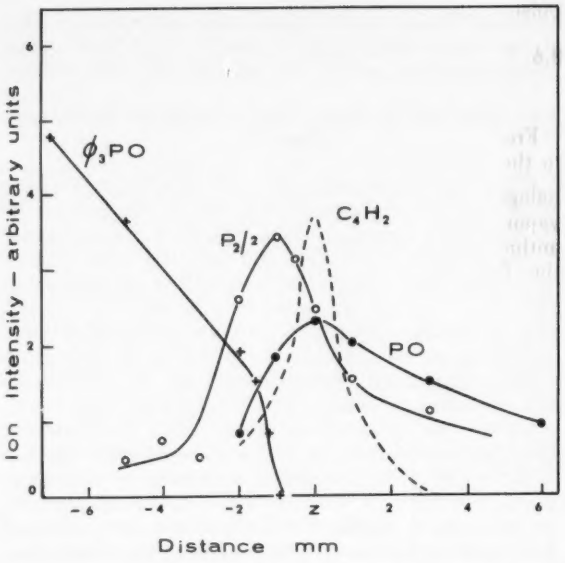

FIGURE 13. *Concentration profiles for species resulting from triphenylphosphine oxide addition to a 1 atm fuel-rich* CH_4-O_2-Ar *flame: distance measurements are relative to the reaction zone at* z, *(Hastie, [76]).*

3.8. Smoke Suppression

Recent studies involving the mechanism of metal additives on smoke suppression indicate that there appears to be a close relationship to flame inhibition processes.

The suppression of carbon formation in combustion systems can be achieved by (a) adjustment of the operational parameters such as fuel ratio and aerodynamic flow conditions as has been suggested for smoke reduction in jet engines [77]; (b) use of electrical techniques which take advantage of the charged character of flame particulates as has been suggested, for example, by Hardesty and Weinberg [78]; and (c) the use of chemical additives to catalyze the oxidation of carbon within the flame. The use of Ba additives in diesel fuel to suppress exhaust smoke is an example of the chemical inhibitor approach [79].

As was the case with flame inhibition, one is faced with the problem of setting up criteria for defining the degree of effectiveness of additives as smoke reducers Thus Cotton et al. [80] chose the threshold value of the equivalence ratio at which soot was produced for correlation with the degree of effectiveness. Other workers [81] apparently chose a parameter related to the amount of soot produced. As pointed out by Miller [82], these two studies cannot be compared directly and the order of effectiveness of various metals as smoke inhibitors differs considerably.

The smoke inhibition mechanism suggested by Cotton et al. [80] is particularly interesting, as it involves another aspect of the metal oxide-hydroxide catalytic process on H-atoms which was suggested as a mechanism for flame inhibition. It also serves to demonstrate the subtle dependence of the function of flame additives on varying flame conditions.

The survey of Cotton et al. [80], involved the effect of some forty metals on the smoke point of propane-oxygen diffusion flames at atmospheric pressure. These flames in essence had cylindrical symmetry and were non-turbulent. Temperatures were typically in the region of 2100 K. The metals were introduced into the fuel stream as atomized aqueous solutions with N_2 as a carrier gas.

The efficiencies of the various metals, relative to Ba, as soot suppressants are represented in the figure 14. The concentration levels of metals were typically in the region of 10^{-4}–10^{-5} mol fraction.

The metals not shown in this figure had essentially no effect relative to Ba and they include Ag, Al, As, Be, Cd, Co, Cu, Fe, Mg, Ni, Pb, Si, Th, Ti, Tl, U, and Zn. Notably, several of these, namely Fe, Pb, Si, and

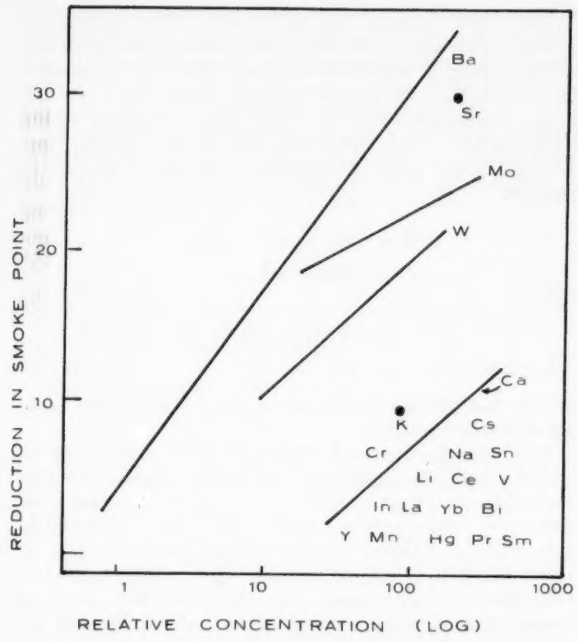

FIGURE 14. *Effect of metal flame additives on smoke reduction relative to that for* Ba, *(from Cotton, et al., [80]).*

Ti, were found to be very good flame inhibitors as discussed elsewhere. From the figure 14, two groups may be distinguished: the group Ba, Sr, Mo, and perhaps W, represent the highly effective smoke inhibitors. Before discussing the significance of these observations, it is pertinent to note that Fe, which has a zero ranking in these studies, is actually used as a commercial smoke inhibitor in the form of ferrocene. Also Spengler et al. [83], found the addition of Fe in the form of the pentacarbonyl, or as ferrocene, as well as Mn, in the form of methylcyclopentadienyl manganese tricarbonyl, to have a beneficial effect on smoke reduction in several diffusion flames and also a Diesel engine.

A common mechanism was proposed for the soot suppression activity of Ba, Sr, Ca, NO, and SO_2. From known rate data, the mechanism was demonstrated rather convincingly, at least at a semiquantitative level. Basically the model is as follows. Under the fuel rich conditions necessary for soot production, the active radical concentrations are low and in fact may even be below the equilibrium level. This follows from the well known self-inhibiting effect of hydrocarbons, i.e.,

$$C_nH_m + H \rightarrow C_nH_{m+1}$$

and from the reaction

$$C(s) + OH \rightarrow CO + H$$

which is considered by most workers to be the primary reaction for the oxidation of solid carbon in flames.

The flame condition should be contrasted with that found in faster burning flames, where premixing and less fuel rich conditions exist, with the result that the reaction zone radical levels are well in excess of the equilibrium concentrations. Under these latter conditions Cotton et al. [80], found that Ba and other alkali earth metals catalyzed the recombination of H-atoms. The essence of the smoke suppression mechanism involves a reversal of this recombination process under conditions of low radical concentrations. That is, the metals are involved in a gas phase catalysis of the decomposition of molecular hydrogen or water vapor. The individual steps in this mechanism are given in table 22.

TABLE 22. *Mechanism for catalytic oxidation of smoke* [a]

$MO + H_2$	$\rightarrow$	$MOH + H$	[1]
$MOH + H_2O$	$\rightarrow$	$M(OH)_2 + H$	[2]
$M(OH)_2 + (X)$	$\rightarrow$	$MO + H_2O + (X)$	[3]
$H + H_2O$	$=$	$OH + H_2$	[4]
$OH + C(s)$	$=$	$CO + H$	

[a] From Cotton et al., [80].
Note: H is initially below equilibrium concentration.

The presence of MO in flames, where M is Ba, Sr or Ca, is well established, as is the formation of the metal hydroxide intermediates. Also the balanced nature of reaction 4 is well established, at least for the hotter flame regions. Thus the net effect of these processes is to increase the formation of OH radicals and hence the oxidation of solid carbon. Note that the reaction 2 leading to the production of the metal dihydroxide is endothermic, and this suggests that the suppression of smoke will be much less effective as the temperature is decreased.

From this model it can be argued that it is not possible to utilize metals for the simultaneous reduction of smoke and flame propagation. This is also suggested by the observation that, as the flames become increasingly more fuel-rich, the catalytic effect on radical recombination is substantially diminished.

Also in real fires, the degree of fuel-oxidant mixing will be an important factor in determining the effectiveness of metallic inhibitors. From arguements such as these, it is not at all surprising that the effectiveness of fire retardant treatments may vary according to the test conditions used. It is also evident that the presence of solid carbon in flames has an inhibiting effect on flame propagation. We may recall that the use of halogens as flame inhibitors often involves an increase in smoke production. Thus smoke production and flame propagation are intimately related phenomena and the use of additives to exclusively suppress one of these, without affecting the other, does not appear to be possible.

3.9. Pressure Effects

As much of the experimental evidence for the present understanding of flame inhibition has been derived from molecular studies on low pressure flames, it is important, for scaling purposes, to consider the effect of pressure on inhibition.

Bonne et al. [84] found that as the flame pressure was lowered, the inhibiting action of $Fe(CO)_5$ decreased and at low pressure had little effect on the OH concentration or the flame temperature. Inhibition was found to be about a factor of three greater at 1 atm than at half an atmosphere. Similar results were obtained for the effect of trimethyl phosphate (TMP) on the flame inhibition chemistry of H_2—O_2—Ar flames [75]. Flames at 0.13 atm pressure were unaffected by additions of 10^{-3} mol fraction TMP, whereas at 1 atm pressure inhibition was observed. A factor of two reduction in the H-atom concentration was also observed when a 10^{-3} mol fraction of TMP was added to the 1 atm flames. Fenimore et al., [75] suggested that the lack of an observable inhibition effect for the low pressure flames may be the result of the much greater relative concentration of H-atoms present in low pressure flames.

More recently, Homann and Poss [85] have found that the degree of inhibition, as represented by a reduction in burning velocity for an ethylene-air flame, is significantly less at 132 torr than at 1 atm for the additives $Fe(CO)_5$, CH_3I, CH_3Br, and CH_2Br_2 but not for CH_2Cl_2. In particular, the $Fe(CO)_5$ inhibitor was the system most affected by a pressure change. The authors suggest the possibility that this effect is indicative of the role of termolecular reactions, in addition to the normally considered bimolecular steps, in the inhibition process. Such an argument is in keeping with the proposed model for metal oxide inhibition via the hydroxide intermediate.

From these few observations it is clear that one should proceed with caution in attempting to extrapolate the results of inhibition studies on low pressure flames to the "real-life" application of 1 atm systems.

4. Conclusions

It is evident that inorganic systems containing halogens (other than F) or certain metals can provide a degree of flame inhibition which is considerably greater than that allowed by physical processes. It also appears that high temperature species such as metal halides, oxides and hydroxides play an important part in the flame inhibition process. As the flame inhibiting processes are kinetically controlled and rely rather stringently on a special set of energetics, the need for basic thermochemical and kinetic data, in support of flame inhibition mechanistic studies, is apparent. Rates of vaporization under pyrolysis and flame conditions also appear to be important quantities in the overall flame inhibition process.

The basic feature of all of the flame inhibiting systems considered is their interaction with H-atoms as the mode of inhibition. In this connection it should be noted that hydrocarbons are themselves strong flame inhibitors. This is particularly evident when hydrocarbons are introduced into H_2-air flames [45]. The inhibiting effect is thought to be due to reactions such as:

$$H + CH_4 \rightarrow H_2 + CH_3$$

and

$$H + C_2H_4 \rightarrow C_2H_5$$

where the product radicals are far less reactive than the H-atom.

From the flame speed studies of Miller et al., [45] it is evident that the inhibitors are more effective in the more fuel-rich flame mixtures, i.e., at fuel equivalence ratios of greater than about two. Such conditions favor the presence of H-atoms rather than O or OH as the predominant radical species. Hence the suggested inhibition mechanisms, which basically involve catalysis of H-atom recombination, are supported by these macroscopic observations.

It also appears that the inhibition of H atoms can be effectively achieved in both preflame and reaction zone flame regions. The most reasonable model for the inhibiting effect of metals is one involving participation of metal oxide and hydroxide species. This effect is believed to be important primarily in the region of the reaction zone. From the high metal-halogen bond energies for additives such as $TiCl_4$ and $SiCl_4$ it is most unlikely that any appreciable formation of the monoxide would occur prior to the reaction zone. For such low concentrations of metal additives it is not unreasonable that the onset of condensation and particle formation should lead to a reduction in the rate of inhibition with additive concentration. The formation of particulates would tend to lower the collision probability of radicals with the additive.

As an example of the complexity involved in assessing, from basic principles, the potential of metals as flame inhibitors, consider the Cr system. From the flame speed measurements it is known that Cr has an overall flame inhibiting effect. Similarly the catalytic enhancement of H-atom recombination is also indicative of possible flame inhibition. However, the second stage of hydrocarbon combustion in flames, namely the oxidation of CO to CO_2 is actually accelerated by the presence of Cr at the ppm concentration level (e.g., see Matsuda et al., [86]). A similar enhancement is found with Ni and Fe additions, but Pb and Te show a retarding effect on this oxidation.

It is apparent that the various suggested mechanisms do not satisfy all of the macroscopic observations and general questions arise. For example, why do PCl_3 and PBr_3 have the same effectiveness in *n*-hexane-air mixtures when Br_2 and HBr are substantially superior to Cl_2 or HCl? Why is the inhibiting action of halogens

more pronounced for fuels with low hydrogen content (e.g., C_6H_6) than for H_2 or CH_4 [43]? Why is $Fe(CO)_5$ much less effective in H_2-fueled flames? Similarly, why is $Fe(CO)_5$ less effective in an O_2-CH_4 flame than an air-CH_4 stoichiometric flame [43]?

Answers to such questions and a definitive understanding of the mechanisms involved in flame inhibition can only result from molecular level studies of flame reaction kinetics.

5. References

[1] Drake, G. L., Fire-resistant Textiles, Kirk-Othmer Encyclopedia of Chemical Technology, 2d ed., Vol. **7**, (Wiley-Interscience, New York, 1964) p. 300.

[2] Lyons, J. W., The Chemistry and Uses of Fire Retardants, (Wiley-Interscience, New York, 1970).

[3] Thiery, P., Fireproofing, Chemistry, Technology and Applications, English translation by J. H. Goundry (Elsevier, Barking, England, 1970).

[4] Hindersinn, R. R., and Wagner, G. M., Fire Retardancy, Encyclopedia of Polymer Science and Technology, Vol. **7** (Interscience, New York, 1967), p. 1.

[5] Ranney, M. W., Flame Retardant Textiles 1970, Noyes Data Corporation, Park Ridge, New Jersey, (1970).

[6] Hilado, C. J., Flammability Handbook for Plastics (Technomic Publishing Company, Stanford, Connecticut, 1969).

[7] Lyons, J. W., J. Fire and Flammability, 1, (1970), p. 302.

[8] Fristrom, R. M., The mechanisms of pyrolysis, oxidation, and burning of organic materials. Nat. Bur. Stand. (U.S.), Spec. Publ 357, 199 pages (June 1972).

[9] Fristrom, R. M., and Sawyer, R. F., Flame Inhibition Chemistry, presented at the Thirty-seventh AGARD Symp. Aircraft, Fuels, Lubricants and Fire Safety, The Hague, 12 May (1971).

[10] Friedman, R., Fire Research Abstracts and Reviews, **13**, (1971), p. 187.

[11] Creitz, E. C., J. Res. Nat. Bur. Stand. (U.S.), **74A**, 521–530 (July-Aug. 1970).

[12] McHale, E. T., Fire Research Abstracts and Reviews, **11**, (1969), p. 90.

[13] Friedman, R., Fire Research Abstracts and Reviews, **3**, (1961), p. 128.

[14] Pumpelly, C. T., Fire Extinguishing and Fire Proofing, p. 657 in Bromine and its Compounds, Ed., Z. E. Jolles, Academic Press, (1966).

[15] Pitts, J. J., J. Fire and Flammability, **3**, (1972), p. 51.

[16] Tesoro, G., Synergism During Fire Retardation, presented at Conference on Flammability Characteristics of Polymeric Materials, University of Utah, (June 1970).

[17] Little, R. W., Flameproofing Textile Fabrics, ACS Monograph Series, No. 104 (Reinhold Publishing Company, New York, 1947), p. 240.

[18] Nametz, R. C., Ind. Eng. Chem. **59**, (1967), p. 99.

[19] Learmonth, G. S., Nesbitt, A., and Thwaite, D. C., Br. Polym. J., **1**, (1969), p. 149.

[20] Learmonth, G. S., and Thwaite, D. C., Br. Polym. J. **1**, (1969), p. 154.

[21] Lindemann, R. F., Ind. Eng. Chem. **61**, (1969), p. 70.

[22] Fenimore, C. P., and Martin, F. J., Combust. Flame, **10**, (1966), p. 135.

[23] Trends in Usage of Antimony, Report of the Panel on Antimony of the Committee on the Technical Aspects of Critical and Strategic Materials, National Materials Advisory Board Publication 274, Washington, D.C., (Dec. 1970).

[24] Read, N. J., and Heighway-Bury E. G., J. Soc., Dyers and Colourests, **74**, (1958) p. 823.

[25] Schmidt, W. G., Trans. J. Plastics Inst., (1965), p. 247.

[26] Rhys, J. A., Chem. and Ind. (1969), p. 187.

[27] Fenimore, C. P., and Jones, G. W., Combust. Flame **10**, (1966), p. 295.

[28] Belluomini, C., Fornaseri, M., and Nicoletti, M., Period. Mineral. **36**, (1967), p. 147.

[29] Pitts, J. J., Scott, P. H., and Powell, D. G., J. Cellular Plastics **6**, (1970), p. 35.

[30] Jan-Khan, M., and Samuel, R., Proc. Phys. Soc. (London) **48**, (1936), p. 626.

[31] Einhorn, I. N., Fire Retardance of Polymer Materials, Presented at Polymer Conference series on "Flammability Characteristics of Polymeric Materials," Univ. Utah, June 15 (1970).

[32] Hastie, J. W., Mass Spectrometric Studies of Flame Inhibition-The Antimony Oxyhalide System, Presented at 162nd National ACS Meeting, Washington, D.C., Sept (1971); also data to be published.

[33] Woods, W. G., and Bower, J. G., Modern Plastics **47** (1970), p. 140.

[34] Eichhorn, J., J. Appl. Polymer Sci. **8** (1964), p. 2497.

[35] Bostic, J., and Barker, R., from Ph. D. Thesis of Bostic, Clemson University (1972).

[36] Hastie, J. W., and Blue, G. D., Fire Retardancy Studies on Polyester Systems at the Molecular Level, presented at the 164th National ACS meeting, Dallas, April (1973), to be published.

[37] Milne, T. A., Green, C. L., and Benson, D. K., Combust. Flame **15**, (1970), p. 255.

[38] Simmons, R. F., and Wolfhard, H. G., Trans. Faraday Soc. **52**, (1956), p. 53.

[39] Smith, S. R., and Gordon, A. S., J. Phys. Chem. **60**, (1956), p. 759.

[40] Fenimore, C. P., and Martin, F. J., in The Mechanisms of Pyrolysis, Oxidation, and Burning of Organic Materials, Nat Bur. Stand. (U.S.), Spec. Publ. 357, 199 pages (June 1972).

[41] Dixon-Lewis, G., Proc. Roy. Soc. Lond. **A317**, (1970), p. 235.

[42] Wilson, W. E., Jr., O'Donovan, J. T., and Fristrom, R. M., Twelfth Symposium (International) on Combustion, The Combustion Institute, Pittsburgh, (1969), p. 929.

[43] Lask, G., and Wagner, H. G., Eighth Symposium (International) on Combustion (Williams and Wilkins Co., 1962), p. 432.

[44] Morrison, M. E., and Scheller, K., Combust. Flame **18**, (1972), p. 3.

[45] Miller, D. R., Evers, R. L., and Skinner, G. B., Combust. Flame **7**, (1963), p. 137.

[46] Hastie, J. W., Mass spectrometric analysis of 1 atm flames-apparatus and the CH_4-O_2 system, Combust. Flame, (1973), p. 187.

[47] Eltenton, G. C., J. Chem. Phys. **15**, (1947), p. 455.

[48] Foner, S. N., and Hudson, R. L., J. Chem. Phys. **21**, (1953), p. 1374.

[49] Ingold, K. U., and Bryce, W. A., J. Chem. Phys. **24**, (1956), p. 360.

[50] Westenburg, A. A., and Fristrom, R. M., J. Phys. Chem. **64**, (1960), p. 1393.

[51] Fenimore, C. P., and Jones, G. W., J. Chem. Phys. **41**, (1964), p. 1887.

[52] Dixon-Lewis, G., and Williams, A., Ninth Symposium (International) on Combustion (Academic Press, New York, 1963), p. 576.

[53] Milne, T. A., and Greene, F. T., J. Chem. Phys. **44**, (1966), p. 2444.

[54] Pownall, C., and Simmons, R. F., Thirteenth Symposium (International) on Combustion, The Combustion Institute (1971), p. 585.

[55] Mills, R. M., Combust. Flame **12**, (1968), p. 513.

[56] Rosser, W. A., Wise, H., and Miller, J., Seventh Symposium (International) on Combustion (Butterworth, London, 1959), p. 175.

[57] Petrella, R. V., Studies of the combustion of hydrocarbons by kinetic spectroscopy. II. The explosive combustion of styrene inhibited by halogen compounds, private communication (1972).

[58] Levy, A., Droege, J. W., Tighe, J. J., and Foster, J. F., Eighth Symposium (International) on Combustion (Williams and Wilkins Co., 1962), p. 524.

[59] Wilson, W. E., Jr., Tenth Symposium (International) on Combustion, Combustion Institute, (1965). p. 47.

[60] Day, M. J., Stamp, D. V., Thompson, K., and Dixon-Lewis, G., Thirteenth Symposium (International) on Combustion, Combustion Institute, (1971), p. 705.

[61] Hastie, J. W., Combust. Flame, **21**, (1973), p. 49.

[62] Simmons, R. F., and Wolfhard, H. G., Trans. Faraday Soc. **51**, (1955), p. 1211.
[63] Friedman, R., and Levy, J. B., Combust. Flame **2**, (1958), p. 105.
[64] Jost, W., Bonne, U., and Wagner, H. G., Chem. Eng. News **39**, (1961), p. 76.
[65] Dodding, R. A., Simmons, R. F., and Stephens, A., Combust. Flame **15**, (1970), p. 313.
[66] Rosser, W. A. Jr., Inami, S. H., and Wise, H., Combust. Flame, **7**, (1963), p. 107.
[67] Friedman, R., and Levy, J. B., Combust. Flame **7**, (1963), p. 195.
[68] Birchall, J. D., Combust. Flame **14**, (1970), p. 85.
[69] Kaskan, W. E., Tenth Symposium (International) on Combustion, Combustion Institute, (1965), p. 41.
[70] Bulewicz, E. M., and Padley, P. J., Proc. Roy. Soc. **A323**, (1971), p. 377.
[71] Cotton, D. H., and Jenkins, D. R., Trans. Faraday. Soc. **67**, (1971), p. 730.
[72] Vree, P., and Miller, W. J., Fire Research Abstracts and Reviews **10**, (1968), p. 12.
[73] Bulewicz, E. M., and Padley, P. J., Thirteenth Symposium (International) on Combustion, Combustion Institute, 1970), p. 73.
[74] Bulewicz, E. M., and Padley, P. J., Trans. Faraday Soc. **67**, (1971), p. 2337.
[75] Fenimore, C. P., and Jones, G. W., Combust. Flame **8**, (1964), p. 133.
[76] Hastie, J. W., unpublished observations (1973).
[77] Linden, L. H., and Heywood, J. B., Combustion Science and Technology **2**, (1971), p. 401.
[78] Hardesty, D. R., and Weinberg, F. J., Fourteenth Symposium (International) on Combustion, to be published Combustion Institute, (1973).
[79] Golothan, D. W., Soc. Auto. Eng. Trans. **76**, (1967), item 670092.
[80] Cotton, D. H., Friswell, N. J., and Jenkins, D. R., Combust. Flame **17**, (1971), p. 87.
[81] Addecott, K. S. B., and Nutt, C. W. Mechanism of Smoke Reduction by Metal Compounds, Symposium on Deposit, Wear, and Emission Control by Lubricant and Fuel Additives, Div. of Petroleum Chem., ACS meeting, New York, Sept. 1969; as cited by W. Miller, i.e., ref. [82].
[82] Miller, W. J., presented at the Fourteenth Symposium (International) on Combustion, to be published Combustion Institute, (1973).
[83] Spengler, G., and Haupt, G., Erdol. Kohle, Erdgas. Petrochem. **22**, (1969), p. 679.
[84] Bonne, U., Jost, W., and Wagner, H. G., Fire Research Abstracts and Reviews **4**, (1962), p. 6.
[85] Homann, K. H., and Poss, R., Combust. Flame **18**, (1972), p. 300.
[86] Matsuda, S., and Gutman, D., J. Phys. Chem. **75**, (1971), p. 2402.

(Paper 77A6–796)

JOURNAL OF RESEARCH of the National Bureau of Standards—A. Physics and Chemistry
Vol. 77A, No. 6, November–December 1973

The Effect of Temperature and Pressure on the Refractive Index of Some Oxide Glasses

Roy M. Waxler and G. W. Cleek

Institute for Materials Research, National Bureau of Standards, Washington, D.C. 20234.

(August 15, 1973)

The change in refractive index with temperature has been determined for some oxide glasses from about −200 to 700 °C. The change in refractive index with applied hydrostatic pressure has been determined at room temperature from a pressure of 10^5 to 10^8 Pa. All measurements were made using the yellow spectral line of helium. A calcium aluminate glass, an aluminum magnesium phosphate glass, a binary barium borate glass and a multicomponent germanate glass were studied, as were four commercial specimens of fused silica. From the data at room temperature, it has been possible to calculate the change in electronic polarizability with temperature at constant volume. This parameter has been found to be very high for the glasses as compared to crystals, and this agrees with the results of earlier research on silica-based optical glasses. Furthermore, over the entire temperature range, the change of refractive index with temperature is shown to be due predominantly to the temperature dependence at constant volume of the electronic polarizability. The relevance of the data to the molecular scattering of light in glasses is discussed.

Key words: Intermerometry; light scattering; oxide glasses; polarizability; pressure; refractive index; temperature coefficient of refractive index; thermal expansion.

1. Introduction

The dependence of refractive index, n, upon temperature, T, is important in optical design where systems must operate at inconstant temperature or at temperature extremes. The change of refractive index with hydrostatic pressure yields information on change with density which is interesting in itself and is important in elucidating thermo-optic theory because of the change in volume with temperature [1][1].

The thermal coefficient of refractive index has assumed greater practical importance with the advent of the laser because of the thermal lens effect which arises when an optical beam passes through a medium of finite absorption. The resulting temperature rise focuses the beam if the index increases with increasing temperature ($dn/dT > 0$). It has been shown that constraining stresses can cause thermal self-focusing even though the conventional value of ($dn/dT < 0$) [2]. Self-focusing, in general, has attracted much attention, as it is considered a precursor to filamentary damage in laser materials exposed to the high intensities obtained from oscillator-amplifier combinations in Q-switch operations [3].

The data are also of interest because of their relevance to the theory of molecular scattering of light in solids [4]. The theory predicts that the scattering is caused by small changes in the high frequency dielectric constant (or refractive index) that are induced by changes of density and temperature. At the same time, it has been observed that the central Rayleigh line in light scattered from glasses is much greater in intensity than the theory predicts. It was hoped that the basic data to be obtained in this study would help to resolve this problem. Also, to be able to reduce the optical attenuation caused by light scattering in glass would be of great practical interest for the development of optical transmission lines capable of carrying signals over large distances [5]. This might be accomplished by making a glass of the appropriate composition.

Investigations of the thermal change in refractive index and reports on the photoelastic constants for various commercial glasses have been reviewed by Baak [6]. The effect of hydrostatic pressure on refractive index may be calculated from a knowledge of the photoelastic constants. Measurements on the refractive index change resulting from the direct application of hydrostatic pressure have been reported for fused SiO_2 by Vedam et al. [7], and for fused SiO_2 and two commercial glasses by Waxler and Weir [8].

For solid dielectrics, including glasses, it is frequently assumed that dn/dT depends directly upon the temperature-induced change in density, ρ, but not on temperature itself. In fact,

$$\frac{dn}{dT} = \left(\frac{\partial n}{\partial T}\right)_\rho + \left(\frac{\partial n}{\partial \rho}\right)_T \left(\frac{\partial \rho}{\partial T}\right), \tag{1}$$

[1] The figures in brackets indicate literature references at the end of this paper.

520-812 O-LF - 73 - 5

or

$$\frac{dn}{dT}=\left(\frac{\partial n}{\partial T}\right)_{\rho}-\left(\frac{\rho\partial n}{\partial \rho}\right)_{T}(\gamma) \qquad (2)$$

where γ is the coefficient of volume expansion. For most substances, the first term in (2) is much smaller than the second, and dn/dT is essentially equivalent to the second term. It has been found in an earlier study that, for three optical glasses, $(\partial n/\partial T)_{\rho}$ was much larger than expected [8].

In the present study we have measured the effect of both temperature and pressure on the refractive index of some oxide glasses of different compositions and compared the values on glass with data on certain crystalline materials. We have also assessed some of of parameters of interest in optical and laser design. The materials studied were fused silica, a calcium aluminate glass, an aluminum magnesium phosphate glass, a binary barium borate glass, and a multicomponent germanate glass. The batch compositions in weight percent are listed in table 1. In addition, for the purpose of intercomparison, measurements were made on specimens of fused silica produced by Corning Glass Works, Dynasil Corporation of America and the General Electric Company. The brands are identified as Corning Code 7940 fused silica, Dynasil high-purity synthetic fused silica, General Electric Type 104 and General Electric Type 151.[2]

TABLE 1. *Glass batch compositions weight percent*

Oxide	Fused SiO_2	Glass			
		Calcium aluminate F75	Phosphate F1329	Barium borate E1583	Germanate F998
SiO_2	100	5.0			35.9
GeO_2					
B_2O_3				59.0	
P_2O_5			77.7		
Al_2O_3		41.5	12.0		
MgO		5.0	10.3		
CaO		48.5			
BaO				41.0	21.0
BaF_2					5.3
La_2O_3					17.4
Ta_2O_5					3.4
TiO_2					6.1
ZnO					6.2
ZrO_2					4.7

2. Experimental Method

2.1. Change of Index Versus Temperature

The interference method employed by Austin and Pierce [9] offers the attractive features of high precision of measurement and the use of a small specimen, which reduces thermal gradients. The apparatus and experimental technique have been described earlier [10, 11], and will be mentioned only briefly here. Using this method the thermal expansion and thermal change in refractive index can be determined simultaneously.

The index specimen consisted of a small plate about 0.5 cm in thickness with flat, polished faces. The expansion specimen was a small tripod of the same material and thickness which separated two optical flats. For both the index and expansion specimen, a pattern of localized Fizeau-type interference fringes could be seen through a Pulfrich viewer when illuminated with collimated helium light of wavelength 587.6 nm. With change of temperature, a continuous photographic recording of the shift in fringes permitted a simultaneous measurement of the change of thickness, Δt, of the expansion specimen and the change in optical path length, $\Delta(nt)$, of the glass plate. From the photographic recording of the two fringe shifts, it was possible to calculate the change in refractive index, Δn. For the low temperature work, the specimens were enclosed in a cryostat [11] in which liquid nitrogen was used to reduce the temperature, and data were obtained from about +20 to −192 °C. For the high temperature range, the specimens were enclosed in a furnace [10] which permitted measurements from about +20 to +700 °C.

Because of the very low coefficient of thermal expansion of fused silica, no attempt was made to make this measurement (see sec. 3.2). However, for both high and low temperatures, the change in optical path length was measured on four specimens simultaneously, each specimen representing one of the brands mentioned in the introduction.

2.2. Change of Index Vs. Applied Hydrostatic Pressure

The apparatus and technique for finding the change in refractive index with applied hydrostatic pressures to 1×10^8 Pa have been described in previous publications [8, 10]. The same platelet, wavelength and technique of measuring the shift in Fizeau fringes described above was used to find the change in optical path length as a function of pressure. A pressure vessel equipped with glass windows and containing a highly transparent mineral oil was used. Pressure was generated by compressing the oil and was measured with a Heise gage to an accuracy of 1 percent or better. These measurements were made only at room temperature.

The change in thickness of the specimen was calculated from a knowledge of the elastic constants, which are shown in table 2. These constants were determined by an ultrasonic pulse echo technique for Glasses E1583 and F1329. A dynamic resonance technique was used for Glasses F75 and F998. All these measurements on the elastic constants are estimated to have an accuracy of ±2 percent. The change in refractive index with pressure for fused SiO_2 has been previously reported [8] where the compression data of Bridgeman were used, and the elastic constants of fused SiO_2 are not reproduced here.

[2] Commercial materials are identified in this paper to specify the particular substance on which the data were obtained. In no instance does such identification imply recommendation or endorsement by the National Bureau of Standards or that the material identified is necessarily the best for any application.

TABLE 2. *Elastic constants*

	Glass			
	Calcium aluminate F75	Phosphate F1329	Barium borate E1583	Germanate F993
Young's Modulus, E	10.98×10^{10}Pa	5.90×10^{10}Pa	6.54×10^{10}Pa	9.08×10^{10}Pa
Shear Modulus, G	4.25	2.40	2.54	3.55
Bulk Modulus, K	8.79	3.63	5.08	6.78
Poisson's ratio, γ	0.292	0.230	0.290	0.277

3. Results and Discussion

3.1. Stress-Optic Data

The quantity $\rho\frac{\partial n}{\partial\rho}$ was calculated according to the relationship:

$$\rho\frac{\partial n}{\partial\rho}=\left(\frac{1}{B}\right)\left(\frac{dn}{dP}\right) \tag{3}$$

where B is the compressibility. The results are shown in table 3. The dependence of refractive index change upon density can be studied according to the theoretical Lorentz-Lorenz or Drude equations. Following Ramachandran [1], we have chosen the Drude equation:

$$(n^2-1)/4\pi N=\alpha \tag{4}$$

where N is the number of oscillators per unit volume and α is the polarizability. If α were rigorously constant, eq (4) may be differentiated to obtain the change of index with density:

$$\left(\rho\frac{\partial n}{\partial\rho}\right)_{\text{Theor.}}=\frac{n^2-1}{2n}. \tag{5}$$

In eq (5), the subscript, Theor., has been added to the partial derivative to indicate that there may be a change in polarizability which has been neglected. Mueller [12, 1] has introduced the strain polarizability constant, Λ_0, to measure the change in polarizability by means of the relationship:

$$\left(\rho\frac{\partial n}{\partial\rho}\right)=(1-\Lambda_0)\left(\rho\frac{\partial n}{\partial\rho}\right)_{\text{Theor.}} \tag{6}$$

where $\Lambda_0=\left(\frac{\rho}{\alpha}\right)\left(\frac{\partial\alpha}{\partial\rho}\right)$. Values of Λ_0 have been calculated according to the above equations and the results are given in table 3. It can be seen from the table that in every case Λ_0 has a positive value. This decrease in polarizability with increase in density is typical behavior for condensed phases.

The change in refractive index resulting from applied hydrostatic pressure on cubic crystals and glasses is attributed then to two opposing effects: (1) The increase in N, the number of scattering centers per unit volume which always produces an increase, and (2) a contraction of the electronic cloud which affords a decrease in atomic polarizability and the refractive index; this is shown by the positive values of Λ_0. For MgO, diamond, and ZnS, this second effect outweighs the first and these crystals exhibit negative values of $\left(\rho\frac{\partial n}{\partial\rho}\right)$ [13].

3.2. Thermo-Optic Data

For each glass, data on $\Delta t/t$ versus temperature and Δn versus temperature were fitted by computer to a cubic equation of the form $(y)_T-(y)_{T=0}=aT+bT^2+cT^3$, where T is the temperature in °C and t represents the thickness of the specimen at the beginning of the expansion. The parameters in the above equation are given in tables 4 and 5, and hold for a temperature range from −200 °C to an elevated temperature just short of the region of rapid thermal expansion. For convenience of presentation the data were made to have values of zero at 0 °C. The goodness of fit can be judged from the fact that, in every case, the standard deviation of the scatter of points about the fitted curve was no greater than 0.2×10^{-4}. The fitted data were printed out by computer at 10 degree temperature intervals, and the results are presented in tables 6 and 7.

TABLE 3. *Analysis of change in refractive index and polarizability for glasses at wavelength, 587.6 nm*

	n_0	$(dn/dT)\times10^5$	$\gamma\times10^5$	$\rho\frac{\partial n}{\partial\rho}$	$(\partial n/\partial T)_\rho\times10^5$	Λ_0	$P\times10^5$	$Q\times10^5$	$R\times10^5$
Fused SiO_2	1.45846	0.87	0.13	0.32	0.91	0.17	−0.05	0.01	0.91
Calcium aluminate glass, F-75	1.67155	0.75	2.15	0.19	1.16	0.65	−1.2	0.74	1.2
Phosphate glass F-1329	1.48905	0.46	1.48	0.33	0.95	0.19	−0.61	0.12	0.95
Barium borate glass, E-1583	1.5822	−0.11	1.85	0.40	0.63	0.16	−0.88	0.14	0.63
Germanate glass F-998	1.8550	0.86	2.18	0.39	1.71	0.41	−1.4	0.58	1.7

TABLE 4. *Parameters for determining the thermal expansion according to the equation,* $\Delta t/t = aT + bT^2 + cT^3$

Glass	*a*	*b*	*c*
Calcium aluminate F-75	6.82884E-2	6.87984E-5	−5.13289E-8
Phosphate F-1329	4.63538E-2	6.12428E-5	−7.68437E-8
Barium borate E-1583	5.92004E-4	5.20094E-5	−4.05277E-8
Germanate F-998	.0699	5.88163E-5	−3.21704E-8

TABLE 5. *Parameters for determining the change in the refractive index with temperature according to the equation,* $\Delta n = aT + bT^2 + cT^3$

Glass	*a*	*b*	*c*
Fused SiO_2	8.16638E-2	1.04124E-4	−5.59781E-8
Calcium aluminate F-75	6.99293E-2	1.02150E-4	−7.81014E-8
Phosphate F-1329	4.31093E-2	6.17585E-5	−2.17470E-10
Barium borate E-1583	−1.33162E-2	4.75242E-5	1.37501E-10
Germanate F-998	7.94345E-2	1.28399E-4	−8.96982E-8

TABLE 6. *Increase in length per unit length,* $\Delta t/t$ *as a function of temperature*

Temperature °C	Calcium aluminate glass F75	Phosphate glass F1329	Barium borate glass E1583	Germanate glass F998
−200	-10.5×10^{-4}	-6.2×10^{-4}	-9.4×10^{-4}	-11.4×10^{-4}
−190	−10.1	−6.1	−9.1	−10.9
−180	−9.8	−5.9	−8.7	−10.5
−170	−9.4	−5.7	−8.4	−10.0
−160	−9.0	−5.5	−8.0	−9.5
−150	−8.5	−5.3	−7.6	−9.1
−140	−8.1	−5.1	−7.2	−8.5
−130	−7.6	−4.8	−6.7	−8.0
−120	−7.1	−4.5	−6.3	−7.5
−110	−6.6	−4.3	−5.8	−6.9
−100	−6.1	−3.9	−5.4	−6.4
−90	−5.6	−3.6	−4.9	−5.8
−80	−5.0	−3.3	−4.4	−5.2
−70	−4.4	−2.9	−3.9	−4.6
−60	−3.8	−2.5	−3.4	−4.0
−50	−3.2	−2.2	−2.8	−3.3
−40	−2.6	−1.8	−2.3	−2.7
−30	−2.0	−1.3	−1.7	−2.0
−20	−1.3	−0.9	−1.2	−1.4
−10	−0.7	−0.5	−0.6	−0.7
0	0.0	0.0	0.0	0.0
10	0.7	0.5	0.6	0.7
20	1.4	1.0	1.2	1.4
30	2.1	1.4	1.8	2.2
40	2.8	1.9	2.4	2.9
50	3.6	2.5	3.1	3.6
60	4.3	3.0	3.7	4.4
70	5.1	3.5	4.4	5.2
80	5.9	4.1	5.0	6.0
90	6.7	4.6	5.7	6.8
100	7.5	5.2	6.4	7.6
110	8.3	5.7	7.1	8.4
120	9.1	6.3	7.8	9.2
130	9.9	6.9	8.5	10.0
140	10.8	7.5	9.2	10.9
150	11.6	8.1	9.9	11.7
160	12.5	8.7	10.6	12.6
170	13.3	9.3	11.4	13.4

TABLE 6. *Increase in length per unit length, $\Delta l/l$ as a function of temperature*—Continued

Temperature °C	Calcium aluminate glass F75	Phosphate glass F1329	Barium borate glass E1583	Germanate glass F998
180	14.2×10^{-4}	9.9×10^{-4}	12.1×10^{-4}	14.3×10^{-4}
190	15.1	10.5	12.8	15.2
200	16.0	11.1	13.6	16.1
210	16.9	11.7	14.3	17.0
220	17.8	12.3	15.1	17.9
230	18.7	13.0	15.9	18.8
240	19.6	13.6	16.6	19.7
250	20.6	14.2	17.4	20.7
260	21.5	14.8	18.2	21.6
270	22.4	15.5	19.0	22.5
280	23.4	16.1	19.8	23.5
290	24.3	16.7	20.6	24.4
300	25.3	17.3	21.3	25.4
310	26.3	18.0	22.1	26.4
320	27.2	18.6	22.9	27.3
330	28.2	19.2	23.7	28.3
340	29.2	19.8	24.5	29.3
350	30.1	20.4	25.4	30.3
360	31.1	21.0	26.2	31.3
370	32.1	21.6	27.0	32.3
380	33.1	22.2	27.8	33.3
390	34.1	22.8	28.6	34.3
400	35.0	23.4	29.4	35.3
410	36.0	24.0	30.2	36.3
420	37.0	24.6	31.0	37.4
430	38.0	25.1	31.8	38.4
440	39.0	25.7	32.7	39.4
450	40.0	26.3	33.5	40.4
460	41.0	26.8	34.3	41.5
470	42.0	27.3	35.1	42.5
480	43.0	27.9	35.9	43.6
490	43.9	28.4	36.7	44.6
500	44.9	28.9	37.5	45.6
510	45.9	29.4		46.7
520	46.9	29.9		47.7
530	47.9	30.3		48.8
540	48.9			49.8
550	49.8			50.9
560	50.8			51.9
570	51.8			53.0
580	52.7			54.1
590	53.7			55.1
600	54.7			56.2
610				57.2
620				58.3
630				59.3
640				60.4

TABLE 7. *Change in refractive index, (Δn), as a function of temperature at 587.6 nm*

Temperature °C	Fused SiO_2	Calcium aluminate glass F75	Phosphate glass F1329	Barium borate glass E1583	Germanate glass F998
−200	-11.8×10^{-4}	-9.3×10^{-4}	-6.1×10^{-4}	4.6×10^{-4}	-10.0×10^{-4}
−190	−11.6	−9.1	−6.0	4.2	−9.8
−180	−11.3	−8.8	−5.8	3.9	−9.6
−170	−11.0	−8.6	−5.5	3.6	−9.4
−160	−10.7	−8.3	−5.3	3.3	−9.1
−150	−10.3	−7.9	−5.1	3.1	−8.7
−140	−9.8	−7.6	−4.8	2.8	−8.4
−130	−9.3	−7.2	−4.6	2.5	−8.0
−120	−8.8	−6.8	−4.3	2.3	−7.5
−110	−8.2	−6.4	−4.0	2.0	−7.1
−100	−7.6	−5.9	−3.7	1.8	−6.6
−90	−6.9	−5.4	−3.4	1.6	−6.0
−80	−6.2	−4.9	−3.1	1.4	−5.5
−70	−5.5	−4.4	−2.7	1.2	−4.9
−60	−4.8	−3.8	−2.4	1.0	−4.3
−50	−4.0	−3.2	−2.0	0.8	−3.6

TABLE 7. *Change in refractive index, (Δn), as a function of temperature at 0.5876 μm*—continued

Temperature °C	Fused SiO_2	Calcium aluminate glass F75	Phosphate glass F1329	Barium borate glass E1583	Germanate glass F998
−40	-3.2×10^{-4}	-2.6×10^{-4}	-1.6×10^{-4}	0.6×10^{-4}	-3.0×10^{-4}
−30	−2.4	−2.0	−1.2	0.4	−2.3
−20	−1.6	−1.4	−0.8	0.3	−1.5
−10	−0.8	−0.7	−0.4	0.1	−0.8
0	0.0	0.0	0.0	0.0	0
10	0.9	0.7	0.4	−0.1	0.8
20	1.7	1.4	0.9	−0.3	1.6
30	2.5	2.2	1.3	−0.4	2.5
40	3.4	3.0	1.8	−0.5	3.4
50	4.3	3.7	2.3	−0.5	4.3
60	5.3	4.5	2.8	−0.6	5.2
70	6.2	5.4	3.3	−0.7	6.2
80	7.2	6.2	3.8	−0.8	7.1
90	8.2	7.1	4.4	−0.8	8.1
100	9.2	7.9	4.9	−0.9	9.1
110	10.2	8.8	5.5	−0.9	10.2
120	11.2	9.7	6.1	−0.9	11.2
130	12.3	10.6	6.6	−0.9	12.3
140	13.3	11.6	7.2	−0.9	13.4
150	14.4	12.5	7.9	−0.9	14.5
160	15.5	13.5	8.5	−0.9	15.6
170	16.6	14.5	9.1	−0.9	16.8
180	17.8	15.4	9.8	−0.9	17.9
190	18.9	16.4	10.4	−0.8	19.1
200	20.1	17.4	11.1	−0.8	20.3
210	21.2	18.5	11.8	−0.7	21.5
220	22.4	19.5	12.5	−0.6	22.7
230	23.6	20.5	13.2	−0.5	24.0
240	24.8	21.6	13.9	−0.5	25.2
250	26.1	22.6	14.6	−0.4	26.5
260	27.3	23.7	15.4	−0.2	27.8
270	28.5	24.8	16.1	−0.1	29.0
280	29.8	25.9	16.9	0.0	30.3
290	31.1	27.0	17.7	0.1	31.7
300	32.4	28.1	18.5	0.3	33.0
310	33.7	29.2	19.3	0.4	34.3
320	35.0	30.3	20.1	0.6	35.6
330	36.3	31.4	20.9	0.8	37.0
340	37.6	32.5	21.8	1.0	38.3
350	38.9	33.6	22.6	1.2	40.0
360	40.3	34.8	23.5	1.4	41.1
370	41.6	35.9	24.4	1.6	42.4
380	43.0	37.0	25.3	1.8	43.8
390	44.4	38.2	26.2	2.0	45.2
400	45.7	39.3	27.1	2.3	46.6
410	47.1	40.5	28.0	2.5	48.0
420	48.5	41.6	29.0	2.8	49.4
430	49.9	42.7	29.9	3.1	50.8
440	51.3	43.9	30.9	3.3	52.2
450	52.7	45.0	31.9	3.6	53.6
460	54.2	46.2	32.9	3.9	55.0
470	55.6	47.3	33.9	4.3	56.4
480	57.0	48.5	34.9	4.6	57.8
490	58.4	49.6	35.9	4.9	59.2
500	59.9	50.7	37.0	5.2	60.6
510	61.3	51.9	38.0		62.0
520	62.8	53.0	39.1		63.4
530	64.2	54.1	40.2		64.8
540	65.7	55.3			66.2
550	67.1	56.4			67.6
560	68.6	57.5			69.0
570	70.0	58.6			70.4
580	71.5	59.7			71.8
590	72.9	60.8			73.1
600	74.4	61.9			74.5
610	75.9				75.9
620	77.3				77.2
630	78.8				78.6
640	80.2				79.9
650	81.7				

The values of thermal expansion for fused silica were taken from the data of Scheel and Heuse [14] which are recommended by Sosman [15], and are not reproduced in table 3. The data on Δn for fused silica given in table 7 agree with the values of Austin [9, 16] within the experimental error over the entire temperature range. Comparison showed that this same agreement pertained between the data for the four commercial brands of fused silica which have been mentioned in the introduction. An irregularity in the values of Δn in the range from 500 to 600 °C, which has been reported by several authors [17, 18, 19, 20] was not observed in this study nor in the research of Austin [16].

It can be seen in table 3 that for fused silica

$$\frac{dn}{dT}=0.87\times10^{-5}$$

at 25 °C. This agrees exactly with the value reported by Schott and Gen. [21], and there is very close agreement with the value of 0.85×10^{-5} calculated from the equation given by Austin and Pierce [9]. However, higher values have been found by other workers; both Tilton and Tool [22] and Rodney and Spindler [23] reported a value of 0.99×10^{-5}, and Malitson [24] reported 1.0×10^{-5}; a value of 1.08×10^{-5} was reported by Prod'homme [25].

Considering this quantity, (dn/dT), at room temperature, it has been found that some crystals exhibit negative values while others have an increase in refractive index with increase in temperature [1]. These latter crystals are the very ones which exhibit negative values of $(\rho\,\partial n/\partial\rho)$, i.e., MgO, diamond, and ZnS, so that with change of temperature, the attendant change in density is still of paramount importance. The sign of dn/dT depends on whether the contribution from change in N or the change in polarizability caused by density change predominates. However, earlier data on a few glasses indicate that, for these solids, both $(\rho\,\partial n/\partial\rho)$ and (dn/dT) are positive [8]. In table 3, room temperature values of n_0, dn/dT, γ and $\rho\,\partial n/\partial\rho$ are given, as are values of $(\partial n/\partial T)_\rho$, which have been calculated from eq (2).

Starting with the Drude equation, Ramachandran [1] has shown that dn/dT consists of the sum of three independent contributions which he labels P, Q, and R. P is dependent only on change of density and arises from the change in the number of scattering centers, Q denotes the change in polarizability caused by change in density, and R represents the change in polarizability arising from temperature change alone. The equations are:

$$P=-\gamma\left(\frac{n^2-1}{2n}\right) \tag{7}$$

$$Q=-\gamma\left[\rho\frac{\partial n}{\partial\rho}-\frac{n^2-1}{2n}\right] \tag{8}$$

$$R=dn/dT+\gamma\frac{\rho\,\partial n}{\partial\rho}. \tag{9}$$

Values of P, Q, and R for the five glasses have been determined and are shown in table 3. It can be seen that P is always negative, reflecting the lessening in the number of scattering centers with rise in temperature. Values of P and Q for fused silica are very small because of the very small coefficient of thermal expansion. It can also be seen that R is positive and is significantly larger than Q in all cases, indicating that the change in polarizability is largely dependent solely on temperature change; this is not true for crystals where R may be of either sign and is always smaller than Q [1].

Polarizability is the fundamental optical property and in comparing the thermo-optic properties of different materials, it is necessary to compare values of Λ_0, γ, and τ_0, where $\tau_0=\frac{1}{\alpha}\left(\frac{\partial\alpha}{\partial T}\right)_\rho$ is the temperature coefficient of polarizability. Ramachamdran has shown that the change in polarizability with temperature can be written as

$$\alpha_T=\alpha_0[1+\Lambda_0\gamma T+\tau_0 T] \tag{10}$$

and that

$$\frac{dn}{dT}=\frac{n^2-1}{2n}\,[-\gamma+\Lambda_0\gamma+\tau_0]. \tag{11}$$

Calculations of Λ_0 and τ_0 for the glasses of the present study may be made from the entries of table 3 according to the equations

$$\Lambda_0=-Q/P \tag{12}$$

and

$$\tau_0=-R\gamma/P. \tag{13}$$

Values of Λ_0, $\Lambda_0\gamma$, τ_0, and τ_0/γ have been listed in table 8 where corresponding values for cubic crystals studied in this laboratory have also been listed for comparison. In the case of the cubic crystals, Ramachandran has noted that τ_0 is much smaller than $\Lambda_0\gamma$ indicating that the change in polarizability, due to the pure temperature effect, is much smaller than that due to a change in the lattice parameter. It can be seen from the table that, for the five glasses, the relative importance of the two contributions is reversed. For the glass systems studied here, it is apparent that the polarizability is essentially dependent upon temperature change at constant density. The same conclusion can be drawn on considering the column of figures for Λ_0 and τ_0/γ. This distinctive property of glasses is brought out explicitly here from measurements on change of refractive index caused by changes of pressure and temperature, although it had been inferred by Ramachandran from a study restricted to thermo-optic data alone over an extended temperature range [26].

Primak and Post have attributed this great dependence of polarizability to the strained bond configuration of the oxygen ions in the glasses [27]. Ramachandran has inferred that this effect is associated with a band edge shift of the ultraviolet frequencies toward lower energy with increase of temperature that is also essentially independent of change in lattice parameter [26]. This idea of Ramachandran has been

TABLE 8. *Strain and temperature coefficients of polarizability for glasses and crystals*

	$\Lambda_0\gamma \times 10^5$	$\tau_0 \times 10^5$	Λ_0	τ_0/γ
Fused SiO_2	0.02	2.4	0.17	18.2
Calcium aluminate glass, F–75	1.4	2.2	0.65	1.0
Phosphate glass F–1329	0.28	2.4	0.19	1.6
Barium borate glass, E–1583	0.30	1.3	0.16	0.72
Germanate glass F–998	0.89	2.6	0.41	1.2
LiF	6.3	0.0	0.62	0.0
NaCl	4.6	−0.89	0.38	−0.07
KCl	2.6	0.24	0.23	0.02
KBr	2.9	1.3	0.24	0.11
CaF_2	2.5	0.0	0.43	0.0
MgO	6.0	0.68	1.53	0.17

extended by more recent studies [28, 29]: Apparently, the lack of long-range order and the random molecular structure in glass induces a broadening of the exitonic levels and a tail on the ultraviolet absorption edge, which varies exponentially with energy [28].

From the present study which includes an aluminate, phosphate, borate and germanate glass, it is inferred that this iso-volume effect is an important additional consideration in understanding the thermo-optic behavior of all glasses as distinguished from crystals. However, more glass systems should be studied, and it is recognized at the outset that for each particular glass (as for a crystal) there are important unique considerations of internal structure, i.e., whether the atoms are arranged in the form of chains or rings or sheets.

The data reported in tables 6 and 7 has been terminated just before the region of rapid expansion in the glass. However, it is interesting to consider the course of the refractive index curve and the thermal expansion curve over the whole range of temperatures up to the softening point. The barium borate glass, E1583, has been selected as being representative of the others, and curves for thermal expansion and change in refractive index for this glass are shown in the lower part of figure 1. There is a minimum in the refractive index curve around 150 °C, which behavior is typical of optical glass. Molby has reported on several optical glasses where dn/dT was initially negative and then became positive with rise in temperature [30]. The barium borate glass of this study is distinctive in that the minimum value is so high, most of the glasses reported by Molby had must lower minimum values, usually well below 0 °C. No minimum in refractive index was noted for the remaining glasses of this study, but the data indicate that all of them are approaching minimum values at the lowest temperatures.

From the figure, it can be seen that dn/dT diminishes rapidly and then becomes negative as the temperature increases through the region of rapid thermal expansion. This dip in the refractive index curve is interpreted as resulting from the large decrease in the number of scattering centers per unit volume.

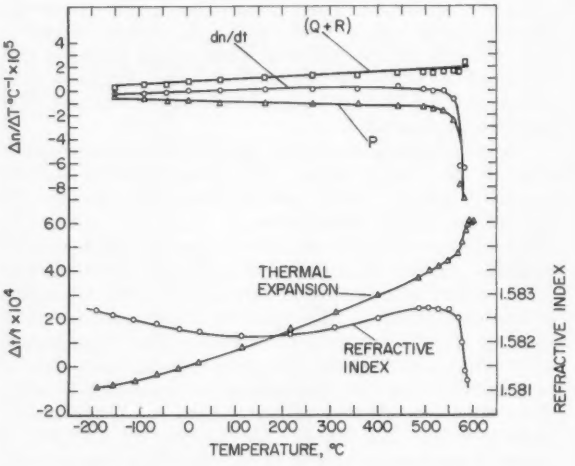

FIGURE 1. *Analysis of the thermo-optical behavior of barium borate glass, E1583.*

Because measurements were made at specific temperature intervals, it is possible to make some analysis of dn/dT over the entire temperature range following the earlier treatment of dividing dn/dT into contributions, P, Q, and R. However, the treatment must be limited to values of P and $(Q+R)$ because measurements of the change in refractive index caused by applied hydrostatic pressure were restricted to room temperature. Calculations have been made and curves denoting dn/dT, P and $(Q+R)$ are shown in the upper part of figure 1. It can be seen that P and $(Q+R)$ are of opposite sign and that dn/dT is the sum of the two.

Because of the opposite sign, the sum is small until the region of rapid expansion is reached, whereupon dn/dT largely follows the course of P. An important

point to be made is that $(Q+R)$ is nearly a straight line over the entire temperature range. This would imply that R must be significantly greater than Q over the whole range, because Q itself depends on change in density. Another point to be made is that $(Q+R)$ appears to approach zero at the lowest temperatures, which had been predicted by Ramachandran on the basis of thermo-optic behavior of glasses at higher temperatures [26].

3.3. Relevance of the Data to the Molecular Scattering of Light

As mentioned in the introduction, small changes in refractive index caused by changes of density and temperature account for the molecular scattering of light in transparent materials [4]. The theoretical formulations are usually expressed in terms of the optical dielectric constant, ϵ, where $\epsilon = n^2$. In both the well-known Einstein-Smoluchowski and Landau-Placzek formulations, the quantity $(\partial\epsilon/\partial T)_\rho$, has been treated as being negligibly small, but Fabelinskii [31] has developed an exact equation for the intensities of scattered light which includes the quantity $(\partial\epsilon/\partial T)_\rho$. O'Connor and Schlupf [32] have presented equations for the transformation of variables, so that the input parameters of the theoretical equations may be calculated from the refractive index data of this paper. Because $(\partial\epsilon/\partial T)_\rho = 2n(\partial n/\partial T)_\rho$ and we have found $(\partial n/\partial T)_\rho$ to be very high (see table 3), it was thought that this neglected factor could account for the fact that the intensity of light scattered from optical glasses greatly exceeds theoretical predictions [33]. However, calculations showed that it was not possible to account for the experimental data of fused SiO_2 [34] by inserting parameters determined from this report.

It was concluded that, because glass is unstable thermodynamically, a theoretical formulation based on equilibrium conditions would be inadequate to account for the observed effects. Indeed, the current theory of light scattering in glass attributes the high intensity of the central Rayleigh line to nonpropagating density and composition fluctuations that are frozen into the melt as it is cooled through the transition range [35, 36, 37, 38]. The frozen-in density flucutations affect the intensity through the parameter, $(\rho\,\partial\epsilon/\partial\rho)$, and $(\rho\,\partial\epsilon/\partial\rho) = (2n\,\rho\,\partial n/\partial\rho)$. It can be seen from table 3 that there are significant differences in values of $(\rho\,\partial n/\partial\rho)$. Although composition fluctuations would remain a problem, the point may be made here that $(\rho\,\partial n/\partial\rho)$ could be reduced to zero or some other low value by the proper adjustment of glass composition. This same point has been made before for the elimination of electrostriction in laser glasses [39], which phenomenon also manifests itself through the parameter $(\rho\,\partial\epsilon/\partial\rho)$.

4. References

[1] Ramachandran, G. N., in Progress in Crystal Physics, Volume **1**, edited by Krishnan, R. S., (Interscience Publishers, New York, London, 1958), pp. 139–167.
[2] Zverev, G. M., and Pashkov, V. A., Zh. Eksperim i. Teor. Fiz. Pis'ma Redaktsiyu **57**, 1128 [Soviet Phys.–JETP, **30**, 616 (1970)].
[3] Feldman, A., Horowitz, D., and Waxler, R. M. (to be published).
[4] Fabelinskii, I. L., Molecular Scattering of Light, (Plenum Press, New York, 1968).
[5] Schroeder, J., Mohr, R., Montrose C. J., and Macedo, P. B. (to be published).
[6] Bååk, T., Optics Athermalization, Report No. 8744, Systems Engineering Group, Research and Technology Division, Air Force Systems Command, USAF Wright-Patterson Air Force Base, Ohio (1967).
[7] Vedam, K., Schmidt, E. D. D., and Roy, R., J. Am. Ceram. Soc. **49**, 531 (1966).
[8] Waxler, R. M., and Weir, C. E., J. Res. Nat. Bur. Stand. (U.S.), **69A** (Phys. and Chem.), No. 4, 325 (July–Aug. 1965).
[9] Austin, J. B. and Pierce, R. H. H., Jr., Physics **6**, 43 (1935).
[10] Waxler, R. M., Cleek, G. W., Malitson, I. H., Dodge, M. J. and Hahn, T. A., J. Res. Nat. Bur. Stand. (U.S.), **75A** (Phys. and Chem.), No. 3, 163 (May–June 1971).
[11] Waxler, R. M. and Cleek, G. W., J. Res. Nat. Bur. Stand. (U.S.), **75A**, (Phys. and Chem.), No. 4, 279 (July–Aug. 1971).
[12] Mueller. H., Physics **6**, 179 (1935).
[13] Vedam, K. and Ramaseshan, S., in Progress in Crystal Physics, Volume I, edited by Krishnan, R. S. (Interscience Publishers, New York, London, 1958), pp. 102–138.
[14] Scheel, K. and Heuse, W., Verh. Deutsch, Physik, Ges. **16**, 1–3 (1914).
[15] Sosman, R. B., The Properties of Silica, (Chemical Catalog Co., New York, 1927), pp. 403–406.
[16] Austin, J. B., Physics **3**, 240 (1932).
[17] Rinne, F., Nues Jahrb, Mineral, Beil. **39**, 388 (1914).
[18] See Reference 15, p. 687.
[19] Chandrasekhar, S. Proc. Indian Acad. Sci. **A34**, 275 (1951).
[20] Narayanan, P. S., Proc. Indian Acad. Sci. **A35**, 9 (1953).
[21] See reference 6, p. 114.
[22] Tilton, L. W. and Tool, A. Q., J. Res. Nat. Bur. Stand. (U.S.), **3**, 619 (1929) RP112.
[23] Rodney, W. S. and Spindler, R. J., J. Res. Nat. Bur. Stand. (U.S.), **53**, No. 3, 185 (Sept. 1954).
[24] Malitson, I. H., J. Opt. Soc. Am. **55**, No. 10, 1205 (1965).
[25] Prod'homme, L., Phys. and Chem. of Glasses **1**, No. 4, 119 (1960).
[26] Ramachandran, G. N., Proc. Indian Acad. Sci. **25A**, 498 (1947).
[27] Primak, W. and Post, D., J. App. Phys. **30**, No. 5, 779 (1959).
[28] Dow, J. D. and Redfield, D., Phys. Rev. Letters **26**, No. 13, 762 (1971).
[29] Wood, D. L. and Tauc, J., Phys. Rev. B **5**, No. 8, 3144 (1972).
[30] Molby, F. A., J. Opt. Soc. Am. **39**, 600 (1949).
[31] See reference [4], p. 96.
[32] O'Connor, C. L. and Schlupf, J. P., J. Chem. Phys. **47**, No. 1, 31 (1967).
[33] See reference [4], Chapter VII.
[34] Flubacher, P., Leadbetter, A. J., Morrison, J. A. and Stoicheff, B. P., Int. J. Phys. Chem. Solids **12**, 53 (1960).
[35] Mueller, H., Proc. Roy. Soc. A, **166**, 425 (1938).
[36] Maurer, R. D., J. Chem. Phys. **25**, 1206 (1956).
[37] Pinnow, D. A., Candau, S. J., La Macchia, J. T. and Litovitz, T. A., J. Acoust. Soc. Am. **43**, 131 (1968).
[38] Mohr, R., Schroeder, J., Macedo, P. B. and Montrose, C. J., J. Am. Ceram. Soc. (to be published).
[39] Waxler, R. M., IEEE J. Quantum Electron, QE–7, 166 (1971).

(Paper 77A6–797)

JOURNAL OF RESEARCH of the National Bureau of Standards—A. Physics and Chemistry
Vol. 77A, No. 6, November-December 1973

Publications of the National Bureau of Standards*

Citations with Selected Abstracts

Monogr. 126. **Platinum resistance thermometry,** J. L. Riddle, G. T. Furukawa, and H. H. Plumb, Nat. Bur. Stand. (U.S.), Monogr. 126, 129 pages (Apr. 1973) $2.10, SD Catalog No. C13.44:126.

Key words: Calibration; calibration errors; cryostat; fixed points; freezing point; International Practical Temperature Scale; platinum resistance thermometer; Thermodynamic Temperature Scale; thermometry; triple point.

The monograph describes the methods and equipment employed at the National Bureau of Standards for calibrating standard platinum resistance thermometers (SPRT) on the International Practical Temperature Scale (IPTS-68). The official text of the scale is clarified and characteristics of the scale are described. Several designs of SPRT's are shown and discussed in the light of the requirements and recommendations on the text of the IPTS-68. Possible sources of error such as those due to the internal and external self-heating effects and the immersion characteristics of SPRT's are described in detail. Precautions and limitations for the mechanical and thermal treatment and for the shipment of SPRT's are indicated, and a guide is given for those desiring the thermometer calibration services of NBS. The description of equipment employed at the National Bureau of Standards for maintaining the IPTS-68 includes the triple point of water cell, tin point cell, zinc point cell, oxygen normal boiling point comparison cryostat, the 13 to 90 K comparison cryostat, and the reference SPRT's upon which the NBS- IPTS-68 in the region 13 to 90 K is based. Methods are given for calculating temperatures from the calibration data and observed resistances; the propagation of calibration errors is discussed. Supplemental information given in the Appendixes includes the authorized English version of the text of the IPTS-68, tabular values of the "reference function" used below 0 °C, tabular values of the differences between IPTS-68 and IPTS-48, analysis of the first derivatives at 0 °C of the IPTS-68 formulations, methods for calibrating potentiometers and Mueller bridges, and the derivation of the coefficients used in the analysis of error propagation.

SP260, 1973 Edition. **Standard reference materials 1973 catalog,** Nat. Bur. Stand. (U.S.), Spec. Publ. 260-1973 catalog, 96 pages (Apr. 1973) $1.25, SD Catalog No. C13.10:260-1973 cat.

Key words: Analysis; characterization, composition; General Materials; properties; Research Materials; Standard Reference Materials.

This Catalog lists and describes the Standard Reference Materials (SRM's), Research Materials (RM's), and General Materials (GM's) currently distributed by the National Bureau of Standards, as well as many of the materials currently in preparation. SRM's are used to calibrate measurement systems and to provide a central basis for uniformity and accuracy of measurement. The unit and quantity, the type, and the certified characterization are listed for each SRM, as well as directions for ordering. The RM's are not certified, but are issued to meet the needs of scientists engaged in materials research. RM's are issued with a "Report of Investigation," the sole authority of which is the author of the report. The GM's are standardized by some other agency other than NBS. NBS acts only as a distribution point and does not participate in the standardization of these materials. Announcements of new and renewal SRM's, RM's, and GM's are made in the semi-annual supplements to this Catalog, SRM Price and Availability List, the NBS Technical News Bulletin, and in scientific and trade journals. Supersedes NBS Special Publication 260, 1970 Edition.

SP378. **Accuracy in spectrophotometry and luminescence measurements,** *Proc. Conf. held at the National Bureau of Standards, Gaithersburg, Md., Mar. 22-24, 1972,* R. Mavrodineanu, J. I. Shultz, and O. Menis, Editors, Nat. Bur. Stand. (U.S.), Spec. Publ. 378, 268 pages (May 1973) $4.85, SD Catalog No. C13.10:378.

Key words: Accuracy; critical parameters; instrumentation; linearity; quantum efficiency; spectrofluorometry; spectrophotometry; standards.

This volume contains the 18 papers presented at the Conference on Accuracy in Spectrophotometry and Luminescence Measurements organized by the Analytical Chemistry Division of the National Bureau of Standards and held from March 22 to 24, 1972.

These papers discuss the problems encountered in accurate spectrophotometry and luminescence measurements of materials. They also define the status of these competences from the standpoint of basic principles, critical factors involved in the measurements, and the instrumenta conditions which must be fulfilled to assure accurate measurements. Particular attention is given to the selection, production and use of Standard Reference Materials in spectrophotometry and spectrofluorometry. Problems related to health are also covered in six of the papers, two of which include original contributions to the application of luminescence techniques to specific biochemical problems.

Reprinted from the National Bureau of Standards Journal of Research, Section A. Physics and Chemistry, Vol. 76A, Nos. 5 and 6, Sept.-Oct., and Nov-Dec. 1972.

SP379. **Report of the 57th National Conference on Weights and Measures 1972,** F. C. Bell and H. F. Wollin, Report Editors, Nat. Bur. Stand. (U.S.), Spec. Publ. 379, 216 pages (May 1973) $1.85, SD Catalog No. C13.6/3:379.

AMS63. **Tables of two-associate-class partially balanced designs,** W. H. Clatworthy, J. M. Cameron, and J. A. Speckman, Nat. Bur. Stand. (U.S.), Appl. Math. Ser. 63, 327 pages (May 1973) $3.45, SD Catalog No. C13.32:63.

NSRDS-NBS43. **Selected specific rates of reactions of transients from water in aqueous solution. 1. Hydrated electron,** M. Anbar, M. Bambenek, and A. B. Ross, Nat. Stand. Ref. Data Ser., Nat. Bur. Stand. (U.S.), 43, 67 pages (May 1973) 90 cents, SD Catalog No. C13.48:43.

Key words: Aqueous solution; chemical kinetics; data compilation; hydrated electron; radiation chemistry; rates.

Rates of reactions of hydrated electrons with over 700 different organic and inorganic molecules, ions, and transients have been tabu-

lated. Most of the data are derived from pulse radiolysis of aqueous solutions; results from photolysis and from steady-state radiolysis by competition kinetics are also included.

FIPS PUB 3-1. **Recorded magnetic tape for information exchange (800 CPI, NRZI),** P. S. Johnson, Standards Coordinator, Nat. Bur. Stand. (U.S.), Fed. Info. Process Stand. Publ. (FIPS PUB) 3-1, 4 pages (1973) 20 cents, SD Catalog No. C13.52:3-1.

Key words: Communications; computers; computer system hardware; data processing; data processing equipment; information systems; magnetic tape recording; magnetic tapes; magnetic tape transports; standards.

This standard specifies the recorded characteristics of 9-track, one-half inch wide magnetic computer tape, including the data format for implementing the Federal Standard Code for Information Interchange at the recording density of 800 characters per inch (CPI). It is one of a series of Federal Standards implementing the Federal Standard Code for Information Interchange (FIPS 1) on magnetic tape media. This revision to FIPS PUB 3 reflects a change in scope from the earlier version of X3.22-1967, and encompasses the recorded tape requirements only. The unrecorded tape standard will include the requirements for the physical properties of the tape and reels that were previously included in FIPS 3. Supersedes NBS FIPS PUB 3.

FIPS PUB 24. **Flowchart symbols and their usage in information processing,** M. Keplinger, Standards Coordinator, Nat. Bur. Stand. (U.S.), Fed. Info. Process. Stand. Publ. (FIPS Pub.) 24, 4 pages (1973) 20 cents, SD Catalog No. C13.52:24.

FIPS PUB 25. **Recorded magnetic tape for information interchange (1600 CPI, phase encoded),** P. S. Johnson, Standards Coordinator, Nat. Bur. Stand. (U.S.), Fed. Info. Process Stand. Publ. (FIPS PUB) 25, 4 pages (1973) 20 cents, SD Catalog No. C13.52:25.

Key words: Communications; computers; computer systems hardware; data processing; data processing equipment; information systems; magnetic tape recording; magnetic tapes; magnetic tape transports; standards.

This standard specifies the recorded characteristics of 9-track, one-half inch wide magnetic computer tape, including the data format for implementing the Federal Standard Code for Information Interchange at the recording density of 1600 characters per inch (CPI). It is one of a series of Federal Standards implementing the Federal Standard Code for Information Interchange (FIPS 1) on magnetic tape media.

FIPS PUB 27. **Take-up reels for one-inch perforated tape for information interchange,** P. S. Johnson, Standards Coordinator, Nat. Bur. Stand. (U.S.), Fed. Info. Process Stand. Publ. (FIPS PUB) 27, 4 pages (1973) 20 cents, SD Catalog No. C13.52:27.

Key words: Data processing; Federal Information Processing Standard; information interchange; information processing; paper tape; paper perforator tape.

This standard specifies the physical dimensions of paper tape take-up (or storage) reels, with either fixed or separate flanges. The two types of reels specified differ in the size and shape of the drive hub, but both are intended for use with one-inch perforated paper tape devices.

TN594-5. **Optical Radiation Measurements: Stability and temperature characteristics of some silicon and selenium photodetectors,** K. Mohan, A. R. Schaefer, and E. F. Zalewski, Nat. Bur. Stand. (U.S.), Tech. Note 594-5, 16 pages (June 1973) 35 cents, SD Catalog No. C13.46:594-5.

Key words: Fatigue; light memory; photocells; photodiodes; photometry; radiometry; selenium; silicon; stability; temperature dependence.

This paper describes the comparison of some characteristics of selenium barrier layer photocells and silicon PIN and PN type photodiodes operated in the photovoltaic or nonbiased mode. The work was done to study the suitability of these detectors specifically for goniometric measurements of flux and possibly for other photometric (or radiometric) measurements. The characteristics studied were the stability of detector output over approximately twenty hours, fatigue or light memory effects over short periods of time, and the temperature dependence of detector output.

TN620. **Frequency and phase stabilization of an HCN laser by locking to a synthesized reference,** J. S. Wells and D. Halford, Nat. Bur. Stand. (U.S.), Tech. Note 620, 56 pages (May 1973) 60 cents, SD Catalog No. C13.46:620.

Key words: Fast linewidth; frequency noise; HCN laser; infrared frequency synthesis; laser frequency measurements; laser linewidth; laser stabilization; phase locked laser.

Infrared frequencies as high as 88 THz have recently been synthesized using diode harmonic mixers with accuracies of parts in 10^9. Stabilized lasers are needed to make frequency measurements of higher accuracy. The HCN laser is the lowest frequency basis laser used in these synthesis schemes and its stabilization has been the subject of recent interest. The laser is stabilized by locking it to a phase locked microwave reference chain. Two servo loops are utilized. The first loop is a relatively slow frequency lock loop with the correction applied to a PZT driver. This loop not only accommodates thermal expansion of the laser, but also serves as an acquisition aiding loop for the second servo. The latter is a phase locked system with the correction applied to the laser discharge current.

Details of the laser design and some noise considerations relative to the microwave reference chain are presented along with some experimental data which indicate the results of the stabilization techniques. Data regarding the system stability and improved fast linewidth are included.

TN635. **Some applications of cryogenics to high speed ground transportation,** V. C. Arp, A. F. Clark, and T. M. Flynn, Nat. Bur. Stand. (U.S.), Tech. Note 635, 29 pages (Feb. 1973) 35 cents, SD Catalog No. C13.46:635.

TN637. **Theory of UHF and microwave measurements using the power equation concept,** G. F. Engen, Nat. Bur. Stand. (U.S.), Tech. Note 637, 68 pages (Apr. 1973) 70 cents, SD Catalog No. C13.46:637.

Key words: Microwave measurements; power equation; power measurement; terminal invariant.

Theoretical considerations indicate that, in addition to other advantages, UHF and microwave measurements based on the power equation concept should exhibit reduced sensitivity to certain connector imperfections. This has now been experimentally confirmed in a number of laboratories, and interest in these methods is increasing. The previously described measurement techniques, for implementing this concept, have relied heavily upon tuning procedures, while current trends are towards automation where tuning is impractical if not impossible.

By assuming a phase detection capability (such as is found in automated systems) it is possible to eliminate the tuning requirement. Moreover, this generalization has made it possible to summarize the earlier results in a compact form. In addition, this paper includes a number of new measurement ideas.

It is expected that this report will serve as a major reference in the continuing development of detailed measurement procedures which exploit the power equation concept.

TN710-7. **Building research translation- Weak thermal points or thermal bridges,** J. Berthier, Nat. Bur. Stand. (U.S.), Tech. Note 710- 7, 96 pages (May 1973) $1.25, SD Catalog No. C13.46:710-7.

TN772. **A performance comparison of labeling algorithms for calculating shortest path trees,** J. Gilsinn and C. Witzgall, Nat. Bur. Stand. (U.S.), Tech. Note 772, 92 pages (May 1973) $1.25, SD Catalog No. C13.46:772.

TN773. **Methods of measurement for semiconductor materials, process control, and devices. Quarterly report, October 1 to December 31, 1972,** W. M. Bullis, Ed., Nat. Bur. Stand. (U.S.), Tech. Note 773, 56 pages (June 1973) 80 cents, SD Catalog No. C13.46:773.

Key words: Base transit time; carrier lifetime; delay time; die attachment; electrical properties; electronics; epitaxial silicon; four-probe method; generation centers; germanium; gold-doped silicon; infrared response; methods of measurement; microelectronics; microwave diodes; probing techniques (a-c); pull test; recombination centers; resistivity; resistivity standards; semiconductor devices; semiconductor materials; semiconductor process control; silicon; S-parameters; switching transients; thermal resistance; thermally stimulated measurements; trapping centers; wire bonds.

This quarterly progress report, eighteenth of a series, describes NBS activities directed toward the development of methods of measurement for semiconductor materials, process control, and devices. Significant accomplishments during this reporting period include (1) completion of the investigation of the effects of current, probe force, and surface condition on the measurement of resistivity of bulk silicon wafers by the four-probe method, (2) establishment of operating conditions appropriate for determining the sensitivity of transient thermal response measurements to voids in transistor die attachment, and (3) initiation of an interlaboratory comparison of transistor scattering parameter measurements. Because of the general applicability of the first of these, details are presented in a separate appendix. Work is continuing on measurement of resistivity of semiconductor crystals; characterization of generation-recombination-trapping centers in silicon; study of gold-doped silicon; development of the infrared response technique; evaluation of wire bonds and die attachment; measurement of thermal properties of semiconductor devices; determination of S-parameters, delay time, and related carrier transport properties in junction devices; development of a-c probing techniques; and characterization of noise and conversion loss of microwave detector diodes. Supplementary data concerning staff, standards committee activities, technical services, and publications are included as appendices.

TN774. **Fire service location-allocation models,** D. Colner and D. Gilsinn, Nat. Bur. Stand. (U.S.), Tech. Note 774, 46 pages (June 1973) 75 cents, SD Catalog No. C13.46:774.

Key words: Algorithms; fire station location; heuristics; location-allocation models; location analysis; resource allocation analysis; transportation network analysis.

This paper compiles the various types of location-allocation models which analyze the impact of varying the number and location of fire stations. The assumptions of each model, the relationships between models, and possible heuristics and algorithms are discussed. In addition, a methodology of spatial concepts analogous to those used in transportation planning is presented.

TN776. **A new method for generating waterdrops of specified mass,** J. E. Potzick, Nat. Bur. Stand. (U.S.), Tech. Note 776, 12 pages (May 1973) 35 cents, SD Catalog No. C13.46:776.

Key words: Drop generator; liquid drop; waterdrop.

A waterdrop generator has been constructed, based on the mechanical resonance of a vibrating waterdrop, which can generate drops of 1.5 to 37 mg with standard deviations in the range of 0.1 percent to 10 percent of drop mass. Drop mass over this range and drop interval are remotely controlled.

TN778. **Guidelines for selection of and use of foam polyurethane roofing systems,** W. C. Cullen and W. J. Rossiter, Jr., Nat. Bur. Stand. (U.S.), Tech. Note 778, 46 pages (May 1973) 75 cents, SD Catalog No. C13.46:778.

TN780. **Controlled accessibility bibliography,** S. K. Reed and M. M. Gray, Nat. Bur. Stand. (U.S.), Tech. Note 780, 15 pages (June 1973) 35 cents, SD Catalog No. C13.46:780.

TN781. **A study of six university-based information systems,** B. Marron, E. Fong, D. W. Fife, and K. Rankin, Nat. Bur. Stand. (U.S.), Tech. Note 781, 98 pages (June 1973) $1.25, SD Catalog No. C13.46:781.

TN787. **Heuristic cost optimization of the Federal Telpak network,** R. G. Saltman, G. R. Bolotsky, and Z. G. Ruthberg, Nat. Bur. Stand. (U.S.), Tech. Note 787, 52 pages (June 1973) 80 cents, SD Catalog No. C13.46/787.

This column lists all outside publications by the NBS staff, as soon after issuance as practical. For completeness, earlier references not previously reported may be included from time to time.

Adler, A., Kahan, W., Novick, R., Lucatorto, T., **Measurement of the lifetime and the electron-impact excitation cross section and polarization of the 2^3P term of singly ionized lithium,** *Phys. Rev. A* **7,** No. 3, 967-872 (Mar. 1972).

Key words: Electron-excitation cross section; lifetime; rf resonance spectroscopy; 2^3P term of Li^+.

The lifetime of the $2\ ^3P_J$ states in singly ionized lithium has been measured using an rf magnetic-resonance technique; the value is $\tau = 45\,1\,5$ nsec. Neutral lithium was ionized and excited by a unidirectional beam of electrons which produced an alignment in the excited state. The cross section for the electron-impact excitation $ls^2\,2s\ ^3S \rightarrow ls2p\ ^3P$ near the threshold was measured to be $10^{-22\,\pm\,1}$ cm^2. Implications for the feasibility of rf resonance spectroscopy on the fine and hyperfine structure of the 2^3P term will be discussed.

Artru, M-C., Kaufman, V., **Re-evaluation of parameters for even configurations of triply ionized magnesium,** *J. Opt. Soc. Amer.* **63,** No. 4, 449-450 (Apr. 1973).

Key words: Magnesium; source; spectra; ultraviolet; wavelengths.

In a previous publication, HF values for $2p^4\,3s \leftrightarrow 2p^4\,3d$ interaction parameters were misinterpreted. Correct HF values for these parameters have been used in a new calculation of these configurations.

Baker, M. A., **Weatherability of porcelain enamels,** (Proc. Aluminum Finishing Seminar, Chicago, Ill., Mar. 19-21, 1973), Paper C12 in *Applied Session: Technical Papers,* pp. C12-1 – C12-16 (The Aluminum Ass., New York, N.Y., Mar. 1973).

Key words: Color; gloss; porcelain enamel on aluminum; weather resistance.

An exposure text of porcelain enamels on aluminum was initiated by the National Bureau of Standards and the Porcelain Enamel Institute in 1964. The enameled specimens were returned from exposure sites at Kure Beach, N.C.; Washington, D.C.; New York, N.Y.; Montreal, Canada; and Los Angeles, Calif., to the laboratory at NBS to be measured for changes in gloss and color after 6 months, and 1, 3, and 5 years' exposure. The 5-year data indicate no change in enamel thickness and good color retention at all sites except Kure Beach.

Barger, R. L., Sorem, M. S., Hall, J. L., **Frequency stabilization of a cw dye laser,** *Appl. Phys. Lett.* **22,** No. 11, 573-575 (June 1, 1973).

Key words: Dye lasers; laser frequency stabilization; saturated absorption.

A cw dye laser system frequency stabilized to a high-finesse optical reference cavity is described. Laser frequency is servo controlled to the cavity resonance with residual fluctuations less than 50 kHz for short times (20 μsec) and 100 Hz for long times (10 sec). Drift in absolute laser frequency of about 1.5 MHz/min is observed due to drift of the unstabilized reference cavity. A saturated absorption spectrum of I_2 obtained with this system is shown.

Barnes, I. L., Garner, E. L., Gramlich, J. W., Moore, L. J., Murphy, T. J., Machlan, L. A., Shields, W. R., Tatsumoto, M., Knight, R. J., **Determination of lead, uranium, thorium, and thallium in silicate glass standard materials by isotope dilution mass spectrometry,** *Anal. Chem.* **45,** No. 6, 880-885 (May 1973).

Bennett, J. A., Mindlin, H., **Metallurgical aspects of the failure of the Point Pleasant bridge,** *J. Test. Eval.* **1,** No. 2, 152-161 (Mar. 1973).

Key words: Bridge; failure; fracture toughness; Point Pleasant; stress corrosion cracking.

Examination of the fractured eyebar which caused the collapse of the bridge led to the conclusion that a stress-corrosion crack had penetrated to a depth of 1/8 inch during the 40 years that the bridge was in service. This flaw was sufficient to initiate fracture across the remainder of the 16 in.^{2} area of the lower limb of the eye due to the high local stress and the low fracture toughness of the steel.

Berg, C. A., **Energy conservation through effective utilization,** *NBSIR 73-102,* 53 pages (Feb. 1973).

Key words: Effective utilization; energy conservation.

In two major sectors of the economy (building services and industrial processes), accounting for approximately 75 percent of total national energy consumption, energy utilization is found to be inefficient. It is estimated that in these two sectors, as much as 25 percent of the energy consumed annually by the nation as a whole may be lost through ineffective practices. Possible reasons for existence of ineffective utilization are considered, and possible means of improving effectiveness of utilization are discussed. Three possible levels of effort to promote effective utilization of energy are identified; one promotes effective use of present fuels in present processes; the second promotes utilization of presently unused energy sources; the third promotes more effective investment of energy in durable and maintainable products.

Substantial latitude for improvement of effectiveness is shown to be realizable through technological efforts at these three levels. It is finally recommended that a national program, incorporating efforts at the three levels identified, be undertaken with the ultimate goal of creating and implementing a technology of improved energy utilization.

Braun, W., Bass, A. M., Davis, D. D., **Experimental test of a two-layer model characterizing emission-line profiles,** *J. Opt. Soc. Amer.* **60,** No. 2, 166-170 (Feb. 1970).

Key words: Atoms; hydrogen; resonance; spectra.

Deuterium Lyman-α line profiles, generated from a microwave-powered lamp containing flowing mixtures of deuterium in helium, were examined spectroscopically under high resolution. The primary purpose was to test a simple two-layer model describing the line shape emerging from a discharge zone containing both emitting and absorbing atoms. This simple model characterized the experimentally obtained line shapes under varying conditions of atom densities and line self-reversal. The kinetic (translational) temperature of the discharge could be calculated from the data. Resonance interaction between ground-state D(^{2}S) atoms and excited D(^{2}P) atoms is offered as an explanation for the experimentally observed line asymmetries. The presence of line self-reversal significantly amplifies the small spectral shifts between the absorption and emission lines. These shifts can be calculated from the model.

Burdick, M. D., **Test for the adherence of porcelain enamel cover coats direct-to-steel,** *Porcelain Enamel Inst. Bull.* **T-29,** 1-10 (1972).

Key words: Adherence; direct-on porcelain enamels; impact.

An adherence test for direct-on-cover coat porcelain enamels has been developed. This test consists of deforming the porcelain enameled specimen with a 1/2 inch diameter ball with 80-inch pounds of energy into a 3/4 inch die. The adherence is then evaluated by determining the amount of enamel adhering after impact by measuring it with an adherence meter.

Camarda, H. S., **Monte Carlo studies of D_2O and H_2O neutron moderators for time of flight experiments,** *Nucl. Instrum. Methods* **106,** 205-212 (1973).

Key words: Deuterium; moderator; Monte Carlo; neutrons; oxygen; protons, time delay; time smearing.

Calculations of neutron moderation in finite D_2O and H_2O media have been performed. Neutron spectrum shapes, time delays, and time smearings have been determined over a neutron energy range $1.8\ \text{keV} \leq E \leq 1\ \text{MeV}$.

Caswell, R. S., Berger, M. J., **Theoretical aspects of radiation dosimetry,** (Proc. Conf. on Particle Accelerators in Radiation Therapy, Los Alamos, N. Mex., Oct. 2-5, 1972), Paper in *Conference on Particle Accelerators in Radiation Therapy,* **LA-5180-C,** 60-74 (Mar. 1973).

Key words: Absorbed dose distribution; electrons; heavy ions; interpretation of measurements; neutrons; pions; protons; radiation dosimetry; radiation quality; radiation transport theory.

A review of made of the role of theoretical dosimetry in interpretation of measurements, determination of the spatial distribution of absorbed dose, and in providing detailed physical information about radiation quality. The state of the art in calculating absorbed dose distributions in homogeneous tissue equivalent media is examined by comparisons with experiments for electron, proton, neutron, and pion beams. In cases where physical properties of the beam and medium are particularly well known, the accuracy can sometimes approach 5 percent. In a larger number of cases the accuracy is 10-15 percent or worse. Knowledge of absorbed dose distributions in realistic inhomogeneous media is rudimentary: new methods, schematizations, and further calculations are required. For improved absorbed dose calculations, further neutron and pion medium energy cross section information is needed.

Radiation transport calculations are providing detailed physical information needed for the various models of radiation action on biological materials. Such detailed information is usually not available from experiment. Improvement in these calculations will depend on improved knowledge of the interaction of electrons and heavy ions with matter. New pertinent atomic data are being generated, but the cross section data base for low energy calculations is far from complete.

Cattaneo, L. E., Yokel, F. Y., **Structural tests of mechanical connections for concrete panels,** *NBSIR 73-126,* 118 pages (Nov. 1972).

Cezairliyan, A., **High-speed (subsecond) simultaneous measurement of specific heat, electrical resistivity, and hemispherical total emittance of Ta-10 (wt.%)W alloy in the range 1500 to 3200 K,** *High Temp.-High Pressures* **4,** 541-550 (1972).

Key words: Electrical resistivity; emittance; high-speed measurement; high temperature; specific heat; Ta-W alloy.

Simultaneous measurements of specific heat, electrical resistivity, and hemispherical total emittance of Ta-100(wt.%)W alloy in the temperature range 1500 to 3200 K by a subsecond-duration pulse-heating technique are described. Estimated inaccuracies of measured properties are: 3% for specific heat and hemispherical total emittance, and 0.5% for electrical resistivity. Properties of the alloy are com-

pared with the properties of the constituent elements. The values of measured specific heat are approximately 2% higher than the values computed according to Kopp's additivity law. However, this difference is within the combined estimated errors. The electrical resistivity results indicate a significant departure from Matthiessen's law. Like tantalum, the alloy showed a negative departure from linearity in the temperature dependence of electrical resistivity.

Cezairliyan, A., **Measurement of melting point, normal spectral emittance (at melting point), and electrical resistivity (about 2650 K) of niobium by a pulse heating method,** *High Temp.-High Pressures* **4,** 453-458 (1972).

Key words: Electrical resistivity; emittance; high-speed measurements; high temperature; melting point; niobium.

A subsecond duration pulse heating method is used to measure the melting point, normal spectral emittance (at the melting point), and electrical resistivity (above 2650 K) of niobium. The results yield a value of 2750 K for the melting point on the International Practical Temperature Scale of 1968. Normal spectral emittance at the melting point is 0.338, and remained constant during melting. At 2740 K electrical resistivity is 90.11×10^{-8} ohm m. Estimated inaccuracy is 10 K in the melting point, 3 percent in normal spectral emittance and 0.5 percent in electrical resistivity.

Costrell, L., **CAMAC instrumentation system—introduction and general description,** *IEEE Trans. Nucl. Sci.* **NS-20,** No. 2, 3-8 (Apr. 1973).

Key words: CAMAC; dataway; instrumentation; modules; nuclear; standards.

The CAMAC instrumentation system developed by the ESONE Committee of European Laboratories has been endorsed by the U. S. AEC NIM Committee as a dataway system complementary to the NIM (Nuclear Instrument Module) system. CAMAC is described in a general way in this introductory paper which is followed by papers that discuss the system in greater detail. This paper is an updated version of the introductory paper that appeared in the April 1971 IEEE Transactions on Nuclear Science.

Costrell, L., Editor, **CAMAC—A modular instrumentation system for data handling,** (AEC Committee on Nuclear Instrument Modules), *AEC Report No. TID-25875,* 66 pages (U.S. Atomic Energy Commission, Washington, D.C., July 1972).

Key words: CAMAC; computer interfacing; control systems; instrumentation; instrumentation standards; nuclear instrumentation; standards.

CAMAC is a digital data handling system in widespread use with on-line digital processors and computers. The system is based on a digital highway for data and control. Mechanical and signal standards are specified to ensure physical and operational compatibility between units from different sources. Except for pages i-vi, 46A and 46B, this report is identical to EURATOM Report EUR 4100e dated 1972. AEC Report TID-25877 constitutes a supplement to and is to be used in conjunction with this report. This revised specification introduces several new features but is consistent with the previous version (EUR 4100e, 1969).

The CAMAC system was specified by European laboratories through the ESONE Committee and has been endorsed by the U.S. AEC NIM Committee.

Costrell, L., Editor, **Supplementary information on CAMAC instrumentation system,** (AEC Committee on Nuclear Instrument Modules), *AEC Report No. TID-25877,* 45 pages (U.S. Atomic Energy Commission, Washington, D.C., Dec. 1972).

Cotton, I. W., **A position paper—panel session on intelligent terminals—chairman's introduction,** (Proc. 1973 National Computer Conference and Exposition, New York, N.Y., June 4-8, 1973), Paper in *AFIPS Conference Proceedings* **42,** 217-218 (AFIPS Press, Montvale, N.J., 1973).

Cotton, I. W., **Intelligent terminals,** *Datamation* **19,** No. 5, 149 (May 1973).

Coxon, B., Schaffer, R., **Analysis of a cortisol clinical standard by Fourier transform, proton magnetic resonance spectroscopy,** *Anal. Lett.* **6,** No. 4, 291-300 (1973).

Key words: Chemical shifts; clinical Standard Reference Materials; cortisol; Fourier transform, proton magnetic resonance spectroscopy.

Cortisol intended for use as a clinical Standard Reference Material has been subjected to liquid chromatography and the resulting fractions analyzed by thin layer chromatography and Fourier transform, proton magnetic resonance spectroscopy at 90 MHz. Four steroid impurities and one artifact have been characterized by means of computer measured chemical shifts.

Craw, A. R., **A summary of the relationships between accident indices and rates following a redefinition of "failure," NBSIR 73-154,** 17 pages (Mar. 1973).

Key words: Accident indices; accident rates; failure indices; failure rates; highway accidents.

Using Cerrelli's association of "failure" with active involvements in the case of two vehicles accidents, one can define failure indices, accident involvement indices, failure rates, accident involvement rates for 1-vehicle, 2-vehicle and for the union class of 1- and 2-vehicle accidents. This note presents in a condensed form all of the definitions of these measures, and a number of useful relationships and interrelationships that exist between these different measures. These formulae should prove useful in the calculation of the resulting indices and rates and of converting from one set of measures to another.

Craw, A. R., **Time series forecasting of highway accident fatalities,** *NBSIR 73-138,* 37 pages (Mar. 1973).

Key words: Exponential smoothing; fatalities; highway accidents; time series.

Using twelve years of time series data on highway fatalities, the methodology currently employed by the National Highway Traffic Safety Administration (NHTSA) to forecast the annual (calendar year) total of highway accident fatalities were compared with those obtained by several computer routines based on exponential smoothing techniques and available at the National Bureau of Standards. The use of unadjusted and seasonally adjusted data was also examined.

It is found that there is no coercive evidence to lead to abandoning the present NHTSA methods in favor of readily available computer routines based on exponential smoothing methods.

Of the methods examined in this study, the best results were obtained with the EXPSMOOTHING routine using unadjusted fatality data.

Danos, M., **Baryon resonances in nuclei,** *J. Phys.* **33,** Supplement to No. 8-9, 171-182 (Aug.-Sept. 1972).

Key words: Baryons; duality; exchange currents; magnetic moments; mesons; nuclear structure.

The problems one encounters when incorporating baryon resonances and mesons into the nuclear wave function are discussed. Since no workable strong interaction theory exists they must be attacked in a quasi-theoretical step-by-step manner. The present status in the understanding is discussed and the possible future development suggested.

Danos, M., Gillet, V., **Quartet effects in the nuclear masses and excitations,** *Z. Phys.* **249,** 294-311 (1972).

Key words: Nuclear binding energies; nuclear quartets; nuclear reactions; nuclear structure; quartet model; super-multiplet theory.

The assumptions of the quartet model are given and it is shown that they are consistent with the fine structure of the nuclear mass curves throughtout the table. It is also shown by an analysis of the nuclear masses that the quarteting effect accounts for 2/3 of the neutron binding energies. The consequences of the quartet picture for the existence of low-lying many-particle many-hole states in medium and heavy nuclei are discussed.

Davis, R. M., **Automation technology for the retail industry (welcome address),** *Proc. Conf. Automation Technology for the Retail Industry, held at the National Bureau of Standards, Gaithersburg, Md., Mar. 15, 1972,* COM-72-10495, pp. 1-7 (National Technical Information Service, Springfield, Va., 1972).

Deslattes, R. D., ***L*-series emission spectrum of germanium,** *Phys. Rev.* **172,** No. 3, 625-627 (Aug. 15, 1968).

Key words: Emission spectrum; germanium; profile measurement; valance emission bands.

Measurements are reported on the *L*-series emission spectrum of germanium which lead to line identifications at variance with other recent work. Some features of the *K*-emission spectrum were also recorded to confirm previous work there and aid in the location of the valence emission bands in the *L* series. It is shown that these are of extremely low intensity, so low in fact as to preclude for the present a detailed profile measurement.

Dickens, B., Brown, W. E., **The crystal structure of $CaKAsO_4 \cdot 8H_2O$,** *Act. Crystallogr.* **B28,** Part 10, 3056-3065 (Oct. 1972).

Key words: Calcium arsenates; calcium phosphates; inorganic hydrate; ion hydration; single crystal x-ray diffraction.

$CaKAsO_4 \cdot 8H_2O$ crystallizes in the orthorhombic unit cell $a=7.146(1)$, $b=11.696(2)$, $c=7.100$ (2) Å at 25 °C with cell contents of $2[CaKAsO_4 \cdot 8H_2O]$. The density calculated from the x-ray data is 2.027 $g \cdot cm^{-3}$; that calculated from the refractive indices is 2.10 $g \cdot cm^{-3}$. The structure has been refined to $R_w=0.037$, $R=0.043$ in space group *Cm2m*, using 1023 observed reflections measured on an automated diffractometer and corrected for absorption. Allowance was made for anomalous dispersion and secondary isotropic extinction. All ions in $CaKAsO_4 \cdot 8H_2O$ are completely hydrated. Ca coordinates to eight water oxygen atoms with Ca...O distances in the range 2.460(5) to 2.490(3) Å. K coordinates to eight water oxygen atoms with K...O distances ranging from 2.756(3) to 2.960(7) Å. The coordination polyhedron of Ca shares one face of four water molecules and two edges with neighboring coordination polyhedra of K. Each oxygen atom of the AsO_4 ion is the acceptor in hydrogen bonds from four water molecules and forms no bonds with the cations. The two crystallographically different As-O distances in the AsO_4^{3-} ion are 1.682(4) and 1.684(4) Å when uncorrected for thermal motion, and 1.690 and 1.692 Å with the riding model correction. The structure of $CaKAsO_4 \cdot 8H_2O$ is related to that of $MgNH_4PO_4 \cdot 6H_2O$, struvite. This structural type may be common to several calcium phosphates and related compounds.

Dillon, T. A., Stephenson, J. C., **Effect of the straight path approximation and exchange forces on vibrational energy transfer,** *J. Chem. Phys.* **58,** No. 9, 3849-3854 (May 1, 1973).

Key words: CO_2; exchange forces; hydrogen halides; line widths; straight path; vibrational energy transfer.

A wide variety of theories exist for calculating fundamental molecular collision processes such as line broadening or energy transfer rates. All of these theories involve evaluation of a "phase" integral or Fourier transform of the intermolecular potential. In this paper we consider two major sources of error that can occur in the evaluation of phase integrals. "Universal" phase integrals calculated in a straight path model are compared with calculations based on trajectories determined by solution of classical orbit equations. Serious discrepancies are pointed out and practical computational alternative is suggested. A simple empirical model for exchange forces is introduced in calculations of linewidths and *V-V* transfer for hydrogen halides in a CO_2 atmosphere. These calculations show that exchange forces can have a large effect but that the simple procedure of adding "a short range" contribution to a cross section calculated from attractive multipolar forces gives a totally incorrect picture.

Dodge, M. J., Malitson, I. H., Mahan, A. I., **A special method for precise refractive index measurement for uniaxial optical media,** *Appl. Opt.* **8,** No. 8, 1703-1705 (Aug. 1969).

Key words: Refractive index; refractometry; ruby.

A method was developed for measuring the refractive index of optical glasses and uniaxial crystalline solids when established refractometric methods are not feasible. A synthetic ruby cuboid was contacted to a prism of known refractive index and a spectrometer was used to measure the angles describing the optical path through the ruby-glass combination. Ray tracing equations were derived to compute the refractive index accurate within 3×10^{-5}. Index values for both polarizations of ruby are given at selected wavelengths from 0.4358 μm to 0.7065 μm.

Donaldson, J. R., **On uncertainty in mass measurement,** *NBSIR 7-151,* 10 pages (Mar. 1973).

Drummond, D., Gallagher, A., **A low resolution scanning multiple Fabry-Perot spectrometer,** *Rev. Sci. Instrum.* **44,** No. 4, 396-399 (Apr. 1973).

Key words: Fabry-Perot; spectrometer.

A low resolution scanning multiple Fabry-Perot spectrometer has been built for the observation of very weak extended light sources. The instrument consists of three sets of 7.6 cm diam Fabry-Perot plates operated in central order; their spacings are in a 3-4-5 ratio and are servo controlled using reference light provided by a single master grating monochromator. The instrument is scanned by varying the wavelength setting on the grating instrument. The resolution of the instrument is variable through the range 0.5-15 A, and its luminosity is equal to that of a 5 cm interference filter with a 65% peak transmittance. The free spectral range is about 125 times the peak half-width. Wavelengths in that range are transmitted at a level of 10^{-4} or less of the central transmission peak.

Ehlers, V. J., Gallagher, A., **Electron excitation of the calcium 4227-Å resonance line,** *Phys. Rev. A* **7,** No. 5, 1573-1585 (May 1973).

Key words: Calcium; electron excitation.

We have measured the optical-excitation function and polarization of the 4227-Å line, using crossed electron and calcium beams, for electron energies from threshold to 1400 eV. In the high-energy region, from 100-450 times the threshold energy, we have used the Bethe theory to normalize our experimental results. An excellent signal-to-noise ratio combined with ~ 0.3-eV full width at half-maximum electron-energy resolution has enabled observation of structure in the excitation function and polarization curves below 5 eV. We observed a threshold polarization limit of $(98 \pm 3)\%$, consistent with the expected + 100%. The data are also consistent with a logarithmic approach to a high-energy polarization of − 100%.

Ehrlich, M., **Influence of size of CaF_2:Mn thermoluminescence dosimeters on ^{60}Co gamma-ray dosimetry in extended media,** *Proc. 3d Int. Conf. on Luminescence Dosimetry, held at the Danish AEC Research Establishment Risø, Roskilde, Denmark, Oct. 11-14, 1971,* Risø Report No. 249, Part II, 550-560 (Dec. 1971).

Key words: Absorbed dose; CaF_2:Mn; ^{60}Co gamma radiation; extended media; interface; theory.

Absorbed-dose distributions were measured in CaF_2:Mn TLD of thicknesses between 0.5 and 3.5 mm, irradiated with an essentially plane-parallel beam of ^{60}Co gamma rays in media of aluminum (homogeneous case), polystyrene, copper, and lead. Change of average absorbed dose with dosimeter thickness was deduced from the dose distribution. Since dosimeter sizes were of the order of secondary-electron ranges, total energy absorption was found to be critically affected by interface effects, which caused a loss of linearity of energy absorbed with dosimeter thickness for polystyrene and lead. A relatively strong asymmetry in the absorbed-dose distributions was found near front and rear interfaces, absorbed dose being ~ 10 percent higher in front for polystyrene, and ~ 15 and ~ 30 percent lower for copper and lead, respectively. Comparisons of relative experimental values of average absorbed dose for different dosimeter thicknesses with values computed according to Burlin's scheme (which does not consider front-rear asymmetries) were not conclusive for polystyrene and lead, since the assumptions regarding the electron spectrum at the dosimeter site proved to be critical for polystyrene, and the assumptions regarding the photon spectrum critical for lead. For copper, there was agreement to within the limits of experimental reproducibility.

Fabry, A., Jenkins, J. D., **Calculation of the ΣΣ facility with ENDF/B-versions II and III and comparison with experiment,** *Trans. Amer. Nucl. Soc.* **15,** No. 2, 1 (Nov. 1972).

Key words: Comparison; fast; integral-measurements; neutron; nuclear-data; spectra; standard; theory.

The intermediate-energy standard neutron spectrum facility ΣΣ is a permanent, clean, and reproducible standard neutron source characterized by a central radiation field typical of zero-power fast breeder test assemblies. It consists of a spherical shell of natural uranium of 24.5-cm o.d. x 5-cm thickness embedded at the center of a 50-cm-diam spherical cavity in a graphite thermal column: it contains a spherical shell of natural boron carbide 15 mm thick, which surrounds the central exposure zone of 11-cm diam. The ΣΣ central neutron spectrum and reaction rates have been computed with the evaluated nuclear data files ENDF/B Versions II and III. The one-dimensional discrete ordinates transport calculations were performed in the $S_{16}P_3$ approximation. Extensive measurements of infinitely dilute reaction rates in ΣΣ are compared to these calculations using detector cross sections from a current neutron dosimetry library. Sizable discrepancies are apparent. For the detector ratios with major response in the energy range above 50 keV, theory is presently unable to reproduce the observed spectral indexes, especially the $^{238}U(n,f)/^{235}U(n,f)$ ratio: the deviation with respect to the trend indicated by the other threshold reactions is similar to the one previously suggested in cavity fission neutron spectrum integral measurements. The neutron spectrum between ~ 300 eV and 5 keV has been found very sensitive to the shape and intensity of the excitation function for the 45-keV ^{238}U level.

Fabry, A., Jenkins, J. D., **Wall return neutron fluxes for high- and intermediate-energy cavity neutron sources,** *Trans. Amer. Nucl. Soc.* **15,** No. 2, 975-976 (Nov. 1972).

Key words: Carbon; cavity; fast neutron; spectra; theory.

Spherical cavities in graphite thermal columns of nuclear reactors provide an ideal environment for the production of comparatively intense, energy distributed neutron fields, i.e., either intended pure fission neutron spectrum sources or intermediate-energy standard neutron spectra. Cavities of 50 cm diameter are used in various laboratories; a 30 cm diameter cavity is operated at NBS and a 1 meter diameter cavity has recently been implemented at CEN-SCK.

Numerical computations of graphite wall-return neutron spectra have been performed by means of the discrete ordinates multigroup method in one-dimensional spherical geometry. The evaluated nuclear data files KEDAK, ENDF/B Version 3 have been used and the convergence of the S_n multigroup multitable treatment has been established systematically.

Within the cavity, a good approximation of the wall return is

$$\phi_W(r,\mu,E;r_s) = \phi_W(E).$$

This relationship is correct to better than 2% for r, $r_s \leq R/2$ where R is the cavity radius and r_s the radius of a thin, fission spectrum source shell. This fundamental property has led to the development of an experimental method for determining wall-return backgrounds.

Fey, L., **A time code for the Omega worldwide navigation system,** *Proc. IEEE* **60,** No. 5, 630 (May 1972).

Finkel, P. W., Miller, T. R., **Executive summary of a proficiency test assessment of clinical laboratory capability in the United States,** *NBSIR 73-162*, 9 pages (May 1973).

Key words: Accuracy; clinical chemistry; hematology; medical usefulness; microbiology, proficiency testing.

The proficiency of a selected sample of physician, hospital and independent laboratories was assessed with respect to their ability to analyze clinical chemistry and hematology samples and to identify microbiological organisms. For the assessment of clinical chemistry and hematology proficiency, the laboratories were grouped and determinations of group accuracy and group precision were made. Further analyses were performed to determine relative accuracy and precision of the techniques presently applied to these groups. There was no significant difference at the 95% confidence level in the accuracy achieved by the various laboratory groups involved in clinical chemistry and hematology analysis. In clinical chemistry, the Medicare-Certified Independent Laboratories, CDC Tested Laboratories and JCAH-Members generally proved more precise than Physicians' Office and Medicare-Certified Hospital Laboratories. However, none of the laboratory groups were sufficiently accurate to permit the monitoring over time of variation in an individual patient's constituent concentrations. It would appear that poor selection of techniques was an important contributor to this low performance level. In hematology the Physicians' Office Laboratories proved to be the least precise of the groups. There was no noticeable difference in precision between participants in the CDC proficiency testing program and nonparticipants. With respect to microbiology, 7.6% of the identifications by laboratories participating in the CDC testing program were incorrect, while 19.4% of all other identifications were incorrect.

Flynn, H. G., Cook, R. K., **The effects of sonic boom and similar impulsive noise on structures,** *Environmental Protection Agency Report No. NTID200.12*, 19 pages (available as PB206725 from the National Technical Information Service, Springfield, Va. 22151, Dec. 31, 1971).

Key words: Damage by sonic booms; noise pollution; sonic boom.

This report is a review and summary of recently published studies on the effects of sonic booms, mainly physical and financial effects on property. It has been prepared in partial response to Title IV – Noise Pollution, of the Clean Air Amendments of 1970 (Public Law 91-604). It will be published and distributed, concurrently with its presentation to the President and Congress, by the Environmental Protection Agency. A bibliography of recent papers and studies on the damage done by sonic booms is included.

Fong, J. T., Simmons, J. A., **A decomposition theorem on the scalar potential of a compressible BKZ fluid,** *J. Appl. Math. Phys.* **23,** No. 5, 780-794 (1972).

520-812 O-LF - 73 - 6

Key words: Anisotropy; BKZ fluid; composite material; continuum mechanics; hyperelasticity; isothermal; nonlinear; variational principle; viscoelasticity.

Based on the existence of a caloric equation of state in the thermodynamic theory of a nonlinear viscoelastic fluid (Bernstein, Kearsley and Zapas, 1964), and the additional assumption that the local entropy production along any instantaneous deformation path is finite, we first show that such a fluid behaves as a perfectly elastic material whenever the deformation gradient suffers from a jump-type discontinuity. The nature of the apparently perfectly elastic material serving to interpret results in the instantaneous deformation depends on the previous history only through two parameters, namely, the density and the temperature of the fluid immediately prior to the jump. This result is then applied, in conjunction with the usual conditions of isotropy and objectivity as well as an application of Schur's Lemma on irreducible sets of matrices, to obtain a decomposition of the scalar potential of the compressible Bernstein-Kearsley-Zapas Fluid (abbrev. BKZ Fluid).

Franklin, A. D., **Density of CaF_2 containing low concentrations of GdF_3,** *J. Nonmetals* **1,** 27-34 (1972).

Key words: Calcium fluoride; cation vacancies; density; gadolinium impurity; interstitial anions; lattice parameter; point defects.

The density relative to that of pure crystals has been measured for CaF_2 crystals containing mole fractions from 0 to 4.6×10^{-3} of GdF_3, and the lattice parameters of these and also of pure crystals were measured. The doped crystals had been annealed at temperatures from 500 to 1100 °C in an atmosphere of He plus HF. No influence of annealing was seen on either the density or the lattice parameter. The precision of both measurements is, however, not quite good enough to rule out definitely an earlier suggestion that cation vacancies play an important role in the annealing behavior of this system. However, the density changes accompanying the incorporation of these amounts of GdF_3 in CaF_2 are too large to be accounted for by the usual model in which Gd^{3+} occupies a cation site and is accompanied by an extra F^- ion in an interstitial site. The changes do agree with a model in which one HF molecule accompanies each GdF_3 unit added, but attempts to detect the HF in nmr and infra-red absorption experiments were unsuccessful.

Franklin, A. D., **Point defects in alkaline earth fluorides,** (Proc. 3rd Int. Conf. on Sintering and Related Phenomena, University of Notre Dame, Notre Dame, Indiana, June 5-7, 1972), Paper in *Mater. Sci. Res.*, G. C. Kuczynski, Ed., **6,** 19-27 (Plenum Publ. Corp., New York, N.Y., 1973).

Key words: Alkaline earth fluorides; CaF_2; clusters; defect models; GdF_3; mass transport; point defects.

Alkaline earth fluorides containing substitutional trivalent cations are known to contain fluorine interstitials as well, providing charge balance. It has been customary to assume that at low temperatures association between these impurity cations and interstitial anions controls the anion interstitial concentrations. However, an examination of EPR and optical data on quenched specimens of CaF_2: GdF_3 shows that this is probably not the case. Rather, interstitial clusters are formed at low temperatures. Sample calculations with a model of quenched crystals based upon this notion reproduces the main features of our previous data on variation of the relative concentrations of associated and unassociated Gd^{3+} ions with GdF_3 content and annealing temperature.

Frommer, M. A., Murday, J. S., Messalem, R. M., **Solubility and diffusivity of water and of salts in an aromatic polyamide film,** *Eur. Polym. J.* **9,** 367-373 (1973).

Key words: Aromatic polyamide membranes; desalination; diffusion; membranes; NMR; permeation in polymers; polymeric films; reverse osmosis; salt-polymer interactions.

The solubility and the diffusivity for water and NaCl in a fully aromatic polyamide (PA) film have been determined. From these the "intrinsic permeability characteristics" of this polymer have been calculated and its suitability for desalination by reverse osmosis is compared with that of the commonly used cellulose acetate (CA). It has been found that, although the solubility of NaCl in the PA film is higher than that in a CA film, PA membranes will reject salt better than CA membranes having identical structure and morphology. This is because the diffusivity of NaCl through the PA film is substantially lower, and the permeability of water through it (as well as the solubility and the diffusivity of water in it) are higher than the comparable values for CA films.

Fuller, G. H., **Problems of compiling and evaluating or what is the nuclear moment?** (Proc. Int. Conf. on Nuclear Moments and Nuclear Structure, Osaka, Japan, Sept. 4-8, 1972), *J. Phys. Soc. Jap.* **34,** Supplement, 153-154 (1973).

Gans, W. L., Nahman, N. S., **Fast Fourier transform implementation for the calculation of network frequency domain transfer functions from time domain waveforms,** *NBSIR 73-303*, 53 pages (Dec. 1972).

Garvin, D., Hampson, R. F., **Atmospherical modelling and the chemical data problem,** *Proc. AIAA/AMS Int. Conf. on the Environmental Impact of Aerospace Operations in the High Atmosphere, Denver, Colo., June 11-13, 1973,* AIAA Paper No. 73-500, 1-6 (American Institute of Aeronautics and Astronautics, New York, N.Y., 1973).

Key words: Atmosphere; carbon monoxide; chemical kinetics; data evaluation; hydroxyl; nitric acid; nitric oxide; nitrogen dioxide; oxygen atom; ozone; photochemistry; stratosphere.

The chemistry of the stratosphere is determined by 50 to 100 reactions. Accurate data for these reactions are needed as input in models of the chemical dynamics of the stratosphere.

A program to provide reliable rate and photochemical data is described. The present status of some of the reactions involving O, O_3, NO_2, HO and HNO_3 is discussed. Recommended values are given for rate constants for a number of chemical reactions. Reactions requiring further study are indicated.

Goldberg, R. N., Prosen, E. J., **Evaluation of heats of transition in scanning calorimetry,** *Thermochimica Acta* **6,** No. 1, 1-11 (1973).

Key words: Heats of transition; scanning calorimetry; theory of calorimetry; thermal analysis.

A procedure for the evaluation of heats of transition in scanning calorimetry has been developed. A formula for evaluation of the energy of fusion of a compound at its melting point is derived that takes into account the baseline shift that is attributable to the heat capacity change on melting. Several other calorimeter parameters of importance are discussed. These include heat exchange between calorimeter vessel and jacket, the time constant of the instrument, the scanning rate, and the heater placement.

Grundl, J. A., **Brief review of integral measurements with fission spectrum neutrons,** (Proc. of the Consultants' Meeting, Vienna, Austria, Aug. 1971), Paper in *Prompt Fission Neutron Spectra*, pp. 29-32 (International Atomic Energy Agency, Vienna, Austria, 1972).

Key words: Fission spectra; integral measurements; cross sections.

The paper is an edited transcript of the introduction to the discussion of integral measurements of fission cross-sections averaged over fission spectra given by the author at the meeting.

Grundl, J. A., **Measurement of the average fission cross-section ratio, $\sigma_f(^{235}U)/\sigma_f(^{238}U)$ for ^{235}U and ^{239}Pu fission neutrons,** (Proc. Specialists' Meeting on Prompt Fission Neutron Spectra, Vienna, Austria, Aug. 1971), Paper in *Prompt Fission Neutron Spectra*, pp. 107-111 (International Atomic Energy Agency, Vienna, Austria, 1972).

Key words: Fission cross sections; fission neutrons; integral measurements.

Average fission cross-section ratios, $\sigma_f(^{235}U)/\sigma_f(^{238}U)$, have been measured for ^{235}U and ^{239}Pu fission neutrons. A cavity fission source, a fission ionization chamber, and a redundant determination of fission foil weight ratios were employed for the measurements. The result for ^{235}U fission neutrons is 3.71 ± 0.17, a value that confirms earlier integral microscopic results and is 12 to 20% discrepant with predictions based on differential microscopic data. The observed ratio of average cross-section ratios, χ_{49}/χ_{25}, is 0.970 ± 0.012. This value represents a departure from unity that is less than one-half of that predicted by differential microscopic data. The measurements described remain in progress.

Grundl, J. A., Spiegel, V., Jr., Eisenhauer, C., **Measurement of ^{235}U and ^{238}U fission cross sections for ^{252}Cf spontaneous fission neutrons,** *Trans. Amer. Nucl. Soc.* **15,** No. 2, 945-946 (1972).

Key words: Absolute fission cross section; californium neutron source.

Absolute ^{235}U and ^{238}U fission cross sections have been measured with a small, low-mass ^{252}Cf spontaneous fission source and a lightweight, double fission ionization chamber.

Guttman, C. M., Flynn, J. H., **On the drawing of the base line for differential scanning calorimetric calculation of heats of transition,** *Anal. Chem.* **45,** No. 2, 408-410 (Feb. 1973).

Key words: Base line determination; differential scanning calorimetry (DSC); heats of transition; thermal analysis; thermoanalytical calorimetry.

The heat of transition has been computed from a Differential Scanning Calorimetry (DSC) trace by drawing a base line related only to the heat capacity of the transition's upper state.

Hadley, S. G., Keller, R. A., **Direct determination of the extinction coefficients for triplet ← triplet transitions in naphthalene, phenanthrene, and triphenylene,** *J. Phys. Chem.* **73,** No. 12, 4351-4355 (Dec. 1969).

Key words: Aromatics; electronic spectroscopy; intersystem crossing; quantum yields; triplet states.

Extinction coefficients for triplet ← triplet absorption have been directly determined for several aromatic hydrocarbons. A high intensity photolysis lamp was used to populate the triplet state and the concentration of triplets was measured by monitoring the depletion of the ground state. The values of the extinction coefficients $\epsilon \times 10^{-4}$ (l. mol^{-1} cm^{-1}) and their estimated uncertainties at the most prominent maximum λ(nm) are: naphthalene-h_8, 4.0 ± 0.6, 414.0; naphthalene-d_8, 4.0 ± 0.6, 414.0; phenanthrene-h_{10}, 3.8 ± 0.6, 492.5; phenantrene-d_{10}, 3.1 ± 0.5, 492.5; triphenylene-h_{12}, 1.56 ± 0.23, 430.0; and triphenylene-d_{12}, 1.20 ± 0.18, 431.0. For anthracene, $\epsilon_T \geq 9 \times 10^4$ l. mol^{-1} cm^{-1} at 427.3 nm.

Hall, J. L., **Saturated absorption spectroscopy with applications to the 3.39 μm methane transition,** (Proc. 3rd Int. Conf. on Atomic Physics, Boulder, Colorado, Aug. 1972), Chapter in *Atomic Physics*, S. J. Smith and G. K. Walters, Eds., **3,** 615-646 (Plenum Publ. Corp., New York, N.Y., Feb. 1973).

Key words: Laser; methane; optical frequency standards; saturated absorption; spectroscopy.

In basic research we are grateful to be able to pursue research in profitable directions, e.g., those directions where the boundaries of experimental or theoretical possibilities seem most susceptible to growth. Of course we know of some areas that could be investigated and many numerical data recorded, but we are uneasy in not knowing how to make use of the data. As physicists we especially like to make progress synthesizing specialized concepts into more general forms. We savor the similarities—and differences—when ideas developed in one area prove useful in another set of circumstances. Just now it is optical resonance physics that seems to be ripe for explosive growth using new laser techniques and "classical" resonance ideas. This paper represents a direct effort to sketch, in the opinion of a certain class of partisans, "where the action is." We begin with a brief discussion of experiments in which a laser is useful but not necessary, and a consideration of the basic optical facts of life. The bulk of the paper explores the exciting land beyond the Doppler limit.

Halsey, N., Mitchell, R. A., Mordfin, L., **Evaluation of GRP rod and rope materials and associated end fittings,** *NBSIR 73-129*, 87 pages (Dec. 1972).

Hampson, R. F., Jr., Okabe, H., **Collisional stimulation of the $O(^1S)-O(^1D)$ emission of oxygen atoms formed in vacuum-ultraviolet photolysis of nitrous oxide,** *J. Chem. Phys.* **52,** No. 4, 1930-1933 (Feb. 15, 1970).

Key words: Collisional stimulations; N_2O; O^1S-O^1D emission; photodissociation; vacuum ultraviolet.

Oxygen atoms in the ^1S state have been produced by the vacuum-ultraviolet photolysis of N_2O and observed by their emission at 5577 Å in the $^1S-{}^1D$ transition. The stimulation of this emission by collision with added gases has been studied. The emission has been found to be proportional to the pressure of the added gas. Xenon is the most efficient stimulator of the gases used, followed in order of decreasing efficiency by Kr, Ar, N_2, H_2, and He. Data gotten by photolysis of NO_2 and CO_2 have been used to estimate their quantum yields for formation of $O(^1S)$.

Hudson, R. P., **Book: Principles and application of magnetic cooling,** *Series in Low Temperature Physics* **2,** 1-230 (North-Holland Publishing Co., Amsterdam, The Netherlands, 1972).

Key words: Adiabatic demagnetization; cryogenics; cryothermometry; magnetic cooling; magnetism.

Magnetic cooling is discussed in terms of basic thermodynamic principles, then supplemented by a review of paramagnetism theory, and descriptions of experimental techniques (including thermometry) involved in applying the magnetocaloric effect to real systems.

Hutchinson, J. M. R., Lantz, J. L., Mann, W. B., Mullen, P. A., Rodriguez-Pasqués, R. H., **An anti-coincidence shielded NaI(Tl) system at NBS,** *IEEE Trans. Nucl. Sci.* **NS-19,** No. 1, 117-118 (Feb. 1972).

Key words: Anti-coincidence shielding; low-level radioactivity measurements; scintillation counting; sodium-iodide crystals.

The anti-compton anti-coincidence shielded 8″ NaI(Tl) crystal system recently installed at N.B.S. is described. This apparatus is composed of two 8″×4″ well crystals which can be used in coincidence, and a 30″ diameter 20″ long cylindrical anti-compton anti-coincidence scintillation plastic shield. The instrument is discussed as a particularly powerful tool for low level radioactivity calibration.

Jespersen, J. L., Blair, B. E., Gatterer, L. E., **Characterization and concepts of time-frequency dissemination,** *Proc. IEEE* **60,** No. 5, 502-521 (May 1972).

Key words: Dissemination of time and frequency; portable clocks; radio propagation; satellite time dissemination; television time and frequency dissemination; time signal noise; time-frequency system designs; transfer standards.

Fundamental considerations that arise in designing a time or frequency dissemination system, are discussed and some dissemination methods are surveyed. A section on "Signal design for time and frequency dissemination" briefly summarizes radio propagation characteristics, discusses time signal format design, and considers how noise affects time and frequency signals.

We point out fundamental techniques of time and frequency dissemination and describe similarities between systems for time dissemination and navigation. The use of synchronous satellite transponders and commercial television systems for time dissemination is emphasized because of their great promise. No attempt is made to cover every existing dissemination system; some systems are treated elsewhere in this *Special Issue on Time Frequency*. The concluding section gives three categories of users according to their required accuracy and shows typical systems which can provide desired accuracies. Various dissemination techniques are charted and evaluated in terms of salient characteristics such as accuracy, geographical coverage, cost factors, and others. To alleviate an existing frequency spectrum problem, we suggest that designers of communication and navigation systems consider opportunities for including time and frequency dissemination in their systems.

Jespersen, J. L., Fey, L., **"Time-telling" techniques,** *IEEE Spectrum* **9,** No. 5, 51-58 (May 1972).

Key words: Automatic vehicle location; dissemination of time and frequency; portable clocks; radio propagation; satellite time dissemination; television time and frequency dissemination; time-frequency; time signal noise; system designs; transfer standards.

A brief, historical development of astronomical time scales and their use in navigation, including the present use of an atomic time scale. Frequency standards are compared in terms of accuracy, stability, and practical parameters such as cost.

Time and frequency dissemination methods are treated, including radio propagation effects, factors involved in precise time broadcasts, and use of radio navigation systems for time broadcasts. Various artificial satellite time broadcast techniques are compared. TV time techniques are discussed, as well as portable clock use and other specialized methods. The various time dissemination techniques are compared according to various parameters of interest to the user.

Some basic similarities of systems employing time and frequency are pointed out. Growing complexities of systems requiring time and frequency as an integral part are noted. This generates pressure toward diversification of the designer but emphasizes the need for further integration of time and frequency technology.

Jones, M. C., **Use of superconductors in thermal insulations,** *Cryogenics* **13,** No. 2, 83-84 (Feb. 1973).

Key words: Niobium; superconductors; thermal radiation shields; total emissivity.

A suggestion is made for using superconductors as thermal radiation shields at or below liquid helium temperatures. Calculations are described which predict total emissivities for niobium of $10^{-4} - 10^{-5}$ at 4 K and $10^{-6} - 10^{-7}$ for temperatures of $1 - 2$.

Kaldor, A., Maki, A. G., **High resolution infrared spectrum and the molecular structure of sulfur trioxide,** *J. Mol. Struct.* **15,** 123-130 (1973).

Key words: Air pollution; bond distances; infrared spectroscopy; molecular structure; spectra; sulfur trioxide.

The $2\nu_3^2(E')$ band of sulfur trioxide has been measured with a resolution of 0.03 cm^{-1}. The analysis of this band yields a set of rotational constants which fit the data to within a standard deviation of 0.003 cm^{-1} (which is the expected error limit). From the rotational constant $B_0 = 0.34857 \pm 0.00006$ cm^{-1} the S-O bond distance is found to be $r_0 = 1.4198 \pm 0.0002$ Å. This value is in agreement with earlier infrared measurements, but represents a considerable improvement in accuracy.

Kamper, R. A., Simmonds, M. B., Adair, R. T., Hoer, C. A., **A new technique for RF measurements using superconductors,** *Proc. IEEE* **61,** No. 1, 121-122 (Jan. 1973).

Key words: Josephson effect; quantum interference; rf attenuation; rf measurements; superconductivity.

The quantization of magnetic flux in a superconducting circuit can serve for the measurement of electrical quantities in the same way that we use the wavelength of light to measure length. We report a demonstration of this function in the measurement of attenuation ratio at a frequency of 30 MHz.

Kessler, B. V., Meijer, P. H. E., **Calculation of behavior of paramagnetic systems with dipolar and exchange interactions,** *Phys. Rev. B* **7,** No. 6, 2839-2850 (Mar. 15, 1973).

Key words: Cerium ethyl sulfate; cerous magnesium nitrate; cobaltous fluosilicate; cupric potassium sulfate; dipole-dipole interaction; entropy; exchange interaction; ferric methyl ammonium alum; low temperature paramagnetism.

This paper deals with a precise calculation of the b_2 coefficients in the specific heat for a number of ultralow-temperature compounds. The result is given for the actual dipole-dipole interaction plus a varying amount of isotropic exchange J. Comparison with experimental data leads to a determination of J. Usually two values are possible as a result of the quadratic dependence of b_2 on J. Similar calculations are performed for the T^{-3} term in the specific heat. In this case there are two types of contributions: one from the two-point summation and one from the three-point sum or ring diagram. The value of each is determined as a function of J. The values of J as determined from the comparison of the experimental values of b_2 with the calculated values of b_2 are substituted in b_3 and the values thus predicted, on the basis of isotropic exchange, are given.

Kirby, R. K., **Thermal expansion of tungsten from 293 to 1800 K,** *High Temp.-High Pressures* **4,** 459-462 (1972).

Key words: Standard Reference Materials; thermal expansion; tungsten.

Measurements on the thermal expansion of three samples of tungsten were made with a twin-microscope method in the range of 1000 to 1800 K. Measurements were also made on one of these samples with a Fizeau interferometer in the range below 1100 K. The results obtained indicated that the values for the expansion of the three samples, two prepared by sintering and one by arc melting, are in reasonable agreement with one another and with some of the data in the literature.

Kirchhoff, W. H., Lide, D. R., Jr., **Microwave spectrum, dipole moment, and quadrupole coupling constant of trifluoramine oxide,** *J. Chem. Phys.* **51,** No. 1, 467-468 (July 1, 1969).

Key words: Dipole moment; hyperfine structure; microwave spectrum; quadrupole coupling; Stark effect; symmetric top; trifluoramine.

The microwave spectrum of trifluoramine oxide, NF_3O, has been observed and is consistent with a symmetric top structure for the molecule. The dipole moment has been measured from the Stark effect of the $K = 1, J = 1 \rightarrow 2$ transition and its value is 0.0370 ± 0.0004 Debyes where the uncertainty indicated is twice the standard error obtained from a least squares fit of the data. The quadrupole coupling constant of the nitrogen nucleus was calculated from the hyperfine splitting of the $K = 1, J = 1 \rightarrow 2$ transition. Its value is $eqQ = -1.52 \pm 0.15$ MHz where the uncertainty is based on an estimated uncertainty of 0.05 MHz in the measured hyperfine splitting.

Kirchhoff, W. H., **Microwave spectroscopy—a molecular probe,** *Ind. Res.* **12,** No. 2, 38-41 (Feb. 1970).

Key words: Chemical analysis; dipole moment; microwave; molecular structure; radio astronomy.

A brief state-of-the-art description of microwave spectroscopy is presented. The discussion includes a description of those molecular properties which may be derived from a microwave spectrum, the physical model describing the origin of a microwave spectrum and a discussion of some of the potential uses of microwave spectroscopy as a tool for chemical analysis.

Ku, H. H., **Analysis of information-an alternative approach to the detection of a correlation between the sexes of adjacent sibs in human families,** *Biometrics* **27,** 175-182 (Mar. 1971).

Ku, H. H., Kullback, S., **Analysis of multidimensional contingency tables: An information theoretic approach,** *Contributed Papers 37th Session of the International Statistical Institute, London, England, Sept. 3-11, 1969,* pp. 156-158 (Sept. 11, 1969).

Ku, H. H., Varner, R., Kullback, S., **Analysis of multidimensional contingency tables,** *Proc. 14th Conf. on the Design of Experiments in Army Research Development and Testing, Edgewood Arsenal, Md., Oct. 23-25, 1968,* ARO-D Report 69-2, pp. 141-180 (1969).

Kushner, L. M., **Progress report on activities of the National Bureau of Standards under the 1967 Amendments to the Flammable Fabrics Act,** *Proc. 3d Annual Meeting of the Information Council on Fabric Flammability, New York, N.Y., Dec. 4, 1969,* pp. 156-163 (Information Council on Fabric Flammability, New York, N.Y., 1969).

Key words: Flammable fabrics; flammability standards; National Advisory Commission for the Flammable Fabrics Act; 1967 Amendments to the Flammable Fabrics Act.

Presents a summary of activities at the National Bureau of Standards since enactment of the 1967 Amendments to the Flammable Fabrics Act.

Kusuda, T., **Climatological data at the proposed prototype sites in the United States for the evaluation of HUD Operation BREAKTHROUGH housing systems,** *NBSIR 73-144,* 137 pages (Apr. 10, 1973).

Lang, R., Bender, P. L., **Analytic approximation for the saturation behavior of OH emission regions,** *Astrophys. J.* **180,** No. 2, 647-660 (Mar. 1, 1973).

Key words: OH microwave transition; radio astronomy; saturation; stimulated emission.

One of the simplest models for a cosmic maser consists of a homogeneous spherical region in which inverted population is created at a uniform rate. We have investigated the radiation transfer problem including saturation for this case under the following assumptions: (1) two levels only, without magnetic sublevels; (2) a square line shape; (3) excitation by spontaneous emission at a uniform rate through the region; and (4) no scattering in the medium or reflection at the boundary. An approximate analytic solution has been found which closely satisfies the radiation transfer equation under conditions of substantial saturation. This analytic solution has been checked against numerical solutions which are intended to approximate the flux and apparent size of the -43.7 km s^{-1} feature in W3. Both the analytic solution and the numerical models show that the actual size of an emitting region can be considerably larger than for a region of uniform population difference which has the same apparent size.

LaVilla, R. E., **Carbon and fluorine x-ray emission and fluorine *K* absorption spectra of the fluoromethane mmecules, $CH_{4-n}F_n$ ($0 \leq n$ 4). II,** *J. Chem. Phys.* **58,** No. 9, 3841-3848 (May 1, 1973).

Key words: Calculated relative x-ray emission; carbon $K\alpha$ emission; fluorine *K* absorption; fluorine $K\alpha$ emission; fluoromethane molecules; methane; molecular orbital level sequence.

The carbon and fluorine $K\alpha$ emission and the fluorine *K* absorption spectra of the molecular gases $CH_{4-n}F_n$($0 \leq n \leq 4$) are reported. All the spectra were obtained on a single flat crystal spectrometer with photon counting. The emission spectra, which were excited by direct electron bombardment, are in fair agreement with an interpretation based on electric dipole transitions between single vacancy states and molecular orbital theory for the molecules. The applicability of x-ray emission spectra to the determination of orbital order of a molecule is illustrated. The proximity of the resonance structure in the fluorine *K* absorption spectra for $CH_{4-n}F_n$($1 \leq n \leq 4$) to their respective fluorine *K* shell thresholds suggests that the resonance structure is due to transitions to excited valance states $1a \rightarrow V^*$ rather than Rydberg states.

Ledbetter, H. M., **Estimation of Debye temperatures by averaging elastic coefficients,** *J. Appl. Phys.* **44,** No. 4, 1451-1454 (Apr. 1973).

Key words: Debye temperature; elastic constants of solids; elasticity.

Elastic Debye temperatures θ were calculated by averaging elastic stiffness coefficients. For cubic symmetry, eight averaging methods were evaluated with respect to a computationally exact θ. Reuss's θ, corresponding to uniform stress, gave better agreement than Voight's θ, corresponding to uniform strain. Hill's geometrical θ gave the best agreement.

Liebman, J. F., Vanderspurt, T. H., **Polarization of X-F bonds,** *J. Fluorine Chem.* **2,** 413-424 (1972/73).

Key words: Fluorine; polarization of bonds; proton assisted reactions; X-F bonds.

We discuss in this paper several reactions of compounds containing X-F (X = C, N, O, F, S and Xe) bonds. An attempt to unify these reactions conceptually is made by suggesting the importance of X-F bond polarization by protic media. Related Lewis-acid-induced polarization reactions can usually be envisioned. Some new reactions and mechanisms are suggested as a consequence of our analysis.

Linsky, J. L., Ayres, T., **Stellar model chromospheres. I. On the temperature minima of F, G, and K stars,** *Astrophys. J.* **180,** No. 2, Part 1, 473-481 (Mar. 1, 1973).

Key words: Spectral line formation; stellar chromospheres.

Brightness temperatures are deduced for the H_{1V} and K_{1V} features of the Ca II resonance lines in Procyon (F5 IV-V), Arcturus (K2 IIIp), and the Sun (G2 V). The brightness temperatures of Procyon and the Sun are in the same ratio as their effective temperatures, suggesting a simple scaling law for the temperature minima of F and early G stars. Arcturus departs from this law in a way that can be explained by CO line blanketing.

Linsky, J. L., **The moon as a proposed radiometric standard for microwave and infrared observations of extended sources,** *Astrophys. J. Suppl. Ser.* **25,** No. 216, 163-204 (Feb. 1, 1973).

Key words: Absolute radiometric calibration—astronomical; absolute radiometric calibration—infrared; absolute radiometric calibration—microwave; lunar surface; lunar thermal emission; moon.

Measured values of the average midnight and morning terminator infrared brightness temperatures of the central portion of the lunar disk can quite accurately determine the mean surface temperature despite likely horizontal and vertical inhomogeneities of the thermal properties of the lunar soil. These data together with laboratory measurements on lunar soil and in situ temperature measurements in and on the lunar surface lead to a mean surface temperature of 220.5 K ± 2.5 percent and a mean temperature 35 K hotter at a depth of 1 m. The monthly average brightness temperature is then estimated as a

function of wavelength between 10 μm and 100 cm taking into account likely temperature dependencies of the thermal conductivity and loss tangent, and the variation of emissivity with wavelength. The accuracy with which the moon can be used as an absolute radiometric standard for extended sources is estimated based on the likely range of lunar thermal and electromagnetic properties.

Loebenstein, W. V., **Adsorption of water on tooth components and related materials,** *J. Dent. Res.* **52,** No. 2, 271-280 (Mar.-Apr. 1973).

Key words: Adsorption; dental materials; hysteresis; sorption; surface area; teeth; water vapor.

By use of a novel, simply constructed, vapor-circulating apparatus, complete water adsorption isotherms, and surface areas derived therefrom, were obtained for tooth components and representative dental materials. Characteristic hysteresis loops were found for all materials studied.

Ludtke, P. R., **Development of insulation transfer-standards using a flat plate calorimeter,** *NBSIR 73-301,* 43 pages (Mar. 1973).

Key words: Calorimeters; fiber glass; foam insulation; insulation transfer-standard; multilayer insulation; thermal insulation; transfer standards.

This program was initiated to develop insulation transfer-standards to be used for evaluating calorimeters at different locations throughout the country. Various types of insulation materials were evaluated for use as transfer-standards. Samples were prepared for preliminary evaluation from selected candidate insulation materials. A 30.5 cm diameter double guarded flat plate calorimeter at MSFC was provided for testing. The calorimeter was checked and the boiloff-gas instrumentation updated. Thermal conductivity screening tests were conducted using liquid nitrogen on open and closed cell foam and fiber glass samples. The mean thermal conductivity values of the samples tested during the screening tests are presented. Compliance with the proposed ASTM Standard Method of Test for Heat Flux Through Evacuated Insulations was stressed.

Mabie, C. P., Jr., **Petrographic study of the refractory performance of high-fusing dental alloy investments: I. High-fired, phosphate-bonded investments,** *J. Dent. Res.* **52,** No. 1, 96-110 (Jan.-Feb. 1973).

Key words: Alloy; casting; dental; investment; petrography.

Detailed x-ray, optical microscopic, optical emission, and electron probe analyses of a phosphate-bonded investment before and after firing and after casting were made. Complex sintering reactions that involve incipient liquefaction generate bonds in the fired investment. The refractory behavior of this investment, which is reflected by the extent of liquefaction induced by casting, may influence casting roughness, fit, and porosity.

Mele, A., Okabe, H., **Distribution of the excess energy in CN $B\,^2\Sigma$ produced in photodissociation of cyanogen halides and hydrogen cyanide,** *J. Chem. Phys.* **51,** No. 11, 4798-4808 (Dec. 1, 1969).

Key words: BrCN; CN $B\,^2\Sigma$; ClCN; energy partition; HCN; ICN; photodissociation; vacuum ultraviolet.

The vibrational and rotational excitations of CN $B^2\Sigma$ produced in photodissociation of cyanogen halides and hydrogen cyanide in the vacuum ultraviolet have been measured as a function of incident wavelengths. More than 70 percent of the total population is in levels up to $v'=3$. No population inversion was observed, indicating the photodissociation takes place without much change in the equilibrium C-N bond distance. The percent conversion of the excess energy to vibration is approximately 20 percent for cyanogen halides and about 12 percent for hydrogen cyanide, irrespective of the amount of excess energy, which is much less than that expected from the equipartition of energy in all vibrational degrees of freedom of the molecule. The rotational levels of CN $B\,^2\Sigma$ are highly excited for all molecules. The extent of conversion of the excess energy to rotation is of the order of 10-20 percent for ICN and ClCN, and only several percent for BrCN and HCN. The remaining energy must be distributed as kinetic energy between CN $B\,^2\Sigma$ and atoms. The vibrational and rotational distributions are discussed in terms of the equilibrium geometries of the ground and excited molecules and of the final products. The CN $A\,^2\Pi$ state is also formed in photodissociation and apparently not directly but through the CN $B\,^2\Sigma$. The intensity of the CN red emission is much less than that of the violet. Various other photodissociation processes are discussed. In general, the extent of conversion of the excess energy to vibration is much less than that expected from the equipartition theory for most triatomic molecules. No vibrational population inversion has been observed.

Mihalas, D., Hummer, D. G., **Analyses of light-ion spectra in stellar atmospheres. III. Nitrogen III in the O stars,** *Astrophys. J.* **179,** No. 3, 827-845 (Feb. 1, 1973).

Key words: Dielectronic recombination; doubly ionized nitrogen; emission lines; O-stars; stellar atmospheres; stellar spectra.

An analysis of the N III emission lines in O stars has been carried out on the basis of a detailed solution of the coupled statistical-equilibrium and transfer equations for a multiline, miltilevel, multi-ion ensemble. Our calculations, using static, plane-parallel models reproduce successfully the observed emission at λλ4634, 4640, 4641 ($3p\,^2P^0 - 3d^2D$) and absorption at λλ4097, 4103 ($3s\,^2S - 3p\,^2P^0$). The $^2P^{0-2}D$ multiplet is found to come into emission at the observed temperature for both main-sequence and low-gravity objects. The equivalent widths of the emission lines agree very well with those measured for the class of Of stars thought to have compact atmospheres, i.e., those classified as O((f)) by Walborn. In these stars the basic physical mechanism responsible for this phenomenon is the overpopulation of $3d$ by means of dielectronic recombinations from the low-lying $2s2p(^1P^0)3d$ autoionizing states with cascades $3d \rightarrow 3p$. The $3p$ state is drained by the "two-electron jumps" coupling $3p$ to the $2s - 3p$ lines. $3s$-$3p$ lines. The possible importance of the Swings mechanism to the fully developed Of stars (in Walborn's sense) is pointed out, and the irrelevance of the Bowen mechanism to all Of stars is firmly demonstrated. The fact that the N III emission lines can be produced in static nonextended atmospheres in radiative equilibrium has the far-reaching significance that the presence of emission lines in a spectrum is not in itself sufficient evidence for the existence of a stellar chromosphere (i.e., an extended, nonradiatively heated region).

Milligan, D. E., Jacox, M. E., **Matrix isolation spectroscopy,** Chapter 1 in *MTP (Medical and Technical Publishing) International Review of Science. Physical Chemistry Series One. Vol. 3. Spectroscopy,* D. A. Ramsay, Ed., pp. 1-32 (Butterworth & Co., Ltd., London, England and University Park Press, Baltimore, Md., 1972).

Key words: Atomic spectra; electronic spectra; free radicals; high-temperature species; matrix isolation; molecular ions; reactive molecules; rotation in matrices; vibrational spectra.

Studies of the infrared and ultraviolet spectra of atoms and molecules isolated in inert solid matrices at cryogenic temperatures are reviewed, with emphasis on the basic principles of the technique and on publications during the period 1969-1971.

Milligan, D. E., Jacox, M. E., McAuley, J. H., Smith, C. E., **Matrix isolation study of the vacuum-ultraviolet photolysis of $HCClF_2$ and of $HCCl_2F$. Infrared spectra of the parent molecules and of the $ClCF_2$ and $FCCl_2$ free radicals,** *J. Mol. Spectrosc.* **45,** No. 3, 377-403 (Mar. 1973).

Key words: $ClCF_2$; $DCClF_2$; $DCCl_2F$; $FCCl_2$; $HCClF_2$; $HCCl_2F$; infrared spectrum; matrix isolation; vacuum ultraviolet photolysis.

Studies of the vacuum-ultraviolet photolysis of $HCClF_2$ and of $HCCl_2F$ isolated in argon and nitrogen matrices at 14 K have led to the infrared spectroscopic identification of the free radicals $ClCF_2$ and FCl_2, respectively. Support for this identification has been obtained from studies of the vacuum-ultraviolet photolysis of $DCClF_2$, of $DCCl_2F$, and of $H^{13}CCl_2F$, as well as from studies of halogen-atom abstraction from $CClF_3$ and from CCl_3F by sodium atoms in an argon matrix environment. The C–Cl bonds of $FCCl_2$, like those of CCl_3 and of $HCCl_2$, appear to be exceptionally strong. Gas-phase infrared spectral data are also reported for $DCClF_2$ and for $DCCl_2F$, not previously studied. Vibrational assignments are proposed for these two molecules, and data supporting the reassignment of one of the C–F stretching fundamentals of $HCClF_2$ are presented.

Moore, R. T. **Penetration resistance tests of reinforced concrete barriers,** *NBSIR 73-101*, 83 pages (Dec. 1972).

Key words: Barrier penetration; intrusion detection; physical security; reinforced concrete.

This report describes the results of a series of penetration tests on six concrete slabs. The tests were conducted at the U.S. Army Corps of Engineers Construction Engineering Research Laboratory in Champaign, Ill., during the period October 31 through November 3, 1972. Several alternative methods of attack were employed, and the time to penetrate, and in some instances, to produce a 96-inch^2 opening, was measured, and estimates were developed regarding the acoustic, ultrasonic and vibrational disturbances produced by the attacks.

Depending upon the attack technique, a man-passable opening can be made in 4-inch thick reinforced concrete in times ranging from 4 to nearly 15 minutes. The corresponding times for 8-inch thick reinforced regular concrete range from about 7 to 25 minutes and from about 20 to 30 minutes fibrous concrete.

With the exception of the diamond core drill, detection should be relatively easy by the combined acoustic, ultrasonic or vibrational disturbances produced by the attacks even though not all techniques produce all three types of disturbances.

Nahman, N. S., **A note on the transition (rise) time versus line length in coaxial cables,** *IFEE Trans. Circuit Theory* **CT-20,** No. 2, 165-167 (Mar. 1973).

Nahman, N. S., **Miniature superconductive coaxial transmission lines,** *Proc. IEEE* **61,** No. 1, 76-79 (Jan. 1973).

Key words: Cables; coaxial; cryogenic; miniature; pulse delay; superconducting; telecommunications; transmission lines.

This is a review paper concisely tracing the development of miniature superconductive coaxial transmission lines from the original invention as a vertical channel signal delay line for fractional nanosecond pulse oscillography to present-day work towards highly compact, broad-band, and low-loss telecommunication cables. The present state of development yields a 1.6-mm coaxial line operating at 4.2 K and having Pb conductors, polyethylene dielectric, $Z_0 = 50 \pm 0.3\ \Omega$ and a 1-GHz attenuation of the order of 1 dB/km. The attenuation up to 1 GHz is mainly due to dielectric losses.

Okabe, H., Mele, A., **Photodissociation of NCN_3 in the vacuum-ultraviolet production of CN $B\ ^2\Sigma$ and NCN $A\ ^3\Pi$,** *J. Chem. Phys.* **51,** No. 5, 2100-2106 (Sept. 1, 1969).

Key words: Absorption coefficient; bond dissociation energies; CN $B\ ^2\Sigma$; NCN $A\ ^3\Pi$; NCN_3; photodissociation; vacuum ultraviolet.

The photodissociation of NCN_3 in the vacuum ultraviolet has yielded CN $B\ ^2\Sigma$ and NCN $A\ ^3\Pi$. No NCN $^1\Pi$ was detected. The fluorescence intensity of the CN violet emission, I_f/I_0, was measured as a function of incident wavelength, λ. The I_f/I_0-vs-λ curve shows structure, indicating that the process

$$NCN_3 \rightarrow CN\ B\ ^2\Sigma + N_3,$$

is predissociative. The yield at 1216 Å is estimated to be approximately 2.5 percent. The threshold wavelength of incident photons to yield CN $B\ ^2\Sigma$ is 1685 ± 20 Å. The production of NCN $A\ ^3\Pi$ is attributed to the formation of $N_2\ A\ ^3\Sigma$

$$NCN_3 \rightarrow NCN\ \chi\ ^3\Sigma + N_2\ A\ ^3\Sigma,$$

with the threshold wavelength of 1915 ± 30 Å followed by the sensitized reaction, $N_2\ A\ ^3\Sigma + NCN_3 \rightarrow NCN\ A\ ^3\Pi + 2N_2$. Bond dissociation energies obtained from threshold energies are $D(NC-N_3) = 4.2 \pm 0.1$ eV ($= 96 \pm 2$ kcal mole^{-1}) and $D(NCN-N_2) = 0.3 \pm 0.1$ eV ($= 7 \pm 2$ kcal mole^{-1}) where the error limit indicates an experimental uncertainty of the threshold energy measurements. Estimated heats of formation are $\Delta H_f^\circ(NCN_3) = 4.7 \pm 0.2$ eV ($= 108 \pm 5$ kcal mole^{-1}) and $\Delta H_f^\circ(NCN) = 5.0 \pm 0.2$ eV ($= 115 \pm 5$ kcal mole^{-1}) from which $D(N-CN)$ of 4.3 ± 0.2 eV ($= 99 \pm 5$ kcal mole^{-1}) is obtained. The absorption coefficient of NCN_3 in the region 1200 to 2000 Å has been measured. A comparison is made of bond energies of several azide compounds.

Page, C. H., **Ambiguities in the use of unit names,** *Science* **179,** 873-875 (Mar. 2, 1973).

Key words: Gyromagnetic ratio; measurement units; physical constants; SI units.

Experimental determinations of physical constants are usually reported in the literature in accepted units, such as SI. The actual measurements are *not* made in terms of the reported units, but in terms of the units maintained by a standards laboratory. This lack of precise identification of the results leads to ambiguities in comparing data from different countries, and in adjusting constants to make a most consistent set.

The semantics and algebra of the situation are presented, with a tentative resolution of the problem.

Parker, R. L., **Crystal growth,** Article in *Yearbook of Science and Technology, McGraw-Hill Encyclopedia of Science and Technology*, pp. 158-160 (McGraw-Hill Book Co., New York, N.Y., 1973).

Key words: Crystal growth; crystallization; growth techniques; morphological stability.

The field of crystal growth is briefly reviewed and a number of new developments noted.

Pezoldt, V. J., Persensky, J. J., **Human factors evaluation of a voice encoding system,** *NBSIR 73-131*, 57 pages (Mar. 1973).

Key words: Feasibility; keyboard alternative; man-machine interface; postal sorting; voice encoding.

The feasibility of employing voice encoding as an alternative to keyboard entry for postal sorting application was investigated in two phases. Phase I was a simulated parcel sorting situation. Phase II was performed to determine man-machine interface limitations. The results of this study led to the following conclusion and recommendations. Voice encoding would be of limited value to high speed parcel sorting unless it was used only during slack periods or the current facer and keyer both use a VES. Voice encoding could be applied to other sorting tasks. USPS tasks should be analyzed for the possibility of such application. Other voice encoding systems should be evaluated. These systems should have single command training capability, a cancel capability accessed by other than a unique verbal command, and should require infrequent system training.

Phelps, A. V., **Collision cross sections for electrons with atmospheric species,** (Proc. IAGA Symp. on Aurora and Airglow, Moscow, Aug. 1971), *Ann. Geophys.* **28,** No. 3, 611-625 (1972).

Key words: Atmospheric gases; cross sections; electron-ion recombination; electrons; review of data.

Recent laboratory measurements have yielded much detail concerning cross sections for the elastic and inelastic scattering of electrons by stable atmospheric species. Measurements of the energy and angular distributions of inelastically scattered electrons have yielded cross sections for excitation of the principal levels of N_2, O_2 and He

and for the distribution of secondary electron energies resulting from collisional ionization of these gases. Electron beam measurements of cross sections for the production of radiation from N_2, O_2 and N_2^+ provide dnta of direct applicability to calculations of auroral intensities, etc. Similar data are also obtained from measurements of electron induced fluorescence. Swarm experiments provide cross section data for vibrational and rotational excitation of O_2 and N_2 at electron energies below about 1 eV. Afterglow and shock tube measurements have yielded the electron energy and temperature dependence of the electron-ion recombination for a few positive ions. Theoretical calculations of the cross sections for excitation of atomic oxygen and nitrogen are particularly important since laboratory measurements are not generally available.

Quigley, D. F., **USAC transferability,** *NBSIR 73-183*, 71 pages (Apr. 1973).

Quindry, T. L., **Acoustical evaluation of a single family attached steel-frame modular housing system constructed on an Operation BREAKTHROUGH prototype site,** *NBSIR 73-190*, 21 pages (Apr. 1973).

Quindry, T. L., **Acoustical evaluation of a single family attached wood-frame modular housing system constructed on an Operation BREAKTHROUGH prototype site,** *NBSIR 73-191*, 21 pages (Apr. 1973).

Quindry, T. L., **Acoustical evaluation of a single family detached honeycomb panel housing system constructed on an Operation BREAKTHROUGH prototype site,** *NBSIR 73-192*, 19 pages (Apr. 1973).

Reader, J., **Comment on "Configuration interaction in the x-ray photoelectron spectra of alkali halides,"** *Phys. Rev. A* **7**, No. 3, 1431-1433 (Apr. 1973).

Key words: Photoelectron spectra; potassium; rubidium; sodium; x-rays.

Recently obtained data on doubly ionized Rb in the free state indicate that the satellite of the Rb(4s) resonance in the photoelectron spectra of RbF and RbCl is primarily due to a $4s^24p^24d\ ^2S$ final state rather than a $4s^24p^45s\ ^2S$ one. For the potassium salts, the satellite of the K(3s) resonance is most likely due to a $3s^23p^43d\ ^2S$ final state. The absence of a satellite for the Na(2s) resonance for the sodium salt is due to the nonexistence of 2d electrons.

Reed, R. P., Schramm, R. E., Clark, A. F., **Mechanical, thermal, and electrical properties of selected polymers,** *Cryogenics* **13**, No. 2, 67-82 (Feb. 1973).

Key words: Compilation; electrical properties; mechanical properties; plastics; polymers; thermal properties.

An extensive compilation has been completed on the mechanical, thermal, and electrical properties of six commercially available polymers. These data are discussed and summarized here as a function of temperature, radiation, and frequency. A brief description and characterization of each polymer is included.

Richmond, J. C., Walters, E. L., **Development of a standard for passive night vision devices, a progress report,** (Proc. Carnahan Conf. on Electronic Crime Countermeasures, Lexington, Ky., Apr. 25-27, 1973), Paper in *Proceedings 1973 Carnahan Conference on Electronic Crime Countermeasures*, UKY Bull. 102, 145-156 (Apr. 1973).

Key words: Contrast transfer function; distortion; flare; image intensifiers; law enforcement; light equivalent background; light induced background; night vision devices; optical gain.

The National Bureau of Standards is developing a standard for night vision devices for use by law enforcement agencies. This work is sponsored by the Law Enforcement Standards Laboratory of NBS, which is financed by the National Institute of Law Enforcement and Criminal Justice of the Department of Justice.

The paper discusses image quality criteria in general, and gives reasons for selecting contrast transfer function (CTF) and distortion as the primary criteria for image quality of night vision devices. The test equipment and procedures used at NBS for testing night vision devices will be described. Specific tests to be included are optical gain, light equivalent background, and flare in addition to contrast transfer function and distortion.

Roberts, J. R., Andersen, T., Sørensen, G., **Determination of atomic lifetimes and absolute oscillator strengths for neutral and ionized titanium,** *Astrophys. J.* **181**, 567-586 (Apr. 15, 1973).

Key words: Absolute transition probabilities; arc; beam foil; experimental; lifetimes; titanium.

Measurements of atomic lifetimes by the beam-foil technique and branching ratios by use of a gas-flow stabilized arc have led to an experimental determination of absolute oscillator strengths of Ti II. Some lifetimes of Ti I, Ti III, and Ti IV are also presented.

Roberts, J. R., Andersen, T., Sørensen, G., **Determination of atomic lifetimes and absolute oscillator strengths for neutral and ionized vanadium,** *Astrophys. J.* **181**, 587-604 (Apr. 15, 1973).

Key words: Absolute transition probabilities; arc; beam foil; experimental; lifetimes; vanadium.

Measurements of atomic lifetimes by the beam-foil technique and branching ratios by use of a gas-flow stabilized arc have led to an experimental determination of absolute and relative oscillator strengths of V I and V II. Some lifetimes of V III are also presented.

Robertson, B., **Introduction to field operators in quantum mechanics,** *Amer. J. Phys.* **41**, 678-690 (May 1973).

Rossiter, W. J., Jr., **Outdoor performance of plastics. Z. Final update of weathering data,** *NBSIR 73-146*, 103 pages (Mar. 1973).

Ruff, A. W., Ives, L. K., **On the temperature dependence of stacking fault energy in cubic and hexagonal silver-tin alloys,** *Phys. Status Solidi A*, No. 16, 133-149 (1973).

Key words: Annealing; cubic alloy; dislocation; electron microscopy; hexagonal alloy; silver-tin alloy; stacking fault energy.

Measurements on extended dislocation nodes and double ribbons have been made between room temperature and 500 °C using transmission electron microscopy. Two low stacking fault energy (SFE) alloys with compositions near the mixed phase region were principally studied; 9 at% Sn (f.c.c.) and 11.9 at% Sn (hexagonal). The SFE in the cubic alloy increased *reversibly* with increasing temperature from 270 to 500 °C; a corresponding decrease in SFE was observed in the hexagonal alloy. Both alloys showed a substantial *irreversible* change in faulted defect size upon annealing, comparing results in as-deformed specimens with those from material annealed above 270 °C. The irreversible behavior is attributed to solute pinning of the partial dislocations. The dependence of SFE on composition throughout the f.c.c. and hexagonal phase regions is considered in light of these results.

Shaver, J. R., Masters, L. W., Reichard, T. W., Pielert, J. H., **Environmental evaluation of polyurethane foam core sandwich panel construction,** *NBSIR 73-105*, 47 pages (Dec. 1972).

Shields, J. Q., **Phase-angle characteristics of cross capacitors,** *IEEE Trans. Instrum. Meas.* **IM-21**, No. 4, 365-368 (Nov. 1972).

Key words: Capacitor; cross capacitor; dielectric films; loss angle; phase angle.

It has been found that under proper conditions thin dielectric films on the electrodes of certain types of cylindrical cross capacitors tend only to produce equal and opposite contributions to the phase angles

of the two cross capacitances. To a lesser degree, this same type of cancellation effect has been found to be associated with toroidal cross capacitors.

Shoub, H., Son, B. C., **Fire endurance tests of plywood on steel joist floor assemblies, with and without ceiling,** *NBSIR 73-141*, 37 pages (Mar. 1972).

Sindt, C. F., **Insulation of liquid oxygen dewars,** *NBSIR 73-308*, 44 pages (Apr. 1973).

Key words: Cryogenic insulation; insulation; LOX dewars; microspheres; polyurethane foam.

The Navy has experienced failure of vacuum insulation in dewars used for storage and handling of liquefied breathing oxygen for aircraft pilots. Because of the vacuum insulation failures, a search was made for a more rugged insulation that has thermal performance similar to the currently used vacuum with multilayer or powder. No system was found that compared in thermal performance and did not require a vacuum. Two systems were experimentally evaluated that did not require vacuum. One was polyurethane foam with an intermediate fiber glass shell and the other was glass bubbles in argon gas at one atmosphere pressure. The polyurethane foam system was successful in that no cracks penetrated to the outside surface; however, the average thermal conductivity was 160 μW/cm-K which is about 15 times greater than vacuum and powder. The glass bubbles in argon gas was also successful since the argon gas pressure always remained high enough to prevent air and moisture from entering the insulation through small leaks in the outer shell. The thermal performance was poorer than the polyurethane foam. The average thermal conductivity was 212 μW/cm-K or about 20 times greater than for the same glass bubbles in a vacuum.

Son, B. C. **Fire endurance test of a fiber glass reinforced polyester double wall assembly,** *NBSIR 73-168*, 27 pages (Apr. 1973).

Son, B. C., **Fire endurance test of an interdwelling double wall constructed of polyurethane foam-filled sandwich panels,** *NBSIR 73-170*, 27 pages (Apr. 1973).

Son, B. C., **Fire endurance test of an interdwelling double wall construction of paper honeycomb and gypsum board,** *NBSIR 73-166*, 24 pages (Apr. 1973).

Son, B. C., **Fire endurance test of a roof/ceiling construction of paper honeycomb and gypsum board,** *NBSIR 73-167*, 20 pages (Jan. 1973).

Son, D. C., **Fire endurance test of a steel sandwich panel floor construction,** *NBSIR 73-164*, 25 pages (Apr. 1973).

Son, B. C., **Fire endurance test of a wood stud interdwelling double wall construction,** *NBSIR 73-169*, 21 pages (Apr. 1973).

Son, B. C., **Fire endurance test of plywood-faced exterior walls for single family housing,** *NBSIR 73-140*, 24 pages (Mar. 1973).

Son, B. C., **Fire endurance test on a steel tubular column protected with gypsum board,** *NBSIR 73-165*, 23 pages (Apr. 1973).

Son, B. C., **Fire endurance tests of steel sandwich panel exterior wall and roof/ceiling constructions,** *NBSIR 73-135*, 38 pages (Dec. 1972).

Son, B. C., Shoub, H., **Fire endurance tests of double module walls of gypsum board and steel studs,** *NBSIR 73-173*, 32 pages (Apr. 1973).

Spencer, L. V., Woolf, S., **"Forced-reflection" collimators and the n-n scattering experiment,** *Nucl. Instrum. Methods* **97,** 567-576 (1971).

Key words: Air ducts in shields; collimators; neutron instrumentation; neutron-neutron scattering; neutron penetration; reentrant holes.

An approach to neutron collimator design is suggested in which wall-emergent neutrons are forced to reflect from the surface of each (tapered) segment beyond the point of emergence. Designs of this type, together with a suggested design for a proposed neutron-neutron scattering experiment, are compared in simple Monte Carlo and analytic studies.

Spicer, B. M., Danos, M., **Quartet structure and collective effects in the scandium isotopes,** *Z. Phys.* **246,** 97-103 (1971).

Key words Core polarization; electromagnetic transitions; nuclear spectroscopy; nuclear structure; quadrupole moment; quartet structure.

The systematics of the excitation energies of the non-normal parity states of the scandium isotopes are interpreted in terms of the formation of a quartet of $1f_{7/2}$ nucleons. Calculation of the *B(E2)* value for a typical radiative transition between non-normal parity states in ^{43}Sc, using this model, shows that the transition must involve more than the single quartet formed in the $1f_{7/2}$ shell; that is, that core polarization is an important factor in determining the *B(E2)* value.

Stabler, T. M., **U.S. membership in the International Organization of Legal Metrology,** *NBSIR 73-159*, 12 pages (Apr. 1973).

Stein, P. G., Boyle, D. R., **How to cope with nickel and diming in your minicomputer,** (Proc. IEEE Minicomputer Conf. on Trends and Applications, National Bureau of Standards, Gaithersburg, Md., Apr. 4, 1973), *Symposium Record*, IEEE Catalog No. 73CHO 760-9 C, pp. 5-7 (1973).

Stein, P. G., **Communications protocols: The search for SYN,** *Datamation* **19,** No. 4, 55-57 (Apr. 1973).

Stephenson, J. C., **Vibrational excitation and relaxation of the CO($v=1$) and CO($v=2$) states,** *Appl. Phys. Lett.* **22,** No. 11, 576-578 (June 1, 1973).

Key words: Carbon monoxide; infrared lasers; laser pumping of molecules; vibrational energy transfer.

Pulses from a CO_2 laser have been frequency doubled in a tellurium crystal and used to optically pump the first vibrational level in room-temperature CO. By monitoring infrared fluorescence from the $v=1$ and $v=2$ states, the rate constant for the process $CO(v=1)+CO(v=1)\rightarrow CO(v=0)+CO(v=2)$ has been determined. Other rate constants involving the $CO(v=1)$ level are also reported.

Stoltenberg, R. E., **RF null detector NBS/SND,** *NBSIR 73-302*, 88 pages (June 1973).

Swartzendruber, L. J., Evans, B. J., **Giant hyperfine field at the antimony site in the Heusler-alloy Pd_2MnSb,** *Phys. Lett.* **38A,** No. 7, 511-512 (Mar. 27, 1972).

Key words: Alloys; hyperfine field; Mn; Mössbauer effect; Pd; Sb.

The magnetic hyperfine field at ^{121}Sb in Pd_2MnSb has the anomalously large value (at 100 k) of $\pm 579 \pm 5$ kG. In the closely related compound PdMnSb we find $\pm 302 \pm 5$ kG, similar to other ferromagnetic intermetallics containing Mn and Sb.

Taragin, M. F., Eisenstein, J. C., Haller, W., **Mössbauer study of Fe^{57} in an aluminophosphate glass,** *Phys. Chem. Glasses* **13,** No. 5, 149-152 (Oct. 1972).

Key words: Aluminophosphate glass; Fe^{57}; glass; iron; Mössbauer spectra; phosphate glass.

Mössbauer spectra of an aluminophosphate glass which contains 10 percent Fe_3O_4 were obtained from room temperature to 450 °C. Fe^{2+} and Fe^{3+} ions are present. The isomer shift and quadrupole splitting for these ions are each given as a function of temperature, and it appears that both ions are in octahedral coordination. The ratio of the product of the Mössbauer fraction multiplied by the concentration ratio of Fe^{3+} to Fe^{2+} was determined. This ratio varies with temperature. A possible explanation is that the effective Debye temperatures are different for the two ionic species, being 385 K for Fe^{3+} and 230 K for Fe^{2+}. The difference may possibly be attributed to differences in the sites occupied by Fe^{3+} and Fe^{2+} in the glass structure.

Tate, E. L., **Anglo-American code implementation,** Paper in *Advances in Librarianship* **3,** 167-194 (Seminar Press, Inc., New York and London, 1972).

Taylor, B. N., **Determining the Avogadro constant to high accuracy via improved measurements of the absolute ampere,** *Metrologia* **9,** No. 1, 21-23 (1973).

Key words: Absolute ampere; Avogadro number; fundamental constants.

It is shown how an improved measurement of the absolute ampere, that is, the ratio of a particular as-maintained unit of current to the absolute or *Systeme International d'Unites* (SI) unit of current, can now lead to an improved value of the Avogadro constant.

Thurber, W. R., Lewis, D. C., Bullis, W. M., **Resistivity and carrier lifetime in gold-doped silicon,** *NBSIR 73-128,* 56 pages (Jan. 31, 1973).

Utech, H. P., **Injuries show what protection improved clothing should offer,** *Fire Eng.* **125,** No. 4, 47-49 (Apr. 1972).

Key words: Firefighter injuries; injury statistics; occupational injuries; protective clothing; protective equipment.

Firefighting continues to be one of this country's most hazardous occupations. Statistics on firefighter injuries are analyzed to identify the problem areas. This analysis indicates that improvement in the design of protective clothing and equipment can lead to the reduction of firefighter injuries. Improved respiratory protection, reduction in the weight and bulk of clothing and equipment, and better protection against impact, are the primary needs.

Waksman, D., Skoda, L. F., Clark, E. J., Godette, M., **Evaluation of lead paint hazard elimination methods, Part II,** *NBSIR 73-127,* 77 pages (Mar. 1973).

Key words: Deleading methods; lead paint poisoning; performance; properties.

Four major classifications of procedures that should be considered when selecting a method for the elimination of the lead paint hazard are analyzed in this report. They are: surface repair methods, surface finish methods, cover up methods with unfinished membrane materials, and cover up methods with prefinished rigid materials. The attributes associated with each type of method were considered and analyzed in terms of inaccessibility of the leaded paint and implementation considerations. Recommendations are made for the in-use performance properties of surfaces.

Waxman, M., Hilsenrath, J., Chen, W. T., **Compressibility factor and the second virial coefficient of boron trifluoride from 0 to 225 °C and for pressures up to 250 bar,** *J. Chem. Phys.* **58,** No. 9, 3692-3701 (May 1, 1973).

Key words: Boron trifluoride; density, second virial coefficients; gas, compressibility.

The isothermal compressibility factor of boron trifluoride has been determined from a regression analysis of Burnett PVT measurements to an accuracy of 0.1% at 13 temperatures from 0 to 225 °C and for pressures up to 250 bar. The analysis has also yielded the second virial coefficient for each temperature. A correction for the presence of sorption has been included in the data reduction.

Weisman, I. D., **^{109}Ag Knight shift in an $Ag_{0.96}Al_{0.04}$ alloy,** *J. Chem. Eng. Data* **18,** No. 2, 146 (Apr. 1973).

Wiederhorn, S. M., Johnson, H., **Effect of electrolyte pH on crack propagation in glass,** *J. Amer. Ceram. Soc.* **56,** No. 4, 192-197 (Apr. 1973).

Key words: Crack propagation; fracture; fracture mechanics; glass; strength; stress corrosion.

Crack velocities in glass in various acids, bases, and neutral solutions were studied using the double-cantilever-beam technique. Results are explained in terms of crack-tip pH, which is controlled by the electrolyte at low crack velocities and by the glass composition at high velocities. The crack velocity data are consistent with the known dependence of strength on pH for soda-lime silicate glass. Results also suggest that the slope of the universal fatigue curve should depend on surface pH.

Wiederhorn, S. M., Johnson, H., **Influence of sodium-hydrogen ion exchange on crack propagation in soda-lime silicate glass,** *J. Amer. Ceram. Soc. Discussions and Notes* **56,** No. 2, 108-109 (Feb. 1973).

Key words: Crack propagation; fracture; fracture mechanics; glass; strength; stress corrosion.

The effect of sodium-hydrogen ion exchange on crack propagation was studied. It was concluded that stresses arising from ion exchange play a minor role in determining the strength of glass when strength is controlled by crack propagation.

Wiederhorn, S. M., **Prevention of failure in glass by proof-testing,** *J. Amer. Ceram. Soc.* **56,** No. 4, 227-228 (Apr. 1973).

Key words: Crack propagation; failure prevention; fracture; glass; proof testing.

A method of predicting the minimum lifetime of glass under static load is presented. The method involves proof testing and a knowledge of the growth behavior of cracks in glass.

Wong, C. Y., Tamura, T., Marshak, H., Langsford, A., **Effects of nuclear collectivity on the total neutron cross section,** *Particles Nucl.* **4,** 163-174 (1972).

Key words: Coupled channel calculations; holmium^{165}; nuclear collectivity; nuclear Ramsauer effect; optical model; total neutron cross section.

A study is made of the effect of the nuclear collectivity on the variation of the total neutron cross section with respect to the incident energy ranging from 4 to 20 MeV. It is found that the higher the collectivity, the smoother is the excitation function, for both deformed and vibrational nuclei. This feature is understood qualitatively in terms of the nuclear Ramsauer effect and is explained quantitatively by coupled-channel calculations. These calculations further reveal that deformed nuclei have larger total cross sections and smoother variations than do the vibrational nuclei. For vibrational nuclei, it is also found that the quadrupole deformation has a slightly larger effect on the smoothness than does the octupole deformation, if they have the same deformation parameter.

Yakowitz, H., Jacobs, M. H., Hunneyball, P. D., **Analysis of urban particulates by means of combined electron microscopy and x-ray microanalysis,** *Micron* **3,** 498-505 (1972).

Key words: Air pollution; composite dust; electron microanalysis; electron microscopy; submicrometer; urban particulates.

Particles from four samples of urban particulate matter collected in the U.S.A. were analysed by combined electron microscopy and

microanalysis (EMMA). In the case of material collected at Baltimore, Md., lead was found to be present only in particles ranging from 0.05 μm to about 0.3 μm in size. The lead bearing particles did not seem to associate with other particles. Analysis of a fly ash specimen showed no qualitative or significant quantitative variation in chemistry as a function of size for the most prevalent type of particle found. Since it may be crucial to have information about particles smaller than 0.5 μm in air pollution studies, EMMA should be included with spectrometric analysis, x-ray diffraction, scanning electron microscopy and electron probe microanalysis as a primary tool for particulate analysis.

Yancey, C. W., Somes, N. F., **Structural tests of a wood-frame housing module,** *NBSIR 73-121*, 111 pages (Mar. 26, 1973).

Yokel, F. Y., Reichard, T. W., **Evaluation of the column connections used in a precast concrete modular housing system,** *NBSIR 73-148*, 90 pages (Mar. 26, 1973).

Yokel, F. Y., **Study of the local resistance of conventional plywood subflooring to concentrated load,** *NBSIR 73-116*, 64 pages (Mar. 26, 1973).

Yule, H. P., **Conversational text editor for a laboratory minicomputer,** *Anal. Chem.* **44,** No. 2, 430 (Feb. 1972).

Key words: Assembly; conversational; editor; language; minicomputer; text.

A conversational text editing program for the Varian 620i minicomputer is described. Virtually identical in operation with a commercially available, time-sharing, conversational text editor, this program permits rapid and easy modification of text, including insertion, deletion, and editing of lines of text.

Zalewski, E. F., Keller, R. A., **Pressure dependence of intersystem crossing and triplet internal conversion in naphthalene vapor,** (Proc. Int. Conf. on Luminescence, University of Delaware, Newark, Del., Aug. 25-29, 1969), *J. Lumin.* **1, 2,** 143-153 (1970).

Key words: Internal conversion; intersystem crossing; naphthalene vapor absorption spectrum; pressure effect on absorption spectrum; radiationless transitions.

The pressure dependence of intersystem crossing and internal conversion in the triplet manifold of naphthalene vapor was studied by monitoring the concentration of both the singlet ground state at the peak of and one minute after flash excitation, and the lowest triplet state at the peak of the flash. Helium was used as the foreign gas up to pressures of 460 torr. The pressure of naphthalene was 0.026 torr in all cases. In summary, the experimental results are: (1) Ground state depletion during the flash is independent of pressure. (2) The population of the lowest triplet state, experimentally zero initially, increases with increasing helium pressure and becomes constant above 100 torr. (3) Photodecomposition decreases with increasing pressure of helium and finally approaches zero at pressures greater than 100 torr. The conclusions which result from these observations are: (1) In the absence of collisions, photochemical decomposition of excited triplet molecules can compete effectively with internal conversion. (2) Intersystem crossing is not pressure dependent in naphthalene.

Zimmerman, J. E., **Possible parametric capacitance in Josephson junctions,** *Phys. Lett.* **42A,** No. 5, 375-376 (Jan. 1, 1973).

Key words: Josephson effect; parametric capacitance.

The capacitance of a Josephson junction is much larger (at least in the low frequency limit) than the classical value $\epsilon A/l$, and is a function of the phase difference θ_0.

**Publications with prices and SD Catalog numbers may be purchased directly from the Superintendent of Documents, U.S. Government Printing Office, Washington, D.C. 20402 (foreign: one-fourth additional). Microfiche copies are available from the National Technical Information Service (NTIS), Springfield, Va. 22151. Reprints from outside journals and the NBS Journal of Research may often be obtained directly from the authors.*

JOURNAL OF RESEARCH of the National Bureau of Standards—A. Physics and Chemistry
Vol. 77A, No. 6, November–December 1973

INDEX TO VOLUME 77A

January to December 1973

A

Page

Absolute isotopic abundance ratio and atomic weight of a reference sample of rhenium ... 691
Absolute ratio ... 691
Acetylene formation ... 109
AgBr ... 569
AgCl ... 569
AgI ... 569
$AgNO_3$ ... 569
Air flow rate as a test for gage block wringing ... 667
Alumina ... 391
Aluminum fluoride ... 341
Aluminum hydrofluorides ... 341
An adiabatic solution calorimeter ... 179
An Alumina standard reference material for resonance frequency and dynamic elastic moduli measurement. II. Characteristic values for use from 25 °C to 1000 °C ... 391
An experimental search for gaseous reactivity between AlF_3 and HF near 1200 K ... 341
Anderson, R. L., Guildner, L. A., Edsinger, R. E., Air flow rate as a test for gage block wringing ... 667
Anionic polystyrenes ... 157
Anisotropic ... 713
Atomic weight ... 691
Ausloos, P., Rebbert, R. E., Photochemistry of methane in the photoionization region ... 101
—, —, Radiolysis of methane. Formation of acetylene ... 109
—, —, *Lias, S. G.*, Pulse radiolysis of methane ... 249
—, —, *Wijnen, M. H. J.*, Gas phase far ultraviolet photolysis and radiolysis of vinyl chloride ... 243
Avinmelech, Y., Moreno, E. C., Brown, W. E., Solubility and surface properties of finely divided hydroxyapatite ... 149

B

BaF_2 ... 659
BeF_2 ... 227
$Hf°_{298.15K}/BeF_2(c)$ ... 227
Bennett, H. S., Internal electric fields near isolated defects in ionic crystals ... 413
—, Optical properties of *U* centers in alkali halides and alkaline earth fluorides ... 659
Bennett, L. H., Zhukov, V. V., Weisman, I. D., Nuclear magnetic resonance of ^{113}Cd and ^{199}Hg in Cd-Mg and Cd-Hg solid solutions ... 713
BeO(c) ... 227
$\Delta Hf°_{298.15K}/BeO(c)$ ... 227
BeO(c), enthalpy of reaction in HF(aq) ... 217
BeO(c), enthalpy of soln in HCl(aq) ... 217
BeO(c), enthalpy of soln in Hf(aq) ... 217
Berg, C. A., Salama, M., Compressive fatigue coaxing in composites ... 369
Beryllium fluoride ... 227
Beryllium oxide ... 217, 227
Bestul, A. B., Chang, S. S., Heat capacities of polyethylene from 2 to 360 K. I. Standard samples of linear and branched polyethylene whole polymer ... 395
Bigge, W. R., Furukawa, G. T., Riddle, J. L., The International Practical Temperature Scale of 1968 in the region 13.81 K as maintained at the National Bureau of Standards ... 309
Binary borates ... 259
Binary silicates ... 259
Bone mineral ... 149
Boron glass ... 259
Branched polyethylene ... 395
Brown, R. L., A numerical solution of the integral equation describing a photometric integrating sphere ... 343
Brown, W. E., Avinmelech, Y., Moreno, E. C., Solubility and surface properties of finely divided hydroxyapatite ... 149
Brunetti, A. P., Prosen, E. J., Goldberg, R. N., The enthalpy of reaction of tris(hydroxymethyl)aminomethane with hydrochloric acid ... 599
Burgers vector ... 49, 359, 607

C

CaF_2 ... 659
Calcium phosphate ... 149
Calibration ... 671
Calorimetry ... 395
Camus, P., Sugar, J., Meggers, W. F., Spectrum and energy levels of neutral thulium ... 1
Cd ... 713
Cd-Hg ... 713
Chang, S. S. Bestul, A. B., Heat capacities of polyethylene from 2 to 360 K. I. Standard samples of linear and branched polyethylene whole polymer ... 395
Ce II ... 419
Cerium ... 419
Cezairliyan, A., Radiance temperature of niobium at its melting point ... 333
—, *Cezairliyan, A.*, Simultaneous measurement of specific heat, electrical resistivity, and hemispherical total emittance of niobium-1(wt. %) zirconium alloy in the range 1500 to 2700 K by a transient (subsecond) technique ... 45
Cleek, G. W., Waxler, R. M., The effect of temperature and pressure on the refractive index of some oxide glasses ... 755
Coaxing ... 369
Composites ... 369
Compressive fatigue ... 369
Compressive fatigue coaxing in composites ... 369
Concentration of saturated water vapor in air ... 115
Continuum mechanics ... 49, 359, 607
Copolymers ... 353
Corliss, C. H., Wavelengths and energy levels of the second spectrum of cerium (Ce II) ... 419
Correction for reflections ... 699
Cross-linking of rubber ... 171
Crystal equation of state ... 407
Crystallization ... 353
Crystallization of random copolymers ... 353

D

Defect ... 49, 359, 607
DeWit, R., Theory of continuous and discrete disclinations in anisotropic elasticity ... 49
—, Theory of disclinations. III: Continuous and discrete disclinations in isotropic elasticity ... 359
—, Theory of disclinations: IV. Straight disclinations ... 607
Dickson, R. W., Schreiber, E., An alumina standard reference material for resonance frequency and dynamic elastic

Page

moduli measurement. II. Characteristic values for use from 25 °C to 1000 °C ... 391
Dicumyl peroxide ... 171
Dipole ... 49, 607
Disclination ... 49, 359, 607
Dislocation ... 49, 359, 607
Distortion ... 49, 359, 607
Douglas, T. B., Krause, R. F., Jr., An experimental search for gaseous reactivity between AlF_3 and HF near 1200 K ... 341

E

Eby, I. C., Sanchez, I. C., Crystallization of random copolymers ... 353
Edsinger, R. E., Guildner, L. A., The Thermodynamic Kelvin Temperature Scale from 273.15 K to 415 K ... 383
—, —, *Anderson, R. L.*, Air flow rate as a test for gage block wringing ... 667
Effect of temperature and pressure on the refractive index of some oxide glasses ... 755
Elastic modulus ... 391
Elastic theory of rubber ... 171
Electric fields ... 413
Electrical resistivity ... 45
Electron scattering resonance ... 411
Electron scavenger ... 109
Electron scavengers ... 249
Emittance ... 45
End lengths standards ... 667
Energy levels ... 1, 419
Enhancement factor ... 115
Enchancement of water vapor in carbon dioxide-free at 30, 40, and 50 °C ... 115
Enthalpies of formation ... 227
Enthalpies of formation of BeO(c) and BeF_2(c) ... 227
Enthalpies of precipitation of silver halides; entropy of the aqueous silver ion ... 569
Enthalpies of reaction of tris(Hydroxymethyl)aminomethane in HCl(aq) and in NaOH(aq) ... 581
Enthalpies of solution of BeO(c) in HF(aq) and in HCl(aq) ... 217
Enthalpy of dilution ... 569
Enthalpy of reaction ... 581, 599
Enthalpy of reaction of H_2SO_4 in aqueous NaOH ... 179
Enthalpy of reaction of tris(hydroxymethyl)aminomethane with hydrochloric acid ... 599
Enthalpy of solution ... 217, 569
Enthalpy of solution of low quartz (α-quartz) in aqueous hydrofluoric acid ... 205
Enthalpy of soln, SiO_2 ... 205
Entropy ... 569
Entropy component ... 171
Equilibrium constant ... 341
Excited states N^- ... 411
Excited states N_2 ... 411

F

F centers ... 413
Fatigue ... 369
Fetters, L. J., Wall, L. A., Strauss, S., Florin, R. E., Pyrolysis of anionic and thermally prepared polystyrenes ... 157
Fire retardants ... 733
Flame inhibition ... 733
Flames ... 733
Florin, R. E., Wall, L. A., Straus, S., Fetters, L. J., Pyrolysis of anionic and thermally prepared polystyrenes ... 157
Frequency distribution ... 407
Frost-point ... 671
Furukawa, G. T., Riddle, J. L., Bigge, W. R., The International Practical Temperature Scale of 1968 in the region 13.81 K to 90.188 as maintained at the National Bureau of Standards ... 309

G

Gage blocks ... 667
Garner, E. L., Gramlich, J. W., Murphy, T. J., Shields, W. R., Absolute isotopic abundance ratio and atomic weight of a reference sample of rhenium ... 691
Gas phase ... 243, 249
Gas phase for ultraviolet photolysis and radiolysis of vinyl chloride ... 243
Gas thermometry ... 383
Gaussian function ... 413
Gel point ... 171
Generator ... 671
Glass ... 259
Glass transition ... 395
Goldberg, R. N., Brunetti, A. P., Prosen, E. J., The enthalpy of reaction of tris(hydroxymethyl)aminomethane with hydrochloric acid ... 599
Gramlich, J. W., Murphy, T. J., Garner, E. L., Shields, W. R., Absolute isotopic abundance ratio and atomic weight of a reference sample of rhenium ... 691
Greenspan, L., Low frost-point humidity generator ... 671
Green's tensor ... 49, 359, 607
Ground state wave function ... 725
Growth rate ... 353
Grüneisen constant ... 407
Grüneisen equation of state ... 407
Guildner, L. A., Anderson, R. L., Edsinger, R. E., Air flow rate as a test for gage block wringing ... 667
—, Edsinger, R. E., The Thermodynamic Temperature Scale from 273.15 K to 415 K ... 383

H

H_2SO_4, enthalpy of reaction in NaOH(aq) ... 179
Hastie, J. W., Molecular basis of flame inhibition ... 733
Heat capacity ... 395
Heat capacities of polyethylene from 2 to 360 K. I. Standards samples of linear and branched polyethylene whole polymer ... 395
Heat of reaction ... 569
Heat of reaction of H_2SO_4 in aqueous NaOH ... 179
Heat of solution ... 217, 581
Heat of solution of H_2SO_4 in aqueous NaOH ... 179
Heat of soln, SiO_2 ... 205
Heat of sublimation ... 237
High-speed measurements ... 45
High temperature ... 45, 333
Holtsmark function ... 413
Homogenization of glass melts ... 259
Humidity ... 671
Hydrogen fluoride ... 341
Hydrosyapatite ... 149
Hyland, R. W., Wexler, A., The enhancement of water vapor in carbon-dioxide free air at 30, 40, and 50 °C ... 115
—, —, The second interaction (cross) virial coefficient for moist air ... 133

I

Immiscible glass melts ... 259
Immiscibility gaps ... 259
Incompatibility ... 49, 359, 607
Inelastic scatter ... 411
Integrating sphere ... 343
Interaction virial coefficients ... 133
Interferometry ... 755
Internal electric fields near isolated defects in ionic crystals ... 413
Internal Mg oxidation ... 713
International Practical Temperature Scale ... 309
International Practical Temperature Scale of 1968 ... 383
International Practical Temperature Scale of 1968 in the region 13.81 K to 90.188 K as maintained at the National Bureau of Standards ... 309
Ion-molecule reaction ... 101
Ion-molecule reactions ... 249
Ion pair yield ... 101
Ion pair yields ... 109
Ionic polarization ... 659
Isolated defects ... 413
Isotropic ... 713
Isotropic abundance ... 691

J

Page

Joining 667

K

KBr 569
KCl 569, 659
Kilday, M. V., Prosen, E. J., An adiabatic solution calorimeter and measurements of a standard reaction for solution calorimetry 179
−, −, Enthalpies of reaction of tris(hydroxymethyl)aminomethane in HCl(aq) and in NaOH(aq) 569
−, −, The enthalpy of solution of low quartz (α-quartz) in aqueous hydrofluoric acid 205
−, −, Wagman, D. D., Enthalpies of solution of BeO(c) in HF(aq) and in HCl(aq) 217
−, *Wagman, D. D.*, Enthalpies of precipitation of silver halides; entropy of the aqueous silver ion 569
Knight shift 713
Krause, R. F., Jr., Douglas, T. B., An experimental search for gaseous reactivity between AlF_3 and HF near 1200 K 341
Krauss, M., Neumann, D., Valence of resonance states of N_2^- ... 411

L

Lamella thickness 353
Langmuir vaporation 237
Lias, S. G., Rebbert, R. E. Ausloos, P., Pulse radiolysis of methane 249
Light scattering 755
Linear polyethylene 395
Liquid ^{4}He 725
Loop 49, 607
Low frost-point humidity generator 671

M

Mavrodineanu, R., Mielenz, K. D., Reflection correction for high-accuracy transmittance measurements on filter glasses ... 699
Meggers, W. F., Sugar, J., Camus, P., Spectrum and energy levels of neutral thulium 1
Melting 333
Melting temperature 353
Methane 101, 109, 249
Mielenz, K. D., Mavrodineanu, R., Reflection correction for high-accuracy transmittance measurements on filter glasses ... 699
Modulus of natural rubber cross-linked by dicumyl peroxide. II. Comparison with theory 171
Modulus of rubber 171
Moist air 115, 133
Moisture content of saturated air 115
Molecular basis of flame inhibition 733
Molecular weight distributions 157
Molecular weights 157
Mollow-Ivey relations 659
Mopsik, F. I., The quasi-harmonic approximation and a generalized Grüneisen equation of state 407
Moreno, E. C., Avinmelech, Y., Brown, W. E., Solubility and surface properties of finely divided hydroxyapatite 149
Mountain, R. D., Raveché, H. J., The pair correlation Function in liquid ^{4}He 725
Murphy, T. J., Gramlich, J. W., Garner, E. L., Shields, W. R., Absolute isotopic abundance ratio and atomic weight of a reference sample of rhenium 691

N

N_2^- 411
NaCl 659
NBS-IPTS-68 309
NBS-1955 provisional scale 309
Neuman, D., Krauss, M., Valence of resonance states of N_2^- 411
Neutralization 249
Neutron diffraction data 725
Niobium 333
Niobium pentoxide 705
Niobium-zirconium alloy 45
Nuclear magnetic resonance of ^{113}Cd and ^{199}Hg in Cd-Mg and Cd-Hg solid solutions 713
Numerical solution of the integral equation describing a photometric integrating sphere 343

O

Optical properties of *U* centers in alkali halides and alkaline earth fluorides 581
Oxide glasses .....

P

Pair correlation function 725
Pair correlation function in ^{4}He 725
Parker, H. S., Waring, J. L., Roth, R. S., Temperature-pressure phase relationships in niobium pentoxide 705
Parker, V. B., The enthalpies of formation of BeO(c) and BeF_2(c) 227
Phase relationships 705
Photochemistry 101
Photochemistry of methane in the photoionization region 101
Photoionization 101
Photolysis 243
Photometry 343
Plante, E. R., Sessoms, A. B., Vapor pressure and heat of sublimation of tungsten 237
Plasticity 49, 359, 607
Platinum resistance thermometer 309
Point-ion potential 659
Polarizability 755
Polyethylene 395
Polymers 157
Polystyrene degradation 157
Pressure 705, 755
Prosen, E. J., Brunetti, A. P., Goldberg, R. N., The enthalpy of reaction of tris(hydroxymethyl)aminomethane with hydrochloric acid 599
−, *Kilday, M. V.*, An adiabatic solution calorimeter and measurements of a standard reaction for solution calorimetry 179
−, −, Enthalpies of reaction of tris(hydroxymethyl)aminomethane in HCl(aq) and in NaOH(aq) 581
−, −. The enthalpy of solution of low quartz (α-quartz) in aqueous hydrofluoric acid 205
−, −, *Wagman, D. D.*, Enthalpies of solution of BeO(c) in HF(aq) and in HCl(aq) 217
Pulse radiolysis 109, 249
Pulse radiolysis of methane 249
Pyrolysis 157
Pyrolysis of anionic and thermally prepared polystyrenes 157

Q

Quantum yield 243
Quantum yields 101
Quartz, soln in HF(aq) 205
Quasi-harmonic approximation 407
Quasi-harmonic approximation and a generalized Grüneisen equation of state 407

R

Radiance temperature 333
Radiance temperature of niobium at its melting point 333
Radiolysis 243
Radiolysis of methane. Formation of acetylene 109
Rate of vaporization 237
Raveché, H. J., Mountain, R. C., The pair corr correlation function in liquid ^{4}He 725
Rebbert, R. E., Ausloos, P., Photochemistry of methane in the photoionization region 101
−, −, Radiolysis of methane. Formation of acetylene 109

Page

—, —, *Wijnen, M. H. J.*, Gas phase for ultraviolet photolysis and radiolysis of vinyl chloride ... 243
—, *Lias, S. G., Ausloos, P.*, Pulse radiolysis of methane ... 249
Reference material, soln calorimetry ... 205
Reflection correction for high-accuracy transmittance measurements on filter glasses ... 699
Reflections, multiple ... 699
Relation of vitron theory to 2-layer-liquid immiscibility in binary silicate and borate glass melts ... 259
Refractive index ... 755
Resonance frequency ... 391
Rhenium ... 691
Riddle, J. L., Furukawa, G. T., Bigge, W. R., The International Practical Temperature Scale of 1968 in the region 13.81 K to 90.188 K as maintained at the National Bureau of Standards ... 309
Roth, R. S., Waring, J. L., Parker, H. S., Temperature pressure phase relationships in niobium pentoxide ... 705
Rubber, elasticity ... 171

S

Salama, M., Berg, C. A., Compressive fatigue coaxing in composites ... 369
Sanchez, I. C., Eby, R. K., Crystallization of random copolymers ... 353
Saturated air ... 115
Schreiber, E., Dickson, R. W., An alumina standard reference material for resonance frequency and dynamic elastic moduli measurement. II. Characteristic values for use from 25 °C to 1000 °C ... 391
Second virial coefficient ... 133
Sessoms, A. B., Plante, E. R., Vapor pressure and heat of sublimation of tungsten ... 237
Shear modulus ... 391
Shields, W. R., Gramlich, J. W., Murphy, T. J., Garner, E. L., Absolute isotopic abundance ratio and atomic weight of a reference sample of rhenium ... 691
Short range behavior ... 725
Short wave ... 725
Silica glass ... 259
Simultaneous measurement of specific heat, electrical resistivity, and hemispherical total emittance of niobium-1 (wt. %) zirconium alloy in the range 1500 to 2700 K by a transient (subsecond) technique ... 45
SiO_2(c), soln in HF(aq) ... 205
Solubility and surface properties of finely divided hydroxyapatite ... 149
Solubility of water vapor in air ... 115
Solubility product ... 149
Solution calorimetry ... 179, 569, 581, 599
Sorption ... 383
Specific heat ... 45
Spectrophotometry, high accuracy ... 699
Spectrum ... 1, 419
Spectrum and energy levels of neutral thulium ... 1
SrF_2 ... 659
Stability limits ... 341
Standard reference material ... 391, 581, 599
Statistical theory of rubber elasticity ... 171
Steam point ... 383
Strain ... 49, 359, 607
Straus, S., Wall, L. A., Florin, R. E., Fetters, L. J., Pyrolysis of anionic and thermally prepared polystyrenes ... 157
Structure factor ... 725
Structure of glass ... 259
Sugar, J., Meggers, W. F., Camus, P., Spectrum and energy levels of neutral thulium ... 1
Surface ... 149
Surface roughness ... 333
Superfluid transition ... 725
Systematic bias in spectrophotometry ... 699

T

Temperature ... 705
Temperature coefficient of refractive index ... 755
Temperature-pressure phase relationships in niobium pentoxide ... 705
Temperature standards ... 383
THAM ... 581
Theory of continuous and discrete disclinations in anisotropic elasticity ... 49
Theory of disclinations. III. Continuous and discrete disclinations in isotropic elasticity ... 359
Theory of disclinations: IV. Straight disclinations ... 607
Thermal analysis ... 395
Thermal expansion ... 755
Thermal polystyrene ... 157
Thermochemistry ... 179, 205, 217, 227, 569, 581, 599
Thermodynamic Kelvin Temperature Scale ... 383
Thermodynamic Kelvin Temperature Scale from 273.15 K to 415 K ... 383
Thermodynamic properties ... 395
Thermodynamics ... 45
Thermodynamics of rubber elasticity ... 171
Thermolysis ... 157
Thulium ... 1
Tilton, L. W., Relation of vitron theory to 2-layer-liquid immiscibility in binary silicate and borate glass melts ... 259
Transmittance, correction ... 699
Transpiration measurements ... 341
TRIS ... 581
Tris(hydroxymethyl)aminomethane ... 581, 599
Tungsten ... 237

U

U centers ... 659

V

Vacuum ultraviolet photolysis ... 109
Valence excited states ... 411
Valence of resonance states of N_2^- ... 411
Vapor pressure ... 237
Vapor pressure and heat of sublimation of tungsten ... 237
Vinyl chloride ... 243
Vinyl radical ... 243
Virial coefficients ... 133
Vitron theory ... 259
Volterra ... 49, 607

W

Wagman, D. D., Kilday, M. V., Enthalpies of precipitation of silver halides; entropy of the aqueous silver ion ... 569
—, —, *Prosen, E. J.*, Enthalpies of solution of BeO(c) in HF(aq) and in HCl(aq) ... 217
Wall, L. A., Straus, S., Florin, R. E., Fetters, L. J., Pyrolysis of anionic and thermally prepared polystyrenes ... 157
Waring, J. L., Roth, R. S., Parker, H. S., Temperature-pressure phase relationships in niobium pentoxide ... 705
Water vapor ... 115, 133, 671
Wavelengths ... 1, 419
Wavelengths and energy levels of the second spectrum of cerium (Ce II) ... 419
Waxler, R. M., Cleek, G. W., The effect of temperature and pressure on the refractive index of some oxide glasses ... 755
Weisman, I. D., Zhukov, V. V., Bennett, L. H., Nuclear magnetic resonance of ^{113}Cd and ^{199}Hg in Cd-Mg and Cd-Hg solid solutions ... 713
Wexler, A., Hyland, R. W., The enhancement of water vapor in carbon dioxide-free air at 30, 40, and 50 °C ... 115
—, —, The second interaction (cross) virial coefficient for moist air ... 133
Wijnen, M. H. J., Ausloos, P., Rebbert, R. E., Gas phase for ultraviolet photolysis and radiolysis of vinyl chloride ... 243
Wiring test ... 667
Wood, L. A., Modulus of natural rubber cross-linked by dicumyl peroxide. II. Comparison with theory ... 171
Wring test ... 667
Wringing ... 667

Y

Young's modulus ... 391
Zhukov, V. V., Weisman, I. D., Bennett, L. H., Nuclear magnetic resonance of ^{113}Cd and ^{199}Hg in Cd-Mg and Cd-Hg solid solutions ... 713

U. S. GOVERNMENT PRINTING OFFICE : 1973 O-LF - 520-812

SJRA UNIVE300UA R 1
UNIVERSITY MICROFILMS INC
ATTN SERIALS SECTION
300 NORTH ZEEB RD
ANN ARBOR MI 48106

GOVERN
PUBL
WA
OFFICIAL BUSINESS
PENALTY FOR PRIVATE USE, $300

U.S. DEPARTMENT OF COMMERCE
POSTAGE AND FEES PAID
COM-375

JOURNAL OF RESEARCH of the National Bureau of Standards
A. Physics and Chemistry

Vol. 77A, No. 6 Nov.–Dec. 1973

Contents

Page

Absolute isotopic abundance ratio and atomic weight of a reference sample of rhenium. John W. Gramlich, Thomas J. Murphy, Ernest L. Garner, and William R. Shields. 691

Reflection correction of high-accuracy transmittance measurements on filter glasses. K. D. Mielenz and R. Mavrodineanu. 699

Temperature-pressure phase relationships in niobium pentoxide, J. L. Waring, R. S. Roth, and H. S. Parker. 705

Nuclear magnetic resonance of ^{113}Cd and ^{199}Hg in Cd-Ag and Cd-Hg solid solutions. V. V. Zhukov, I. D. Weisman, and L. H. Bennett. 713

The pair correlation function in liquid ^4He. Raymond D. Mountain and Harold J. Raveché. 725

Molecular basis of flame inhibition. J. W. Hastie. 733

The effect of temperature and pressure on the refractive index of some oxide glasses. Roy M. Waxler and G. W. Cleek. 755

Publications of the National Bureau of Standards 765

Index to volume 77A, January to December 1973 783

Library of Congress Catalog Card Number: 62–37059

For sale by the Superintendent of Documents, U.S. Government Printing Office, Washington, D.C. 20402. (Order by SD Catalog No. C 13.22/sec.A:77/6). Single copy price varies. This issue $1.85 Subscription price: $17.00 a year; $4.25 additional for foreign mailing.

UNITED STATES GOVERNMENT PRINTING OFFICE, WASHINGTON : 1973